

# **Ceramic wasteforms for wastes arising from potential future fuel cycles**

Daniel Joseph Bailey

Thesis

Submitted for the degree of Doctor of Philosophy



The  
University  
Of  
Sheffield.

Department of Materials Science and Engineering

University of Sheffield

September 2017

# Abstract

The UK produces considerable volumes of radioactive materials as a result of nuclear power generation and subsequent reprocessing of spent nuclear fuel. Spent fuel is currently reprocessed using the PUREX process and the subsequent High Level Waste is immobilised in a borosilicate glass matrix, however, some elements present in the waste complicate the vitrification process either through volatilisation or the formation of undesirable secondary products. Proposed future fuel cycles offer the opportunity for enhanced segregation of wastes and therefore open up the possibility of more tailored disposal routes such as immobilisation in ceramic matrices. This thesis presents a series of studies on the immobilisation of problematic elements by the use of ceramic matrices. The wastes selected were: caesium, iodine, technetium, plutonium and Mixed Oxide Fuel residues.

A summary of the main results for each waste are provided below:

**Caesium-** The titanate phase hollandite was selected as the host matrix of choice for this study. A range of Cs containing iron hollandites were synthesised via an alkoxide-nitrate route and the structural environment of Fe in the resultant material characterised by Mössbauer and X-ray Absorption Near Edge Spectroscopy. The results of spectroscopic analysis found that Fe was present as octahedrally co-ordinated Fe (III) in all cases and acts as an effective charge compensator over a wide solid solution range.

**Iodine-** Iodine immobilisation in the apatite structured iodovanadinite phase was studied using hot isostatic pressing (HIPing) to minimise iodine volatilisation. Increasing the overpressure during HIPing was found to yield products of superior density. The use of AgI as an iodine source was found to complicate the formation of the apatite phase and when used as the sole source was found to not be incorporated into the target phase at all. The possibility of co-immobilisation of Tc was investigated by using the surrogate molybdenum. Limited substitution of Mo into the apatite structure was observed however, this observation is complicated by the aforementioned non-incorporation of AgI. Further investigation is necessary to investigate the possibility of Mo incorporation when not using AgI as the iodine source. Substitution of Ba into the structure resulted in

the formation of  $\text{Ba}_3(\text{VO}_4)_2$  structured phase with solid-solution behaviour observed between Ba and Pb.

**Mixed Oxide Fuel residues-** Brannerite was selected as the potential host matrix for the disposal of MOX residues due to its high potential waste loading. Ce was used as an inactive structural surrogate for plutonium. The resultant phase assemblage was found to be dependent on both processing atmosphere and waste loading. In air, it was found that decreasing waste loading by substituting the neutron absorber gadolinium improved the phase assemblage. Reacting brannerites in a reducing atmosphere was found to produce a highly unfavourable phase assemblage with large amounts of retained  $\text{UO}_2$ . The most favourable phase assemblage was found to be achieved by sintering in argon however, increasing substitution of Gd was found to have a negative impact. XANES study found that Ti oxidation state remained unchanged whereas Ce was found to reduce from the +4 to the +3 oxidation state in all cases. The use of  $\mu$ -focus XANES confirmed that charge compensation was achieved by the oxidation of U(IV) to higher oxidation states.

**Technetium and plutonium-** Zirconolite was selected as a potential host phase for the co-disposal of technetium and plutonium and studied using the non-active surrogates Ce and Mo. The formation of the zirconolite phase was found to be improved by reaction at higher temperatures and the use of  $\text{CaTiO}_3$  as the Ca precursor instead of  $\text{CaCO}_3$ . Cold pressed and sintered zirconolites were found to be highly porous and this was attributed to the volatilisation of Mo at elevated temperatures. Hot isostatic pressing was found to improve the density of synthesised zirconolites however, the temperature limitations imposed by the use of stainless steel cans resulted in an unfavourable phase assemblage. HIPing for a longer period of time may compensate for the reaction kinetics or HIPing in an alternative can material at a higher temperature.

# Acknowledgements

Firstly, I would like to thank my supervisors Professor Neil Hyatt and Doctor Martin Stennett. The amount of different analysis techniques/data/general science present in this thesis is testament to both of your expertise and enthusiasm. Neil, thank you, not only for all your efforts helping me to complete this thesis but for encouraging my interest in nuclear waste management back when I was still an undergraduate and for giving me the opportunity to carry on learning. Martin, thank you for all your help with both labwork and data analysis and for also putting up with my persistent questioning and badgering.

I would like to thank the EPSRC for financial support through the Nuclear FiRST Doctoral Training Centre

Thank you to everybody in the ISL. You've all helped to make the last few years a pleasure. Within the ISL there is also the exclusive Brotherhood of Dan, I think we've got most aspects of high level waste disposal and spectroscopy covered between us now. I would also like to give special thanks to Dr. Claire Corkhill for all her help and enthusiasm and Dr. Paul Heath, Steph Thornber and Dr. Laura Gardner for all their HIP related help, answering all my questions and fixing everything I managed to break. Sorry!

I must thank the beamline scientists who kindly provided their beamlines for the XAS studies in this thesis: Dr. Daniel Grolimund of SLS, Dr. Ryan Tappero of BNL and lastly Dr. Bruce Ravel of NIST who I also thank for his gracious hospitality during my visits to Brookhaven.

My final thanks go to Isla. Thank you for listening to my griping and grumbling, tolerating 'science talk' and generally putting up with me throughout the course of my studies. You must have the patience and grace of a saint.

# Publications

The author has contributed to the following publications during the production of this thesis:

D. J. Bailey, M. C. Stennett, and N. C. Hyatt, “Synthesis and Characterization of Brannerite Wasteforms for the Immobilization of Mixed Oxide Fuel Residues,” *Procedia Chem.*, vol. 21, pp. 371–377, 2016.

D. J. Bailey, M. C. Stennett, and N. C. Hyatt, “Synthesis and Characterization of Brannerite Compositions for MOX Residue Disposal,” *MRS Adv.*, vol. 2, pp. 557-562, 2016.

D. J. Bailey, M. C. Stennett, B. Ravel, D. Grolimund and N. C. Hyatt, “Synthesis and characterisation of brannerite compositions  $(U_{0.9}Ce_{0.1})_{1-x}M_xTi_2O_6$  ( $M = Gd^{3+}, Ca^{2+}$ ) for the immobilisation of MOX residues,” *RSC Adv.*, vol. 8(4), pp. 2092-2099, 2018.

D. J. Bailey, M. C. Stennett, A. R. Mason and N. C. Hyatt, “Synthesis and characterisation of the hollandite solid solution  $Ba_{1.2-x}Cs_xFe_{2.4-x}Ti_{5.6+x}O_{16}$  for partitioning and conditioning of radiocaesium,” *Journal of Nuclear Materials*, vol. 503, pp. 164–170, 2018.

D. J. Bailey, M. C. Stennett, B. Ravel, D. E. Crean and N. C. Hyatt, “A Synchrotron X-ray Spectroscopy Study of Titanium Co-ordination in Explosive Melt Glass Derived From the Trinity Nuclear Test,” IN REVIEW.

D. J. Bailey, S. M. Lawson, M. C. Stennett and N. C. Hyatt, “A new approach to the immobilisation of Tc and Pu: co-disposal in a zirconolite ceramic matrix,” IN REVIEW

D. J. Bailey, E. V. Johnstone, M. C. Stennett and N. C. Hyatt, “An investigation of iodovanadinite wasteforms for the immobilisation of radio-iodine and technetium,” IN REVIEW

C. L. Corkhill, D. E. Crean, D. J. Bailey, C. Makepeace, M. C. Stennett, R. Tappero, D. Grolimund, N. C. Hyatt, “Multi-scale investigation of uranium attenuation by arsenic at an abandoned uranium mine,” *Nature Materials and Degradation*, vol. 1, pp. 1-7, 2017.

E. V. Jonhstone, D. J. Bailey, M. C. Stennett, J. Heo and N. C. Hyatt, “On the existence of  $\text{AgM}_9(\text{VO}_4)_6\text{I}$  (M=Ba, Pb),” *RSC Adv.*, vol. 7(77), pp. 49004-49009, 2017.

S. T. Barlow, D. J. Bailey, A. J. Fisher, M. C. Stennett, C. L. Corkhill, and N. C. Hyatt, “Synthesis of simulant ‘lava-like’ fuel containing materials (LFCM) from the Chernobyl reactor Unit 4 meltdown,” *MRS Adv.*, vol. 2, pp. 609-614, 2016.

C. L. Corkhill, D. J. Bailey, F. Y. Tocino, M. C. Stennett, J. A. Miller, J. L. Provis, K. P. Travis, and N. C. Hyatt, “Role of Microstructure and Surface Defects on the Dissolution Kinetics of  $\text{CeO}_2$ , a  $\text{UO}_2$  Fuel Analogue,” *ACS Appl. Mater. Interfaces*, vol. 8, pp. 10562-10571, 2016.

M. C. Stennett, T. Lee, D. J. Bailey, E. V. Johnstone, J. Heo, and N. C. Hyatt, “Ceramic Immobilization Options for Technetium,” *MRS Adv.*, vol. 2, pp. 753–758, 2017.

N. C. Hyatt, C. L. Corkhill, D. J. Bailey, A. J. Fisher, and R. J. Hand, “Comment on ‘Preliminary assessment of modified borosilicate glasses for chromium and ruthenium immobilization’, by Farid and Rahman,” *Mater. Chem. Phys.*, vol. 192, pp. 29–32, 2017.

C. Corkhill, E. Myllykyla, D. J. Bailey, S. M. Thornber, J. Qi, P. Maldonado, M. C. Stennett, A. Hamilton, and N. C. Hyatt, “The contribution of energetically reactive surface features to the dissolution of  $\text{CeO}_2$  and  $\text{ThO}_2$  analogues for spent nuclear fuel microstructures.,” *ACS Appl. Mater. Interfaces*, vol. 6, pp. 12279-12289, 2014.

The work in this thesis has also been disseminated at a number of conferences which are listed below:

### **Oral Presentations**

Meeting of the Materials Research Society - Boston, November 2016.

5<sup>th</sup> International ATALANTE Conference on Nuclear Chemistry for Sustainable Fuel Cycles, Montpellier, June 2016.

## **Poster Presentations**

Thermal Treatment of Radioactive Wastes Symposium, Warrington, 2013.

Thermal Treatment of Radioactive Wastes Symposium, Warrington, 2014.

# Contents

Abstract .....	i
Acknowledgements .....	iii
Publications .....	iv
1. Introduction.....	1
2. Literature Review .....	4
2.1. Ionising radiation and nuclear fission .....	4
2.2. Nuclear Power .....	6
2.2.1. Nuclear fuels .....	9
2.2.2. Radioactive wastes and classifications.....	10
2.3. Spent nuclear fuel, reprocessing and advanced extractions .....	11
2.3.1. Reprocessing .....	13
2.3.2. Aqueous extraction methods .....	13
2.3.3. Pyroprocessing .....	17
2.4. Disposal of High Level Waste.....	18
2.4.1. Geological disposal .....	19
2.4.2. Host geology .....	20
2.4.3. Heat generating wastes.....	21
2.5. Wasteforms.....	22
2.5.1. Caesium.....	23
2.5.2. Iodine.....	24
2.5.3. Plutonium and plutonium-rich residues .....	24
2.5.4. Technetium.....	25
3. Experimental Procedures .....	32
3.1. Batching and milling .....	32
3.1.1. The use of surrogates .....	32
3.2. Hollandite synthesis .....	33
3.3. Cold pressing and sintering .....	33
3.4. Hot isostatic pressing (HIP) .....	36
3.5. X-ray diffractometry (XRD).....	41
3.5.1. X-rays and Bragg's law.....	41
3.5.2. X-ray diffractometers and X-ray optics .....	42

3.5.3.	Sample preparation and measurement .....	44
3.5.4.	Rietveld refinement.....	45
3.6.	X-ray absorption spectroscopy (XAS) .....	46
3.7.	Scanning electron microscopy and energy dispersive X-ray spectrometry (SEM-EDX).....	48
3.7.1	Resolution and the use of electrons.....	48
3.7.2	Electron beam generation and imaging.....	50
3.7.3	Electron-specimen interactions .....	51
3.7.4	Energy dispersive X-ray spectroscopy (EDX).....	52
3.7.5	Sample preparation .....	53
3.8.	Transmission electron microscopy (TEM).....	54
3.9.	Mössbauer spectroscopy.....	55
3.9.1.	Resonant absorption in free atoms .....	55
3.9.2.	Resonant absorption in solids .....	57
3.9.3.	Spectroscopic measurements and hyperfine parameters.....	57
3.10.	Gamma spectroscopy.....	59
3.11.	Inductively Coupled Plasma- Mass Spectrometry.....	60
3.12.	Thermal analysis .....	60
3.13.	Gas pycnometry .....	61
4.	Synthesis and characterisation of the hollandite solid solution $Ba_{1.2-x}Cs_xFe_{2.4-x}Ti_{5.6+x}O_{16}$ for partitioning and conditioning of radiocaesium.....	63
5.	An investigation of iodovanadinite wastefoms for the immobilisation of radioiodine and technetium .....	64
6.	Synthesis and characterisation of brannerite compositions $(U_{0.9}Ce_{0.1})_{1-x}M_xTi_2O_6$ ( $M = Gd^{3+}, Ca^{2+}$ ) for the immobilisation of MOX residues.....	65
7.	A new approach to the immobilisation of Tc and Pu: co-disposal in a zirconolite ceramic matrix.....	66
8.	A Synchrotron X-ray Spectroscopy Study of Titanium Co-ordination in Explosive Melt Glass Derived From the Trinity Nuclear Test .....	67
9.	Summary.....	68
9.1.	Chapter 4.....	68
9.2.	Chapter 5.....	69
9.3.	Chapter 6.....	70
9.4.	Chapter 7.....	71
9.5.	Chapter 8.....	73

References .....	75
Appendices .....	84
Table of Figures.....	84
Published Papers.....	86

# 1. Introduction

Significant volumes of radioactive wastes are produced at all stages of the nuclear fuel cycle, including the reprocessing of spent nuclear fuel (SNF). UK SNF is currently reprocessed using the PUREX process (Plutonium URanium EXtraction) at the Thermal Oxide Reprocessing Plant (ThORP) and the Magnox Reprocessing Plant, Sellafield, Cumbria. Reprocessing allows recyclable uranium and plutonium to be extracted from the SNF; the remaining material consists of fission products and minor actinides in a nitric acid solution. This acidic solution is known as Highly Active Liquor (HAL). Due to the high radionuclide content HAL is classed as High Level Waste (HLW). HAL poses an extreme radiological, as well as chemical, hazard and therefore requires suitable treatment before disposal. Current practice is to immobilise HAL in a borosilicate glass matrix and store the glass prior to final disposal in a geological disposal facility (GDF). Geological disposal relies on the multibarrier concept wherein multiple engineered barriers are used to prevent egress of radionuclides from the storage site to the biosphere. Radiogenic heating, caused by the decay of short-lived fission products, limits the efficiency with which GDF space can be used.

Future expansion of the UK's nuclear generating capacity will result in a substantial inventory of SNF. Ensuring sustainability of uranium resources will require fuel recycling, using advanced extraction processes, and enhanced burn-up of nuclear fuel. Any expansion of the civil nuclear energy programme is therefore expected to require a concomitant expansion of the GDF footprint to accommodate the resulting HLW products (which must be well separated due to radiogenic decay heat).

Advanced extraction processes offer the opportunity for further segregation of wastes than the current PUREX process. Further separation of fission products and minor actinides provides an opportunity to better manage the heat load within a repository and also to create tailor-made ceramic wastefoms of potentially superior waste loading and performance relative to current borosilicate waste glasses.

The current project was conceived to design, fabricate and demonstrate novel advanced wastefoms for the disposal of wastes arising from possible future fuel cycles. The

wastestreams investigated are all problematic with regards to disposal in current HLW glass compositions and are therefore prime candidates for immobilisation in ceramic matrices. The wastestreams studied were: separated caesium from reprocessing of SNF, mixed oxide fuel residues resulting from fuel recycle activities, iodine captured in off-gas scrubbers during head-end processes or present as undissolved solids in SNF and co-disposal of long-lived technetium and plutonium wastes that may arise dependent upon future decisions by UK government regarding the status of plutonium.

This thesis also contains a supplementary Chapter detailing the determination of Ti co-ordination environment in an explosive melt glass derived from the Trinity nuclear test by X-ray absorption spectroscopy. This work was completed as part of the Nuclear FiRST DTC programme.

The contribution of the author to the included publications is as follows:

Chapter 4: “*Synthesis and characterisation of the hollandite solid solution  $Ba_{1.2-x}Cs_xFe_{2.4-x}Ti_{5.6+x}O_{16}$  for partitioning and conditioning of radiocaesium.*” The author’s contribution was the production of samples, X-ray diffraction, pycnometry, electron microscopy, Mössbauer spectroscopy, analysis of XAS data and writing of the manuscript. XAS data were acquired by A. R. Mason and M. C. Stennett.

Chapter 5: “*An investigation of iodovanadinite wastefoms for the immobilisation of radio-iodine.*” The author’s contribution was the production of samples, X-ray diffraction, thermogravimetric analysis, SEM/EDX analysis and writing of the manuscript.

Chapter 6: “*Synthesis and characterisation of brannerite compositions  $(U_{0.9}Ce_{0.1})_{1-x}M_xTi_2O_6$  ( $M = Gd^{3+}, Ca^{2+}$ ) for the immobilisation of MOX residues.*” The author’s contribution was the production of samples, X-ray diffraction, electron microscopy, XAS data acquisition and analysis and writing of the manuscript.

Chapter 7: “*A new approach to the immobilisation of Tc and Pu: co-disposal in a zirconolite ceramic matrix.*” The author’s contribution was the production of samples, X-ray diffraction, thermogravimetric analysis, SEM/EDX analysis, analysis of electron diffraction patterns, analysis of XAS data and writing of the manuscript. TEM electron

diffraction patterns were acquired by S. M. Lawson and XAS data were acquired by S. K. Sun.

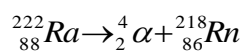
Chapter 8: “*A Synchrotron X-ray Spectroscopy Study of Titanium Co-ordination in Explosive Melt Glass Derived From the Trinity Nuclear Test.*” The author’s contribution was gamma spectroscopy, SEM/EDX analysis, processing of ICP-MS data, XAS data acquisition and analysis and writing of the manuscript. HF digestion and ICP-MS analysis were performed by N. Bramall and XAS data were acquired by M. C. Stennett and N. C. Hyatt.

## 2. Literature Review

### 2.1. Ionising radiation and nuclear fission

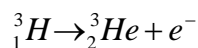
The nucleus of an atom consists of protons and neutrons, collectively known as nucleons. Protons are positively charged and mutually repel other protons, as a result, as the number of protons in a nucleus increases more neutrons are required to stabilise the nucleus. Radioactive decay is a spontaneous process caused by the instability of an atomic nucleus. Energy is released from an unstable nucleus by the emission of ionising radiation. There are three types of ionising radiation: alpha, beta and gamma.

Alpha decay is characteristic of heavy nuclei ( $A > 200$ ). When a nucleus undergoes alpha decay an ‘alpha particle’ (a helium nucleus- two protons, two neutrons) is ejected from the nucleus. As a result, the mass of the parent nucleus is reduced by four and the number of protons is reduced by two. The loss of protons changes the identity of a chemical element; this process is known as transmutation. An example of alpha decay is the decay of radium to form radon.



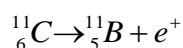
**Equation 1**

There are three types of beta decay; negatron and positron decay ( $\beta^-$  and  $\beta^+$ ) and electron capture. Negatron decay is characteristic of lighter, neutron-rich nuclei. Positron decay and electron capture are characteristic of low and medium mass neutron-poor nuclei. During negatron decay a neutron becomes a proton and a high energy electron is emitted.



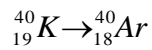
**Equation 2**

In positron decay a proton becomes a neutron and a positron (the positive equivalent of an electron) is emitted.



**Equation 3**

In electron capture a proton captures an electron and becomes a neutron.

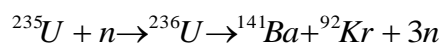


**Equation 4**

Unlike alpha particles, the energy of beta particles is not well defined. Beta particles are instead emitted over a range of energies up to a characteristic maximum,  $E_{\text{max}}$ . The emission of a beta-particle must also be accompanied by the emission of a neutrino or anti-neutrino, ‘massless’ particles with spin and energy, (for  $\beta^+$  and  $\beta^-$  decay respectively) to balance the energy of the transition.

When a nucleus is in an excited state the nucleus de-excites by the emission of a photon, this photon is known as a gamma ray. The energy of the emitted gamma ray is well defined and characteristic of the isotope it is emitted by.

Nuclear power generation relies on the interaction of neutrons with the nuclei of the nuclear fuel. There are four types of nuclear interaction: elastic scattering, inelastic scattering, radiative capture and fission. Elastic scattering results in an exchange of kinetic energy between a neutron and the nucleus, the structure of the nucleus is unchanged. Inelastic scattering results in a net loss of kinetic energy and the target nucleus is left in an excited state; the structure of the nucleus, as with elastic scattering, remains unchanged. When capture occurs the neutron is absorbed by the target nucleus forming a compound nucleus, the newly formed compound nucleus is stabilised by the emission of a gamma ray. When fission occurs, a compound nucleus is formed and then divides into two smaller daughter nuclei, known as ‘fission products’, neutrons are released during this process, see Equation 5. Energy is released during the fission process, in nuclear fuel this energy results in the fuel being heated. The neutrons released during fission can in turn proceed to cause fission in another fissile nucleus and can result in a chain reaction. When controlled, a chain reaction can be used to generate power. If uncontrolled the chain reaction can result in an explosion, as utilised in nuclear weapons.



**Equation 5**

The fission of a nucleus is rarely symmetrical, i.e. the daughter nuclei are rarely the same elements. The formation of symmetrical daughter products is not favoured as one fragment seeks to attain a magic number of nucleons and, consequently, asymmetrical fission is more common. The masses of the fission products of  $^{235}\text{U}$  have maxima near atomic mass of 90 and 137, as shown in Figure 2.1, hence  $^{90}\text{Sr}$  and  $^{137}\text{Cs}$  have relatively high fission yields.

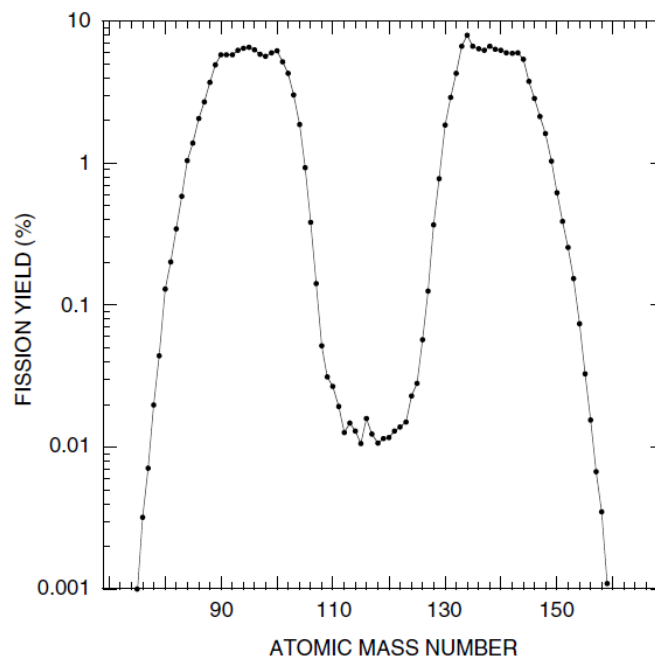


**Figure 2.1:** Yield of fission fragments as a function of atomic mass number  $A$  for thermal fission of  $^{235}\text{U}$  (in percent per fission). Taken from Bodansky (1997) [1].

## 2.2. Nuclear Power

Nuclear power reactors utilise the heat released during the fission of  $^{235}\text{U}$  and  $^{239}\text{Pu}$  to generate electricity.

The core of a nuclear power reactor contains the fuel, the fuel is fabricated into fuel elements for ease of transport and handling. In a thermal reactor, the fuel elements are surrounded by a moderator and a coolant to remove the heat generated during power production. A moderator acts to reduce the speed of neutrons released by fission. The probability of fission (known as the ‘cross section’) is higher for neutrons of lower energy, known as thermal neutrons, see Figure 2.2. Neutrons released during fission are not thermal neutrons and a moderator is therefore required to slow the neutrons and increase

the chance of neutron capture. Fast reactors utilise fast, un-moderated neutrons to achieve fission and consequently do not have a moderator. Control rods, made of neutron absorbing materials, penetrate the core and are used to control neutron flux within the reactor.

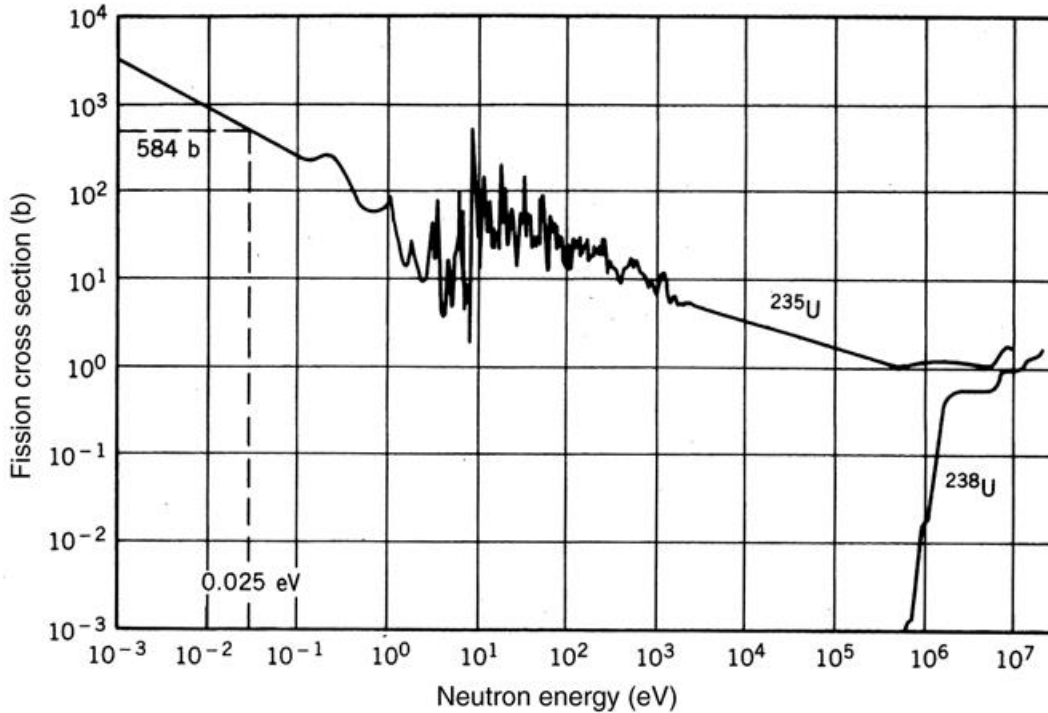


**Figure 2.2:** Neutron-induced fission cross section of  $^{235}\text{U}$  and  $^{238}\text{U}$  as a function of neutron energy,  $E_n$ . Taken from Loveland, Morrisey and Seaborg (2005) [2].

Commercial nuclear power reactors are broadly categorised by the type of coolant that is used; common coolants include carbon dioxide gas and light water but some reactors use coolants such as liquid sodium or heavy water. Indigenous UK reactor designs, Magnox and the Advanced Gas Cooled reactor (AGR), use a pressurised gaseous carbon dioxide coolant in combination with a solid graphite moderator. The pressurised coolant passes through the core and is heated, it then passes through a heat exchanger where it transfers heat to a secondary steam generating loop, see Figure 2.3, the steam produced in this loop is used to drive turbines attached to generators.

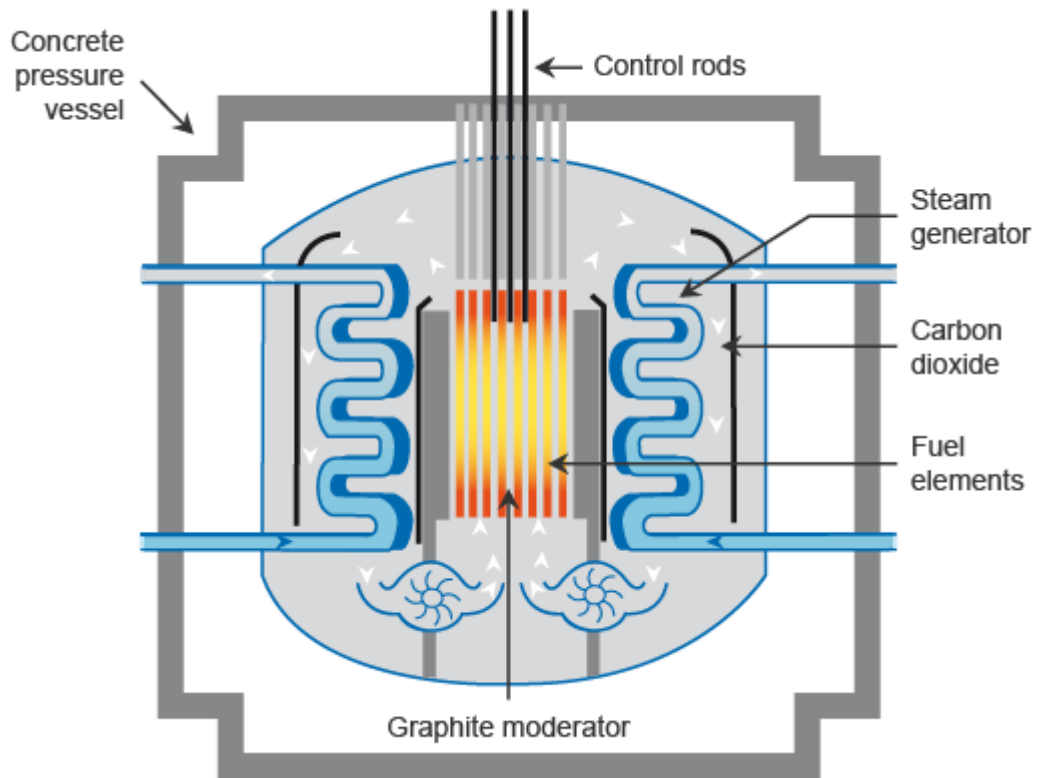


**Figure 2.3:** A schematic of an Advanced Gas-cooled Reactor (AGR) [3].

The most common type of power reactor is the Pressurised Water Reactor (PWR, 291 of 450 reactors worldwide [4]). A PWR uses light water as both moderator and coolant, the water is pressurised to ensure that the coolant remains liquid and does not undergo a phase change. A schematic of a PWR is shown in Figure 2.4. Boiling Water Reactors (BWR) also use light water as a coolant but the coolant is not pressurised and is instead allowed to vapourise; the resultant steam is used directly to generate electricity.

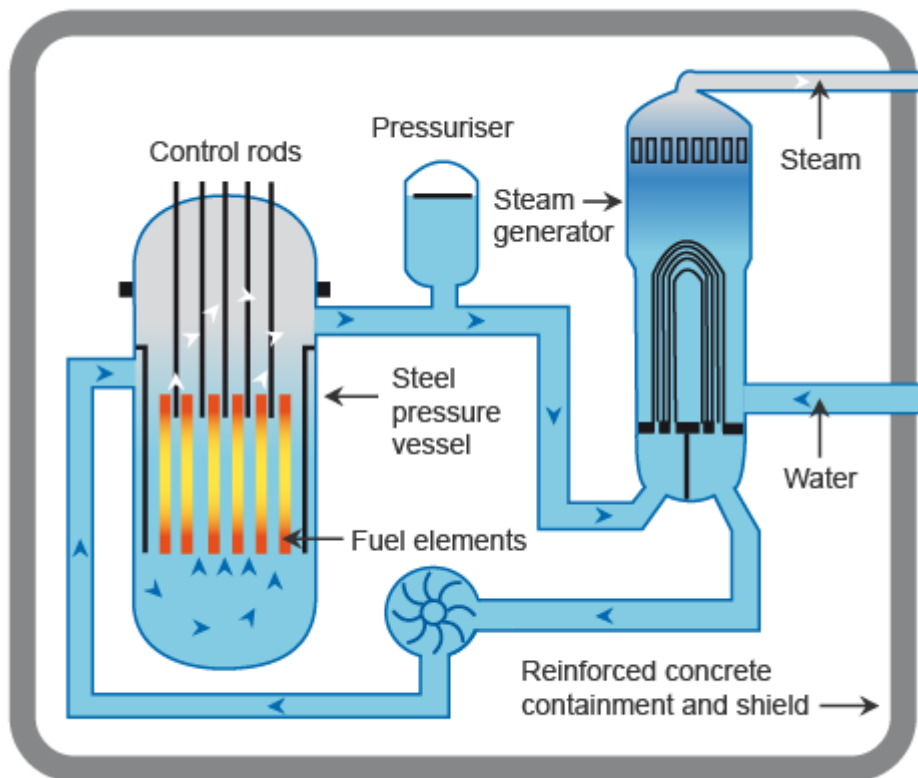


**Figure 2.4:** A schematic of a Pressurised Water Reactor (PWR) [3].

### 2.2.1. Nuclear fuels

The fuels used in nuclear power generation are based upon fissile elements, the most common fissile element used in nuclear fuel is  $^{235}\text{U}$ , however, fuels may also use  $^{239}\text{Pu}$ . It is possible to use fertile isotopes to ‘breed’ more fuel in reactors, fertile isotopes are isotopes that become fissile as a result of neutron absorption e.g. fertile  $^{238}\text{U}$  and  $^{232}\text{Th}$  are transmuted to fissile  $^{239}\text{Pu}$  and  $^{233}\text{U}$  respectively in the neutron flux of the reactor. First generation civil power reactors, such as Magnox, used natural uranium metal fuel. At  $662^\circ\text{C}$  U metal undergoes a phase change from  $\alpha\text{-U}$  to  $\beta\text{-U}$ , this phase change is accompanied by a significant volume expansion and must be avoided in order to prevent undue stresses and potentially cracking within the fuel. Consequently no part of the fuel can exceed this temperature. Magnox stations used U metal fuel but their operating temperature was limited to  $450^\circ\text{C}$  to avoid excessive oxidation of the magnesium alloy cladding [5].

Uranium fuel of natural isotopic distribution contains a low proportion of fissile  $^{235}\text{U}$ , as a result large arrays of fuel elements are required to maintain power, increasing costs. To

solve these problems second generation reactors, such as the AGR, and onwards have used enriched ceramic  $\text{UO}_2$  fuel. Enriched fuel is fuel which contains a higher proportion of  $^{235}\text{U}$  to  $^{238}\text{U}$  relative to that found in natural uranium. The use of oxide fuels instead of metallic fuel requires the use of different cladding materials such as stainless steel or Zircaloy [5].

Mixed oxide fuel (MOX) is a mix of natural or depleted uranium dioxide with up to 8 wt% plutonium dioxide ( $\text{PuO}_2$ ). MOX allows plutonium recovered during reprocessing to be recycled and reduces demand for uranium ore and enrichment. It is possible for thermal reactors to use a core loading of up to 30-40 % MOX fuel without significantly altering the characteristics of the core. Due to the ingrowth of decay products such as  $^{241}\text{Am}$  with time, MOX fuel fabrication plants require additional radiological shielding, increasing the cost of MOX fuel production relative to that of uranium oxide fuel [5].

### 2.2.2. *Radioactive wastes and classifications*

Radioactive wastes are deemed to be materials containing radionuclides that may not be exploited to serve a useful purpose. The nuclear fuel cycle generates radioactive wastes at all stages from ore extraction to fuel reprocessing.

The ionising radiation produced by the decay of radioisotopes in nuclear wastes and spent nuclear fuel (SNF) poses a significant risk to the health of humans. The risk to health is a result of damaging interactions between the ionising radiation and the biological systems of the body and is dependent on the type of radiation ( $\alpha$ ,  $\beta$  or  $\gamma$ ), the energy of the radiation, the dose received and the body part receiving the dose.

The negative effects of radiation dose may be split into two categories: stochastic and deterministic effects. Deterministic effects occur above a threshold dose and become increasingly severe with increasing dose. Deterministic effects are typically the result of cell death and include skin erythema, the destruction of bone marrow and destruction of the gastro-intestinal tract. The threshold dose for deterministic effects is dependent on the body part receiving the dose. Stochastic effects have no threshold dose and the probability of negative effects increases with increasing dose, the severity of stochastic effects are not linked to the dose received.

The dangers posed by radioactive wastes require that they are suitably treated to minimise the chances of danger to the human population

Wastes are varied in their composition and radioactivity. The composition and activity of wastes determines their treatment and final disposal options and they are therefore categorised to simplify their handling.

In the UK solid wastes are classified as either high, intermediate, low level or very low level wastes (HLW, ILW, LLW and VLLW). These waste categories are defined as follows:

- HLW- wastes in which the temperature may rise significantly as a result of their radioactivity, so that this factor has to be taken into account in designing storage or disposal facilities
- ILW- wastes with radioactivity exceeding the upper boundaries for low-level wastes, but which do not require heating to be taken into account in the design of storage or disposal facilities
- LLW- wastes containing radioactive materials other than those acceptable for disposal with ordinary refuse, but not exceeding 4 GBq.t<sup>-1</sup> alpha or 12 GBq.t<sup>-1</sup> beta/gamma
- VLLW- wastes which can be safely disposed of with ordinary refuse (dust-bin disposal), each 0.1 m<sup>3</sup> of material containing less than 400 kBq beta/gamma activity or single items containing less than 40 kBq beta/gamma activity. Such wastes need not be considered further [5].

### **2.3. Spent nuclear fuel, reprocessing and advanced extractions**

Over time the reactivity of nuclear fuel is reduced (due to consumption of fissionable isotopes and build-up of deleterious fission products) necessitating its removal and replacement. After removal from a reactor, fuel is known as spent nuclear fuel (SNF). “Burn-up”, the amount of fission the fuel has undergone, strongly affects the composition and properties of SNF. A typical burn up is in the range 35-45 MWdkg<sup>-1</sup> U. For a burn-up of 40 MWdkg<sup>-1</sup> U, 4 % of the uranium will have transformed into approximately 3 % fission products (e.g. <sup>137</sup>Cs, <sup>90</sup>Sr) and 1 % transuranic elements (e.g. <sup>239</sup>Pu, <sup>237</sup>Np). Due to variations in burn up and the build of fission products within the fuel pellet, SNF has a

highly complicated and heterogeneous structure, as shown in Figure 2.5. The rim of the fuel pellets become enriched in Pu and oxide precipitates of fission products, some fission products also migrate to grain boundaries. Gaseous fission products form bubbles within the microstructure. Discrete metallic alloy phases, known as  $\epsilon$ -particles, are also found throughout the structure.

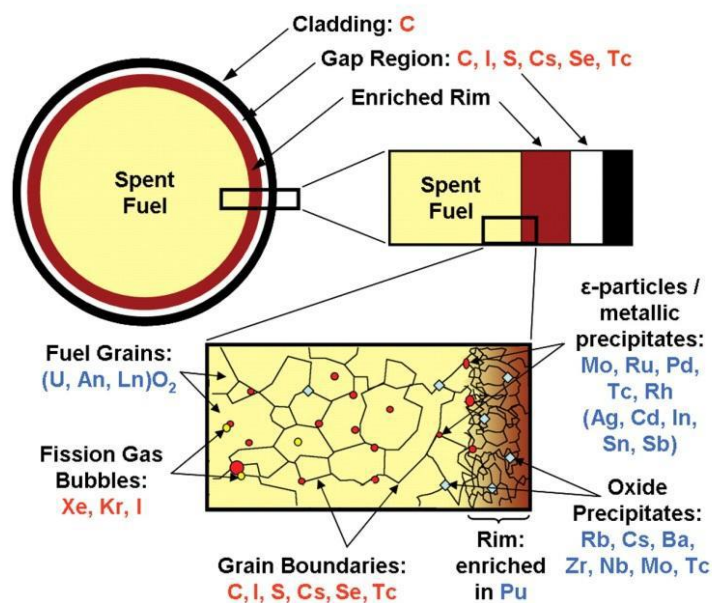


**Figure 2.5:** Schematic illustration of the microstructure of spent fuel, showing the distribution of actinides and fission products following burn up in a reactor. From Bruno and Ewing (2006) [6].

Fission products and transuranic elements significantly increase the radioactivity of SNF, typically by a factor of a million, this equates to an activity of  $10^{17}$  Becquerel/metric tonne (Bq.tonne<sup>-1</sup>). For a higher burn-up, a greater proportion of the U will have undergone fission and therefore there will be a concomitant increase in the proportion of fission products present within the fuel, further increasing the activity of the SNF.

One year after discharge from the reactor, the activity of SNF remains at extremely hazardous levels; the dose rate at one metre from the fuel assembly is  $1 \times 10^6$  millisieverts per hour (mSv.h<sup>-1</sup>). By comparison, the natural dose received from background radiation is 3 mSv.y<sup>-1</sup> [6]. A person exposed to such a high dose rate of radiation, over the whole body, would receive a lethal dose in less than a minute; the hazardous nature of SNF necessitates remote handling.

### 2.3.1. Reprocessing

Nuclear fuel reprocessing is used to extract and recycle the potentially useful components of SNF, U and Pu. In the United Kingdom, reprocessing of spent  $\text{UO}_2$  fuel is performed at the Thermal Oxide Reprocessing Plant, Sellafield, Cumbria (ThORP). After removal from the reactor, SNF is cooled underwater prior to placement in a transport flask and transported to Sellafield for reprocessing. The fuel elements are removed from the transport flasks and transferred to the reprocessing line. Methods of reprocessing include solvent extraction and pyroprocessing. Currently the remaining material after removal of U and Pu, a mix of minor actinides and fission products, is not recycled and is treated as waste.

### 2.3.2. Aqueous extraction methods

Aqueous extraction methods rely on the principle of solvent extraction to achieve the separation of wastestream components. Initially, fuel elements are sheared into smaller parts before the SNF is dissolved in nitric acid ( $\text{HNO}_3$ ). The remaining pieces of undissolved cladding, known as ‘hulls’, are removed, checked for undissolved fuel content using neutron interrogation and treated as intermediate level waste by encapsulation in cement. The dissolved fuel liquor is then subjected to solvent extraction to separate the constituents of the fuel.

Solvent extraction makes use of selective transfer between two immiscible liquids to allow the partitioning of different material streams. For example, assume that two substances, A and B, are soluble in water and an immiscible organic phase, benzene, is added. Substance A is more soluble in water and substance B is more soluble in benzene. When the solvents are mixed and settled the benzene floats on top of the water and substance A is partitioned to the aqueous phase and substance B is partitioned to the organic phase. A number of different solvent extraction methods exist or are proposed for the future, the method currently used in the UK is the PUREX process.

#### 2.3.2.1. PUREX

Two solvents are used in the PUREX process: aqueous nitric acid and a tri-butyl phosphate/diluent mixture (TBP). The UK reprocessing facility, ThORP, uses odourless kerosene (OK) as a diluent for TBP. Plutonium and uranium form neutral nitrate complexes with TBP,  $\text{Pu(IV)(NO}_3)_4 \cdot 2\text{TBP}$  and  $\text{U(VI)O}_2(\text{NO}_3)_2 \cdot 2\text{TBP}$ , respectively.

Neutral adducts partition to non-polar organic solvents (OK) and U and Pu are therefore co-extracted to the organic phase. More than 99% of the fission products, including Cs and Sr, remain in the aqueous phase, known as the raffinate, which is sent for treatment as HLW. Pu (III) is much less soluble in TBP/OK than Pu (IV); Pu (IV) is reduced and stripped from the organic phase using a reductive backwash of U (IV)/hydrazine. In the past, this extraction has been achieved using ferrous sulphamate however, this generates ferric and sulphate ions, complicating waste management and consequently U (IV)/hydrazine is preferred [5]. U (IV) is stripped back to the aqueous phase by contacting with dilute nitric acid and the TBP/OK is recycled.

#### 2.3.2.2. UREX

The UREX process is similar to PUREX, however, it is designed to be proliferation resistant and consequently isolated Pu is not extracted as a product. Uranium and technetium are extracted from an aqueous nitric acid solution using TBP with an odourless kerosene diluent. The extraction of Pu and Np is prevented by the addition of acetohydroxamic acid (AHA). AHA reduces Np (VI) to Np (V) and complexes Pu (IV) and Np (IV) rendering them inextricable [2]. The concentration of nitric acid is low to enhance the extraction of the pertechnetate ion and the complexation of Pu and Np. Tc is stripped from the organic phase by contacting with high concentration HNO<sub>3</sub>. A range of UREX flowsheets exist with additional solvent extraction cycles to extract further groups of elements such as fission products, the results of the processes are given in Table 2.1. The UREX +1a flowsheet is outlined in Figure 2.6.

**Table 2.1:** UREX flowsheets and their products [7].

Process	1 <sup>st</sup> Product	2 <sup>nd</sup> Product	3 <sup>rd</sup> Product	4 <sup>th</sup> Product	5 <sup>th</sup> Product	6 <sup>th</sup> Product	7 <sup>th</sup> Product
UREX+1	U	Tc, I	Cs, Sr	Other FPs	TRU+Ln		
UREX+1a	U	Tc, I	Cs, Sr	FPs	TRU		
UREX+2	U	Tc, I	Cs, Sr	Other FPs	Pu+Np	Am+Cm +Ln	
UREX+3	U	Tc, I	Cs, Sr	FPs	Pu+Np	Am+Cm	
UREX+4	U	Tc, I	Cs, Sr	FPs	Pu+Np	Am	Cm

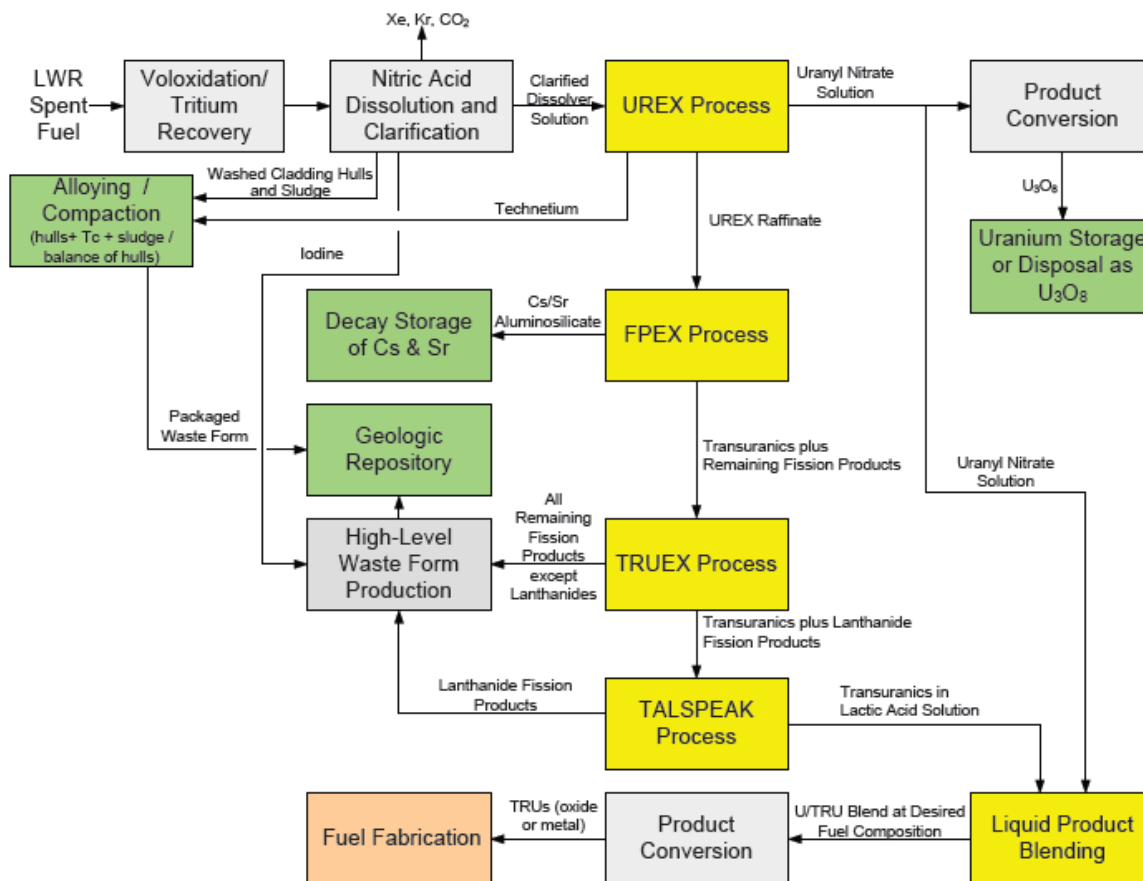


**Figure 2.6:** Outline of UREX + 1a process [7].

#### 2.3.2.3. Fission product extraction processes

The Fission Product Extraction process (FPEX) can be used to remove Cs and Sr from UREX raffinate. FPEX utilises two highly specific extractants: 4,4',5'-Di-(t-butyl)dicyclo-hexano)-18-crown-6 (DtBuCh18C6) and Calix[4]arene-bis-(tert-octylbenzo-crown-6) (BOBCalixC6) to extract Sr and Cs, respectively. Flowsheet testing using centrifugal contactors and simulant HLW raffinate has yielded removal efficiencies of > 99.99 % and > 99.98 % for Cs and Sr, respectively. The FPEX process has also been found to extract Rb and Ba efficiently from the raffinate (99.99 and 99.98% respectively) but does not extract significant amounts of transuranic elements [8]. One issue associated with the FPEX process is the stability of BOBCalixC6. The benzyl ring of BOBCalixC6 is activated towards nitration by the alkyl substituent of its benzyl moiety, nitration does not severely affect BOBCalixC6 as an extractant but it does reduce the extractant solubility in the process solvent.

Another method that can be used to extract Cs and Sr from UREX raffinate is the CCD-PEG process. Chlorinated cobalt dicarbollide (ChCoDiC) is an effective extractant for Cs and, with the addition of polyethylene glycol (PEG), can also partition Sr from acidic waste streams. The acid form of cobalt dicarbollide is completely dissociated in the organic phase; consequently polar solvents, such as nitrobenzene, have been used as a diluent. The ChCoDiC process, with and without PEG, has been demonstrated using actual waste solution in centrifugal contactor pilot plants. Without PEG, the removal efficiency of Cs is 99.99 %. When PEG is added (to allow the extraction of Sr) the removal efficiency of Cs drops to 99.98 %, the removal efficiency of Sr is 96.2 %. Safety concerns regarding the use of nitroaromatics as diluents has resulted in research to develop suitable substitutes such as phenyltrifluoromethyl sulfone [9], [10].

#### 2.3.2.4. Other aqueous extraction processes

The TRUEX process is used to extract transuranics from HLW raffinate. CMPO (octyl(phenyl)-N,N-diisobutylcarbamoylmethyl phosphine oxide) is used as the active extractant with TBP as a phase modifier. The process also uses a hydrocarbon diluent. The process has been tested with actual waste in a centrifugal contactor pilot plant. During testing a removal efficiency of 99.79 % was achieved for gross alpha activity,

reducing activity from  $2.5 \times 10^4$  Bq/mL in the feed to 41 Bq/mL. Removal efficiencies of 99.84, 99.97 and 99.97 % were achieved for  $^{241}\text{Am}$ ,  $^{238}\text{Pu}$  and  $^{239}\text{Pu}$  respectively [9].

The TALSPEAK process (Trivalent Actinide-Lanthanide Separation by Phosphorus reagent Extractant from Aqueous Komplexes) is used for the selective separation of trivalent actinides (Am, Cm) from lanthanides in the raffinate. HDEHP (di-(2-ethylhexyl) phosphoric acid) is used as the extractant and DTPA (diethylenetriamine-N,N,N',N'',N'''-pentaacetic acid) is used to selectively complex trivalent actinides.

Some UREX flowsheets also require the separation of Np and Pu, this is achieved with the NPEX process. The NPEX process generally occurs after the FPEX process and before the TRUEX process with regards to the process flowsheet. The NPEX process uses the same extractant and solvents as the PUREX process. Prior to the NPEX process, it is necessary to adjust the feed to allow the extraction of Pu and Np (rendered inextricable in the first step of the UREX process) this is made possible by thermally destroying the reductant added to suppress extraction during the UREX process, increasing the concentration of nitric acid and converting Np and Pu to the extractable (IV) oxidation state [10].

### 2.3.3. *Pyroprocessing*

Pyroprocessing is an electrorefining process. SNF is dissolved in a bath of a molten eutectic, typically a LiCl-KCl eutectic (melting point  $\sim 500$  °C), and electrolysed [1], [11]–[13]. It is possible to separately extract groups of elements on the basis of their differing potentials. Cs, Sr, Rb and Ba are not reducible to metals *via* electrolytic methods and, as a result, the salt becomes concentrated with these fission products. The concentration of fission products in the salt increases the melting point of the eutectic; consequently, after a period of operation, the salt must be treated to regenerate the eutectic or replaced.

## **2.4. Disposal of High Level Waste**

SNF and the immobilised residues left after reprocessing are highly radioactive and are classed as High Level Waste (HLW, see Section 2.2.2). The treatment and final disposal of these wastes poses a significant challenge to the UK however, several possibilities exist. In order to be regarded as credible, a disposal option must not: contravene international laws or agreements; involve the transfer of UK waste overseas or; require speculative or experimental technology. To avoid the risk of dispersal, in repository or to the biosphere, the disposal of non-consolidated wastes (i.e. liquids and powders) is generally considered unacceptable, e.g., the direct injection of liquid waste into confined rock formations as previously practiced with ILW at Krasnoyarsk, Dimitrograd and Tomsk in the former Soviet Union [14].

Disposal concepts that have been suggested but are not considered to be credible include: disposal in outer space; disposal in ice sheets; disposal in subduction zones; and disposal at sea [15]. Disposal at sea is not a viable option for UK wastes as the UK is a signatory of the London Dumping Convention [16], the same applies for disposal in subduction zones. Disposal in subduction zones is also not credible as there are no subduction zones within UK waters and this disposal option would require the transfer of UK waste overseas, similarly disposal in ice sheets is not possible because it would involve transfer of the waste overseas and would also contravene the Antarctic Treaty [17]. Disposal in outer space would contravene the “Outer Space Treaty” [18], preventing the harmful contamination of celestial bodies, and there are also the issues of cost and possible widespread contamination if a launch was to fail.

Surface and near surface storage and disposal have also been considered [15]. Surface storage in engineered stores is currently how the UK stores both ILW and HLW. Near surface disposal at ground level requires the construction of lined vaults cut into the ground, waste containers are then packed into the vault and, when full, the vault is backfilled and capped with a low permeability membrane. This method of disposal is only considered suitable for LLW and short-lived ILW with negligible amounts of radionuclides with a half-life greater than 30 years and is currently in operation at the Low Level Waste Repository, Drigg, Cumbria. It is generally considered unacceptable to

rely on continued above-ground storage or near surface storage as a disposal concept for high level wastes as it cannot be guaranteed that records and containment structures will be suitably maintained for as long as the waste remains hazardous (>100,000 years).

#### *2.4.1. Geological disposal*

Geological disposal involves the burial of waste deep underground; the large volume of overlying rock provides an additional barrier to the escape of radionuclides. Two disposal concepts that utilise a geological barrier are deep geological disposal in a repository and deep borehole disposal.

Deep borehole disposal requires a borehole to be drilled to a depth of several kilometres in a suitable host rock, waste is then placed in the borehole and, when full, the borehole is backfilled. Radiogenic heating causes partial melting of the host rock and eventually, as the rate of radiogenic heating decreases with time, the waste containers are sealed in fracture free rock [19].

Deep geological disposal in a repository is the disposal method currently favoured by the Nuclear Decommissioning Authority and much research has been carried out to devise a generic disposal concept. A deep geological repository, or Geological Disposal Facility (GDF, see Figure 2.7), utilises the multibarrier concept to prevent the escape of radionuclides to the biosphere. As the name suggests, multiple engineered barriers are utilised to ensure the safety of the repository. The first barrier is known as the wasteform and is, ideally, a passively safe material designed to prevent radionuclide release. For HLW the wasteform is typically either SNF, borosilicate glass or a ceramic in which the radionuclides are immobilised after reprocessing. The next barrier is the overpack; it surrounds and encapsulates the wasteform and is designed to minimise corrosion and surface dose. Common proposed overpack materials include copper and stainless steel. The next barrier is a buffer material; it must have low hydraulic conductivity to prevent water ingress and radionuclide egress. The buffer material must also have high plasticity enabling it to deform with ground movement and self-seal; it is also required to have a high absorption capacity to absorb migrating radionuclides. Bentonite clay is a widely proposed buffer material. The final barrier is the geological barrier, i.e. the overlying rock

between the repository and the surface. The host geology must be free of faulting, have a low fracture density and have high thermal conductivity. Ideally, the host rock must also be free of valuable resources to avoid the possibility of future human intrusion.

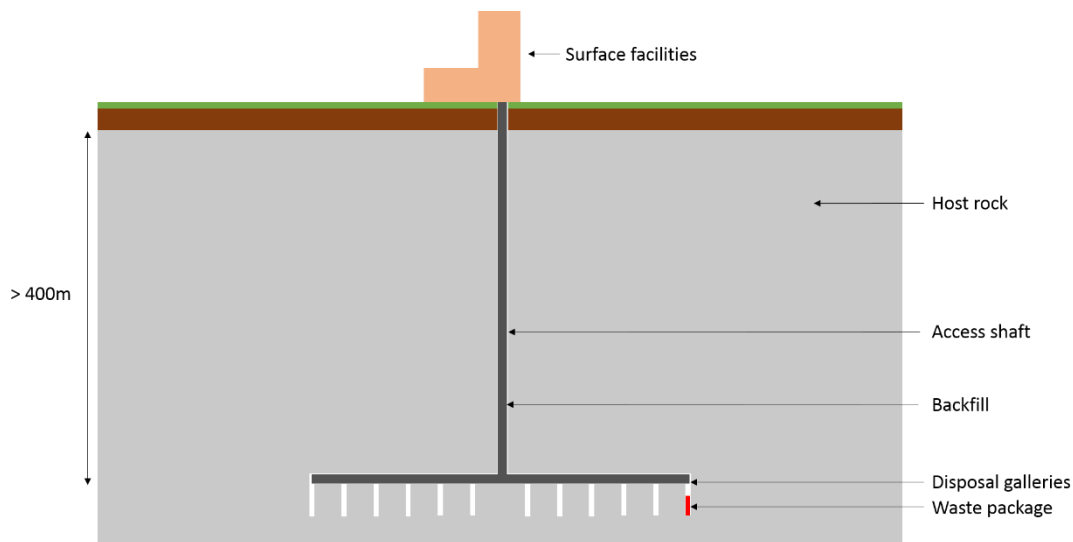


**Figure 2.7:** Simplified diagram of a Geological Disposal Facility

#### 2.4.2. *Host geology*

Three different types of host geology have been considered for a GDF: high strength rock (HSR, sometimes sub-divided into igneous, metamorphic and high strength sedimentary rock [15]), evaporites and low strength sedimentary rock (LSR) [20]. Both LSR and evaporites are subject to creep and have the advantage of being self-sealing with time. Repositories constructed in HSR do not have the advantage of self-sealing and, therefore, require backfilling, replacing the excavated rock with a suitable material after repository operations are complete.

Evaporite formations result from the evaporation of water from bodies containing dissolved rock salts, examples include anhydrite (anhydrous calcium sulphate) and halite (rock salt). Due to diapirism, salts force their way through denser surrounding rocks resulting in bulge shaped salt formations. As a result of the anhydrous nature of evaporite formations there is much interest in their use as a host for a GDF. Nations interested in the use of evaporite formations for HLW disposal include the United States, Switzerland, Denmark and Germany [20]. The United States has already begun disposing of defence related trans-uranic wastes in a salt-based repository at the Waste Isolation Pilot Plant (WIPP), New Mexico.

Low strength sedimentary rocks are typically geologically young sedimentary rocks, such as clays. Fluid movement tends to be through the rock mass. Clays have been the subject of studies in several countries e.g. Swiss Opalinus and Belgian Boom clays have been investigated as possible host media for a HLW GDF in Switzerland and Belgium respectively [20].

Higher strength rocks are typically crystalline igneous and metamorphic rocks, though geologically old sedimentary rocks can also be considered to be HSR. Any fluid movement is through discontinuities in the rock. Granite is considered to be a good example of HSR and is the chosen host geology for the SNF repositories currently under construction in both Sweden and Finland.

#### *2.4.3. Heat generating wastes*

A limiting factor in the design of a GDF is the temperature increase as a result of radiogenic heating. The temperature limit of a GDF is dependent upon the host geology and backfill material used in the design. Repositories constructed in evaporite formations must not exceed a temperature of 200 °C [21]; exceeding this temperature results in excessive creep of the host geology. The temperature limit of LSR repositories and repository designs utilising clay-based buffer materials is 100 °C. Exceeding 100 °C results in unacceptable alteration of the clays and consequently must be avoided [22]. The temperature within a repository (and therefore the size of a repository) is affected by four main factors: the heat output of the waste packages and the thermal conductivity, specific heat capacity and density of the host rock. It is not possible to adjust the latter three factors and therefore any reduction in repository size must be accompanied by a concomitant reduction in the heat output of the waste packages.

Isotopes with short half-lives can generate significant amounts of heat due to the greater rate of decay relative to longer lived isotopes. A greater rate of decay results in more rapid deposition of energy into the surrounding environment, if this energy is not removed it results in heating of the surrounding material. The fission products  $^{137}\text{Cs}$  and  $^{90}\text{Sr}$  both have half-lives of the order of ~30 years, this results in significant radiogenic heating.

The radiogenic heating caused by Cs and Sr is a significant factor to be considered in the design of a geological disposal facility. It is possible to reduce the heat output of waste packages by removing the major heat generating radionuclides e.g.  $^{241}\text{Am}$ ,  $^{137}\text{Cs}$  and  $^{90}\text{Sr}$  during reprocessing, as outlined above. Wigeland et al (2006) hypothesised that by removing 99.99 % of all Cs, Sr, Am and Pu from the waste it could be possible to reduce the size of a repository by up to a factor of 43, the reduced heat generation means that waste packages can be packed closer together without exceeding the temperature limits of the repository [23]. Once separated, the heat generating radionuclides require treating and solidifying prior to disposal, as with any other waste.

## **2.5. Wasteforms**

As stated in Section 2.4.1, a wasteform is a passively safe material designed to prevent radionuclide release. Ideally a wasteform is dense, easily processed, cheap and highly leach resistant. Resistance to dissolution and leaching is a key property limiting the release of radionuclides to the environment. A dense wasteform is desirable as a lower volume of waste is produced, simplifying the handling and final disposal of the waste. A high density wasteform should also be less porous and consequently more leach resistant as a result of reduced surface area. Ease of processing is desirable due to the difficulties of processing HLW. The simpler a process is, the less there is to go wrong and subsequently waste processing throughputs are higher.

There are three broad categories of potential HLW wasteforms: glasses, ceramics and glass-ceramics. Glasses are defined by the American Society for Testing and Materials as “An inorganic product of fusion which has cooled to a rigid condition without crystallising.” Ceramics are crystalline materials most often formed from metallic and non-metallic elements. The word ceramic is derived from the Greek *keramikos*, roughly translated as “burnt stuff”, a reference to the firing process used in the production of ‘traditional’ ceramics [24]. Glass-ceramics are defined as polycrystalline materials prepared by the controlled bulk crystallisation of suitable glasses [25].

Although glass wasteforms are attractive due to their ability to accept a wide variety of cations, some, including I, Cs and Ru, are volatile and prove problematic during high temperature processing, e.g. glass melting or sintering of ceramics. Consequently, the

selection criteria for nuclear waste glasses are not only affected by their corrosion resistance but also their melting temperature, precluding the use of many glass compositions. As a result, nuclear waste glass formulations are a compromise between processing temperatures and leach resistance.

The use of ceramics as a host for HLW was first proposed by Hatch in 1953 [26]. Early ceramic wastefoms were based on clays but other candidate systems, known as the ‘supercalcines’, were based on natural minerals such as pollucite and rare earth phosphates [27]. A problem with early ceramic wastefoms, as with many glasses, was the relatively high processing temperatures required to achieve good sintering behaviour resulting in the volatilisation of waste components, including Cs.

Titanate based phases and phase assemblages, of which SYNROC is probably the most well-known, have been the subject of many studies as potential ceramic HLW hosts [28]–[41]. SYNROC is a polycrystalline, multiphase system that uses different titanate phases to immobilise different fractions of the HLW waste stream. The major phases of SYNROC include hollandite ( $\text{BaAl}_2\text{Ti}_2\text{O}_6$ ), perovskite ( $\text{CaTiO}_3$ ), zirconolite ( $\text{CaZrTi}_2\text{O}_7$ ) and rutile ( $\text{TiO}_2$ ) [37]. In addition to these major component phases there are also several minor titanate phases contained within SYNROC, dependent upon formulation, e.g. brannerite ( $\text{UTi}_2\text{O}_6$ ) [42]. Although SYNROC is an assembly of phases, several of the constituent minerals have been suggested as stand-alone host phases for separated radionuclides e.g. hollandite for Cs and zirconolite for transuranic species [12], [33], [43]–[49].

Phosphate-based ceramics, such as sodium zirconium phosphate (NZP,  $\text{NaZr}_2(\text{PO}_3)_4$ ) and monazite wastefoms, have also been the subject of investigation as potential radioactive wastefoms due to their high possible waste loadings, relative insolubility and flexibility [50]–[55].

### 2.5.1. Caesium

Caesium bearing wastestreams represent a particular challenge with regards to immobilisation and disposal. Although it is possible to separate Cs from the aqueous waste streams by using the processes outlined in Section 2.3.2.3, several radioisotopes of Cs exist:  $^{137}\text{Cs}$ ,  $^{135}\text{Cs}$  and  $^{134}\text{Cs}$ . It is not economically viable to separate these isotopes

nor is it viable to transmute the species due to their low neutron capture cross-sections. The vast majority of radioactivity present in the waste is a result of the relatively short-lived  $^{134}\text{Cs}$  and  $^{137}\text{Cs}$ , however, a significant proportion is a result of  $^{135}\text{Cs}$ . Caesium-135 is a long-lived radioisotope ( $t_{1/2} = 2.3$  million years) and it is therefore not possible to simply decay store Cs wastefoms prior to disposal as low level waste. Consequently, Cs-bearing wastefoms must be robust enough to withstand the same rigours as any other wastefom intended for geological disposal. During high temperature processing, significant amounts of Cs may be volatilised and in HLW glasses it can be incorporated in an impurity phase known as ‘yellow phase’. Yellow phase,  $\text{Na}_2\text{MoO}_4$ , is highly soluble in water and waste loadings in HLW glass are consequently limited to 15-20 mass% HLW to avoid crystallisation and phase separation [25].

#### 2.5.1.1. Hollandite

Although hollandite is part of the target phase assemblage of the multiphase SYNROC, numerous studies have focussed on the use hollandite as the host matrix for separated caesium [12], [43], [44], [46], [56]–[60]. Hollandite structured crystals generally conform to the formula  $\text{A}_x\text{B}_y\text{C}_{8-y}\text{O}_{16}$ , where  $x \leq 2$  [61]. A site cations are large and either monovalent or divalent ( $\text{Na}^+$ ,  $\text{Ag}^+$ ,  $\text{K}^+$ ,  $\text{Rb}^+$ ,  $\text{Tl}^+$ ,  $\text{Cs}^+$ ,  $\text{Sr}^{2+}$ ,  $\text{Ba}^{2+}$ ,  $\text{Ra}^{2+}$ ,  $\text{Pb}^{2+}$ ). B and C site cations are more varied with di, tri, tetra and pentavalent cations possible e.g.  $\text{Mg}^{2+}$ ,  $\text{Al}^{3+}$ ,  $\text{Ti}^{4+}$ ,  $\text{Sb}^{5+}$  [61], [62].

The hollandite structure consists of double rutile chains sharing corners and edges with  $\text{BO}_6$  octahedra forming tunnels along the  $c$ -axis of the structure, see Figure 2.8. Tunnels are either (2 x 2) or (1 x 1) octahedra in cross-sectional dimensions. The large A site cations are bound in the (2 x 2) tunnels and are typically eightfold coordinated by oxygen, preventing free migration of A site cations along the tunnels [63], however, oxygen coordination has been known to vary between six and ten [64]. The size of octahedra affects the stability of hollandites and subsequently their ease of synthesis. For example, titanate hollandites are more readily synthesised under ambient conditions compared to silicate or germanate hollandites as they have larger, more easily stabilised octahedra. Silicate and germanate hollandites actually require stabilisation by high pressures where six-fold co-ordination of  $\text{Ge}^{4+}$  and  $\text{Si}^{4+}$  is preferred [65]. In hollandites with  $x < 2$ , vacant and occupied tunnel cation sites are ordered on a larger scale than the unit cell, this leads to

the existence of superstructures. One-dimensional superstructures exist when the systematic occupancy sequences of tunnels are unrelated to neighbouring tunnels. More common three-dimensional superstructures are formed when the vacant and occupied tunnel sites along several neighbouring tunnels are ordered similarly and correlated. The formation of superstructures leads to characteristic diffuse intensities and reflections in electron diffraction patterns [10, 11].

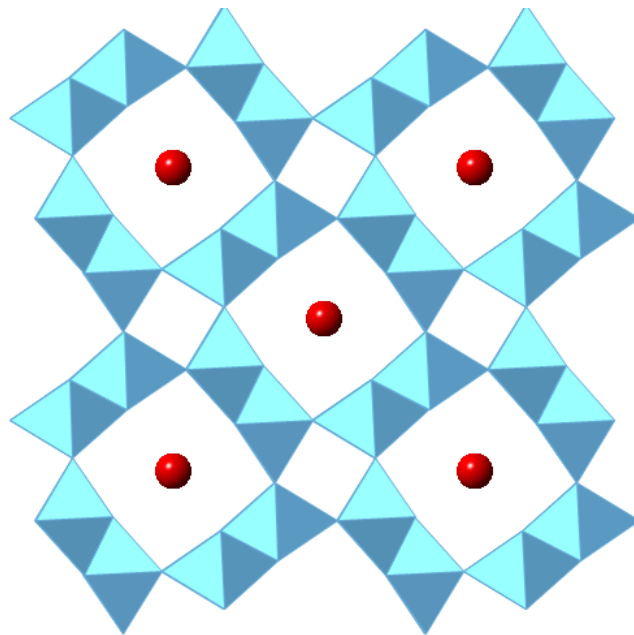


**Figure 2.8:** Crystal structure of hollandite. Blue = Ti and red = Ba/Cs. Oxygen has been omitted for clarity.

### 2.5.2. Iodine

Iodine is another volatile fission product that proves problematic during reprocessing operations. During dissolution of SNF in nitric acid, 94-99 % of iodine is volatilised to the dissolver off-gas system [66]. Volatilised iodine is removed using various off-gas technologies including caustic soda scrubs and contacting with silver exchanged mordenite [5], [66]. Although current practice is to dispose of iodine by discharge to sea and subsequent dilution, future revision of permissible discharges may see this practice severely restricted or banned [25]. Consequently, research is ongoing in the area of iodine wastefoms. Studies have investigated both the immobilisation of spent sorbent materials and separated iodine (I may be desorbed from solid sorbents by heat treatment in a

reducing atmosphere resulting in the formation of HI) [66], [67]. Current proposed wasteforms include AgI-Ag<sub>2</sub>O-P<sub>2</sub>O<sub>5</sub> and Bi<sub>2</sub>O<sub>3</sub>-SiO<sub>2</sub>-PbO glasses, sodalite (Na<sub>8</sub>(AlSiO<sub>4</sub>)<sub>6</sub>I<sub>2</sub>) and iodovanadinite (Pb<sub>5</sub>(VO<sub>4</sub>)<sub>3</sub>I) [25].

#### 2.5.2.1. Iodovanadinite

Iodovanadinite (Pb<sub>5</sub>(VO<sub>4</sub>)<sub>3</sub>I), sometimes referred to as lead iodoapatite, has been identified as a potential host matrix for the immobilisation of <sup>129</sup>I [68]. Iodovanadinite is related to vanadinite (Pb<sub>5</sub>(VO<sub>4</sub>)<sub>3</sub>Cl), an ore of lead and vanadium, which is part of the larger apatite structure family, crystallizing in the hexagonal spacegroup *P6<sub>3</sub>/m*. The corner-sharing PO<sub>4</sub> tetrahedra found in apatites may be replaced with larger structural units, such as VO<sub>4</sub> or AsO<sub>4</sub> tetrahedra. Substituting the PO<sub>4</sub> unit with larger structural units increases the aperture of the tunnel sites and subsequently improves the incorporation of larger anions, such as iodide, within the wasteform [68]–[70]. Apatites containing the ReO<sub>5</sub> structural unit have also successfully been synthesised.

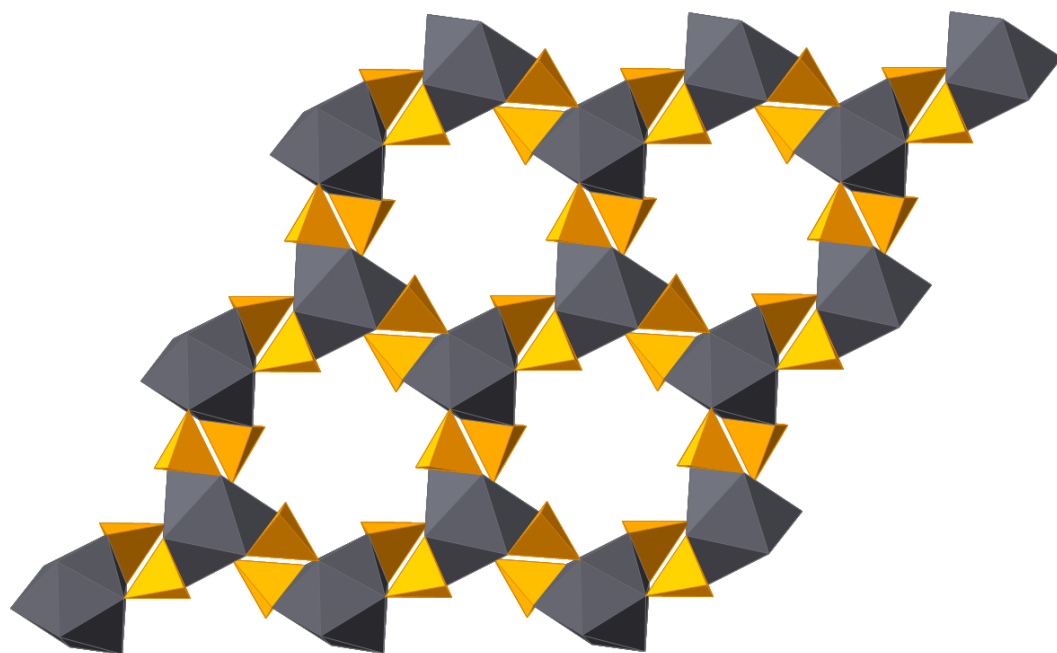


**Figure 2.9:** Structure of the iodovanadinite unit cell. Orange = V, Grey = Pb. Iodine resides in the tunnel sites but has been omitted for clarity.

### 2.5.3. *Plutonium and plutonium-rich residues*

As stated in Section 2.3.1, plutonium is currently extracted from SNF using the PUREX process. Although the original purpose of reprocessing was to extract Pu for use in nuclear weapons, there were also plans to build a fleet of fast reactors that would use the surplus Pu as fuel. Due to the cancellation of the UK fast reactor program, the UK currently possesses a large inventory of separated Pu that is currently stored at Sellafield (122.1 t as of December 2014 [71]). The plutonium stockpile is currently considered to be a zero value asset by the NDA [72]. Future changes in UK government policy could see Pu reclassified as waste and consequently suitable wastefoms must be derived for the disposal of any waste Pu. In addition to separated Pu, there are a range of Pu containing residues that require disposal as they are either unfeasible or uneconomic to recycle e.g. MOX fuel residues and plutonium contaminated materials. Mixed oxide fuel residues are mixed uranium-plutonium oxides that arise from the production of MOX fuels, they may take the form of loose powders, ceramic green bodies or rejected sintered pellets. The immobilisation of Pu and Pu residues has been the subject of extensive study, particularly excess Pu from nuclear weapons programmes [73]–[75]. Possible wastefoms investigated include zirconia, pyrochlore, sphene, monazite, zirconolite and zirconolite based glass ceramics in addition to borosilicate and phosphate based glasses [25]. Due to the strict protocols and the practicalities surrounding obtaining and working with Pu, many studies choose to use analogues typically the inactive, lanthanide Ce or the radioactive, actinides U and Th.

#### 2.5.3.1. Brannerite

Brannerite ( $UTi_2O_6$ ) is a titanate phase commonly found in uranium ore deposits [76]. It is also found as an accessory phase in zirconolite and pyrochlore based ceramics designed for actinide disposition [42], [77]. The high U content, and therefore high potential actinide waste loading, of brannerite (~ 55 wt%) makes brannerite a particularly attractive option for the immobilisation of actinides. Brannerite has a monoclinic crystal structure with space group C2/m, the structure comprises corner and edge sharing  $TiO_6$  octahedra with larger cations in between the layers of octahedra (see Figure 2.10) [78] however,

natural samples are almost completely metamict due to accumulated  $\alpha$ -recoil damage [76]. Although the archetypal stoichiometry of brannerite is  $UTi_2O_6$ , natural samples of brannerite have been found to possess considerable chemical flexibility incorporating elements such as Ca, Y, Pb, Ce and Th on the A-site and Fe, Si and Al on the B-site [76].

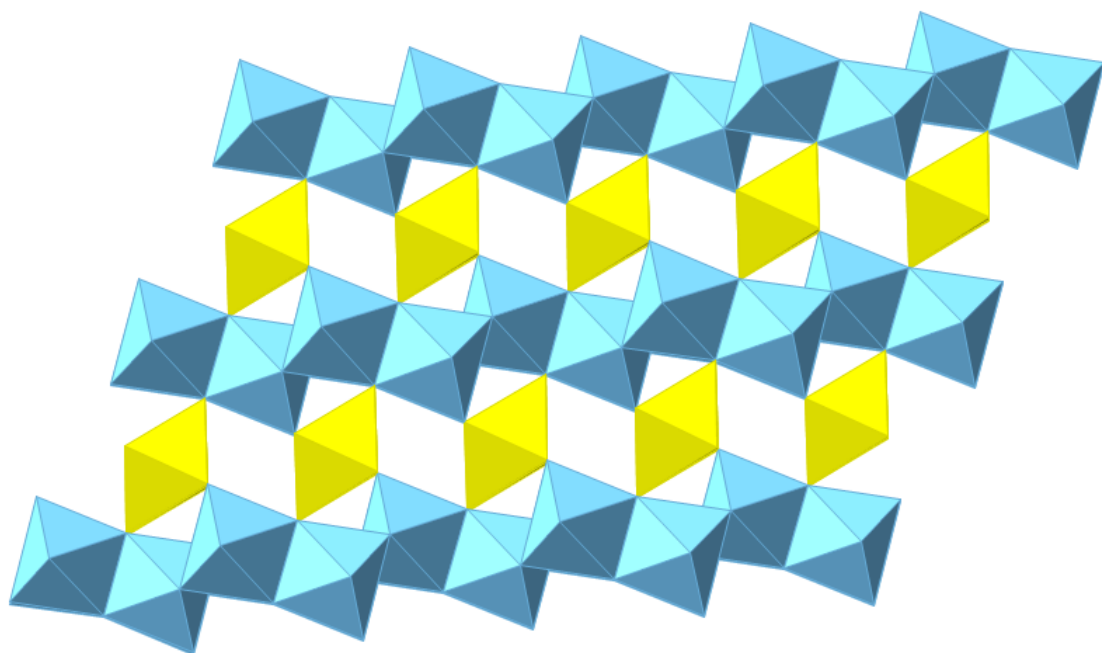


**Figure 2.10:** Brannerite crystal structure. Blue = Ti, yellow = U.

#### 2.5.3.2. Zirconolite

Like hollandite, zirconolite forms part of the SYNROC phase assemblage but is also worthy of consideration as a dedicated wasteform for separated actinide wastes.

The zirconolite structure is a derivative of the pyrochlore structure and comprises alternating layers of  $TiO_6$  octahedra in a hexagonal tungsten bronze array (HTB) and Zr and Ca in seven and eight-fold coordination respectively (see Figures 2.11 and 2.12) [79], [80]. Ti is situated in three separate sites; two fully occupied octahedral sites and a half-occupied trigonal bi-pyramidal site. There are several known polytypes of zirconolite including monoclinic, trigonal and orthorhombic symmetries (2M, 4M, 3T, 6T and 3O) [81], [82]. The various polytypes arise as a result differences in the stacking order of the

TiO<sub>6</sub> layers and may be affected by substitutions on the Ca and Zr sites and synthesis conditions, including oxygen fugacity and temperature [33], [79], [82].

Natural zirconolite samples have been found to accommodate and retain actinides despite metamictisation and several previous studies have investigated the incorporation and retention of actinides (U, Np, Pu, Cm) in synthetic zirconolites [33], [48], [49], [83], [84]. Pu has previously been shown to readily substitute into the zirconolite structure with the crystallographic site occupied by the Pu ion being dependent on Pu valence, processing conditions and the designed stoichiometry [49].

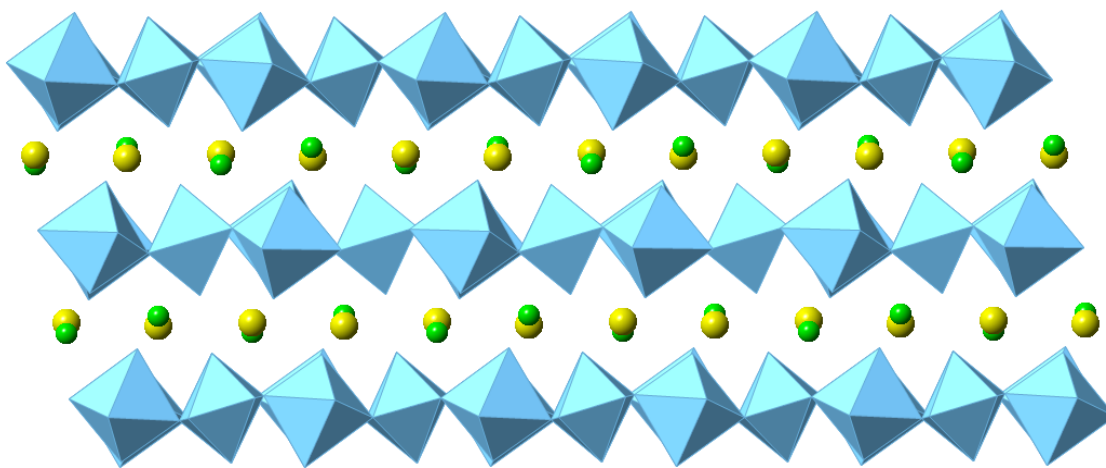


**Figure 2.11:** Zirconolite crystal structure. Blue = Ti, yellow = Ca and green = Zr.

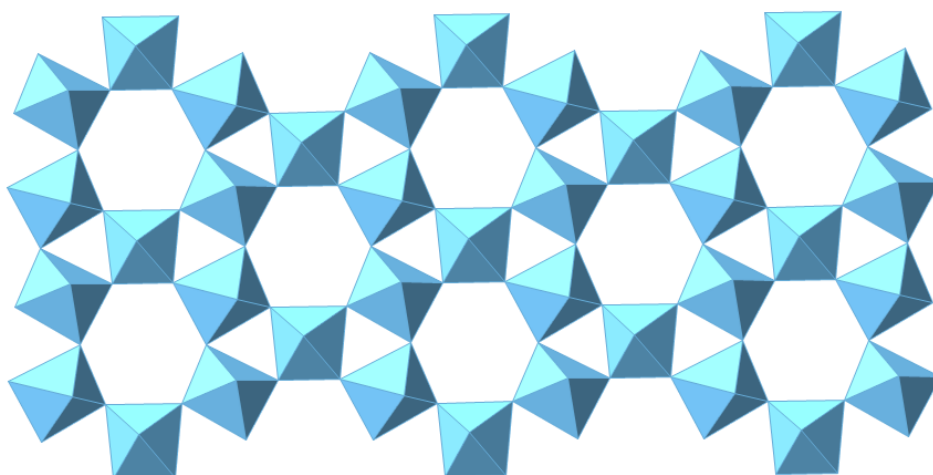


**Figure 2.12:** Hexagonal tungsten bronze array of TiO<sub>6</sub> octahedra.

#### 2.5.4. Technetium

Technetium is a high yield fission product with 22 isotopes all of which are radioactive. Technetium-99 is the most relevant to the long term disposal of radioactive wastes due to its long half-life ( $t_{1/2} = 211000$  years). Like iodine, technetium accumulates in the thyroid gland and is therefore extremely hazardous. With regards to immobilisation, Tc is a problematic element during vitrification, where the relatively low solubility of Tc in borosilicate glasses is exacerbated by the volatilisation of  $Tc_2O_7$  from the melt due to its relatively low boiling point (311 °C). The oxidation of Tc to Tc (VII) is particularly undesirable due to the high mobility of the pertechnetate ion ( $TcO_4^-$ ) in the environment [25]. Tc (IV) oxide ( $TcO_2$ ) is less volatile than pertechnetate (no decomposition up to 1100°C) however, processing of  $TcO_2$  requires careful control of redox chemistry to prevent oxidation to Tc (VII) [85]. Various technetium bearing phases have been investigated including spinel, pyrochlore, sodalite, perovskite and metal alloys [86]–[88].

#### 2.5.5 Aqueous durability testing of ceramic wasteforms

Aqueous durability is an important measure of the effectiveness of a wasteform. It is generally accepted that water ingress into a repository is inevitable, it is therefore imperative that a wasteform is as durable as possible when in contact with aqueous solutions. Numerous methods of durability assessment exist but the most commonly used are the ASTM PCT- B and MCC-1 test methods.

The product consistency test is a testing protocol developed to evaluate the durability of glass wasteforms. Test Method B allows the testing of materials at various test durations, temperatures, particle size, sample mass, leachant composition and volumes. Testing is static and may be conducted in either stainless steel or PTFE vessels [89]. After dissolution, the elemental composition of the leachate is analysed by ICP-OES or ICP-MS. Normalisation of the leachate composition relative to the elemental composition of the wasteform allows the normalised elemental mass loss value ( $NL_i$ ) and, subsequently, the normalised elemental mass loss rate ( $NR_i$ ) to be calculated.

The Materials Characterisation Centre-1 test, MCC-1, is a static leaching methodology developed to study the dissolution behaviour of monolithic wasteforms [90]. The benefit of the MCC-1 is that solution saturation is reached more slowly giving a better estimation

of the initial wastefrom dissolution rate. The use of monolithic samples also allows the surface of the specimen to be inspected for alteration layers and products, this may allow useful information regarding the dissolution mechanism to be gathered. Specimens of known geometry and surface area are submerged in leachant at a temperature of 40, 70 or 90 °C for a predetermined period. The SA/V ratio of the monolith to leachant is  $10.0 \pm 0.5 \text{ m}^{-1}$ . Test vessels may PTFE or stainless steel.

## 3. Experimental Procedures

### 3.1. Batching and milling

Unless otherwise stated, ceramics were produced by mixed oxide synthesis. For oxide synthesis the necessary quantities of oxide or carbonate precursors, for a given composition, were weighed to an accuracy of 0.0001 g. Batch materials were homogenised using an agate pestle and mortar or by milling. Milling was carried out using a rolling mill or planetary mill. Samples prepared by rolling mill were mixed with solvent to form a slurry and milled in Nalgene bottles with yttria-stabilised zirconia media for a period of 12-16 hours. Samples prepared by planetary mill were mixed with solvent to form a slurry and milled in Sialon mill pots with Sialon media for five periods of three minutes at 500 rpm, changing the direction of milling after each period. Batches not containing halides were milled using isopropanol as the carrier fluid whereas halide containing batches were milled using the non-polar solvent cyclohexane. Milled precursors were left to dry before recovery of the batch and sieving to break up agglomerates prior to further processing.

#### *3.1.1. The use of surrogates*

Due to the radiotoxic nature of several of the elements under investigation, the studies presented in this thesis utilised surrogates in place of the envisioned final radionuclides in order to minimise risk.

Radiocaesium and iodine were replaced by inactive Cs and I, the structure and chemistry of these materials were therefore unaffected by the use of surrogates.

Tc was replaced by Mo, Mo (IV) has a similar ionic radius and chemistry to Tc and is therefore a useful structural surrogate, however, the redox chemistry and high temperature behaviour of Mo differs significantly and these differences require careful consideration when applying the results to the design of a final wasteform.

Pu was replaced by Ce, the ionic radii of Ce (III/IV) and Pu (III/IV) are very similar and Ce is therefore a suitable structural analogue. The redox chemistry of Ce and Pu differs significantly, Ce may be present as Ce (III) or (IV) whereas Pu may be present as Pu (III),

(IV), (V) or (VI). Consequently, Ce is only a suitable substitute for the lower valent Pu ions. Ce has also been found to be relatively easier to reduce during processing than Pu [91]. Consequently, any studies using Ce to investigate the processing of Pu wastefoms must consider the effect on relative solid solubility and the charge balancing of a final Pu bearing system.

### **3.2. Hollandite synthesis**

Hollandite ceramics were synthesised using an alkoxide-nitrate co-precipitation route. Stoichiometric amounts of nitrates of barium, caesium, chromium, iron, nickel, zinc or aluminium were dissolved in a stainless steel beaker with warm water and a mixture of isopropanol and titanium (IV) isopropoxide added. The mixture was then stirred using a shear mixer and gently heated to evaporate the majority of the water and solvent. The resultant slurry was dried in an oven overnight at 90 °C. The powder cake was broken up and sieved (212 µm mesh). Denitration of the precursor powder was achieved by heating to a temperature of 750 °C and holding for a period of 1 hour. After denitration, the powder was mixed with isopropanol to form a slurry and ball-milled overnight in a HDPE bottle with yttria-stabilised zirconia milling media, the slurry was allowed to dry after milling. The dried slurry was sieved to separate the milled precursor from the milling media, prior to consolidation by cold uniaxial pressing followed by sintering or hot isostatic pressing.

### **3.3. Cold pressing and sintering**

Dense material is desirable for wastefom applications and for many of the analytical techniques described in this section; consequently, synthesised powders were compacted to form green bodies and sintered. A green body is a compacted, but not fully densified, ceramic body with typically 35-50 % porosity.

Green bodies were formed by uniaxially pressing either precursor or reacted powders in a hardened steel die (diameter 6, 10 or 13 mm) with a pressure of  $2 \times 10^5$  Pa. The green

bodies were transferred to a furnace for sintering. It is important to achieve good packing of powders prior to sintering as this will affect the densification behaviour of the material.

Sintering is the coalescence of powder particles into a dense mass. The driving force behind sintering is the reduction of total particle surface area; particle surface energies are higher than those of grain boundaries. Surface energy reduction is achieved by atom diffusion processes resulting in either grain coarsening or densification. Coarsening does not reduce the actual pore volume and will therefore not contribute to the densification of the ceramic. Densification is the transport of atoms from within grains into the pores resulting in a decrease in porosity and consequently an increase in density. Densification and coarsening are competing processes; if coarsening dominates an undesirable, highly porous structure will be produced. Material and processing parameters affect the densification behaviour of ceramics; therefore, properties such as particle size, applied pressure and the processing atmosphere must be controlled to achieve proper densification [92].

There are three stages of sintering: initial, intermediate and final sintering. During initial sintering, strong bonds (known as necks) are formed at contact points between particles and relative density increases due to increased packing of particles. The majority of densification, and shrinkage, occurs during intermediate sintering. During this stage, the necks between the particles grow and grain boundaries form and move. Pore channels are connected during intermediate sintering and the process is considered to have finished after the pores become isolated, interconnected porosity is eliminated at ~ 95 % theoretical density [93]. Final stage sintering involves the isolation and destruction of pores, there is little densification but grain size does increase during this time. There are at least six mechanisms of sintering, see Figure 3.1, of these six, three lead to densification. Although the remaining mechanisms do not contribute to densification, they aid in the formation of necks and are therefore considered part of the sintering process. [92].

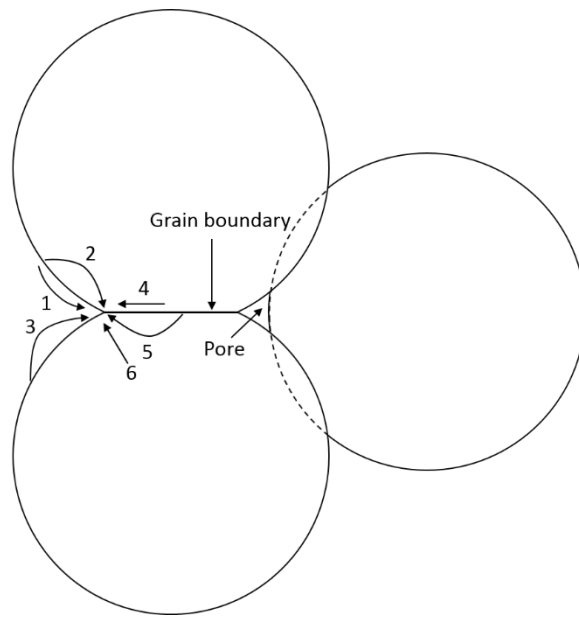


**Figure 3.1:** Six distinct mechanisms can contribute to the sintering of a consolidated mass of crystalline particles: (1) surface diffusion; (2) lattice diffusion from the surface; (3) vapour transport; (4) grain boundary diffusion; (5) lattice diffusion from the grain boundary; and (6) plastic flow. Only mechanisms (1) to (3) lead to densification, but all cause the necks to grow and so influence the rate of densification. Adapted from Rahaman (1996) [92].

### 3.4. Hot isostatic pressing (HIP)

Hot isostatic pressing is a method of powder consolidation. During HIPing the sample is placed in a sealed pressure vessel and heated to elevated temperatures whilst an inert gas, e.g. Ar or He, is used to apply pressure isostatically, see Figure 3.2 [94]. The application of isostatic pressures improves the achievable density of the material during processing by bringing particles closer to one another and counteracting the internal pressure of pores. Internal pore pressure opposes sintering by forcing grain boundaries apart. The total pressure for sintering can be considered as a relationship between the internal pore pressure ( $P_i$ ), external pressure ( $P_e$ ), pore radius ( $r_p$ ) and the specific energy of the pore's internal surface ( $\gamma$ ), see Equation 6.

$$P_T = P_e - P_i + \frac{2\gamma}{r_p} \quad \text{Equation 6}$$

As HIPing uses a gas as the pressurising medium, any open and interconnected porosity will become pressurised, negating the benefits of applying pressure ( $P_e = P_i$ ). Consequently, a non-porous surface is required prior to HIPing, this may be achieved by hermetically sealing the material to be consolidated within an evacuated canister.

Another benefit of heat treating materials in sealed vessels is that the loss of volatile species (e.g. Cs, Mo, I) is avoided. As a result, hot isostatic pressing is the focus of considerable research regarding the immobilisation of volatile radionuclides.

HIPed samples presented in this work were produced by packing and pressing powdered materials in 316 stainless steel or C106 copper canisters using an American Isostatic Presses – 630H HIP rig. The sample preparation station and HIP unit are shown in Figure 3.3 and Figure 3.4 respectively.

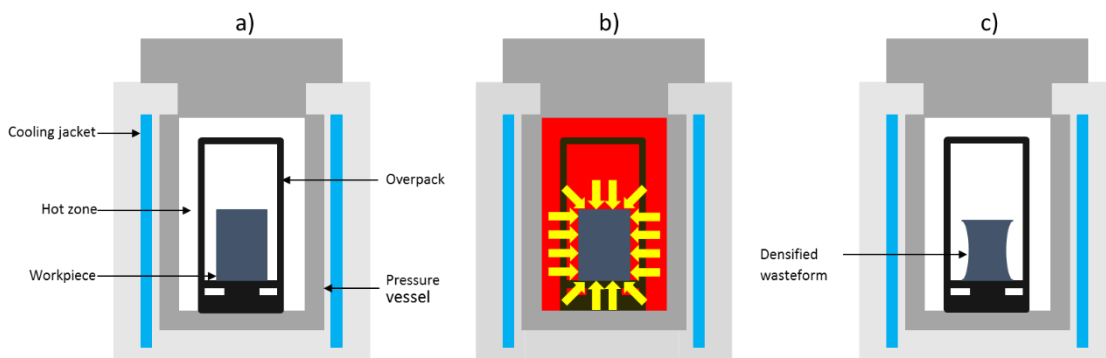


**Figure 3.2:** Schematic of the hot isostatic pressing process:

- The sealed HIP canister is placed within the HIP vessel.
- The canister is heated and isostatically compressed by an inert gas.
- The densified monolith is removed from the HIP vessel.



**Figure 3.3:** HIP sample preparation station

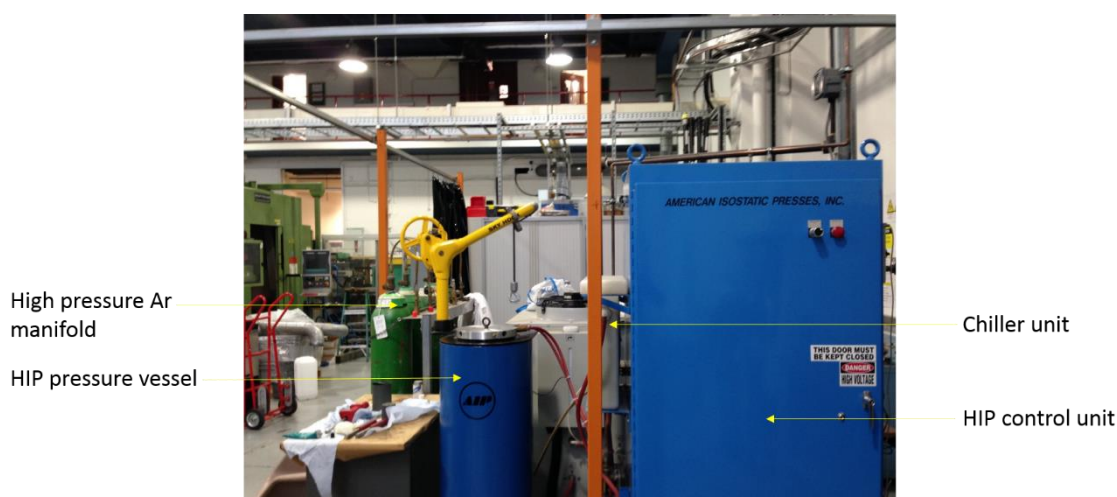


**Figure 3.4:** HIP unit.

HIP samples were prepared on two different scales. Firstly, a small-scale tube which consisted of a 0.25 inch pipe crimped and sealed at one end by autogenous welding before the addition of 1 - 1.5 g of powdered batch material. The batch material was compacted using uniaxial pressure to minimise internal void space. After compaction of the batch material, the tube was partially crimped and a steel wool filter inserted to contain any loose powders during evacuation of the tube. The sample was then evacuated using a vacuum pump to a pressure of approximately 3.3 Pa to test whether the tube would hold vacuum. After successful testing, the tube was placed in a furnace and heated to remove free water, solvents and volatile organics entrained in the sample. After heating, the tube was fully crimped twice above the sample, the tubing above the second crimp was removed and the tube sealed by welding. A schematic of the HIP tube assembly is shown below in Figure 3.5.

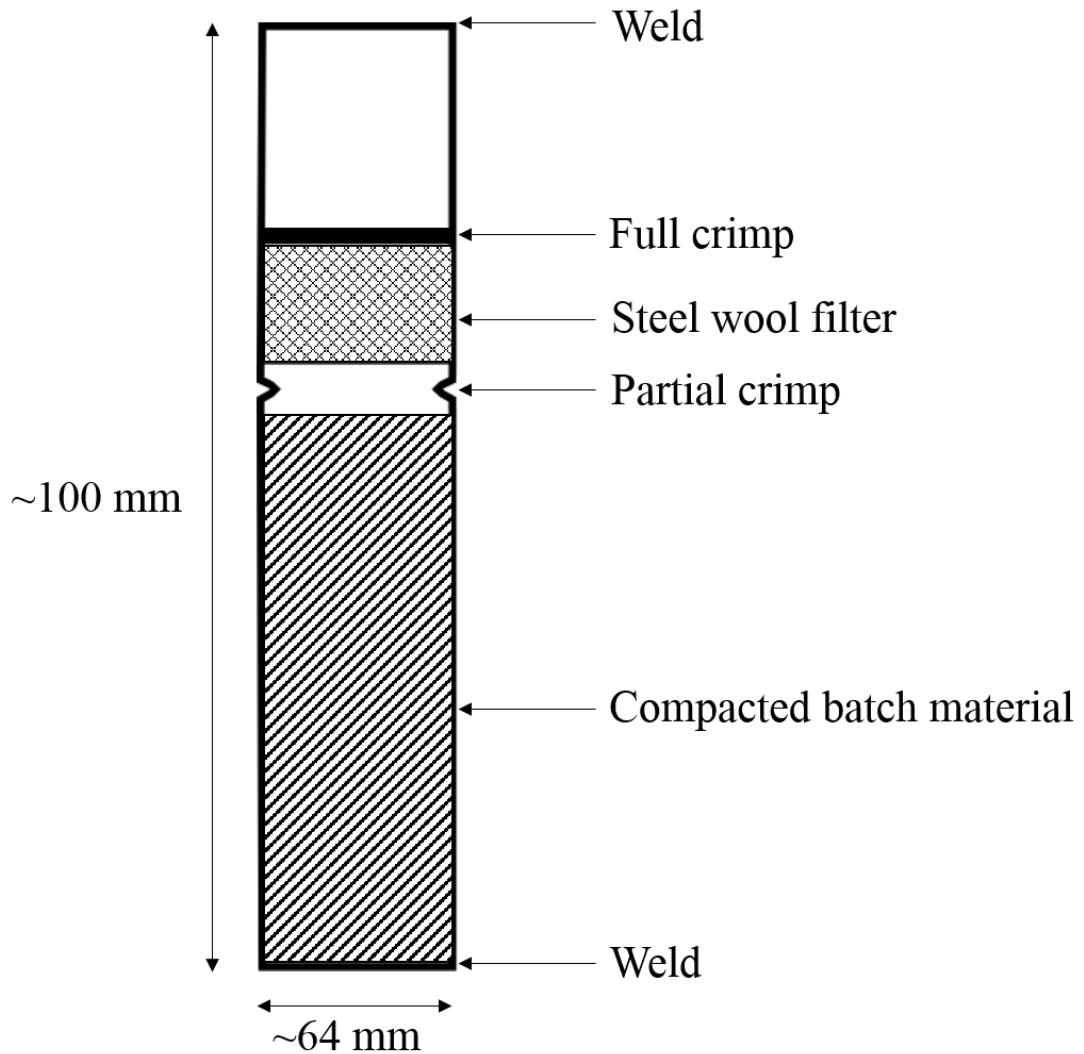


**Figure 3.5:** Schematic of small-scale HIP tube.

The components of the large scale HIP canisters were produced by sectioning stainless steel tubing and bar. Sections of round bar were used to form the end caps of the canister. A hole was drilled in one end cap and an evacuation tube welded in place. The bottom end cap of the canister was welded to the wall tubing before the addition of powdered batch material. The batch material was compacted using uniaxial pressure to minimise internal void spaces. The body of the canister was sealed by welding the upper end cap in place. The HIP cans were then evacuated, vacuum tested, heated and sealed as with the small scale tubes. A schematic of a HIP canister is shown in Figure 3.6.

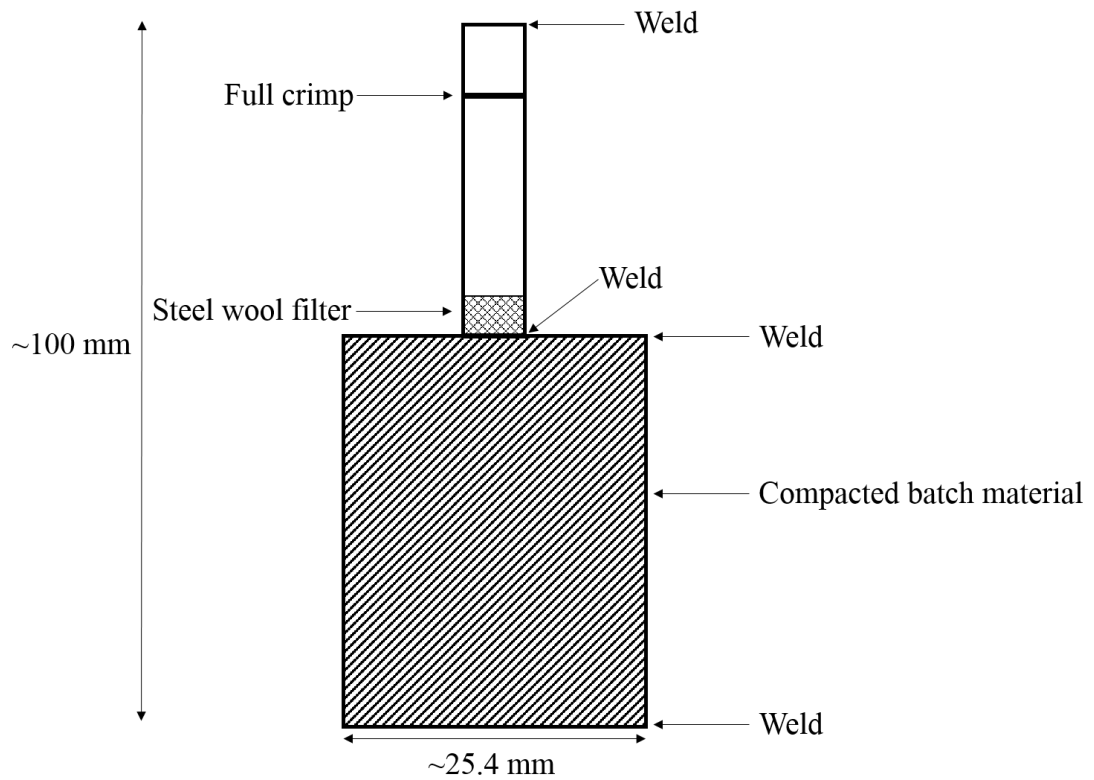


**Figure 3.6:** HIP canister schematic.

Prepared HIP canisters were placed in the HIP pressure vessel and hot isostatically pressed using argon to produce consolidated samples. HIPed samples were prepared for analysis by sectioning the ends of the HIP canisters and then core drilling the sample within.

### 3.5. X-ray diffractometry (XRD)

X-ray diffraction has been used throughout the research presented in this work as a key characterisation technique. This section provides a brief overview of X-ray diffractometry and its use as a tool for the identification and quantification of mineral phases.

#### 3.5.1. X-rays and Bragg's law

X-rays are electromagnetic radiation with wavelength of the order of  $10^{-10}$  m. X-rays are produced when highly energetic, charged particles collide with matter. X-ray spectra have two components, a broad-band emission of wavelengths known as Bremsstrahlung radiation and a number of characteristic monochromatic wavelengths. Bremsstrahlung radiation, also known as 'braking radiation', is produced when charged particles are decelerated due to deflection by another charged particle. The kinetic energy lost by the incoming particle is emitted as a photon (X-ray) thus satisfying the law of conservation of energy. Bremsstrahlung radiation has a calculable, limiting, lower wavelength; at this wavelength all of the energy of the incoming particle is converted to X-rays.

Monochromatic X-rays are produced as a result of electronic transitions between atomic orbitals. If an incident particle has sufficient energy it can ionise a core electron (e.g. 1s). An electron from an outer shell (e.g. 2p or 3p) immediately transitions to fill the vacancy and excess energy is released as X-rays. Electronic transitions have fixed energies, therefore, X-rays produced as a result of electronic transitions have characteristic wavelengths. For example, for copper, a  $2p \rightarrow 1s$  transition ( $K\alpha$ ) produces an X-ray with an average wavelength of 1.5405 Å ( $1 \text{ \AA} = 10^{-10} \text{ m}$ ) whereas a  $3p \rightarrow 1s$  transition ( $K\beta$ ) produces an X-ray with a wavelength of 1.3922 Å. The  $K\alpha$  transition is actually a doublet, two different wavelengths,  $K\alpha_1 = 1.54051 \text{ \AA}$  and  $K\alpha_2 = 1.54433 \text{ \AA}$ , are emitted; this is a result of the two possible spin states of the 2p electron making the transition [95].

Using monochromatic X-rays and Bragg's law it is possible to investigate the crystal structure of materials. Bragg's law considers crystals to be made of planes that act as semi-transparent mirrors such that some X-rays are reflected with an angle equal to that of the angle of incidence and others are transmitted and reflected from subsequent crystal planes. It is possible to derive Bragg's law by considering two X-rays, 1 and 2, reflected from adjacent crystal planes. For the two reflected rays to be in phase the extra distance

travelled by the second X-ray,  $xyz$ , must be equal to a whole number of wavelengths,  $n\lambda$ , see Figure 3.7 and Equation 7.

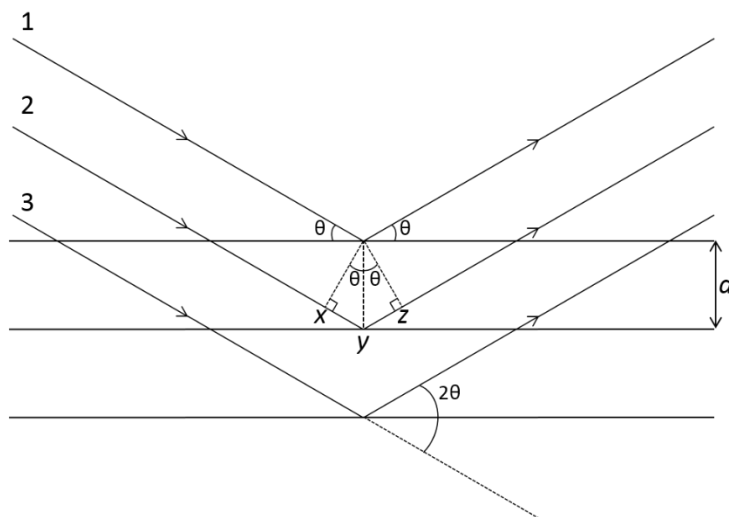


**Figure 3.7:** Derivation of Bragg's Law

Using the inter-layer spacing,  $d$ , the Bragg angle,  $\theta$ , and the distance  $xy$ ; the law is derived thusly:

$$xy = yz = d \sin \theta$$

$$xyz = 2d \sin \theta$$

$$xyz = n\lambda$$

$$n\lambda = 2d \sin \theta$$

**Equation 7**

When the conditions of Bragg's law are satisfied, the reflected X-rays are in phase and constructive interference occurs. When the conditions are not met, destructive interference occurs often leading to complete cancellation. X-ray diffractometry (XRD) utilises this fact to gather data regarding the crystal structure of materials.

### 3.5.2. X-ray diffractometers and X-ray optics

There are three components to a basic XRD experiment: an X-ray source, the sample and a detector to measure the diffracted rays, the entire apparatus is referred to as a goniometer. X-rays are typically generated by the use of an X-ray tube. X-ray tubes

accelerate a stream of electrons, generally from a heated filament or ionisable gas, through an accelerating voltage (30-50 kV) towards a metal target, e.g. copper. When the beam strikes the target the electrons are inelastically scattered resulting in the emission of Bremsstrahlung radiation and X-rays characteristic of the target material. X-rays are emitted in all directions from the target and leave the tube *via* a window. Window materials have low atomic numbers to decrease the scattering of the X-rays and beryllium is a popular choice. In diffractometers utilising Bragg-Brentano parafocussing geometry, the source is fixed and the sample and detector are scanned through a range of angles, see Figure 3.8. The sample is rotated around an axis perpendicular to the beam at a rate of  $\theta^{\circ}\text{min}^{-1}$ . The detector, typically a proportional, scintillation or Geiger counter, rotates around the same axis as the sample at a speed of  $2\theta^{\circ}\text{min}^{-1}$  to ensure the angles of incidence and diffraction are maintained equal.

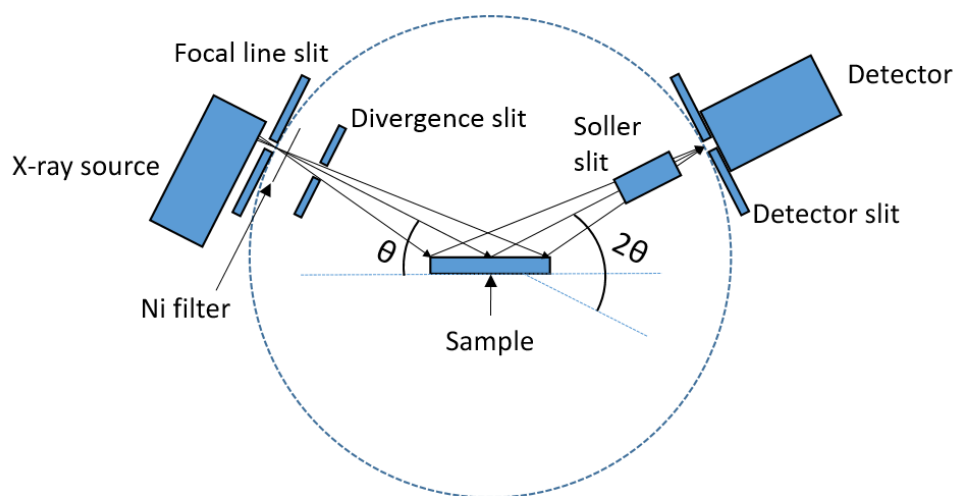


**Figure 3.8:** Bragg-Brentano parafocussing geometry as used in Bruker D2 Phaser.

The X-ray beam may be monochromated by an incident beam monochromator or a diffracted beam monochromator. Some diffractometers may not use a monochromator but may instead utilise a  $K\beta$  filter e.g. a Ni foil in machines using a Cu source;  $K\alpha_2$  contributions may be stripped from the raw data later using processing software. Soller slits are thin, parallel and equally spaced metal plates, typically made from Mo foil. Soller slits ensure that only X-rays travelling in the correct direction reach the sample and suppress the X-ray divergence along the goniometer axis- axial divergence may lead to

asymmetry in peaks. The divergence slits suppress the divergence of the beam within the sample plane and allow the footprint of the X-ray beam on the sample to be controlled. Divergence slits also help to reduce the effect of flat plate specimen error. Scattering slits ensure that only diffracted beams reach the detector. Receiving slits affect how well closely spaced reflections can be differentiated and consequently define the resolution of the system. The X-ray diffractometer used in this thesis was a Bruker D2 Phaser utilising a Ni foil  $K\beta$  filter in Bragg-Brentano reflection geometry. The diffractometer used a Cu X-ray source, with 10 mA current and 30 kV accelerating voltage.

### *3.5.3. Sample preparation and measurement*

Prior to measurement, samples are finely ground to ensure a maximum of crystallites. Ideally the crystallites are arranged randomly in every possible orientation consequently, the lattice planes are also present in every possible orientation. As a result, regardless of orientation, there should be some lattice planes oriented at the Bragg angle and thus diffraction occurs. The resultant peaks in diffraction form concentric rings and it is possible to plot the relative intensity of the diffracted rings relative to  $2\theta$ , an example is shown in Figure 3.9. The diffraction pattern is highly sensitive to the phase or phases present and can be used to perform qualitative phase analysis.

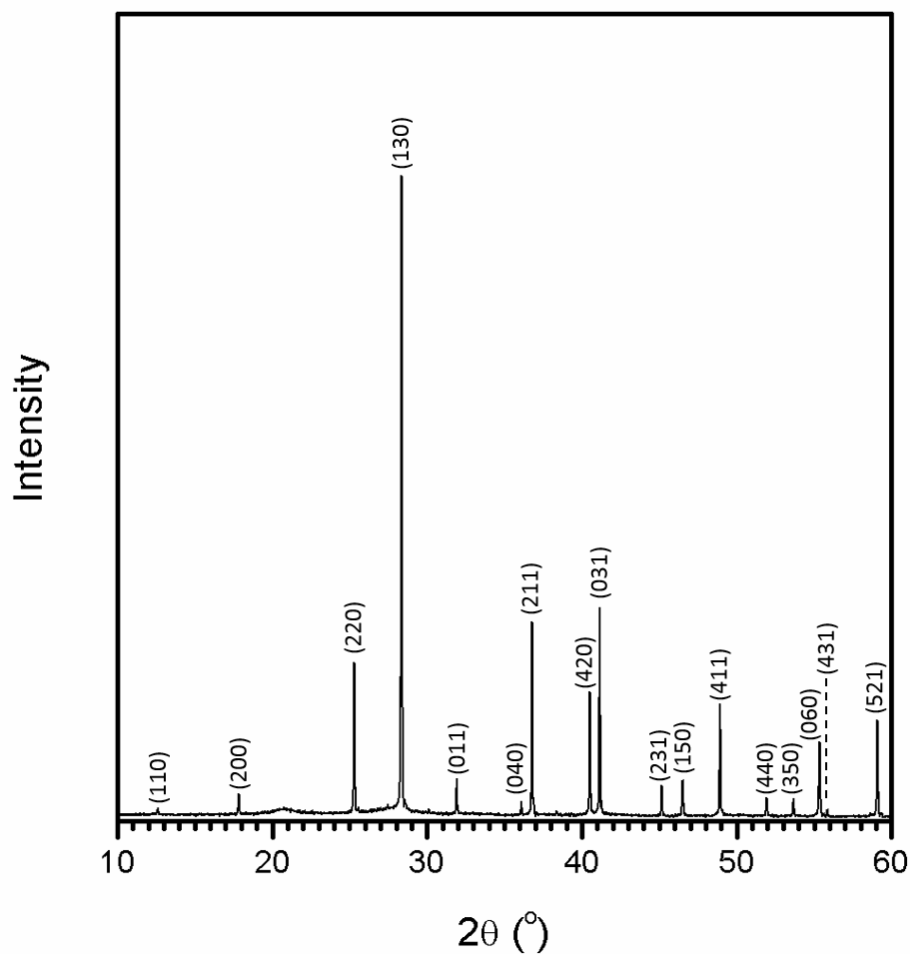


**Figure 3.9:** A typical XRD pattern of an alumino titanate hollandite ( $\text{Ba}_{1.2}\text{Al}_{2.4}\text{Ti}_{5.6}\text{O}_{16}$ ) measured using  $\text{Cu K}\alpha$  radiation.

Peak positions are determined by the size and shape of the unit cell and intensities are affected by the position of atoms within the unit cell, becoming more intense with atomic number and phase concentration. Diffraction peak widths are affected by crystallite size and strain effects.

#### 3.5.4. Rietveld refinement

Rietveld refinement is a computational technique used to perform refinement of theoretical crystal structure models [96]. A least squares approach is used to minimise the weighted sum of the intensities of a simulated diffraction profile ( $y_{c,i}$ ) and that of the observed data ( $y_{o,i}$ ),  $\sum_i w_i (y_{c,i} - y_{o,i})^2$ . The weighted profile factor,  $R_{wp}$ , is used as a tool to assess the quality of the fit and is calculated by Equation 8, a lower  $R_{wp}$  indicates a better

fit. The use of Rietveld refinement allows quantitative phase analysis to be performed and also allows the lattice parameters and atomic co-ordinates of the unit cell to be derived [95]. Rietveld refinement of data was performed using the Bruker Topas software package.

$$R_{wp} = \sqrt{\frac{\sum_i w_i (y_{c,i} - y_{o,i})^2}{\sum_i w_i (y_{o,i})^2}} \quad \text{Equation 8}$$

### 3.6. X-ray absorption spectroscopy (XAS)

X-ray absorption spectroscopy (XAS) is an analytical technique utilising synchrotron radiation that can be used to determine the oxidation state and co-ordination environment of elements within samples. When travelling at relativistic speeds, the deflection of electrons or positrons by a magnetic field results in the emission of synchrotron radiation, a continuous spectrum from microwaves to hard X-rays [97]. Synchrotrons hold several advantages over conventional laboratory X-ray sources.

During an XAS experiment, the sample is placed in the path of a focussed beam of X-rays of well-defined energy. X-ray energies are controlled by means of a monochromator. Some of the X-rays will be absorbed by atoms in the sample resulting in the excitation or ejection of core electrons. It is possible to quantify the degree of absorption by several methods: comparing the intensity of the incident beam to that of the transmitted beam, measuring the fluorescence X-rays generated by core-hole transitions or by measuring ejected Auger electrons as the core hole is filled. The energy of the incident X-rays is varied and the absorption at each energy quantified [98]. Using the gathered data it is then possible to construct an X-ray absorption spectrum, an example is shown in Figure 3.10. When samples are measured in transmission, a general downward trend in absorption may be observed as X-ray energy is increased due to the more penetrating nature of higher energy X-rays. Conversely, when measuring samples in fluorescence, an upward trend may be observed due to the increased number of electronic transitions caused by higher energy X-rays.

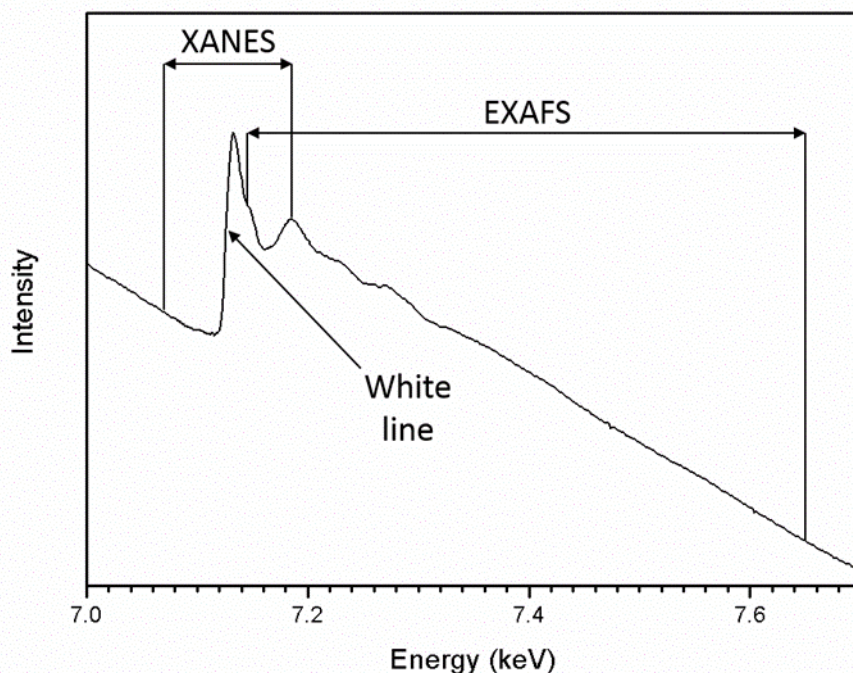


**Figure 3.10:** A typical transmission XAS spectrum (Fe K-edge,  $\text{Ba}_{1.2}\text{Fe}_{2.4}\text{Ti}_{5.6}\text{O}_{16}$ ), indicating the ‘white line’ and the XANES and EXAFS regions.

Due to the quantum nature of electronic transitions, below a threshold energy X-rays possess insufficient energy to promote electrons from a particular orbital, above it they do. This results in a sharp increase in absorption known as the edge or ‘white line’. Absorption edges are characteristic of the electron orbital and element being excited.

The X-ray absorption near edge structure (XANES) can provide details of an element’s co-ordination environment and oxidation state. The XANES region ranges from approximately -50 to +200 eV relative to the absorption edge energy [99]. By comparing the XANES data of samples with that of well characterised standards it is possible to derive both the chemical speciation and co-ordination environment of the element of interest.

The extended X-ray absorption fine structure (EXAFS) region is the normalised oscillatory part of the X-ray absorption spectrum above the absorption edge up to  $\sim +1,000$  eV or higher. Like XANES, EXAFS can be used to provide details of an

element's co-ordination environment but can also be used to determine information such as the interatomic distances and the local structural environment [99].

Samples were prepared for XAS analysis by homogeneously mixing powdered samples with polyethylene glycol and uniaxially pressing to form 13 mm diameter pellets of approximately one absorption length. XAS data were gathered at beamlines X23A2, National Synchrotron Light Source, Brookhaven National Laboratory and X05LA, Swiss Light Source, Paul Scherrer Institute. Data reduction and EXAFS analysis were performed using the programmes Athena and Artemis [100], [101].

### **3.7. Scanning electron microscopy and energy dispersive X-ray spectrometry (SEM-EDX)**

Scanning electron microscopy is an imaging technique primarily used to study the surface features of a sample at greater magnifications than achievable by standard optical microscopy. Energy dispersive X-ray spectroscopy, EDX, is a highly useful analytical technique and can be used to gather information regarding grain structure, phase distribution and phase composition. As the name suggests SEM-EDX utilises electrons to produce images instead of visible light.

#### *3.7.1 Resolution and the use of electrons*

Although optical microscopy is a useful tool for the inspection of specimens, it is often impossible to resolve features of interest as their size is of the same order as that of the wavelength of visible light. Resolution, the smallest distance between two points that may be observed, is a function of wavelength (assuming perfect lenses and very large apertures, the maximum theoretical resolution of an optical light microscope is  $\sim 0.15 \mu\text{m}$ ). If the lenses of a microscope were perfect and introduced no distortions in the image, the resolution would still be limited by diffraction effects. When a parallel beam of light passes through a restricted opening (i.e. the apertures or lenses of a microscope) the light is diffracted and forms a series of cones- these appear as a series of rings known as Airy rings. Due to these diffraction effects, the light from every point of the object is diffracted and even an infinitely small point becomes an Airy disc in the

image. To limit the effects of diffraction on the image, the apertures must be as large as feasibly possible, the effects of aperture size are demonstrated in Figure 3.11.

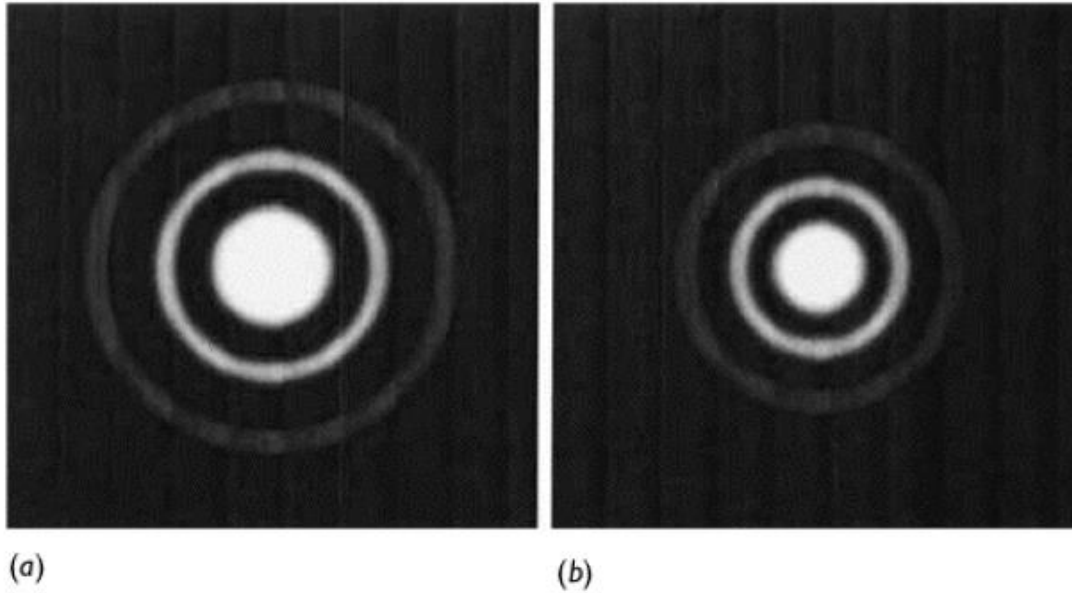


**Figure 3.11:** Airy rings resulting from the diffraction of a laser beam by small apertures: a) 75  $\mu\text{m}$  and b) 100  $\mu\text{m}$ . Taken from Goodhew (2001) [102].

The central spot contains 84 % of all the light intensity and consequently the rings are often ignored and it is possible to assume that all the light falls within a spot with a diameter of  $d_1$  ( $d_1$  is inversely proportional to the size of the aperture). The minimum distance required between two spots of diameter  $d_1$  for them to be distinguishable is the resolution. When the maximum intensity of one spot coincides with the minimum of another the two spots are just distinguishable; this gives a resolution limit of  $d_1/2$ . It is therefore possible, using diffraction theory, to calculate the resolution limit using Equation 9 given below:

$$r_1 = \frac{d_1}{2} = \frac{0.61\lambda}{\mu \sin \alpha} \quad \text{Equation 9}$$

Where  $\lambda$  is the wavelength of the photons,  $\mu$  is the refractive index of the medium between the object and the objective lens and  $\alpha$  is the semi-angle [102].

Consequently, photons with a smaller wavelength must be used to achieve higher resolution, and a higher resolution may be achieved by using electrons instead of visible light.

### 3.7.2 Electron beam generation and imaging

An electron beam is generated by accelerating electrons through a voltage. Electrons can be generated by thermionic emission or by using a field emission gun (FEG). Electrons are charged particles and can be deflected by magnetic fields; a series of two to three electromagnetic lenses are used to focus the beam on the sample surface giving an electron probe size diameter of 1-10 nm. Scan coils are then used to raster the electron beam across the surface of the sample. A simplified schematic of a scanning electron microscope is shown below in Figure 3.12.

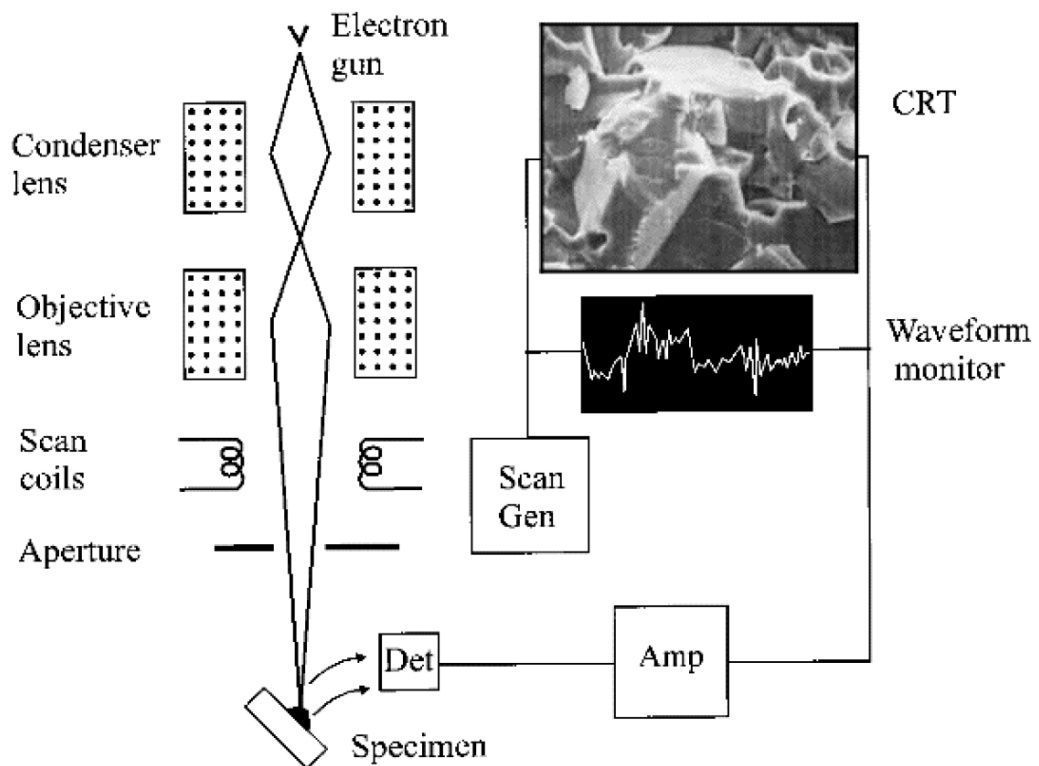


**Figure 3.12:** Schematic diagram of an analogue scanning electron microscope. Taken from Goodhew (2001) [102].

Detectors are used to record the various electrons scattered from the surface of the sample. The amplified current from each spot is used to modulate the brightness of an on screen image. In analogue SEMs the image is produced by scanning the spot of a CRT screen;

in digital SEMs the resultant image is displayed on a computer screen. Magnification of an image is achieved by decreasing the size of the electron beam raster whilst simultaneously increasing the size of the image raster [102]. It is possible to use the different types of electrons produced by electron-specimen interactions, for example backscattered electrons or secondary electrons, to create the image, this may allow the observer to gain a greater understanding of the sample.

### 3.7.3 *Electron-specimen interactions*

When an electron beam impinges upon a sample, the electrons undergo scattering by both elastic and inelastic processes. Gradual loss of energy as a result of multiple scattering events results in a finite range,  $R$ , of electrons within the sample (see Figure 3.13).  $R$  is dependent upon both electron energy and the density of the sample and is of the order of 10 nm – 10  $\mu$ m. Electrons emitted from the sample include secondary electrons (SE), backscattered electrons (BSE) and Auger electrons. X-ray photons, created as a result of electronic transitions, are also emitted. Secondary electrons are relatively low in energy (2 - 5 eV) and result from highly energetic inelastic collisions; the work function of the specimen is exceeded and an electron is liberated. Backscattered electrons have a broad range of energy values ranging from 50 eV to the primary electron energy, this broad spectrum is a result of multiple energy losses caused by multiple collisions and subsequent scattering. Auger electrons result from the ionisation of inner shell electrons and are produced as an alternative to characteristic X-rays. When an outer shell electron transitions to fill a hole left by the liberation of a core electron, the excess energy can be released as an X-ray of characteristic energy or it may be transferred to another atomic electron. The electron then leaves the sample with a characteristic energy equal to that of the characteristic X-ray energy produced by the same transition less the ionisation energy and the work function.

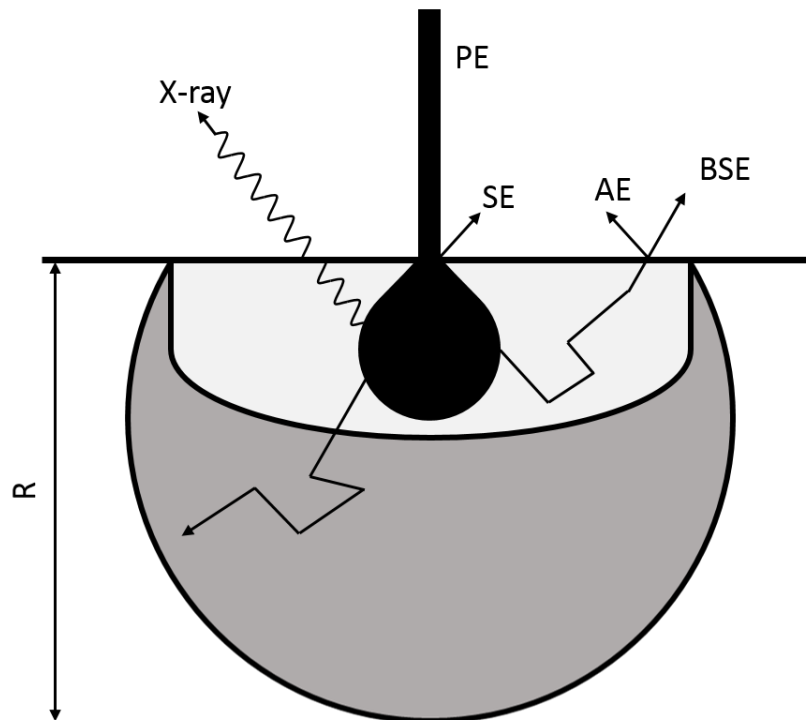


**Figure 3.13:** Origin and information depth of secondary electrons (SE), backscattered electrons (BSE), Auger electrons (AE) and X-ray quanta in the diffusion cloud of electron range  $R$  for normal incidence of the primary electrons (PE). Adapted from Reimer (1998) [103].

Secondary and Auger electrons are easily scattered, consequently, any SE or AE observed originates from within a very thin surface region of the order of a few nanometres thick. SEs and AEs are produced by both primary electrons and backscattered electrons as they return to the surface. Electrons that return to the surface from greater depths typically have longer paths and larger energy losses. The maximum information depth (the depth to which possible contributions to detected signals may originate) is of the order of half the electron range. Semiconductor-based or scintillation detectors are often used to detect BSEs, the nature of these detectors means that electrons of higher energies give a larger contribution to the signal, as a result this effect needs to be taken into account [103].

#### 3.7.4 Energy dispersive X-ray spectroscopy (EDX)

Energy dispersive X-ray spectroscopy utilises the characteristic X-rays emitted as a result of core electron losses to characterise a sample. As stated in Section 3.5.1, X-rays

resulting from electronic transitions are characteristic of the element being excited and the orbitals involved in the transition. With proper calibration, it is possible to use characteristic photons to produce semi-quantitative data regarding sample composition. Light elements, those with  $A_R \leq 20$ , are difficult to detect as the energy of the emitted photons fall below the limitations of many detectors and the ratio of Auger electrons to photons also increases. By scanning the electron beam and collecting EDX spectra over an area it is possible to produce a map of element distribution.

Observed X-ray photons originate from a larger interaction volume than secondary and backscattered electrons. Consequently, the resolution of chemical identification and quantification is lowered.

EDX maps were gathered using a Hitachi TM3030 scanning electron microscope equipped with a Bruker Quantax 70 EDX. EDX maps and spectra were processed using Bruker Quantax 70 software.

#### *3.7.5 Sample preparation*

Samples were prepared for SEM by mounting in epoxy resin. After curing overnight, excess resin was removed using SiC paper to expose the sample surface. The surface was then polished to an optical finish (1  $\mu\text{m}$ ) using progressively finer diamond pastes. To reduce surface-charging, the samples were sputter-coated with carbon using an Agar Scientific Carbon Coater.

### 3.8. Transmission electron microscopy (TEM)

Transmission electron microscopy, like SEM, uses electrons to form images and perform analyses of materials. However, unlike SEM, TEM does not use back scattered or secondary electrons but instead uses electrons that have been transmitted through the sample. Due to the interaction with and absorption of electrons by the sample material it is necessary that samples are sufficiently thin to allow the transmission of electrons. As electrons are transmitted through the sample, lenses are present above and below the sample to allow focussing of the electron beam and the image, see Figure 3.14.

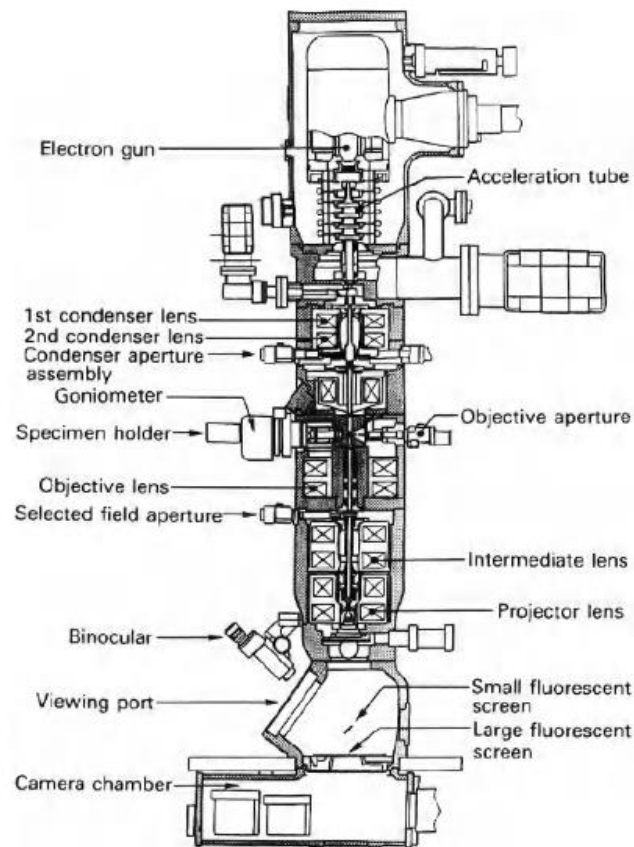


**Figure 3.14:** Schematic of a transmission electron microscope. Taken from Fultz et al (2008) [104].

Samples were prepared for TEM analysis by grinding in a pestle and mortar followed by suspension in acetone. Ground powders were added to a glass vial containing acetone, the vial was then placed in an ultrasonic bath and sonicated to suspend fine particles in

the acetone. A holey copper grid was washed through the suspended fines and the adhered particles were then studied.

Transmission electron microscopy was conducted using a Philips EM420J TEM.

### **3.9. Mössbauer spectroscopy**

Mössbauer spectroscopy is a spectroscopic technique that is used to probe nuclear energy levels. The technique is sensitive to local electron configuration and magnetic interactions allowing the investigation of oxidation states, structural environments and nuclear spin states. Mössbauer spectroscopy relies on the recoil-free emission and resonant absorption of gamma rays by atomic nuclei, otherwise known as the Mössbauer effect [105]. The Mössbauer effect is only observed for certain atoms e.g. Ir and Fe and, consequently, can only be used to investigate solids containing these atoms.

#### *3.9.1. Resonant absorption in free atoms*

When the energy of an incoming gamma ray is sufficient to promote an electron from the ground state to an excited state, the gamma ray will be absorbed. Ideally, when the electron transitions back to the ground state the excess energy is emitted as a gamma ray of equal wavelength to the incident gamma ray, this is known as resonant fluorescence. The excited state has a finite lifetime,  $\tau$ . Considering the Heisenberg uncertainty principle, the energy of emitted gamma ray is no longer precisely defined and instead follows a Breit-Wigner or Lorentzian distribution. Energy distribution is centred around  $E_0$  with full width at half maximum,  $\Gamma_0$  where  $\Gamma_0 = \hbar/\tau$  and  $\hbar$  is Planck's constant divided by  $2\pi$ , see Figure 3.15.

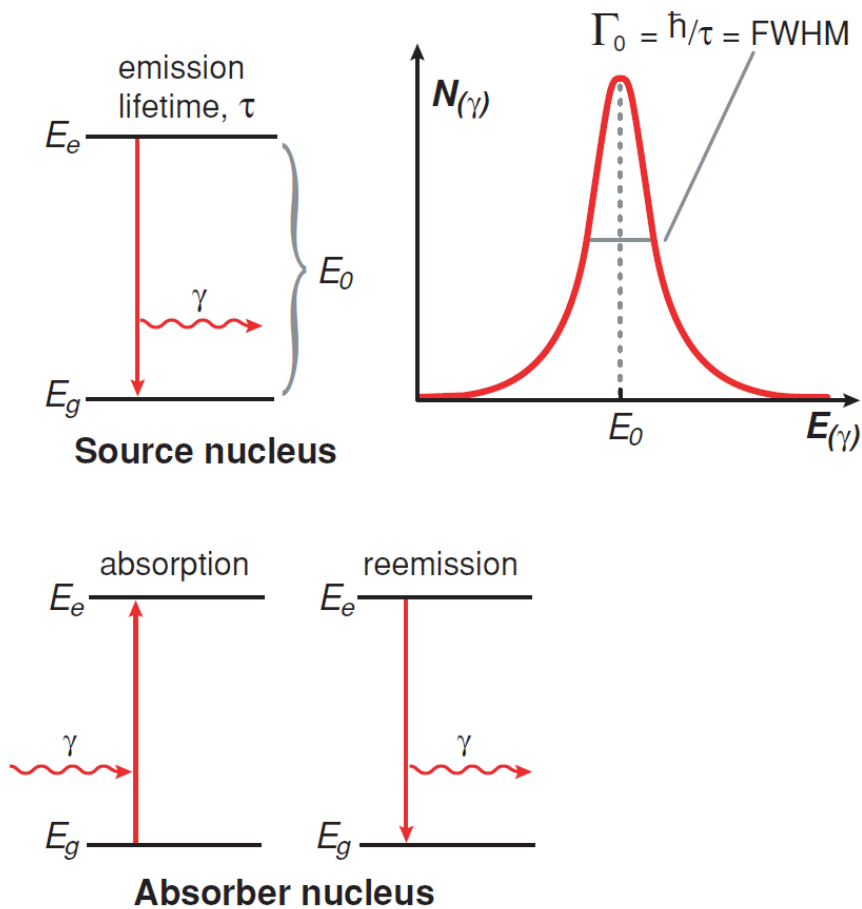


**Figure 3.15:** Ideal resonant absorption.  $E_0$  is the difference in energy between the ground and excited states. Taken from Dyar et al (2006) [106].

The idealised case ignores the conservation of momentum. Assuming that the emitting atom is initially at rest, conservation of momentum dictates that it must recoil and acquire energy,  $E_r$ , proportional to the mass of the nucleus. Consequently, the absorbed photon energy is split between the emitted gamma ray and the recoiling nucleus. Therefore, for a photon to be absorbed by an atom at rest, the incident photon must possess energy equal to the transition energy and an additional energy to account for the recoil of the emitting nucleus. Although the recoil energy is relatively small ( $10^{-4} - 10^{-1}$  eV) it is still large enough in comparison to the gamma emission linewidth ( $10^{-9} - 10^{-6}$  eV) to ensure that resonant absorption-emission cannot occur for atoms at rest. It is possible to achieve resonant absorption by moving the emitting nucleus towards the absorber, thereby Doppler shifting the gamma photon or by increasing the heat within the system and broadening the energy distribution of the emitted photons.

### 3.9.2. Resonant absorption in solids

In the case of solids, there are three possibilities. Firstly, if  $E_r$  is large compared to the binding energy the atom will be displaced from the crystallographic site and the free atom model will apply. Secondly, if  $E_r$  is insufficient to break bonds and the energy is transferred to the lattice as a lattice phonon. The lattice is quantised and energy is transferred in integral amounts. Lastly, if  $E_r$  is less than the energy of a lattice phonon, it is not possible to arbitrarily excite the lattice and energy is not transferred.  $E_r$  is effectively zero and such an event is known as a zero phonon event.

It is possible to explain the observed phenomena by considering the solid as an Einstein solid, with  $3N$  vibrational modes of frequency  $\omega$  ( $N$  = no. atoms in the solid). The only possible changes to the solid are an increase or decrease in the quantum numbers of the vibrational modes, corresponding to absorption or emission of quanta of energy  $\hbar\omega$ . Emission of gamma rays are associated with transfer of multiple integrals of  $\hbar\omega$  to the lattice (0, 1, 2 etc.). The average energy transferred to the lattice is equal to the recoil energy of a free atom,  $E_r$ . It is possible to therefore derive the fraction of absorption-emission events that result in zero excitation of the lattice (i.e. those that give rise to the Mössbauer effect),  $f$ , see Equation 10.

$$E_r = (1 - f)\hbar\omega$$

$$f = 1 - \frac{E_r}{\hbar\omega}$$

**Equation 10**

When the lattice is excited, the effective linewidth is of the same order as the phonon energies. When the lattice is not excited, the linewidth of the zero-phonon component is controlled by the widths of the nuclear levels. The nuclear lifetime is six orders of magnitude smaller than that when the lattice is excited, linewidth  $\sim 10^{-8}$  eV. This linewidth is less than the characteristic magnetic and electronic quadrupole interactions of the nuclei with surrounding electrons, it is therefore possible to probe these interactions using the Mössbauer effect.

### 3.9.3. Spectroscopic measurements and hyperfine parameters

Modulating the gamma source relative to the sample allows a Mössbauer spectrum to be obtained. By varying the velocity of the source, the centre of the emission spectrum is

Doppler shifted from smaller to larger energies relative to the absorption spectrum. The degree of overlap between the emission and absorption spectra determines the intensity of the transmission spectrum (a smaller overlap means less absorption and therefore greater transmission). Differences in absorber and emitter environments can be investigated by comparing the spectra of a standard and the sample of interest.

Energy levels within nuclei are split or shifted by hyperfine interactions (interactions with the electronic environment). These interactions are observable in the absorption spectra, each environment will contribute to the spectrum. Study of the hyperfine parameters allows useful data to be extracted from the spectra.

The isomer shift,  $\delta$ , is caused by interaction between the positively charged nucleus and the electric field of the surrounding electrons. In Mössbauer spectroscopy, absorbers are compared to a common source and differences in electronic environment between the source and the absorber are observed as the isomer shift. The isomer shift is dependent upon the electron density at the nucleus (contact density). As the source contact density is constant,  $\delta$  can be used as a linear measure of the absorber contact density.

Quadrupole splitting arises from the non-spherical distribution of nuclear charge. The shape of nuclear charge distribution is determined by the nuclear quadrupole moment. Asymmetric electric field gradients (EFG) are caused by the asymmetric distribution of electronic charge or ligands. Interaction between asymmetric EFGs and the quadrupolar moment leads to splitting of the normally degenerate nuclear energy levels. As the inner electron shells have spherical symmetry, quadrupolar splitting is affected by the valence electrons and is therefore indicative of the bonding environment and the local electronic structure.

When using  $^{57}\text{Fe}$  as the gamma source, an external magnetic field will remove the degeneracy of the nuclear energy levels resulting in hyperfine splitting. Splitting of the  $I = \pm 1/2$  and  $I = \pm 3/2$  levels, into two and four sub-levels respectively, results in a sextet spectrum.

When combined, hyperfine parameters allow the oxidation state and local environment of the element being investigated to be deduced. Typical hyperfine parameters for Fe in minerals and the associated local environments are shown in Figure 3.16 below.

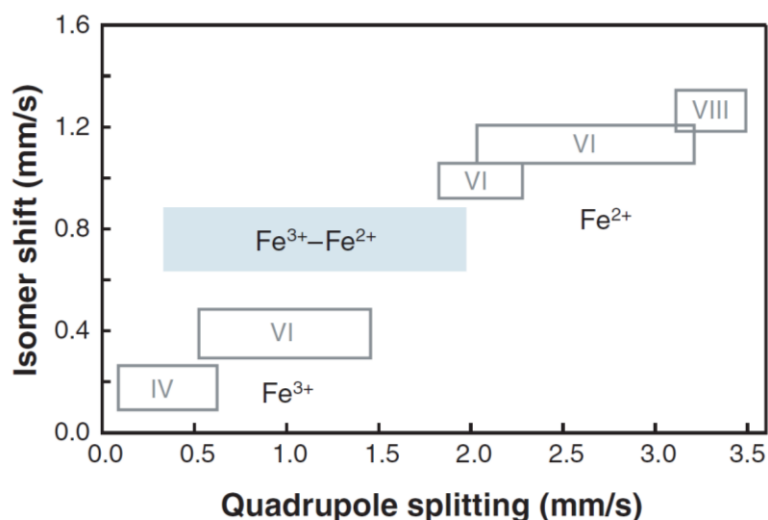


**Figure 3.16:** Typical hyperfine parameters for Fe bearing minerals. Taken from Dyar et al (2006) [106].

$^{57}\text{Fe}$  transmission Mössbauer spectra of powdered samples were gathered at room temperature using a  $^{57}\text{Co}/\text{Rh}$  source. Samples were calibrated relative to an  $\alpha\text{-Fe}$  reference and spectra were measured using a Wissel MRG-500 spectrometer and a constant acceleration waveform with velocity range  $\pm 10 \text{ mm s}^{-1}$ . Data were deconvoluted by assigning Lorentzian doublets to represent different Fe oxidation states and co-ordination environments using the Recoil analysis software [107].

### 3.10. Gamma spectroscopy

Emitted gamma rays are the result of electronic transitions and are therefore characteristic of the parent atom. Measurement of the emitted gamma spectrum of a sample can therefore be used to determine the gamma emitting elements present. Gamma spectrometers utilise either scintillation or semi-conductor based detectors to measure gamma rays emitted by a sample. Scintillation detectors measure the intensity of light emitted by a scintillant crystal. The intensity of light emitted by the crystal is proportional to the energy deposited by an incident gamma ray. Thallium doped sodium iodide crystals are a common example of scintillation crystals. Semi-conductor based detectors measure the generation of electron-hole pairs within the sample caused by incident gamma rays.

Semi-conductor based detectors offer improved resolution relative to scintillation detectors [108].

Gamma spectra of samples were measured using a Canberra BEGe spectrometer (Broad Energy Germanium) equipped with a germanium detector. Calibration of gamma spectra was performed with respect to a 37 kBq (1  $\mu$ Ci)  $^{152}\text{Eu}/^{22}\text{Na}$  standard.

### **3.11. Inductively Coupled Plasma- Mass Spectrometry**

Inductively coupled plasma chemical analyses are techniques that utilise conductive plasmas to determine elemental concentrations within a solution. Samples in this work were analysed by Inductively Coupled Plasma – Mass Spectrometry (ICP-MS) a technique that identifies elements by their mass.

Prior to analysis, solutions are drawn through a nebuliser to form an aerosol, the aerosol is then passed through an  $\text{Ar}^+$  plasma torch and ionised. After generation, the plasma is drawn into the mass spectrometer and through a series of cones by a negative potential creating a stream of plasma. Isobaric interfering species, such as  $\text{Ar}^+$  and  $\text{ArO}^+$ , are removed by a dynamic reaction cell. Ions of selected mass to charge ratio are deflected by deflector plates before entry to the detector thereby blocking photons. Counts detected are proportional to solution concentration and can be quantified by comparison with standard solutions of known concentration.

### **3.12. Thermal analysis**

Thermogravimetric analysis (TGA) continuously measures the mass of a sample as a function of time or temperature. Samples are measured isothermally or at a constant heating rate, it is also possible to measure samples using a custom heating profile. Using TGA it is possible to follow the progression of chemical reactions by monitoring the mass change of the sample.

Differential scanning calorimetry (DSC) measures the amount of energy required to maintain a sample at the same temperature as a reference as a function of temperature. DSC allows the determination of endothermic and exothermic events e.g. melting, crystallisation etc. [109].

Simultaneous thermal analysis (STA) was used to investigate the behaviour of pre-cursor and synthesised materials during heating. STA combines thermogravimetric analysis (TGA) and differential scanning calorimetry (DSC). Measurements were made using a Netzsch TG 449 F3 Jupiter instrument coupled with a 64 channel QMS 403 D Aëolos mass spectrometer for off-gas analysis.

### 3.13. Gas pycnometry

The density of samples was determined by the use of gas pycnometry. Gas pycnometry has its basis in Boyle-Mariotte's law relating pressure and volume. Its use avoids several problems associated with other volume measurements methods (e.g. Archimedes) for instance air entrapment and physiochemical interactions.

Constant volume gas pycnometers measure the volume of a sample of known mass by measuring the difference in gas pressure between two chambers of known volume, one sealed and one containing the sample, as shown in Figure 3.17. Gas pycnometers assume that the gas behaves ideally, the sample and the components of the pycnometer are rigid and that the expanding gas quickly reaches a static equilibrium. The operation of a pycnometer is as follows:

1. The sample is placed in the sample chamber and the pycnometer sealed
2. Both valves are opened and the pycnometer is filled with gas.
3. Valve 1 is closed and the transducer measures the initial gas pressure,  $P_i$
4. Valve 2 is closed, isolating the sample chamber
5. Valve 1 is opened and the tank is evacuated/filled.
6. Valve 1 is closed and the pressure in the tank is measured,  $P_j$
7. Valve 2 is opened and the gas from the sample chamber allowed to expand
8. The transducer measures the final gas pressure,  $P_f$

It is then possible to determine the volume of the sample by using Equation 11.

$$P_f = T_f \frac{(P_i/P_f)(V_c/V_s) + (P_i/T_j)V_t}{V_c - V_s + V_t + \Delta V_z} \quad \text{Equation 11}$$

Where:  $V_s$  is the sample volume;  $V_c$  is the volume of the sample chamber plus the internal volume of Valve 2 and connecting tubing and  $V_t$  is the volume of the tank, pressure transducer and associated tubing.  $\Delta V_z$  is the change in volume of Valve 2 when it is

closed.  $T_i$ ,  $T_j$  and  $T_f$  are the absolute gas temperatures when  $P_i$ ,  $P_j$  and  $P_f$  are measured respectively; they are assumed to be approximately equal [110].

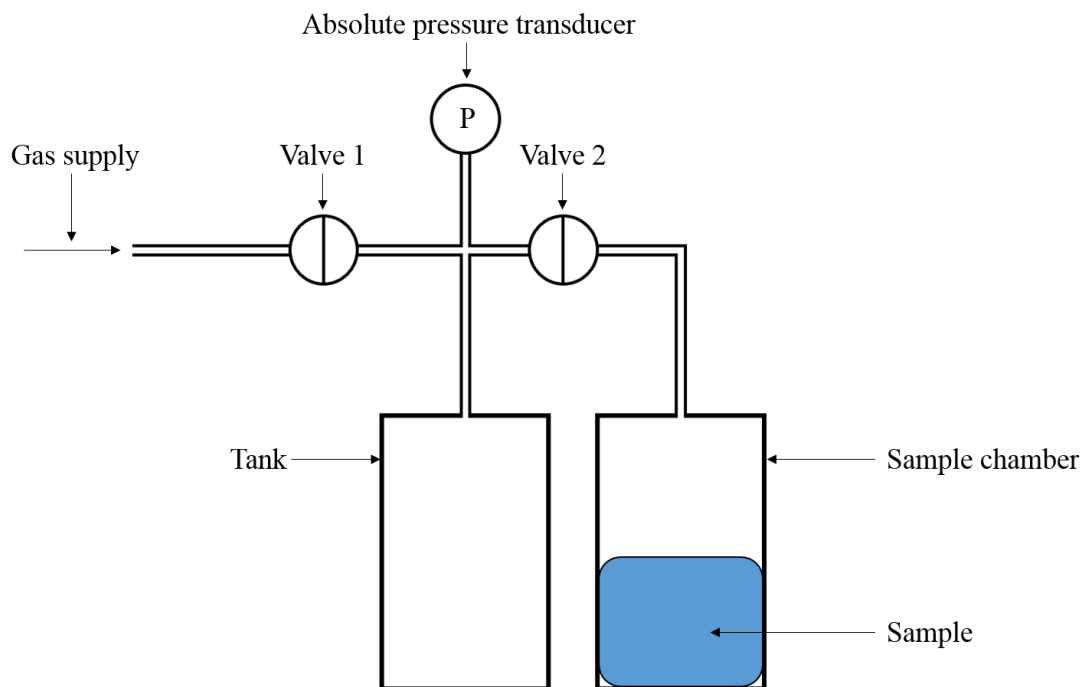


**Figure 3.17:** A schematic of a constant volume gas pycnometer. Adapted from Tamari (2004) [110].

Using the measured volume, it is then possible to calculate the density by calculating the ratio of sample mass to volume. The mass of samples were measured prior to measurement to an accuracy of 0.0001 g.

**4. Synthesis and characterisation of the  
hollandite solid solution  
 $\text{Ba}_{1.2-x}\text{Cs}_x\text{Fe}_{2.4-x}\text{Ti}_{5.6+x}\text{O}_{16}$  for  
partitioning and conditioning of  
radiocaesium**

# Synthesis and characterisation of the hollandite solid solution $\text{Ba}_{1.2-x}\text{Cs}_x\text{Fe}_{2.4-x}\text{Ti}_{5.6+x}\text{O}_{16}$ for partitioning and conditioning of radiocaesium

*Daniel J. Bailey<sup>1</sup>, Martin C. Stennett<sup>1</sup>, Amber R. Mason<sup>1</sup> and Neil C. Hyatt<sup>1</sup>*

1- Immobilisation Science Laboratory, Department of Materials Science and Engineering, University of Sheffield, United Kingdom

## Abstract

The geological disposal of high level radioactive waste requires careful budgeting of the heat load produced by radiogenic decay. Removal of high-heat generating radionuclides, such as  $^{137}\text{Cs}$ , reduces the heat load in the repository allowing the remaining high level waste to be packed closer together therefore reducing demand for repository space and the cost of the disposal of the remaining wastes. Hollandites have been proposed as a possible host matrix for the long-term disposal of Cs separated from HLW raffinate. The incorporation of Cs into the hollandite phase is aided by substitution of cations on the B-site of the hollandite structure, including iron. A range of Cs containing iron hollandites were synthesised via an alkoxide-nitrate route and the structural environment of Fe in the resultant material characterised by Mössbauer and X-ray Absorption Near Edge Spectroscopy. The results of spectroscopic analysis found that Fe was present as octahedrally co-ordinated Fe (III) in all cases and acts as an effective charge compensator over a wide solid solution range.

## 1. Introduction

To improve the thermal budgeting of a future geological disposal facility (GDF) there is interest in the separation of high heat generating radionuclides from high level radioactive wastes (HLW).  $^{137}\text{Cs}$  is considered to be a suitable candidate for such a “partition and condition” concept due its short half-life, high fission yield and heat output ( $t_{1/2} = 30.17$  years, 6.15 % fission yield,  $0.417 \text{ Wg}^{-1}$  <sup>1,2</sup>).  $^{137}\text{Cs}$  can be separated from the wastestream by solvent extraction, however, other Cs isotopes are co-extracted and separation is impractical. These additional isotopes include  $^{135}\text{Cs}$ , a long-lived isotope with  $t_{1/2} = 2.3$  million years. Consequently, in a partition and condition approach separated Cs must be immobilised in a robust host matrix suitable for a period of decay storage and ultimate disposal. Cs is currently vitrified with the rest of HLW raffinate however, a tailored ceramic offers the potential of a more durable wastefrom with higher Cs waste loading <sup>3</sup>.

A proposed host for separated caesium is hollandite,  $\text{A}_x\text{B}_y\text{C}_{8-y}\text{O}_{16}$ , where  $x \leq 2$  <sup>4</sup>. A site cations are large and either monovalent or divalent ( $\text{Na}^+$ ,  $\text{Ag}^+$ ,  $\text{K}^+$ ,  $\text{Rb}^+$ ,  $\text{Tl}^+$ ,  $\text{Cs}^+$ ,  $\text{Sr}^{2+}$ ,  $\text{Ba}^{2+}$ ,  $\text{Ra}^{2+}$ ,  $\text{Pb}^{2+}$ ). B and C site cations are more varied with the accommodation of di, tri, tetra, and pentavalent cations possible e.g.  $\text{Mg}^{2+}$ ,  $\text{Al}^{3+}$ ,  $\text{Ti}^{4+}$ ,  $\text{Sb}^{5+}$  <sup>4,5</sup>. The structure comprises corner and edge sharing  $\text{BO}_6$  and  $\text{CO}_6$  octahedra forming tunnels along the c-axis of the structure, A site ions are located within these tunnels and are typically eight-fold coordinated by oxygen preventing free migration along the tunnels <sup>6</sup>. The radius ratio of A and B site cations dictates the crystal symmetry of the system and when  $R_A/R_B > 2.08$  tetragonal symmetry results (I4/m). For systems where  $R_A/R_B < 2.08$ , the A site is too small for the tunnel and  $\text{BO}_6$  octahedra twist to

reduce the volume of the tunnel resulting in the distortion of the unit cell and the reduction of symmetry to a monoclinic system (C2/m)<sup>7,8</sup>. Barium titanate hollandites are the basis for many wasteform formulations and have previously been synthesised using a range of additional B site cations including Fe<sup>3+</sup>, Al<sup>3+</sup>, Ga<sup>3+</sup>, Zn<sup>2+</sup>, Cr<sup>3+</sup> and Ni<sup>2+</sup><sup>9,10</sup>.

Previous work has synthesised hollandites containing iron and caesium however, the influence of varying Cs content on the local Fe structural environment has not been investigated<sup>2,9,11-13</sup>. This study was devised to investigate the stability of the structure, in particular Fe charge compensation, with respect to Cs substitution. We present a comprehensive study of the structural environment of Fe in hollandites in the hollandite system Ba<sub>1.2-x</sub>Cs<sub>x</sub>Fe<sub>2.4-x</sub>Ti<sub>5.6+x</sub>O<sub>16</sub> where  $0 \leq x \leq 0.6$  as determined by Mössbauer and X-ray absorption spectroscopy measurements.

## 2. Experimental methods

### 2.1 Material synthesis

Hollandite precursors were produced via the alkoxide route in 10 g batches. Stoichiometric amounts of Ba, Cs and Fe (III) nitrates were dissolved in warm water (~ 50 mL) and mixed with a solution consisting of equal parts titanium (IV) isopropoxide and isopropanol. The resultant slurry was stir dried on a hot plate to remove the majority of excess water and then dried in an oven at 95 °C. The dried powder cake was broken up by passing through a 250 µm sieve and then calcined at 750 °C for one hour. The calcined material was mixed with isopropanol to form a thick slurry and ball milled for 16 hours in a HDPE vessel with yttria-stabilised zirconia milling media. After milling, the slurries were dried and passed through a 250 µm sieve prior to further processing.

Consolidated hollandites were produced by cold uniaxial pressing and sintering (CUP). Hollandites were uniaxially pressed in a 10 mm hardened steel die with a load of 2 atmospheres and reacted for 4 hours in air at 1,250 °C (ramp rate = 5 °Cmin<sup>-1</sup>).

### 2.2 Material characterisation

Reacted pellets were ground into a fine powder and characterised by powder X-ray diffraction (XRD). XRD was performed using a Bruker D2 Phaser diffractometer utilising Cu K $\alpha$  radiation, utilising a Ni foil K $\beta$  filter and a point step of 0.02 from 10 – 70 ° 2 $\theta$ . Lattice parameters were determined by performing Le Bail fitting of XRD data using Bruker TOPAS software.

Sintered pellets were characterised by scanning electron microscopy (SEM) using a Hitachi TM3030 SEM equipped with a Bruker Quantax EDX. An accelerating voltage of 15 kV was used for imaging. Sintered pellets were prepared for SEM analysis by mounting in cold setting resin and polishing with SiC paper and progressively finer diamond pastes to an optical finish (1µm). Open porosity was estimated by image analysis using ImageJ, a threshold was applied to images to delineate pores and the area measured. Polishing was performed using oil-based lubricants to prevent the solvation of any Cs-rich phases in aqueous media. Samples were sputter coated with carbon to reduce surface charging effects.

The composition of synthesised hollandites was determined by energy dispersive X-ray fluorescence spectroscopy using a Panalytical Zetium instrument. Measurements were made on sintered, polished pellets under vacuum using Rh X-rays.

$^{57}\text{Fe}$  transmission Mössbauer spectra of powdered samples were acquired at room temperature using a  $^{57}\text{Co}/\text{Rh}$  source. Samples were calibrated relative to an  $\alpha\text{-Fe}$  foil reference and spectra were measured using a constant acceleration waveform with velocity range  $\pm 10 \text{ mm s}^{-1}$ . Data were deconvoluted by assigning Lorentzian doublets to represent different Fe oxidation states and co-ordination environments using the Recoil analysis software <sup>14</sup>.

The density of synthesised hollandites was determined by helium gas pycnometry. Sample volume was determined using a Micromeritics Accupyc 1340 II pycnometer and sample mass was measured to an accuracy of  $\pm 0.0001 \text{ g}$  prior to measurement.

### 2.3 X-ray absorption spectroscopy (XAS)

Fe oxidation state and co-ordination environment were determined by Fe K-edge XANES (7112 eV). Samples were measured at Beamline 10 of the Dortmund Electron Accelerator (DELTA), University of Dortmund. Incident ( $I_0$ ) and transmitted ( $I_t$ ) X-ray intensities were measured using ion chambers, energy calibration was performed using XANES spectra measured with a reference ion chamber ( $I_r$ ) of a standard placed after the transmission ion chamber in the beam path. X-ray energies were tuned with a channel cut Si (111) monochromator and spectra were acquired from 7000 – 7500 eV. Data were acquired in transmission mode. Samples were measured alongside standards of well defined oxidation state and co-ordination environment by oxygen: staurolite (Fe(II) – tetrahedral,  $\text{Fe}_2\text{Al}_9\text{O}_6(\text{SiO}_4)_4(\text{O},\text{OH})_2$ ), siderite (Fe(II) – octahedral,  $\text{FeCO}_3$ ), synthetic  $\text{FePO}_4$  (Fe(III) – tetrahedral) and aegerine (Fe(III) – octahedral,  $\text{NaFeSi}_2\text{O}_6$ ). Fits to Fe pre-edge data of hollandite samples and standards were performed in the energy range 7104-7119 eV (0.3 eV energy resolution) to reveal oxidation state and co-ordination environment information.

The pre-edge features observed in the XANES spectra were fitted following the method proposed by Wilke et al <sup>15</sup>, such fitting permitting direct comparison with other data gathered in previous studies regarding Fe co-ordination in minerals and glass melts. Data were normalised to a unit edge step using the Athena software package <sup>16</sup>, and the rising edge background was fit using an arctangent function. Gaussian components were then fit to the data to describe the components of the pre-edge features. The height and position of the weighted mean centroids of the functions were taken to be representative of the pre-edge feature.

## 3. Results and discussion

X-ray powder diffraction showed that the structure adopted by the reacted hollandites was dependant on the level of Cs substitution. For  $x \geq 0.1$  the system adopted a tetragonal structure whereas when  $x = 0$  a monoclinic structure was observed, see Figure 1 below. The transition from the monoclinic to tetragonal structure between  $0.0 < x < 0.1$  is in agreement with data reported by Cheary et al (1986) <sup>17</sup>. The presence of a secondary rutile phase was evident however, attempts to determine the rutile content by Rietveld refinement were unsuccessful.

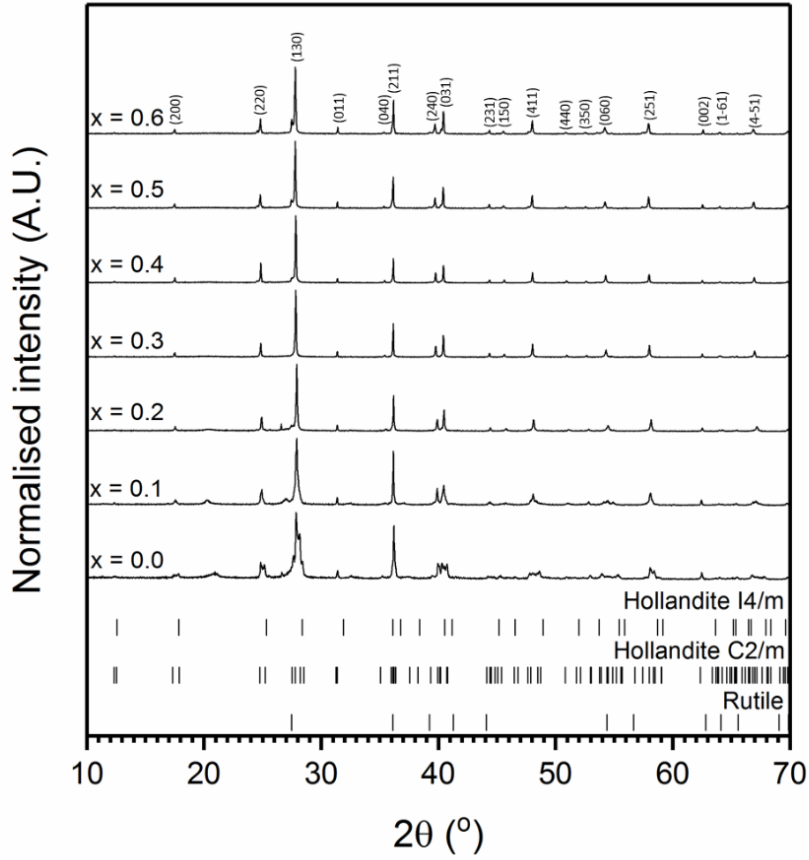


**Figure 1:** XRD patterns of synthesised Ba-Cs-Fe hollandites. Tick marks show allowed reflections for reference materials. Miller indices refer to the I4/m structure. Reference patterns were obtained from the ICSD database (Hollandite I4/m- ICSD 418150, Hollandite C2/m- ICSD 60792 and Rutile- ICSD 33837).

Diffuse intensity and several satellite peaks were observed in the XRD data for  $x = 0.0$  and  $x = 0.1$  compositions, these have been reported in previous studies and are attributed to incommensurate ordering of the A-site cations with satellite peaks becoming sharper with increased ordering<sup>7,18–20</sup>. Unit cell parameters were found by performing a Le Bail fitting of XRD data, the results are given in Table 1.

**Table 1:** Lattice parameters and density of synthesised hollandites as determined by Le Bail refinement and helium pycnometry.

Nominal composition	$r_B$ (Å)	$a$ (Å)	$b$ (Å)	$c$ (Å)	$\beta$ (°)	$V$	$\rho$ ( $g \cdot cm^{-3}$ )
Ba <sub>1.2</sub> Fe <sub>2.4</sub> Ti <sub>5.6</sub> O <sub>16</sub>	0.6170	10.184(1)	2.9735(3)	9.974(1)	90.789(6)	302.321(6)	4.59 (1)
Ba <sub>1.1</sub> Cs <sub>0.1</sub> Fe <sub>2.3</sub> Ti <sub>5.7</sub> O <sub>16</sub>	0.6165	10.106(1)	2.9726(2)	-	-	303.592(2)	4.57 (1)
Ba <sub>1.0</sub> Cs <sub>0.2</sub> Fe <sub>2.2</sub> Ti <sub>5.8</sub> O <sub>16</sub>	0.6160	10.091(1)	2.9681(1)	-	-	302.696(1)	4.54 (1)
Ba <sub>0.9</sub> Cs <sub>0.3</sub> Fe <sub>2.1</sub> Ti <sub>5.9</sub> O <sub>16</sub>	0.6155	10.128(1)	2.9688(1)	-	-	304.541(1)	4.48 (1)
Ba <sub>0.8</sub> Cs <sub>0.4</sub> Fe <sub>2.0</sub> Ti <sub>6.0</sub> O <sub>16</sub>	0.6150	10.128(1)	2.9686(1)	-	-	305.297(1)	4.46 (1)
Ba <sub>0.7</sub> Cs <sub>0.5</sub> Fe <sub>1.9</sub> Ti <sub>6.1</sub> O <sub>16</sub>	0.6145	10.143(1)	2.9680(1)	-	-	305.451(1)	4.49 (5)
Ba <sub>0.6</sub> Cs <sub>0.6</sub> Fe <sub>1.8</sub> Ti <sub>6.2</sub> O <sub>16</sub>	0.6140	10.144(1)	2.9660(1)	-	-	305.860(1)	4.49 (1)

As can be seen from Table 1, at the monoclinic-tetragonal transformation there is sharp decrease in the unit cell  $a$  parameter. With increasing Cs and Ti substitution (for Ba and Fe respectively) there is a general trend of increasing  $a$  parameter after an initial decrease resulting from the change in symmetry (see Figure 2). The  $b$  lattice parameter shows a general decreasing trend with increasing Cs and Ti substitution. The ionic radii of Cs and Ba in eight-fold coordination are 1.74 and 1.42 Å respectively<sup>21</sup>, therefore the general trend of increasing unit cell volume is indicative of increasing amounts of Cs being incorporated in the structure, see Table 1.

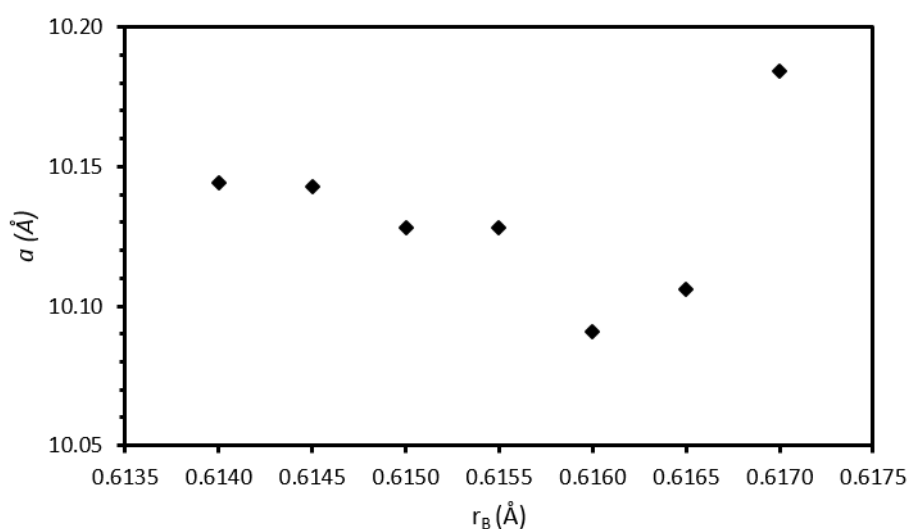


**Figure 2:** Variation of  $a$  lattice parameter with average B-site ionic radius.

Figure 3 shows representative micrographs of the sintered hollandites. As can be seen, hollandite was formed as the majority phase (in agreement with XRD). Secondary rutile was observed throughout the samples often occurring in clusters, see Figure 4. Observed porosity varied from 3 – 12 % with a general increasing trend observed with increasing Cs loading, this indicates that the preparation route could be refined to improve sintering of the materials. Hyatt et al (2006) found that the optimum sintering temperature for Fe-bearing hollandites was 1,330 °C however, these hollandites did not contain Cs and it is likely that increasing the sintering temperature could exacerbate the Cs loss observed (see Figure 5)<sup>9</sup>.

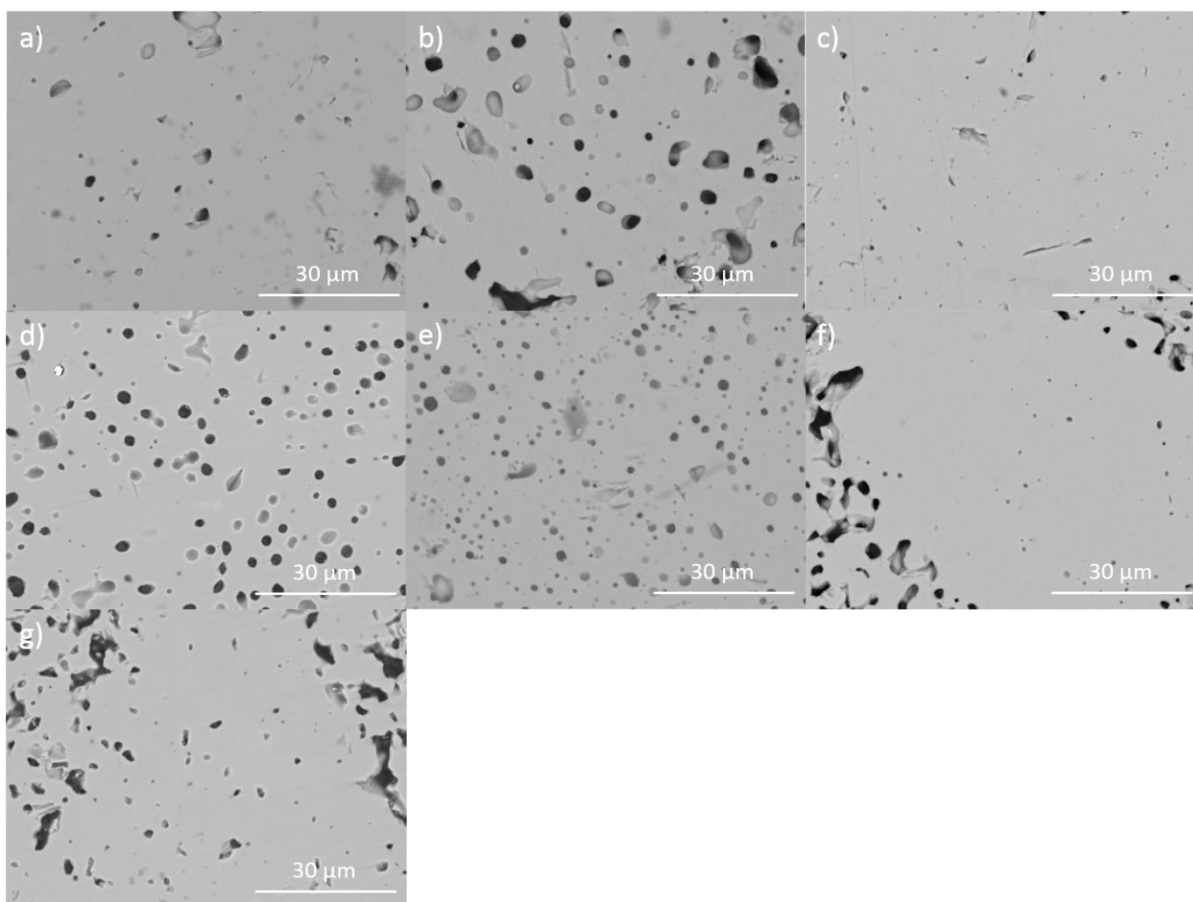


**Figure 3:** Representative backscattered electron micrographs of “well-sintered” regions of cold uniaxially pressed hollandites,  $\text{Ba}_{1.2-x}\text{Cs}_x\text{Fe}_{2.4-x}\text{Ti}_{5.6+x}\text{O}_{16}$ : a)  $x = 0.0$ , b)  $x = 0.1$ , c)  $x = 0.2$ , d)  $x = 0.3$ , e)  $x = 0.4$ , f)  $x = 0.5$  and g)  $x = 0.6$ .

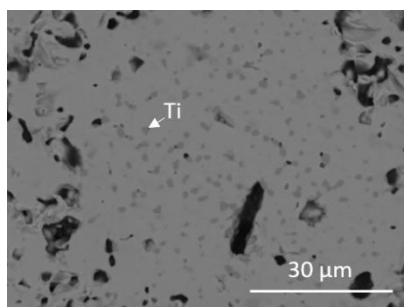


**Figure 4:** Typical rutile cluster in  $\text{Ba}_{0.9}\text{Cs}_{0.3}\text{Fe}_{2.1}\text{Ti}_{5.9}\text{O}_{16}$ .

XRF compositional analysis of the synthesised materials found that Cs loss during synthesis was considerable. Retention showed a general increasing trend from  $x = 0$  to  $x = 0.4$  however, for  $x \geq 0.5$  it was found to decrease with increased loading (Figure 5). The marked drop in Cs retention is indicative of reaching the solid solution limit. It is worth noting that XRF analysis is complicated by the presence of secondary rutile in the synthesised hollandites, the relative Ti concentration is artificially inflated by the presence of rutile and suppresses other elements meaning that Cs retention may be higher than observed. The loss of Cs inventory indicates that, although Cs concentration was increased in the samples, the synthesis procedure must be

optimised. A possible method of improving retention of the Cs inventory would be to hot isostatically press samples, the use of a hermetically sealed can prevents Cs volatilisation.

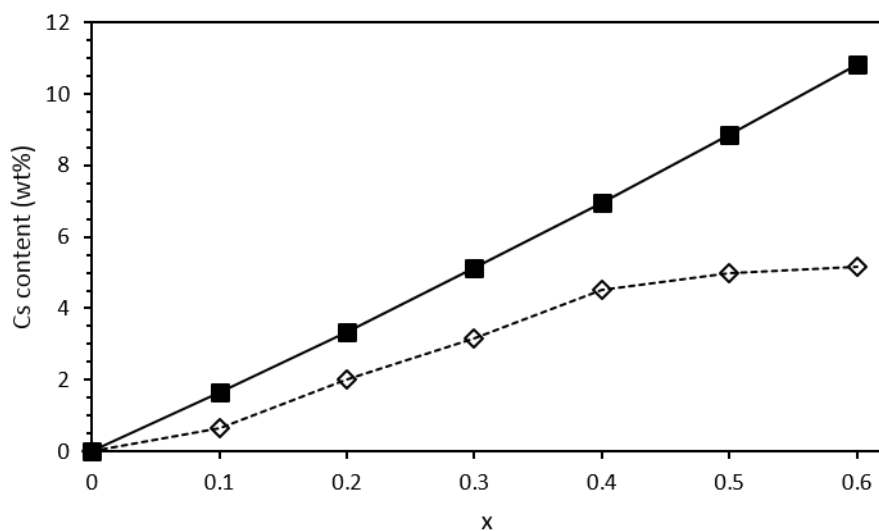


**Figure 5:** Cs content in synthesised hollandites (wt %): target (black squares) and as determined by XRF (open diamonds).

### 3.1 Mössbauer spectroscopy

All of the Mössbauer spectra obtained from the samples exhibited one quadrupolar doublet, see Figure 6. It was possible to fit this doublet using one crystallographic site. Fitting a second, octahedrally co-ordinated site was attempted and marginally improved the fit. However, the uncertainty in refined Mössbauer parameters introduced by this (an increase of one order of magnitude) were too great to allow meaningful conclusions to be drawn. Consequently, it was concluded that all Fe occupied a single crystallographic site in the structure. There is a slight asymmetry in the spectra that is not satisfactorily modelled by the addition of a second site and it was therefore concluded that it was as a result of the Goldanskii-Kariagin effect, as observed by Leinekugel-le-Cocq et al, wherein thermal vibrations lead to asymmetry in the absorption spectrum<sup>2</sup>. Extracted Mössbauer fitting parameters were consistent with Fe (III) randomised on one octahedrally co-ordinated site in the solid solution, see Table 2.

**Table 2:** Mössbauer parameters for  $\text{Ba}_{1.2-x}\text{Cs}_x\text{Fe}_{2.4-x}\text{Ti}_{5.6+x}\text{O}_{16}$  hollandites:  $\delta$  = isomer shift,  $\Delta$  = quadrupolar splitting and  $\Gamma$  = full width at half maximum.

$x$	$\delta$ (mm.s <sup>-1</sup> )	$\Delta$ (mm.s <sup>-1</sup> )	$\Gamma$ (mm.s <sup>-1</sup> )
0	0.385(1)	0.551(2)	0.180(1)
0.1	0.388(1)	0.541(2)	0.176(2)
0.2	0.380(2)	0.542(3)	0.187(2)
0.3	0.385(2)	0.522(3)	0.172(2)
0.4	0.386(2)	0.517(3)	0.174(2)
0.5	0.388(2)	0.514(3)	0.172(2)
0.6	0.391(2)	0.517(4)	0.176(3)

The hyperfine parameters show variation with Cs substitution similar to the refined lattice parameters. The quadrupolar splitting follows a generally decreasing trend and this implies that the Fe site is becoming progressively less distorted from ideal octahedral symmetry.

The Mössbauer data are in agreement with the results previously reported by Leinekugel-le-Cocq et al. for a hollandite with the composition  $\text{Ba}_1\text{Cs}_{0.28}\text{Fe}_{0.82}\text{Al}_{1.46}\text{Ti}_{5.72}\text{O}_{16}$ . Leinekugel-le-Cocq et al determined that Fe was present in the Fe (III) oxidation state <sup>2</sup>. Fe (III) in octahedral co-ordination has also previously been observed in Fe-bearing hollandites by both Birchall et al (1969) for Cs and Cs-Sc containing ferric hollandites ( $\text{Cs}_{0.7}\text{Fe}_{0.7}\text{Ti}_{3.3}\text{O}_8$ ) and by Drofenik and Hanžel (1982) for K containing ferric hollandites ( $\text{K}_{1.45}\text{Fe}_{1.45}\text{Ti}_{6.55}\text{O}_{16}$ ) <sup>12,13</sup>. However, our results are somewhat in contrast to those reported by Nguyen et al (2005) who found that  $\text{Fe}^{3+}$  occupied two distinct sites in ferric Ba-Cs hollandite structures ( $\text{Ba}_1\text{Cs}_{0.28}\text{Al}_{1.46}\text{Fe}_{0.82}\text{Ti}_{5.72}\text{O}_{16}$ , the most analogous to the compositions studied in this investigation and nominally identical to that studied by Leinekugel-le-Cocq et al) and that irradiation led to the formation of a distinct third site <sup>11</sup>. As the tetragonal space group only has one crystallographic site for framework B cations, it is possible to speculate that the pristine samples studied by Nguyen et al were either not single phase or possibly contaminated with other Fe bearing secondary phases. Although there are two Fe sites present in the monoclinic structure, only one quadrupolar doublet is observed for the baseline hollandite composition indicating that Fe is located only on one site in the structure or that, more likely, the two sites are effectively equivalent within the sensitivity of the measurement.

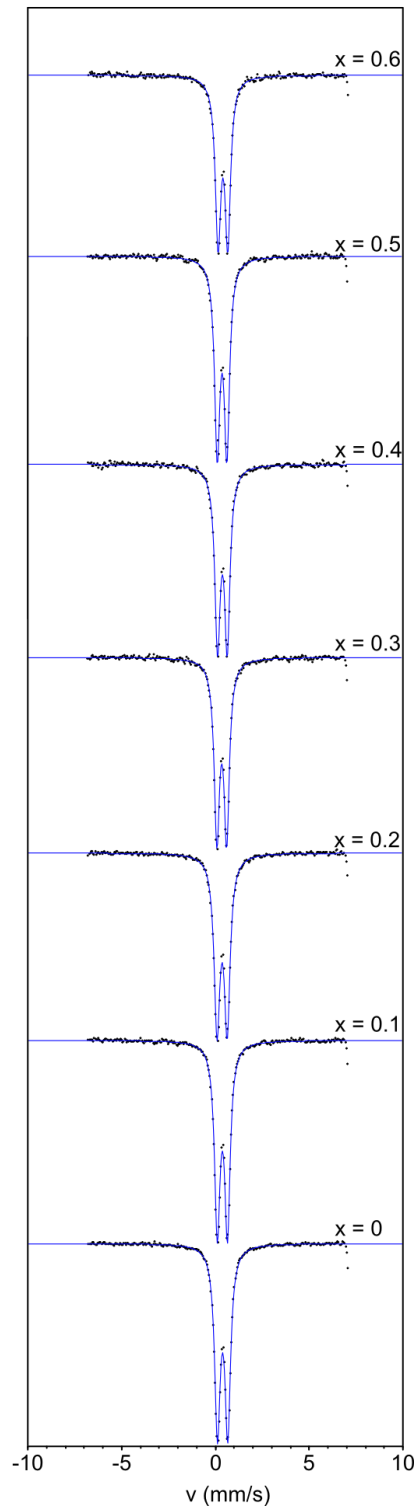


**Figure 6:** Room temperature Mössbauer spectra of Cs substituted Fe-hollandites  $\text{Ba}_{1.2-x}\text{Cs}_x\text{Fe}_{2.4-x}\text{Ti}_{5.6+x}\text{O}_{16}$ . Data are shown by black dots, fit is shown by a blue line.

### 3.2 X-ray absorption spectroscopy

Figure 7a shows the measured XANES spectra of the hollandite samples and standards ( $\text{FePO}_4$ ,  $\text{NaFeSi}_2\text{O}_6$ ,  $\text{Fe}_2\text{Al}_9\text{O}_6(\text{SiO}_4)_4(\text{O},\text{OH})_2$  and  $\text{FeCO}_3$ ). Figure 7b shows a detailed view of the pre-edge region of the XANES spectra in Figure 7a.

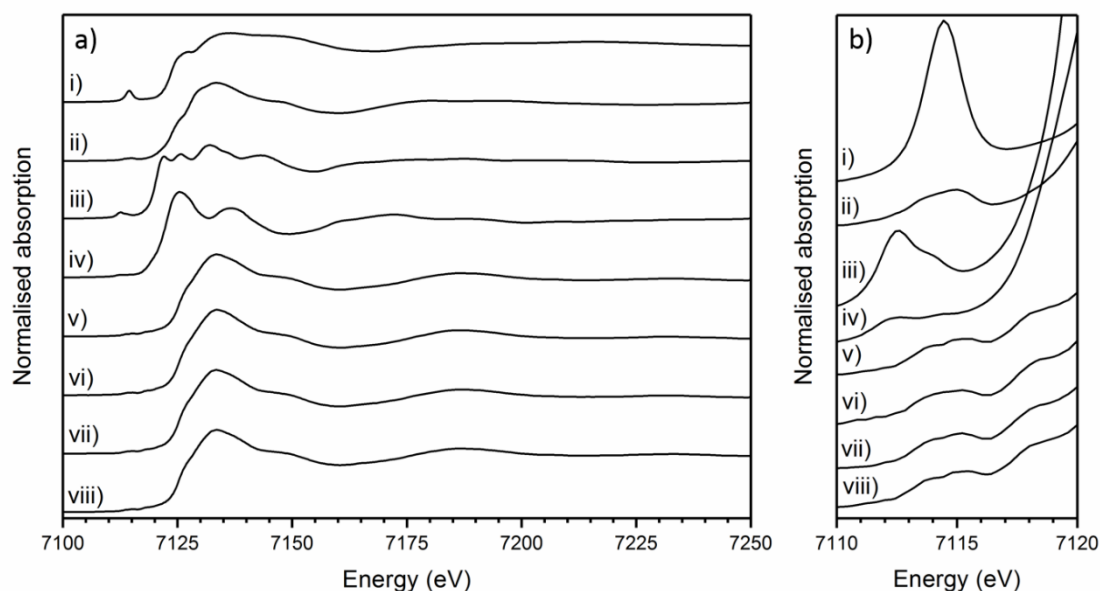


**Figure 7:** (a) Fe K-edge XANES spectra of hollandite samples and standards; (b) detail of pre-edge XANES features.  $\text{FePO}_4$  (i),  $\text{NaFeSi}_2\text{O}_6$  (ii),  $\text{Fe}_2\text{Al}_9\text{O}_6(\text{SiO}_4)_4(\text{O},\text{OH})_2$  (iii),  $\text{FeCO}_3$  (iv),  $\text{Ba}_{0.6}\text{Cs}_{0.6}\text{Fe}_{1.8}\text{Ti}_{6.2}\text{O}_{16}$  (v),  $\text{Ba}_{0.8}\text{Cs}_{0.4}\text{Fe}_2\text{Ti}_6\text{O}_{16}$  (vi),  $\text{BaCs}_{0.2}\text{Fe}_{2.2}\text{Ti}_{5.8}\text{O}_{16}$  (vii),  $\text{Ba}_{1.2}\text{Fe}_{2.4}\text{Ti}_{5.6}\text{O}_{16}$  (viii).

Fe K edge XANES data show that the predominant oxidation state of Fe in all hollandite samples is Fe (III). The pre-edge feature is attributed to quadrupolar transitions from bound Fe 1s to 3d states or dipolar transitions from bound 1s to 4p states<sup>15</sup>. The 1s to 3d transition is formally forbidden by the dipole selection rule  $\Delta l = \pm 1$ . This rule is relaxed when Fe is located in a non-centrosymmetric co-ordination environment resulting in 4p-3d mixing and intensified absorption<sup>22</sup>. Although the weighted mean centroid position and height of the pre-edge feature are related to site symmetry, it has been shown that these features show a linear relationship for average co-ordination number, assuming Fe oxidation state is constant<sup>15</sup>. As can be seen there is no significant variation in the pre-edge height or position of this feature for the hollandite samples, as a function of composition and it can therefore be concluded that Fe exists in the same co-ordination environment in all hollandite samples.

The measured XANES spectra were fitted according to the method described by Wilke et al<sup>15</sup>. Gaussian functions were fitted to the pre-edge envelope and the height and position of the weighted mean centroids of these functions were taken to represent the overall height and energy of the pre-edge feature. An example fit is shown in Figure 8, fitted values are given in Table 3.

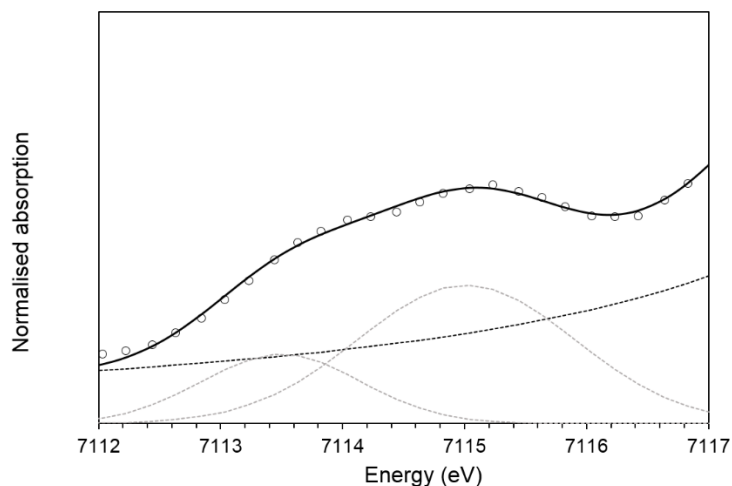


**Figure 7:** Fitting of XANES features for  $\text{BaCs}_{0.2}\text{Fe}_{2.2}\text{Ti}_{5.8}\text{O}_{16}$  sample measured in fluorescence mode. Gaussian (dashed grey lines) and arctangent (dashed black line) functions were used to fit the pre-edge and background features respectively. Data are shown by open symbols, fit is shown by a solid black line.

**Table 3:** Integrated pre-edge intensity and energies of fitted Fe XANES spectra

Sample	Energy (eV) ( $\pm 0.3$ )	Integrated pre-edge intensity ( $\pm 0.03$ )
$\text{Ba}_{1.2}\text{Fe}_{2.4}\text{Ti}_{5.6}\text{O}_{16}$	7114.5	0.06
$\text{BaCs}_{0.2}\text{Fe}_{2.2}\text{Ti}_{5.8}\text{O}_{16}$	7114.6	0.08
$\text{Ba}_{0.8}\text{Cs}_{0.4}\text{Fe}_2\text{Ti}_6\text{O}_{16}$	7114.4	0.06
$\text{Ba}_{0.6}\text{Cs}_{0.6}\text{Fe}_{1.8}\text{Ti}_{6.2}\text{O}_{16}$	7114.6	0.06
$\text{FeCO}_3$	7112.8	0.07
Staurolite	7112.9	0.19
$\text{NaFeSi}_2\text{O}_6$	7114.3	0.08
$\text{FePO}_4$	7114.3	0.33

Figure 9 shows the correlation of pre-edge height and energy with Fe valence and co-ordination environment of Fe bearing standards (solid diamonds) and synthesised hollandites (open squares). As can be seen the hollandite samples have similar pre-edge heights and energies and lie within the region associated with Fe (III) in octahedral co-ordination (within errors). This is in agreement with the results reported by Hyatt et al (2006) for  $\text{Ba}_{1.2}\text{Fe}_{2.4}\text{Ti}_{5.6}\text{O}_{16}$ <sup>9</sup>.

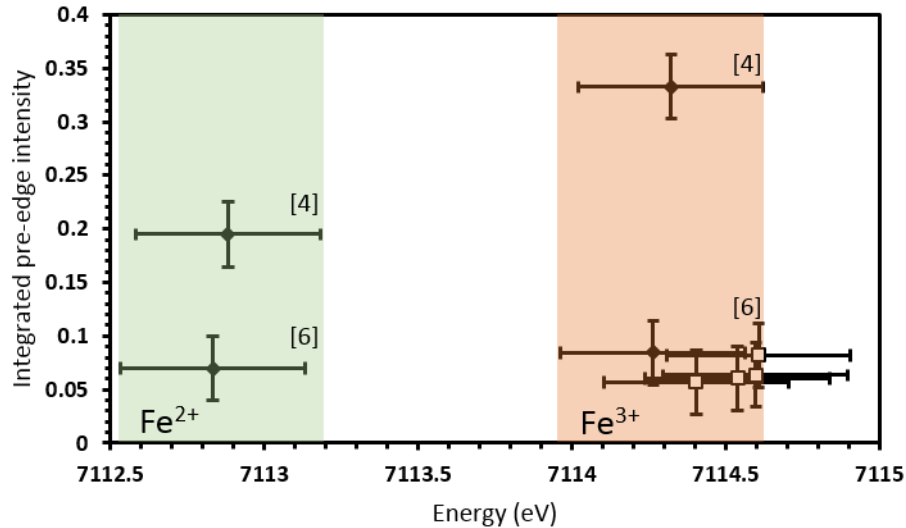


**Figure 9:** Fe co-ordination environment as speciated by pre-edge energy position and integrated pre-edge intensity in Fe K edge XANES. Solid diamonds show data for standards  $\text{Fe}_2\text{Al}_9\text{O}_6(\text{SiO}_4)_4(\text{O},\text{OH})_2$ ,  $\text{FeCO}_3$ ,  $\text{FePO}_4$  and  $\text{NaFeSi}_2\text{O}_6$ . Open squares show data for synthesised hollandites.

#### 4. Conclusions

Ferric hollandites in the system  $\text{Ba}_{1.2-x}\text{Cs}_x\text{Fe}_{2.4-x}\text{Ti}_{5.6+x}\text{O}_{16}$  were synthesised with Cs substitution for Ba ranging from  $0.0 < x < 0.6$  formula units. XRD analysis has found that there is a phase transition from a monoclinic to tetragonal unit cell upon the substitution of Cs with a general trend of increasing lattice parameters with increasing substitution of Cs consistent with the incorporation of Cs into the hollandite structure. Although increased amounts of Cs were incorporated into the hollandite structure it was evident from XRF analysis that a significant portion of the Cs inventory was volatilised during synthesis and that if retention were to be improved a different synthesis procedure, such as hot isostatic pressing, is required.  $^{57}\text{Fe}$  Mössbauer and XANES analysis has confirmed that all Fe within the synthesised hollandites is in the Fe (III) oxidation state and is randomised across a single, six-fold co-ordinated crystallographic site within the structure.

#### Acknowledgements

DJB is funded by the Engineering, Physical Sciences Research Council via the Nuclear FiRST Doctoral Training Centre (Grant EP/G037140/1). ARM is funded by the Engineering, Physical Sciences Research Council via the Next Generation Nuclear Centre for Doctoral Training (Grant EP/L015390/1). NCH is grateful to the Royal Academy of Engineering and Nuclear Decommissioning Authority for funding. This research was performed in part at the MIDAS Facility, at the University of Sheffield, which was established with support from the Department of Energy and Climate Change.

## References

- 1 P. D. Wilson, *The Nuclear Fuel Cycle: From Ore to Waste*, Oxford University Press, Oxford, 1st edn., 1996.
- 2 A. Y. Leinekugel-le-Cocq, P. Deniard, S. Jobic, R. Cerny, F. Bart and H. Emerich, *J. Solid State Chem.*, 2006, **179**, 3196–3208.
- 3 W. E. Lee, M. I. Ojovan, M. C. Stennett and N. C. Hyatt, *Adv. Appl. Ceram.*, 2006, **105**, 3–12.
- 4 A. Byström and A. M. Byström, *Acta Crystallogr.*, 1950, **3**, 146–154.
- 5 A. E. Ringwood, K. D. Reeve, D. M. Levins and E. J. Ramm, in *Radioactive Waste Forms for the Future*, eds. R. C. Ewing and W. Lutze, North Holland Physics Publishing, New York, 1988, pp. 233–335.
- 6 W. Sinclair, G. M. McLaughlin and a. E. Ringwood, *Acta Crystallogr. Sect. B Struct. Crystallogr. Cryst. Chem.*, 1980, **36**, 2913–2918.
- 7 M. L. Carter and R. L. Withers, *J. Solid State Chem.*, 2005, **178**, 1903–1914.
- 8 J. E. Post, R. B. Von Dreele and P. R. Buseck, *Acta Crystallogr. Sect. B Struct. Crystallogr. Cryst. Chem.*, 1982, **38**, 1056–1065.
- 9 N. C. Hyatt, M. C. Stennett, S. G. Fiddy, J. S. Wellings, S. S. Dutton, E. R. Maddrell, A. J. Connelly and W. E. Lee, *Mater. Res. Soc. Symp. Proc.*, 2006, **932**.
- 10 V. Aubin-Chevaldonnet, D. Caurant, a. Dannoux, D. Gourier, T. Charpentier, L. Mazerolles and T. Advocat, *J. Nucl. Mater.*, 2007, **366**, 137–160.
- 11 N. Nguyen, a. Ducouret, F. Studer, V. Aubin, D. Caurant, D. Gourier and J. M. Costantini, *Hyperfine Interact.*, 2005, **166**, 489–493.
- 12 M. Drofenik and D. Hanzel, *Mater. Res. Bull.*, 1982, **17**, 1457–1460.
- 13 T. Birchall, N. N. Greenwood and A. F. Reid, *J. Chem. Soc. A Inorganic, Phys. Theor.*, 1969, 2382.
- 14 D. G. Rancourt and K. Lagarec, *"Recoil, Mössbauer Spectral Analysis Software for Windows"*, 1998.
- 15 M. Wilke, F. Farges, P. E. Petit, G. E. Brown and F. Martin, *Am. Mineral.*, 2001, **86**, 714–730.
- 16 B. Ravel and M. Newville, *Phys. Scr.*, 2005, 1007.
- 17 R. W. Cheary, *Acta Crystallogr. Sect. B Struct. Sci.*, 1986, **42**, 229–236.
- 18 F. C. Mijlhoff, D. J. W. IJdo and H. W. Zandbergen, *Acta Crystallogr. Sect. B Struct. Sci.*, 1985, **41**, 98–101.
- 19 L. A. Bursill and J. Kwiatkowska, *J. Solid State Chem.*, 1984, **52**, 45–52.
- 20 X. J. Wu, F. H. Li and H. Hashimoto, *Acta Crystallogr. Sect. B Struct. Sci.*, 1990, **46**, 111–117.
- 21 R. D. Shannon, *Acta Crystallogr.*, 1976, **32**, 751–767.
- 22 G. A. Waychunas, M. J. Apted and G. E. Brown Jr., *Phys. Chem. Miner.*, 1983, **10**, 1–9.

**5. An investigation of iodovanadinite wasteforms for the immobilisation of radio-iodine and technetium**

# An investigation of iodovanadinite wasteforms for the immobilisation of radio-iodine and technetium

*D. J. Bailey<sup>1,\*</sup>, E. V. Johnstone<sup>1</sup>, M. C. Stennett<sup>1</sup> and N. C. Hyatt<sup>1</sup>*

1- Immobilisation Science Laboratory, Department of Materials Science and Engineering, University of Sheffield, United Kingdom

## Abstract

**Radioactive isotopes, produced as fission products during nuclear power generation, pose a significant long-term radiological health risk. <sup>99</sup>Tc and <sup>129</sup>I are two long-lived, highly soluble and highly mobile fission products that may accumulate in the food chain. A proposed wasteform for the disposal of iodine is iodovanadinite (Pb<sub>5</sub>(VO<sub>4</sub>)<sub>3</sub>I), an apatite-structured vanadate. The apatite structure is relatively flexible and offers the conceptually advantageous possibility of co-disposal of Tc and I. A suite of potential iodovanadinite wasteforms designed for the co-disposal of Tc and I or the sole disposal of I were synthesised *via* hot isostatic pressing. It was found that direct synthesis from oxide and iodide precursors was possible using hot isostatic pressing (HIPing). Increasing overpressure during HIPing was found to improve the density of the final product. XRD and SEM analyses indicated that the use of AgI as the source of iodine affected the formation of the target apatite phase and produced unfavourable phase assemblages.**

## Introduction

Radioactive iodine isotopes are produced as by-products of nuclear fission of uranium fuel during nuclear power production. During reprocessing of spent nuclear fuel (SNF), iodine is liberated. If released to the environment, iodine is highly mobile and accumulates in the food chain and the human thyroid gland. Iodine isotopes are primarily weak beta and gamma emitters and the accumulation of iodine within body tissues, particularly the thyroid, presents a considerable cancer risk. Although many iodine isotopes are relatively short-lived (e.g. <sup>131</sup>I,  $t_{1/2} \approx 8$  days), <sup>129</sup>I has a half-life of 15.7 million years and poses a significant long-term hazard. Consequently, sequestering and immobilising radio-iodine to reduce its long-term environmental hazard is of particular importance. Volatilised iodine is removed using various off-gas technologies, including aqueous scrubs or silver-impregnated solid sorbents that react to form AgI [1], [2]. Although it is possible to subsequently isolate iodine from these extractants, any wasteform that can directly handle AgI would be advantageous [3], [4]. Technetium-99, like <sup>129</sup>I, is a long-lived ( $t_{1/2} = 211,000$  years), highly mobile fission product that may accumulate in the food chain, most notably in shellfish [5]. Technetium is a problematic element with regards to vitrification but may be extracted from SNF during reprocessing [6], [7], this raises the possibility of producing a tailored wasteform for its safe disposal. Given the long half life of <sup>99</sup>Tc and <sup>129</sup>I, co-immobilisation of these two isotopes in a single, tailored wasteform would be conceptually advantageous.

Iodovanadinite (Pb<sub>5</sub>(VO<sub>4</sub>)<sub>3</sub>I), sometimes referred to as lead iodoapatite, has been identified as a potential host matrix for the immobilisation of <sup>129</sup>I [8]. Iodovanadinite is related to vanadinite (Pb<sub>5</sub>(VO<sub>4</sub>)<sub>3</sub>Cl), an ore of lead and vanadium, which is part of the larger apatite structure family, crystallizing in the hexagonal spacegroup *P6<sub>3</sub>/m*. The corner-sharing PO<sub>4</sub> tetrahedra found in apatites may be replaced with larger structural units, such as VO<sub>4</sub> or AsO<sub>4</sub> tetrahedra.

Substituting the PO<sub>4</sub> unit with larger structural units increases the aperture of the tunnel sites and subsequently improves the incorporation of larger anions, such as iodide, within the wasteform [8]–[10]. Apatites containing the ReO<sub>5</sub> structural unit have also successfully been synthesised. Because Re exhibits similar chemistry as its lighter congener, Tc, and is frequently used as an inactive surrogate, such apatite phases demonstrate potential for the co-immobilisation of both iodine and technetium in a single matrix [9], [11].

Although iodovanadinite has previously been successfully synthesised by a variety of methods, including spark plasma sintering (SPS) and microwave synthesis [8], [12], [13]; the volatile nature of iodine greatly complicates the synthesis and consolidation of these compounds. High temperature heat treatment in an open atmosphere results in considerable losses of the initial iodine inventory and, consequently, methods of sample preparation or consolidation that minimise volatilisation, e.g. hot isostatic pressing (HIP) or mechanochemical processing, are of great interest [13]–[18].

In this investigation, iodovanadinites in the Pb<sub>5-x</sub>Ag<sub>x</sub>(VO<sub>4</sub>)<sub>3-x</sub>MoO<sub>4</sub>I and Pb<sub>4.5-x</sub>Ba<sub>x</sub>Ag<sub>0.5</sub>(VO<sub>4</sub>)<sub>3</sub>I<sub>0.5</sub> series were synthesised using HIP with the aim of producing wasteforms suitable for both the sole disposal of AgI and the co-disposal of iodine and technetium. Materials similar to the Pb<sub>4.5-x</sub>Ba<sub>x</sub>Ag<sub>0.5</sub>(VO<sub>4</sub>)<sub>3</sub>I<sub>0.5</sub> series have previously been described but not fully characterised by Uno *et. al.* (2004) [19]. Incorporation of AgI in the Pb<sub>5-x</sub>Ag<sub>x</sub>(VO<sub>4</sub>)<sub>3-x</sub>MoO<sub>4</sub>I series was expected to be charge balanced by the incorporation of Mo as the MoO<sub>4</sub><sup>2-</sup> anion. Although the MoO<sub>4</sub><sup>2-</sup> anion is of a different charge to the pertechnetate anion (TcO<sub>4</sub><sup>-</sup>), Mo was used to probe the possibility of aliovalent doping of the iodovanadinite and its effect on the structure with a view to the potential immobilisation of Tc. Mo was selected for this purpose due to the similarities between Tc and Mo in chemistry and ionic radius (adjacent 5d transition metals, ionic radius Tc<sup>7+</sup> = 0.41 and ionic radius of Mo<sup>6+</sup> = 0.37 in four-fold co-ordination). The resulting materials were characterized by powder X-ray diffraction, scanning electron microscopy and thermal analysis techniques.

## Experimental

Iodovanadinites were prepared by solid state reaction between PbO, V<sub>2</sub>O<sub>5</sub>, MoO<sub>3</sub>, PbI<sub>2</sub>, AgI and Ba<sub>3</sub>(VO<sub>4</sub>)<sub>2</sub> precursors. In the Pb<sub>5-x</sub>Ag<sub>x</sub>(VO<sub>4</sub>)<sub>3-x</sub>(MoO<sub>4</sub>)<sub>x</sub>I series (x = 0, 0.2, 0.4, 0.6, 0.8, 1.0), PbI<sub>2</sub> was incrementally replaced as the iodine source by AgI. In the Pb<sub>4.5-x</sub>Ba<sub>x</sub>Ag<sub>0.5</sub>(VO<sub>4</sub>)<sub>3</sub>I<sub>0.5</sub> series (x = 0, 0.5, 1.0, 1.5, 2.0, 2.5), AgI was the sole iodine source. Precursors were mixed with cyclohexane to form a slurry and ball milled using a Fritsch Pulverisette 6 for five periods of 3 minutes at 500 rpm, changing the direction of milling with each period. Consolidated samples were produced by HIP in C106 copper tubing (~1.5 g sample, 6.5 mm OD, 2 mm ID) for 4 hr at a temperature of 800 °C with an overpressure of 100 MPa. A preliminary set of baseline Pb<sub>5</sub>(VO<sub>4</sub>)<sub>3</sub>I samples were produced to study the effect of overpressure on consolidation by HIPing at overpressures of 5, 10, 25 and 100 MPa and were used as a basis for the processing conditions for subsequent syntheses.

Reacted apatites were ground to a fine powder and characterised by powder X-ray diffraction. XRD was performed using a Bruker D2 Phaser diffractometer utilising Cu K $\alpha$  radiation, utilising a Ni foil K $\beta$  filter and a position sensitive detector. Measurements were made from 10° < 2 $\theta$  < 70° with a step size of 0.02 increments and scan rate of 1 s per step. Phase analysis was completed using Diffrac.Suite Eva V.3 (Bruker) software.

Consolidated apatites were sectioned using a Buehler Isomet Low Speed Saw and the microstructures were characterised by scanning electron microscopy (SEM) in combination with energy dispersive X-ray spectroscopy (EDX) using a Hitachi TM3030 SEM equipped with a Bruker Quantax EDX. An accelerating voltage of 15 kV was used for imaging. EDX data were processed using Bruker Quantax software. Sectioned apatites were prepared for SEM analysis by mounting in cold setting resin and polishing with SiC paper and progressively finer diamond pastes to an optical finish (1 $\mu$ m). Samples were sputter coated with carbon to reduce surface charging effects.

To determine the behaviour of precursor powders during heating, samples were investigated by Thermogravimetric Analysis - Mass Spectrometry using a Netzsch TG449 F3 Jupiter. Samples were heated at a rate of 20 °Cmin<sup>-1</sup> in an argon atmosphere up to a temperature of 800 °C, mass loss of samples was recorded and evolved species were analysed using a 64 channel QMS 403 D Aëolos mass spectrometer.

## **Results and Discussion**

### *The effect of overpressure during HIPing*

Figures 1 and 2 show the results of X-ray diffraction and representative micrographs for baseline iodovanadinite ( $\text{Pb}_5(\text{VO}_4)_3\text{I}$ ) consolidated at overpressures of 5, 10, 25 and 100 MPa, respectively. As can be seen in Figure 1, the iodovanadinite phase is formed under all overpressures; there is also evidence of the retention of a small amount of  $\text{PbI}_2$ . Although the applied overpressure does not have a major effect on the observed phase assemblage, it does have an effect on the final microstructure. Increasing overpressure results in improved densification and lower porosity, yielding a superior wasteform relative to those produced with lower overpressures, an overpressure of 100 MPa was required to eliminate porosity. It is also apparent from SEM (Figure 2) that, while not evident by XRD, a small proportion of  $\text{V}_2\text{O}_5$  is retained (phases were determined by SEM-EDX mapping, see Figure 4, iodine rich regions were assumed to be  $\text{PbI}_2$  based on XRD results thus differentiating them iodovanadinite). Although iodovanadinite has previously been synthesised directly from oxides by mechanochemical processing followed by thermal annealing or spark plasma sintering, this represents the first reported instance of direct synthesis by hot isostatic pressing [16], [20]. The removal of the intermediate  $\text{Pb}_3(\text{VO}_4)_2$  synthesis step reduces the number of necessary operations and may result in cost savings.

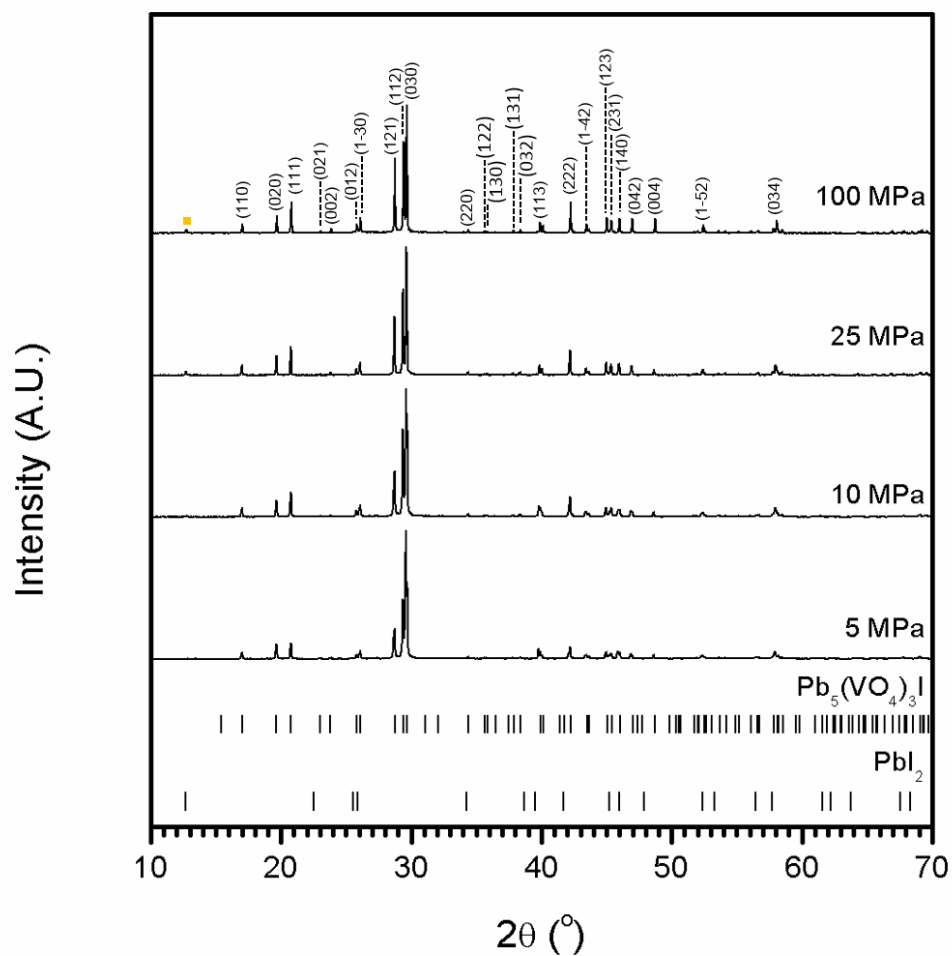


**Figure 1:** Powder X-ray diffraction profiles of iodovanadinite (labelled (hkl) Miller indices) synthesised with varying overpressure. The orange square indicates major  $\text{PbI}_2$  peak. Tick marks show allowed reflections of  $\text{Pb}_5(\text{VO}_4)_3\text{I}$  (ICSD 280065) and  $\text{PbI}_2$  (ICSD 42013).

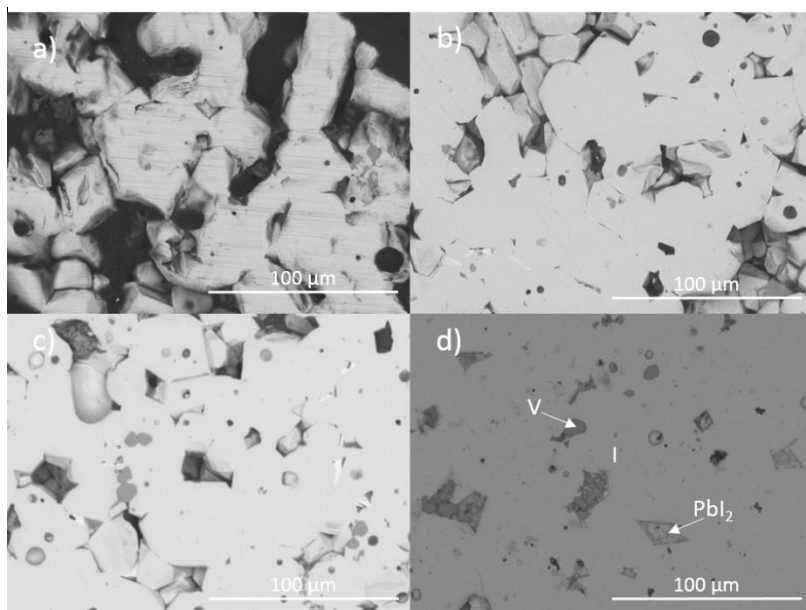


**Figure 2:** Representative backscattered electron micrographs of  $\text{Pb}_5(\text{VO}_4)_3\text{I}$  consolidated with differing overpressures: a) 5 MPa, b) 10 MPa, c) 25 MPa and d) 100 MPa. I = iodovanadinite, V =  $\text{V}_2\text{O}_5$ .

*$\text{Pb}_{5-x}\text{Ag}_x(\text{VO}_4)_{3-x}(\text{MoO}_4)_x\text{I}$  series*

Figure 3 shows the results of X-ray diffraction for the  $\text{Pb}_{5-x}\text{Ag}_x(\text{VO}_4)_{3-x}(\text{MoO}_4)_x\text{I}$  series; the lattice parameters of the synthesised iodovanadinite phase are given in Table 1. As can be seen in Figure 3, even low levels of substitution, i.e.,  $x = 0.2$ , resulted in the formation of various secondary phases and the absence of the target apatite phase above  $x = 0.6$ . Observed secondary phases were  $\text{PbI}_2$ ,  $\text{PbMoO}_4$ ,  $\text{Pb}_3(\text{VO}_4)_2$  and  $\text{AgI}$ . It is evident that increasing substitution of Mo led to increased formation of the  $\text{PbMoO}_4$  phase. The incorporation of  $\text{AgI}$  was also limited as can be seen by the increasing intensity of the associated reflections in the XRD profile.

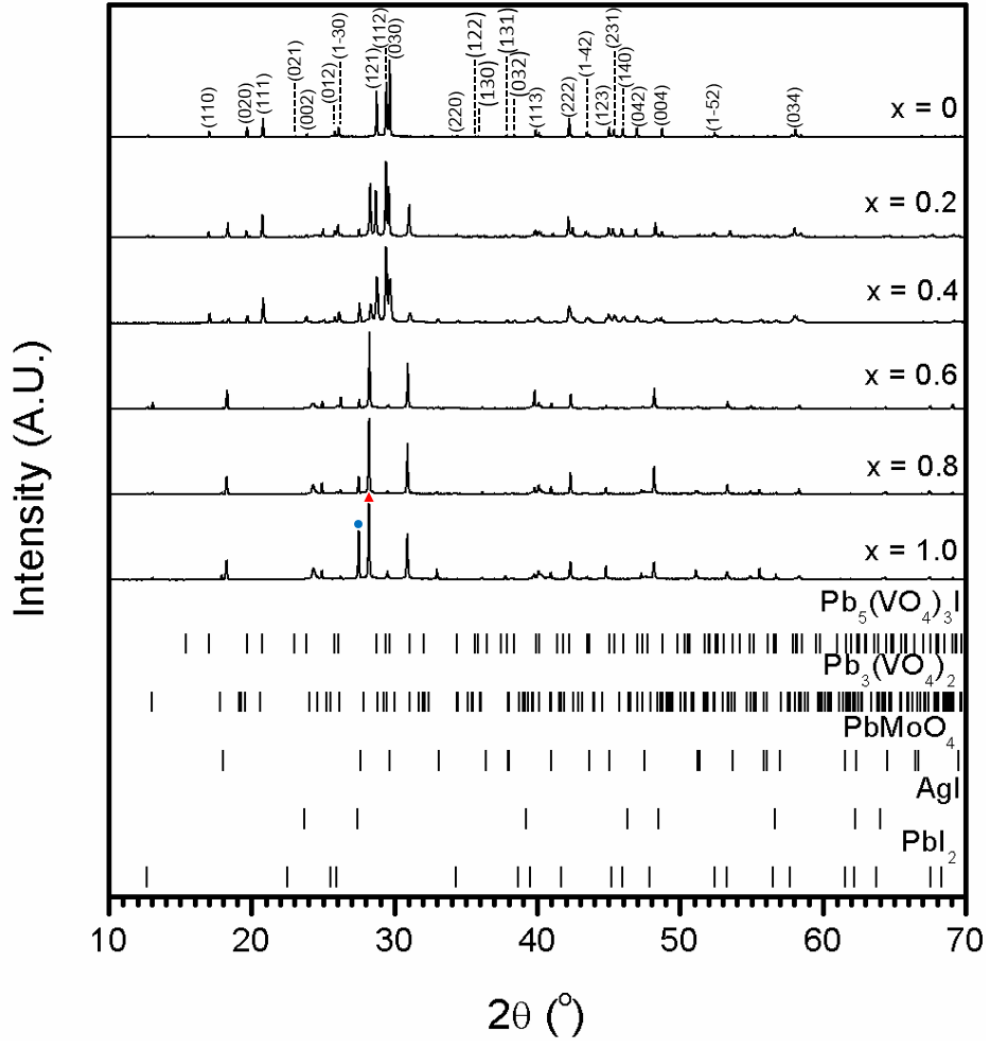


**Figure 3:** Powder X-ray diffraction profiles of synthesised iodovanadinite (labelled (hkl) Miller indices) and apatites in the  $\text{Pb}_{5-x}\text{Ag}_x(\text{VO}_4)_{3-x}(\text{MoO}_4)_x\text{I}$  series. The blue circle and red triangle indicate major  $\text{PbMoO}_4$  and  $\text{Pb}_3(\text{VO}_4)_2$  peaks respectively. Tick marks show allowed reflections for  $\text{Pb}_5(\text{VO}_4)_3\text{I}$  (ICSD 280065),  $\text{Pb}_3(\text{VO}_4)_2$  (ICSD 29360),  $\text{PbMoO}_4$  (ICSD 164725),  $\text{AgI}$  (ICSD 164959) and  $\text{PbI}_2$  (ICSD 42013).

**Table 1:** Lattice parameters of iodovanadinite phase in the  $\text{Pb}_{5-x}\text{Ag}_x(\text{VO}_4)_{3-x}(\text{MoO}_4)_x\text{I}$  series. The iodovanadinite phase did not form for  $x > 0.6$ .

Target composition	$a$ (Å)	$c$ (Å)
$\text{Pb}_5(\text{VO}_4)_3\text{I}$	10.4530(1)	7.4822(1)
$\text{Pb}_{4.8}\text{Ag}_{0.2}(\text{VO}_4)_{2.8}(\text{MoO}_4)_{0.2}\text{I}$	10.4695(2)	7.4816(2)
$\text{Pb}_{4.6}\text{Ag}_{0.4}(\text{VO}_4)_{2.6}(\text{MoO}_4)_{0.4}\text{I}$	10.464(1)	7.483(1)
$\text{Pb}_{4.4}\text{Ag}_{0.6}(\text{VO}_4)_{2.4}(\text{MoO}_4)_{0.6}\text{I}$	-	-
$\text{Pb}_{4.2}\text{Ag}_{0.8}(\text{VO}_4)_{2.2}(\text{MoO}_4)_{0.8}\text{I}$	-	-
$\text{Pb}_{4.0}\text{Ag}_{1.0}(\text{VO}_4)_{2.0}(\text{MoO}_4)_{1.0}\text{I}$	-	-

Figure 4 and 5 show representative BSE images of apatites in the  $Pb_{5-x}Ag_x(VO_4)_{3-x}(MoO_4)_xI$  series. Comparing Figures 4 and 5, the coupled Pb/Ag and V/Mo substitution led to the retention of AgI and formation of  $PbMoO_4$  and  $Pb_3(VO_4)_2$  instead of the desired iodovanadinite.

When  $PbI_2$  was used as the major iodine source, although small inclusions of unreacted  $PbI_2$  were identified in the final sample, iodine incorporation into the iodovanadinite phase was still observed. Conversely, when AgI was used as the major iodine source, the iodovanadinite phase was not observed, and instead, the iodine remained associated as AgI inclusions found within the grain boundaries of the  $PbMoO_4$  and  $Pb_3(VO_4)_2$  phases. It is noted that Klement and Harth (1962) found that  $Pb_3(VO_4)_2$  did not react with NaI to form the iodoapatite; whereas, reactions with NaCl and NaBr yielded the corresponding chloro- and bromoapatite phases [21]. This would suggest that  $PbI_2$  is a more suitable source of iodine for these materials, and that any incorporation of sequestered AgI would need to be preceded by an intermediate processing step to produce a more suitable precursor (such as  $PbI_2$ ).

The overlap of the Pb  $Ma$  and Mo  $La$  emission lines makes it unclear whether Mo is incorporated into both  $Pb_3(VO_4)_2$  and  $PbMoO_4$  (Figure 5). Regarding the formation of secondary  $PbMoO_4$ , Porter *et. al.* (2004) studied the durability of several Pb mineral phases over a wide pH range, and found that the solubility of  $PbMoO_4$  was comparable to chloropyromorphite ( $Pb_5(PO_4)_3Cl$ , an apatite phase isostructural to the target iodovanadinite phase) at  $pH > 7$  and superior at  $pH < 7$  [22]. This may indicate that, although  $PbMoO_4$  is formed as a secondary product, it could, hypothetically, act as a suitable host phase for technetium in a multiphase wastefrom with suitable charge compensation.

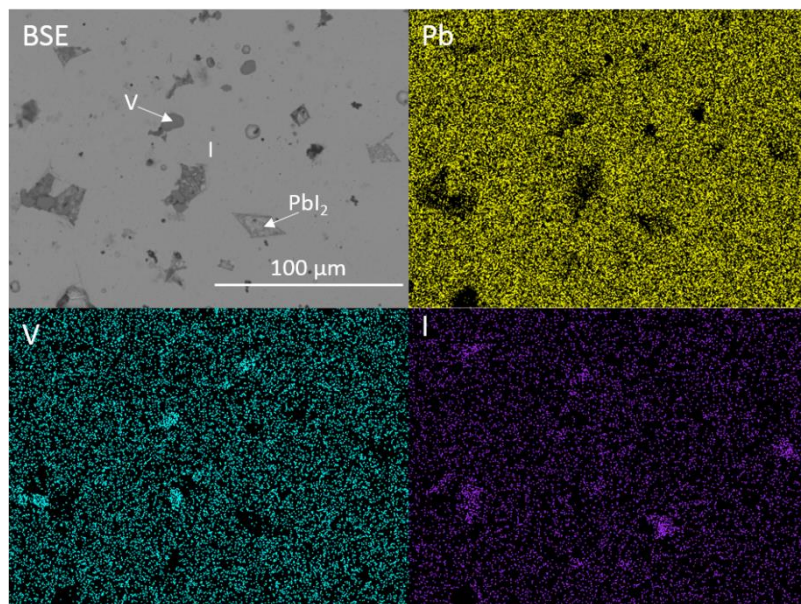


**Figure 4:** BSE micrograph and accompanying EDX maps displaying the microstructure and elemental distribution of Pb, V and I in baseline  $Pb_5(VO_4)_3I$ . I = iodovanadinite, V =  $V_2O_5$ .

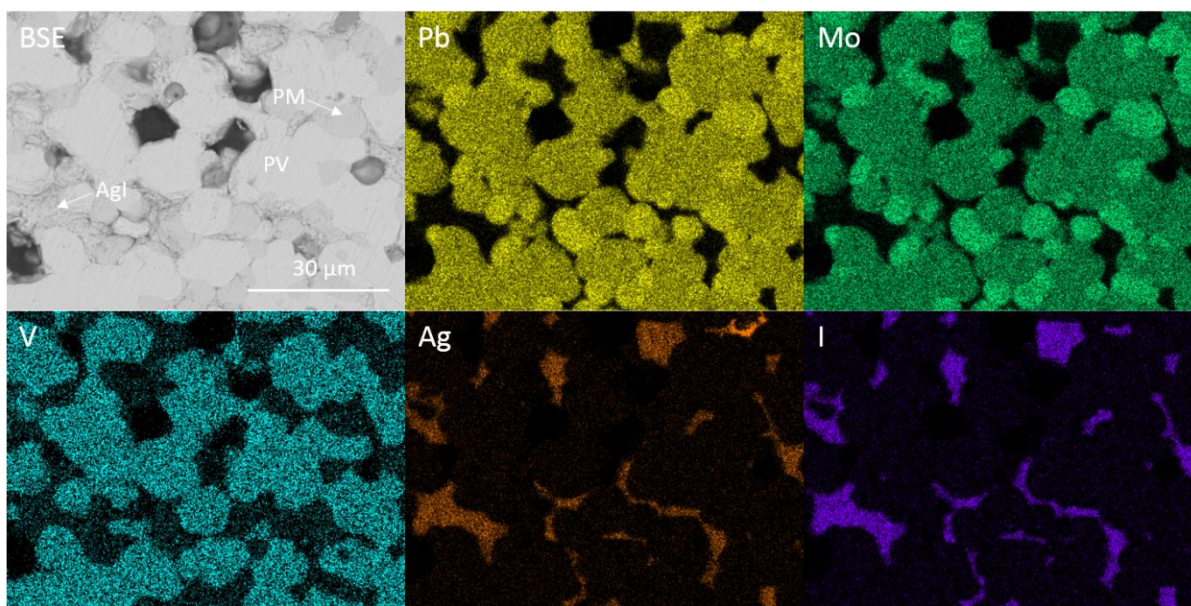


**Figure 5:** BSE micrograph and corresponding EDX maps displaying elemental distribution of Pb, Mo, V, Ag and I in  $\text{Pb}_4\text{Ag}(\text{VO}_4)_2\text{MoO}_4\text{I}$ . PV =  $\text{Pb}_3(\text{VO}_4)_2$ , PM =  $\text{PbMoO}_4$ .

Figure 6 shows the results of coupled thermogravimetric analysis mass spectrometry for the  $\text{Pb}_{5-x}\text{Ag}_x(\text{VO}_4)_{3-x}(\text{MoO}_4)_x\text{I}$  series. For all samples an initial weight loss was observed followed by a larger weight loss, which can be associated with the loss of iodine; an intermediate weight loss step was also observed in samples containing greater amounts of  $\text{PbI}_2$  ( $x = 0 - 0.6$ ). Mass spectrometry of evolved gases confirmed that both monatomic and diatomic iodine (127 and 254 atomic mass units, respectively) were evolved with increasing temperature. It is apparent that when  $\text{PbI}_2$  was used as the iodine source, mass loss was far greater under these conditions, as can be seen in Figure 6a between 390 and 800 °C in the mass spectrum. This mass loss equates to ~ 8.9 wt%, a value comparable with the theoretical maximum iodine loading of 8.4 wt%, indicating complete iodine loss. These results are comparable to those reported by Stennett *et. al.* (2011) and Lu *et. al.* (2014) [13], [16]. Samples containing a greater proportion of AgI were found to lose less iodine as a result of the greater thermal stability of AgI (m.p. = 558 °C) relative to  $\text{PbI}_2$  (m.p. = 402 °C), e.g., mass loss observed for  $\text{Pb}_4\text{Ag}(\text{VO}_4)_2\text{MoO}_4\text{I}$  (made using AgI as the sole iodine source) was only 1.19 wt% over the same temperature range. From these results it clear that any processing of iodovanadinite wastefoms would require a closed system such as a HIP, especially those using a  $\text{PbI}_2$  precursor.

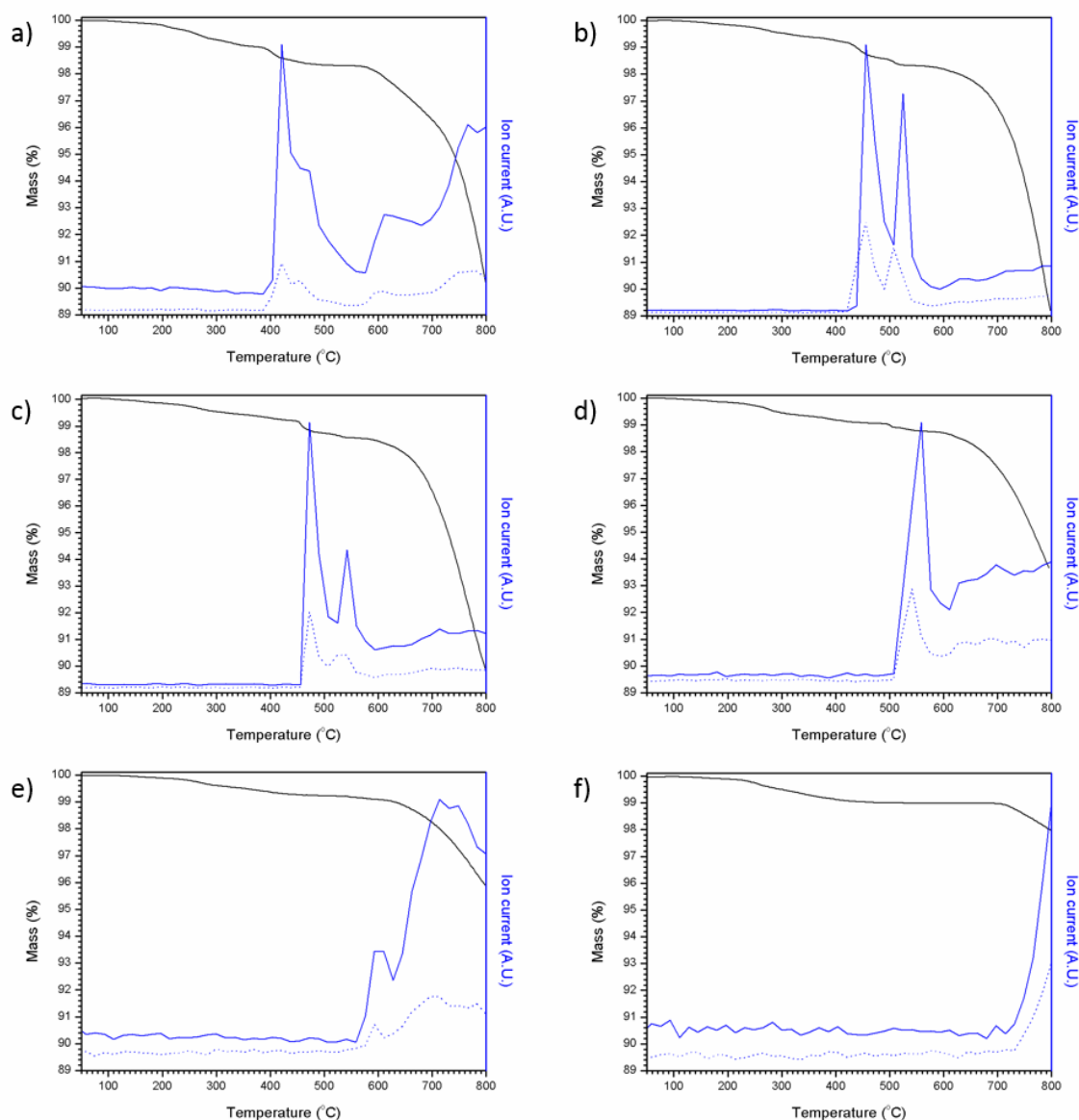


**Figure 6:** TGA-MS results for  $Pb_{5-x}Ag_x(VO_4)_{3-x}(MoO_4)_xI$  series: a)  $x = 0.0$ , b)  $x = 0.2$ , c)  $x = 0.4$ , d)  $x = 0.6$ , e)  $x = 0.8$  and f)  $x = 1.0$ . Solid blue line = 127 AMU and dotted blue line = 254 AMU.

#### *$Pb_{4.5-x}Ba_xAg_{0.5}(VO_4)_3I_{0.5}$ series*

Figure 7 shows the X-Ray diffraction patterns observed for samples in the Ba substitution series. Phase pure iodovanadinite is not formed for any composition in the series. Instead, substitution of Ba for Pb results in the formation of  $Ba_3(VO_4)_2$  structured material at levels as low as  $x = 0.5$  formula units. The shift in the position of major peaks with increasing Ba substitution is indicative of solid solution behaviour between Pb and Ba in the  $Ba_3(VO_4)_2$  structure. This is supported by the refined lattice parameters and EDX spot analyses (Table 2) that show linear variation of the Pb:Ba ratio and that as Ba content increases, unit cell size increases. This is as would be expected, given the larger ionic radius of Ba relative to Pb ( $r_{Ba} = 1.52$  and  $1.61$  and  $r_{Pb} = 1.4$  and  $1.49$  in 10 and 12-fold co-ordination respectively). Further

SEM-EDX analyses of sectioned HIP samples supported the results of XRD. Grains of reacted vanadate material separated by unreacted AgI were observed (Figures 8, 9 and 10). The interconnected AgI affected the sintering of the vanadate material, resulting in poorly consolidated material that is prone to pull-out during polishing as can be seen in the BSE images.

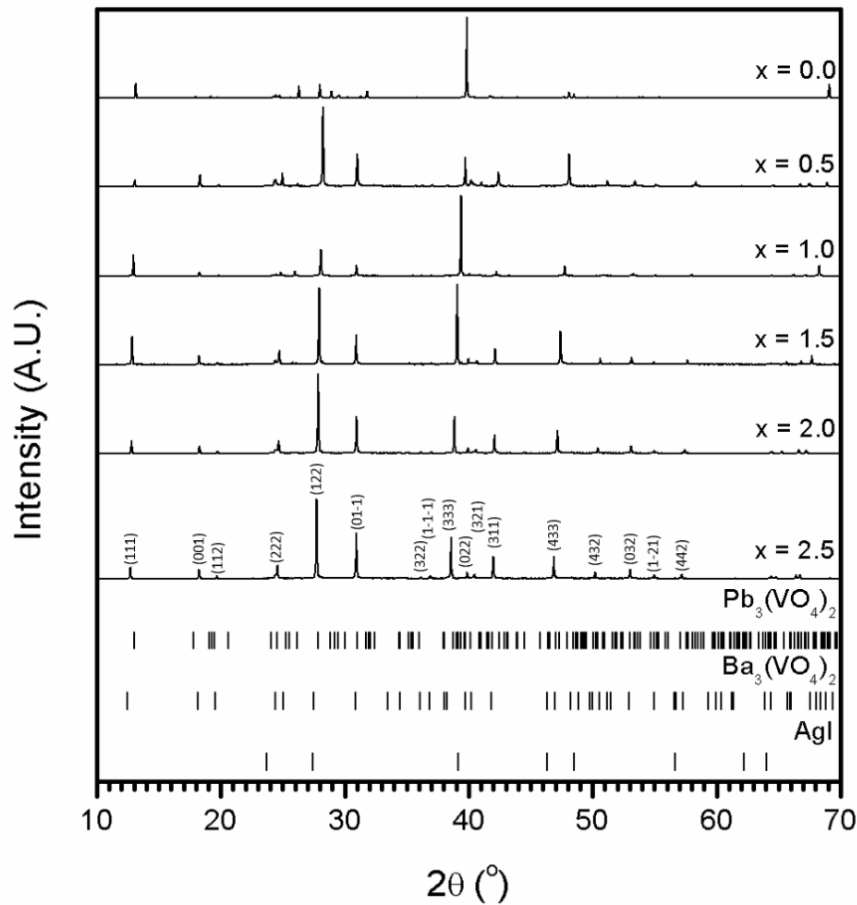


**Figure 7:** Powder diffraction patterns for synthesised apatites in the  $\text{Pb}_{4.5-x}\text{Ba}_x\text{Ag}_{0.5}(\text{VO}_4)_3\text{I}_{0.5}$  series. Tick marks show allowed reflections for  $\text{Pb}_3(\text{VO}_4)_2$  (ICSD 29360),  $\text{Ba}_3(\text{VO}_4)_2$  (labelled (hkl) Miller indices; ICSD 14237) and AgI (ICSD 164959).

**Table 2:** Refined lattice parameters of  $\text{Ba}_3(\text{VO}_4)_2$  structured phase.

Target composition	Vanadate EDX composition	$a$ (Å)	$\alpha$ (°)
$\text{Pb}_{4.5}\text{Ag}_{0.5}(\text{VO}_4)_3\text{I}_{0.5}$	$\text{Pb}_{2.96\pm 0.15}\text{Ag}_{0.04\pm 0.06}(\text{VO}_4)_{2.24\pm 0.17}\text{I}_{0.06\pm 0.05}$	-	-
$\text{Pb}_{4.0}\text{Ba}_{0.5}\text{Ag}_{0.5}(\text{VO}_4)_3\text{I}_{0.5}$	$\text{Pb}_{2.55\pm 0.09}\text{Ba}_{0.44\pm 0.04}\text{Ag}_{0.01\pm 0.02}(\text{VO}_4)_{2.08\pm 0.06}\text{I}_{0.03\pm 0.04}$	7.5900(2)	44.7563(8)
$\text{Pb}_{3.5}\text{Ba}_{1.5}\text{Ag}_{0.5}(\text{VO}_4)_3\text{I}_{0.5}$	$\text{Pb}_{2.16\pm 0.13}\text{Ba}_{0.75\pm 0.33}\text{Ag}_{0.1\pm 0.05}(\text{VO}_4)_{1.39\pm 0.32}\text{I}_{0.03\pm 0.03}$	7.6423(1)	44.5249(7)
$\text{Pb}_{3.0}\text{Ba}_{2.0}\text{Ag}_{0.5}(\text{VO}_4)_3\text{I}_{0.5}$	$\text{Pb}_{1.94\pm 0.13}\text{Ba}_{0.99\pm 0.05}\text{Ag}_{0.07\pm 0.06}(\text{VO}_4)_{1.81\pm 0.18}\text{I}_{0.01\pm 0.02}$	7.6888(1)	44.2586(5)
$\text{Pb}_{2.5}\text{Ba}_{2.5}\text{Ag}_{0.5}(\text{VO}_4)_3\text{I}_{0.5}$	$\text{Pb}_{1.69\pm 0.27}\text{Ba}_{1.24\pm 0.14}\text{Ag}_{0.07\pm 0.06}(\text{VO}_4)_{1.92\pm 0.24}\text{I}_{0.03\pm 0.04}$	7.7334(1)	44.0095(6)
$\text{Pb}_{2.0}\text{Ba}_{3.0}\text{Ag}_{0.5}(\text{VO}_4)_3\text{I}_{0.5}$	$\text{Pb}_{1.30\pm 0.08}\text{Ba}_{1.63\pm 0.09}\text{Ag}_{0.07\pm 0.05}(\text{VO}_4)_{1.78\pm 0.07}\text{I}_{0.01\pm 0.02}$	7.7692(1)	43.7710(5)

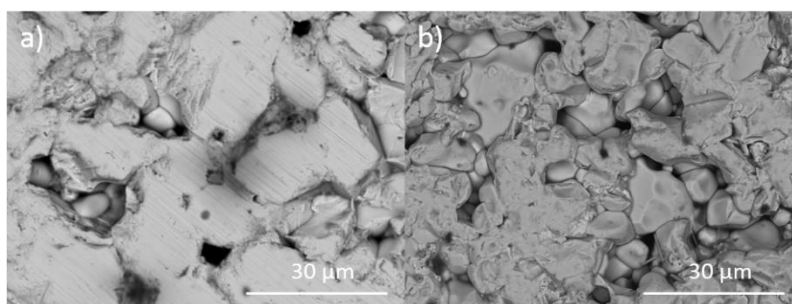


**Figure 8:** Representative backscattered electron images of iodovanadinites in the  $\text{Pb}_{4.5-x}\text{Ba}_x\text{Ag}_{0.5}(\text{VO}_4)_3\text{I}_{0.5}$  series: a)  $\text{Pb}_{4.5}\text{Ag}_{0.5}(\text{VO}_4)_3\text{I}_{0.5}$  and b)  $\text{Pb}_2\text{Ba}_{2.5}\text{Ag}_{0.5}(\text{VO}_4)_3\text{I}_{0.5}$ .

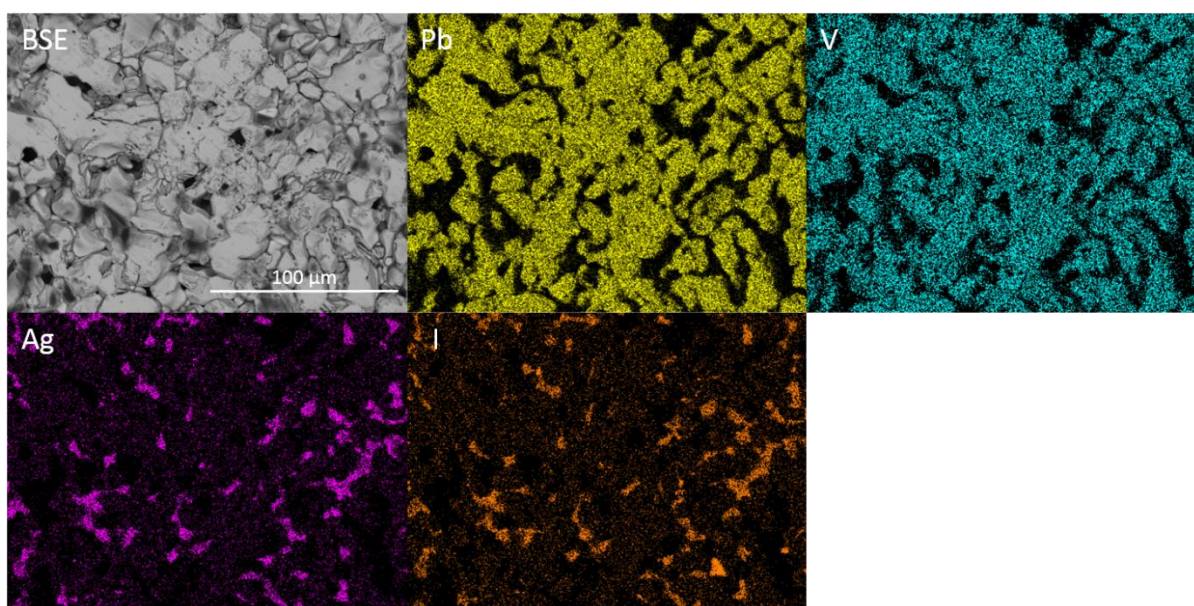


**Figure 9:** BSE image and corresponding EDX maps displaying elemental distribution of Pb, V, Ag and I in  $\text{Pb}_{4.5}\text{Ag}_{0.5}(\text{VO}_4)_3\text{I}_{0.5}$

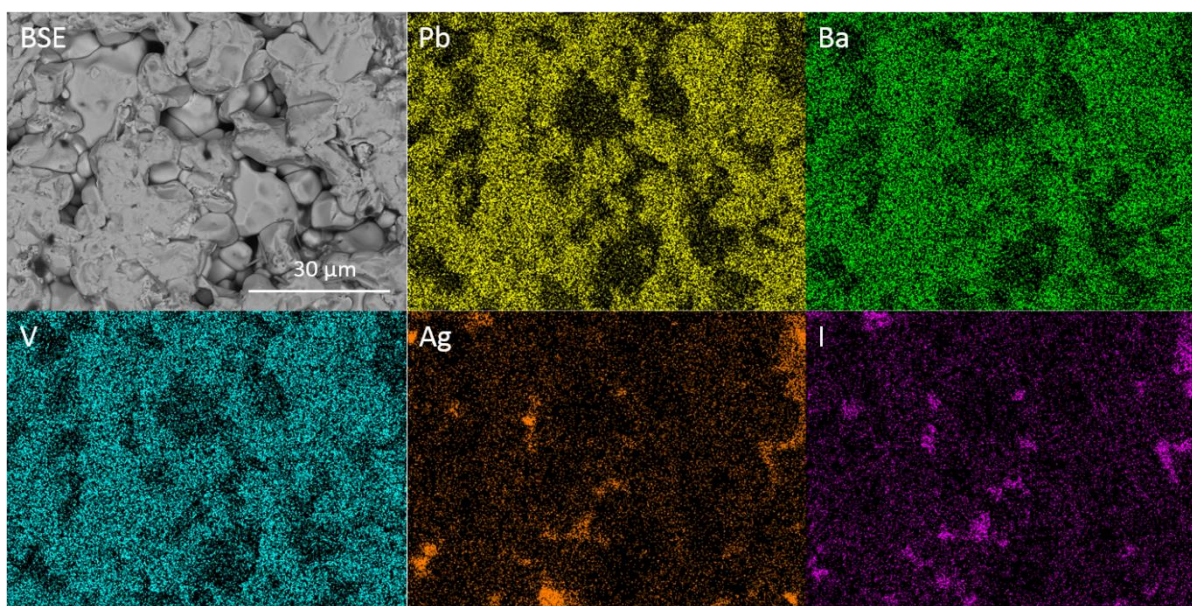


**Figure 10:** BSE image of microstructure and corresponding EDX maps displaying elemental distribution of Pb, Ba, V, Ag and I in  $\text{Pb}_2\text{Ba}_{2.5}\text{Ag}_{0.5}(\text{VO}_4)_3\text{I}_{0.5}$

These results are in agreement with Klement and Harth (1961) who found that barium vanadate did not react with molten NaI or NaBr and remained as  $\text{Ba}_3(\text{VO}_4)_2$ , whereas reaction with molten NaCl yielded the chloroapatite phase [23]. Johnstone *et al* (2017) attempted the synthesis of  $\text{AgPb}_9(\text{VO}_4)_6\text{I}$  and the  $\text{AgBa}_9(\text{VO}_4)_6\text{I}$  phase described by Uno *et al* using AgI,  $\text{Pb}_3(\text{VO}_4)_2$  and  $\text{Ba}_3(\text{VO}_4)_2$  precursors [24]. It was found that, in agreement with the data observed in this study, the AgI did not react with either Pb- or Ba-vanadate and was retained. However, Maddrell and Abraitis (2004) found it was possible to synthesise single-phase  $\text{Pb}_{4.5}\text{Ba}_{0.5}(\text{VO}_4)_3\text{I}$ , indicating that it is likely that the use of AgI as the iodine source that has affected the formation of the apatite phase, and it may be possible to synthesise Ba-containing apatites if a different precursor is used [18]. There is also the possible influence of processing temperature - Maddrell and Abraitis reported that increasing HIPing temperature from 700 °C to 900 °C resulted in a decrease in the quantity of  $\text{Pb}_{4.5}\text{Ba}_{0.5}(\text{VO}_4)_3\text{I}$  formed. As the apatites produced in this study were all processed at the intermediate temperature of 800 °C, it is possible that this has had an effect on the formation of the apatite phase.

Figure 11 shows the results of thermogravimetric analysis-mass spectrometry for the  $\text{Pb}_{4.5-x}\text{Ba}_x\text{Ag}_{0.5}(\text{VO}_4)_3\text{I}_{0.5}$  series. The results of TGA-MS were very similar to those observed for  $\text{Pb}_4\text{Ag}(\text{VO}_4)_2\text{MoO}_4\text{I}$  (AgI used as sole iodine source). An initial weight loss was followed by a plateau from ~ 500 – 700 °C and then a second weight loss in association with the evolution of monatomic and diatomic iodine. These results are in relatively good agreement with the TGA results reported by Uno *et. al.* (2004) who reported the synthesis of a rhombohedral barium end member,  $\text{AgBa}_9(\text{VO}_4)_6\text{I}$  [19]; however, considering the results of this study, this seems unlikely and a more plausible explanation is the formation of a mixture of  $\text{Ba}_3(\text{VO}_4)_2$  (trigonal  $R\bar{3}m$ ) and AgI.

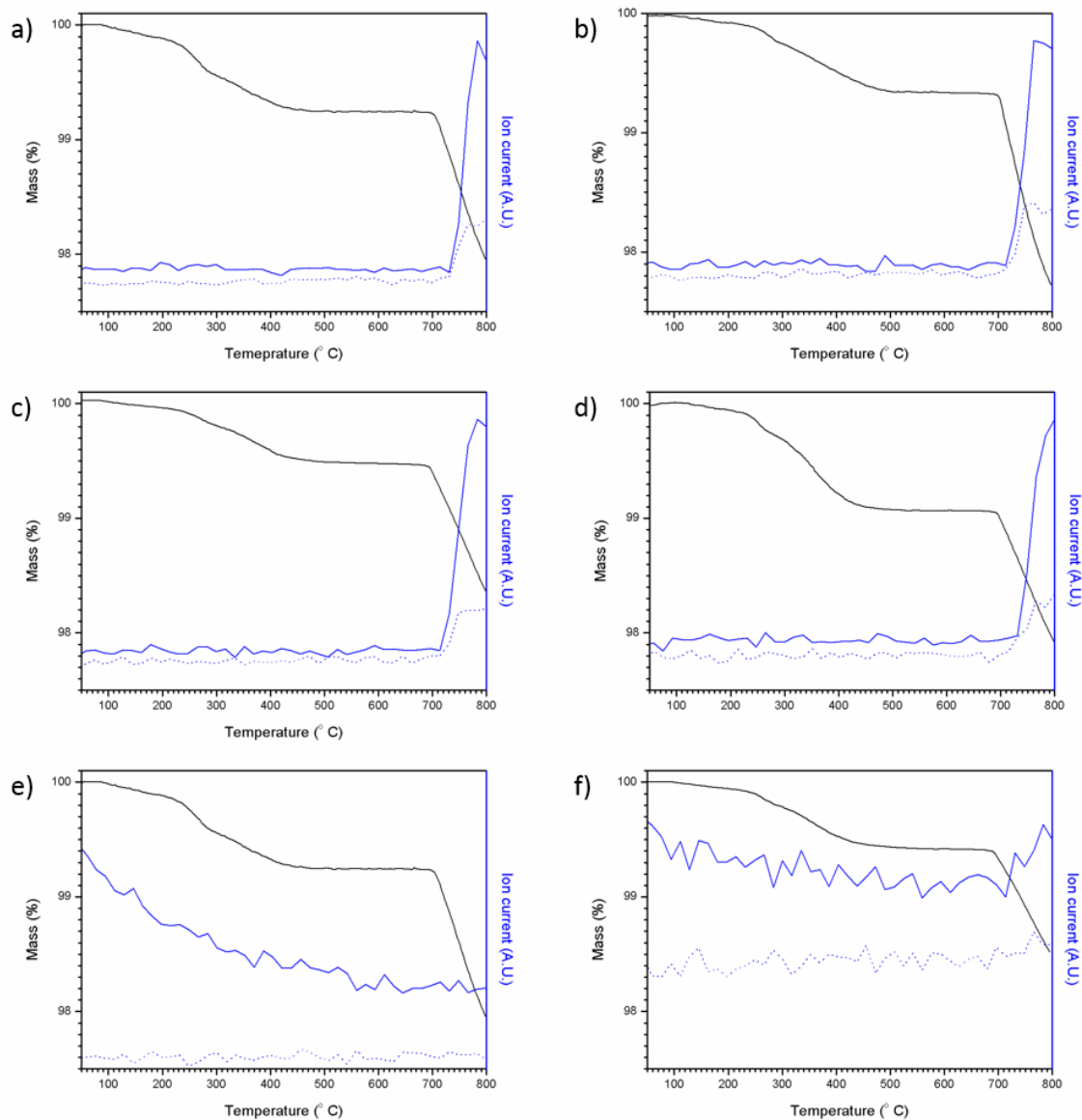


**Figure 11:** TG-MS results for the  $\text{Pb}_{4.5-x}\text{Ba}_x\text{Ag}_{0.5}(\text{VO}_4)_3\text{I}_{0.5}$  series: a)  $x = 0.0$ , b)  $x = 0.5$ , c)  $x = 1.0$ , d)  $x = 1.5$ , e)  $x = 2.0$  and f)  $x = 2.5$ . Solid blue line = 127 AMU and dotted blue line = 254 AMU.

## Conclusions

The viability of directly incorporating AgI into Pb and Pb-Ba based apatites and the possibility of the co-immobilisation of iodine and technetium were investigated. Apatites in the  $\text{Pb}_{5-x}\text{Ag}_x(\text{VO}_4)_3(\text{MoO}_4)_x\text{I}$  and  $\text{Pb}_{4.5-x}\text{Ba}_x\text{Ag}_{0.5}(\text{VO}_4)_3\text{I}_{0.5}$  series were synthesised in closed-system using hot isostatic pressing to prevent iodine volatilisation. Increased overpressure during synthesis was found to yield apatites with improved density. The use of silver iodide as an iodine source was found to be problematic, with very limited incorporation into the apatite phase observed. Increasing replacement of  $\text{PbI}_2$  with AgI was found to result in the non-formation of the target phase, and subsequently it must be concluded that incorporation of sequestered iodine into apatite wasteforms would require an additional processing step to produce a more suitable iodine precursor e.g.,  $\text{PbI}_2$ . Although complicated by the

aforementioned problems regarding iodine source, the potential for Mo, and subsequently Tc, to be incorporated into iodovanadinite remains open.

### Acknowledgements

DJB is funded by the Engineering and Physical Sciences Research Council *via* the Nuclear FiRST Doctoral Training Centre. EVJ would like thank to the Engineering and Physical Sciences Research Council for funding *via* grant number EP/M026566/1. NCH is grateful to the Royal Academy of Engineering and Nuclear Decommissioning Authority for funding. This research was performed at the MIDAS Facility, at the University of Sheffield, which was established with support from the Department of Energy and Climate Change.

### References

- [1] P. D. Wilson, *The Nuclear Fuel Cycle: From Ore to Waste*, 1st ed. Oxford: Oxford University Press, 1996.
- [2] B. J. Riley, J. D. Vienna, D. M. Strachan, J. S. McCloy, and J. L. Jerden, "Materials and processes for the effective capture and immobilization of radioiodine: A review," *J. Nucl. Mater.*, vol. 470, pp. 307–326, 2016.
- [3] E. C. Buck, E. J. Mausolf, B. K. Mcnamara, C. Z. Soderquist, and J. M. Schwantes, "Sequestration of radioactive iodine in silver-palladium phases in commercial spent nuclear fuel," *J. Nucl. Mater.*, vol. 482, pp. 229–235, 2016.
- [4] K. W. Chapman, P. J. Chupas, and T. M. Nenoff, "Radioactive Iodine Capture in Silver-Containing Mordenites through Nanoscale Silver Iodide Formation," *J. Am. Chem. Soc.*, vol. 132, pp. 8897–8899, 2010.
- [5] Y. S. Olsen and J. Vives I Batlle, "A model for the bioaccumulation of  $^{99}\text{Tc}$  in lobsters (*Homarus gammarus*) from the West Cumbrian coast," *J. Environ. Radioact.*, vol. 67, no. 3, pp. 219–233, 2003.
- [6] I. W. Donald, *Waste immobilization in glass and ceramic based hosts*. Chichester: John Wiley & Sons, Ltd., 2010.
- [7] K. Schwochau, *Technetium: Chemistry and Radiopharmaceutical Applications*. Weinheim: Wiley-VCH, 2000.
- [8] F. Audubert, J. Carpenaa, J. L. Lacoutb, and F. Tetard, "Elaboration of an iodine-bearing apatite iodine diffusion into a  $\text{Pb}_3(\text{VO}_4)_2$  matrix," *Solid State Ionics*, vol. 95, pp. 113–119, 1997.
- [9] M. S. Schriewer and W. Jeitschko, "Preparation and Crystal Structure of Isotypic Orthorhombic Sr Perrhenate Halides  $\text{Sr}_5(\text{ReO}_5)_3\text{X}$  ( $\text{X} = \text{Cl}, \text{Br}, \text{I}$ ) and Structure Refinement of the Related Hexagonal Apatite-like Compound  $\text{Ba}_5(\text{ReO}_5)_3\text{Cl}$ ," *J. Solid State Chem.*, vol. 107, pp. 1–11, 1993.
- [10] F. Audubert, J.-M. Savariault, and J.-L. Lacout, "Pentalead tris(vanadate) iodide, a defect vanadinite-type compound," *Acta Crystallogr. Sect. C Cryst. Struct. Commun.*, vol. 55, no. 3, pp. 271–273, 1999.
- [11] G. Baud, J.-P. Besse, G. Sueur, and R. Chevalier, "Structure de nouvelles apatites au rhenium contenant des anions volumineux:  $\text{Ba}_{10}(\text{ReO}_5)_6\text{X}_2$  ( $\text{X} = \text{Br}, \text{I}$ )," *Mater. Res. Bull.*, vol. 14, pp. 675–682, 1979.

- [12] S. Le Gallet, L. Campayo, E. Courtois, S. Hoffmann, Y. Grin, F. Bernard, and F. Bart, "Spark plasma sintering of iodine-bearing apatite," *J. Nucl. Mater.*, vol. 400, no. 3, pp. 251–256, 2010.
- [13] M. C. Stennett, I. J. Pinnock, and N. C. Hyatt, "Rapid synthesis of  $\text{Pb}_5(\text{VO}_4)_3\text{I}$ , for the immobilisation of iodine radioisotopes, by microwave dielectric heating," *J. Nucl. Mater.*, vol. 414, no. 3, pp. 352–359, 2011.
- [14] S. A. T. Redfern, S. E. Smith, and E. R. Maddrell, "High-temperature breakdown of the synthetic iodine analogue of vanadinite,  $\text{Pb}_5(\text{VO}_4)_3\text{I}$ : an apatite-related compound for iodine radioisotope immobilization?," *Mineral. Mag.*, vol. 76, no. 4, pp. 997–1003, 2012.
- [15] Y. Suetsugu, "Synthesis of lead vanadate iodoapatite utilizing dry mechanochemical process," *J. Nucl. Mater.*, vol. 454, no. 1–3, pp. 223–229, 2014.
- [16] F. Lu, T. Yao, J. Xu, J. Wang, S. Scott, Z. Dong, R. C. Ewing, and J. Lian, "Facile low temperature solid state synthesis of iodoapatite by high-energy ball milling," *RSC Adv.*, vol. 4, pp. 38718–38725, 2014.
- [17] M. Zhang, E. R. Maddrell, P. K. Abraitis, and E. K. H. Salje, "Impact of leach on lead vanado-iodoapatite [ $\text{Pb}_5(\text{VO}_4)_3\text{I}$ ]: An infrared and Raman spectroscopic study," *Mater. Sci. Eng. B Solid-State Mater. Adv. Technol.*, vol. 137, pp. 149–155, 2007.
- [18] E. R. Maddrell and P. K. Abraitis, "A Comparison of Wasteforms and Processes for the Immobilisation of Iodine-129," *Mater. Res. Soc. Symp. Proc.*, vol. 807, pp. 1–7, 2004.
- [19] M. Uno, A. Kosuga, S. Masuo, M. Imamura, and S. Yamanaka, "Thermal and mechanical properties of  $\text{AgPb}_9(\text{VO}_4)_6\text{I}$  and  $\text{AgBa}_9(\text{VO}_4)_6\text{I}$ ," *J. Alloys Compd.*, vol. 384, pp. 300–302, 2004.
- [20] T. Yao, F. Lu, H. Sun, J. Wang, R. C. Ewing, and J. Lian, "Bulk Iodoapatite Ceramic Densified by Spark Plasma Sintering with Exceptional Thermal Stability," *J. Am. Ceram. Soc.*, vol. 97, no. 8, pp. 2409–2412, 2014.
- [21] R. Klement and R. Harth, "Über Bleiapatite und tertiäres Bleiphosphat," *Zeitschrift für Anorg. und Allg. Chemie*, vol. 314, no. 3–4, pp. 238–244, 1962.
- [22] S. K. Porter, K. G. Scheckel, C. A. Impellitteri, and J. A. Ryan, "Toxic Metals in the Environment : Thermodynamic Considerations for Possible Immobilization Strategies for Pb, Cd, As, and Hg Toxic Metals in the Environment :," *Crit. Rev. Environ. Sci. Technol.*, vol. 34, pp. 495–604, 2004.
- [23] R. Klement and R. Harth, "Das Verhalten von tertiären Erdalkaliphosphaten , - arsenaten und vanadaten in geschmolzen Halogeniden," *Chem. Berichte Recl.*, vol. 94, no. 6, pp. 1452–1456, 1961.
- [24] E. V. Johnstone, D. J. Bailey, M. C. Stennett, J. Heo, and N. C. Hyatt, "On the existence of  $\text{AgM}_9(\text{VO}_4)_6\text{I}$  ( $\text{M} = \text{Ba}, \text{Pb}$ )," *RSC Adv.*, vol. 7, no. 77, pp. 49004–49009, 2017.

## **6. Synthesis and characterisation of brannerite compositions**



**for the immobilisation of MOX  
residues**



Cite this: *RSC Adv.*, 2018, 8, 2092

# Synthesis and characterisation of brannerite compositions $(U_{0.9}Ce_{0.1})_{1-x}M_xTi_2O_6$ ( $M = Gd^{3+}$ , $Ca^{2+}$ ) for the immobilisation of MOX residues

D. J. Bailey, \*<sup>a</sup> M. C. Stennett, <sup>a</sup> B. Ravel,<sup>b</sup> D. Grolimund<sup>c</sup> and N. C. Hyatt<sup>a</sup>

A suite of uranium brannerites for the disposal of MOX residues, formulated  $(U_{0.9}Ce_{0.1})_{1-x}M_xTi_2O_6$  ( $M = Ca^{2+}$  and/or  $Gd^{3+}$ ), were prepared using a mixed oxide route under oxidising, inert and reducing atmospheres (air, argon and  $H_2/N_2$ ).  $Gd^{3+}$  was added to act as a neutron absorber in the final Pu bearing wasteform and Ce added to function as a structural analogue for Pu. X-ray powder diffraction of the synthesised specimens found that phase distribution was strongly affected by the processing atmosphere and Gd content. In all cases prototypical brannerite was formed, accompanied by different secondary phases dependent on processing atmosphere. Microstructural analysis (SEM) of the sintered samples confirmed the results of the X-ray powder diffraction. Bulk XANES found that Ti remained in the  $Ti^{4+}$  oxidation state whereas Ce was uniformly reduced to the  $Ce^{3+}$  oxidation state regardless of processing conditions or stoichiometry. Micro-focus XANES was used to determine U oxidation in the brannerite phase and showed that U oxidised to higher U oxidation states to charge compensate. It was concluded that the charge balance mechanism was a combination of U oxidation and A-site vacancies.

Received 24th October 2017  
Accepted 21st December 2017

DOI: 10.1039/c7ra11742f

rsc.li/rsc-advances

## 1 Introduction

Separated plutonium stockpiles, accumulated as a result of the continued reprocessing of spent nuclear fuel (SNF),<sup>1</sup> present an ongoing challenge in terms of their safe, long-term management and also a potential proliferation risk.<sup>2</sup> Consequently, reduction of accumulated stockpiles is highly desirable. Re-use of Pu in mixed oxide fuel (MOX), is an option currently favoured by the UK government.<sup>1</sup> During production of mixed oxide fuels, residues rich in Pu and U are generated. Although the majority of MOX residues can be recycled and reused to make fuel, it is inevitable that some fraction will be uneconomic to recycle and will require immobilisation and disposal.

Brannerite ( $UTi_2O_6 \sim 55$  wt% U) is a titanate phase commonly found in uranium ore deposits<sup>3</sup> and as an accessory phase in zirconolite and pyrochlore based ceramics designed for actinide disposition.<sup>4,5</sup> Brannerite has a monoclinic crystal structure with space group  $C2/m$ , comprising layers of edge sharing  $TiO_6$  octahedra linked by octahedra with larger cations (U).<sup>6</sup> Naturally occurring brannerites exhibit considerable chemical flexibility with elements such as Ca, Y, Pb, Ce and Th being incorporated on the U site and Fe, Si and Al substituting on the Ti site. However, they are commonly completely

metamict due to accumulated  $\alpha$ -recoil damage (critical dose  $1-3 \times 10^{16} \alpha \text{ mg}^{-1}$ ).<sup>3,7</sup> Nevertheless, the presence of brannerite as a heavy mineral in alluvial sediments, after the host rock has been weathered, provides an indication of the long term durability of brannerite.<sup>8</sup> Previous studies have shown that it is possible to synthesise Pu-bearing brannerites and also that the Pu analogue, Ce, adopts the brannerite structure.<sup>4,9</sup> The production of a Pu-bearing wasteform may require the incorporation of neutron absorbing species, such as Gd or Hf, for criticality safety; these have been shown to form brannerite solid solutions with Pu by Vance *et al.*<sup>4</sup>

The synthesis of stoichiometric brannerite requires inert conditions.<sup>10</sup> However, it is possible to stabilize the brannerite structure in air by the addition of dopants (Ca, La, Gd).<sup>4,5,11-13</sup> This indicates that both processing conditions and target stoichiometry may affect brannerite formation.

In this study, the production of brannerites suitable for MOX disposal was investigated by synthesising brannerites with a range of conceptual waste loadings ( $(U_{0.9}Ce_{0.1})_{1-x}M_xTi_2O_6$ ) under different atmospheres in an attempt to find a suitable baseline composition and processing conditions.

## 2 Materials and methods

### 2.1 Materials synthesis

Four different compositions of brannerite ( $Gd_{0.1}U_{0.81}Ce_{0.09}Ti_2O_6$ ,  $Gd_{0.2}U_{0.72}Ce_{0.08}Ti_2O_6$ ,  $Gd_{0.25}U_{0.675}Ce_{0.075}Ti_2O_6$  and  $Ca_{0.1}Gd_{0.1}U_{0.72}Ce_{0.08}Ti_2O_6$ ) were synthesised by solid state reaction of component oxides and  $CaCO_3$  under oxidising, inert and

<sup>a</sup>Immobilisation Science Laboratory, Department of Materials Science and Engineering, University of Sheffield, UK. E-mail: d.j.bailey@sheffield.ac.uk

<sup>b</sup>National Institute of Standards and Technology, 100 Bureau Drive, Gaithersburg, MD 20899, USA

<sup>c</sup>Swiss Light Source, Paul Scherrer Institute, Villigen 5232, Switzerland



reducing atmospheres (air, argon and 5% H<sub>2</sub>/N<sub>2</sub>). Gd was added to act as a neutron absorber in a final Pu-bearing wasteform and to stabilise higher U oxidation states (U<sup>5+/6+</sup>) in the brannerite structure by charge compensation (see below). Ce was used as a structural analogue for plutonium. MOX fuel compositions for light water reactors are envisaged to contain 5–10% Pu therefore the atomic ratio of U to Ce was maintained at 9 : 1 in all compositions as an approximation of the upper bounds of expected MOX fuel composition.<sup>14</sup> Charge balancing of di- and trivalent cations (Ca<sup>2+</sup> and Gd<sup>3+</sup>) was expected to occur *via* the oxidation of U<sup>4+</sup> to higher oxidation states (U<sup>5+</sup>, U<sup>6+</sup>) as observed in previous studies.<sup>4,5</sup>

Reagents (UO<sub>2</sub>, CeO<sub>2</sub>, Gd<sub>2</sub>O<sub>3</sub>, TiO<sub>2</sub> and CaCO<sub>3</sub>) were mixed with isopropanol to form a slurry and ball milled for five minutes at a frequency of 30 Hz using a Fritsch Pulverisette 23. The milled slurry was dried in an oven (95 °C) and a sample from each composition (~0.6 g) reacted at 1300 °C for 12 hours under flowing air, argon or 5% H<sub>2</sub>/N<sub>2</sub>.

Sintered pellets were produced by uniaxially pressing reacted powders in a hardened steel die (6 mm diameter) and sintering under atmosphere (argon, air, 5% H<sub>2</sub>/N<sub>2</sub>) at 1320 °C for 12 hours.

## 2.2 Materials characterisation

Reacted powders were ground and characterised by powder X-ray diffraction with a Bruker D2 Phaser X-ray diffractometer using Cu K $\alpha$  radiation. Cu K $\beta$  radiation was filtered using a Ni foil. XRD data were processed using the Bruker Diffraction software package.

Sintered pellets were characterised by scanning electron microscopy and energy dispersive X-ray spectroscopy (SEM-EDX) using a Hitachi TM3030 SEM equipped with a Bruker Quantax EDX. An accelerating voltage of 15 kV was used for imaging. EDX data were analysed using Bruker Quantax software. Sintered pellets were prepared for SEM analysis by mounting in cold setting resin and polishing with SiC paper and progressively finer diamond pastes to an optical finish (1  $\mu$ m). Samples were sputter coated with carbon to reduce surface charging effects.

## 2.3 X-ray absorption near edge spectroscopy

Samples were characterised using X-ray absorption near edge spectroscopy (XANES) to determine the average oxidation state of U, Ce and Ti. Samples were investigated at the Ti K-edge (4966 eV), Ce L-III edge (5723 eV) and U L-III edge (17 166 eV) using a conventional XAS setup at the now decommissioned beamline X23A2, National Synchrotron Lightsource, Brookhaven National Laboratory. Samples were prepared for XAS analysis by homogeneously mixing ground, reacted powders with polyethylene glycol and uniaxially pressing to form 13 mm diameter pellets of approximately one absorption length.

Samples were measured alongside standards of known oxidation states to allow the derivation of the average oxidation state of the element of interest. Ti and Ce edges were measured in fluorescence mode. Ti measurements were made alongside Ti<sup>4+</sup>, Ti<sup>3+</sup>, Ti<sup>2+</sup> and Ti<sup>(0)</sup> standards (TiO<sub>2</sub>, Ti<sub>2</sub>O<sub>3</sub>, TiO and Ti metal foil respectively) and Ce measurements were made alongside Ce<sup>3+</sup> and Ce<sup>4+</sup> standards (CePO<sub>4</sub> and CeO<sub>2</sub> respectively). The U L-III edge was

measured in transmission alongside U<sup>4+</sup>, U<sup>5+</sup> and U<sup>6+</sup> standards: brannerite (U<sup>4+</sup>-UTi<sub>2</sub>O<sub>6</sub>), mixed brannerite (U<sup>5+</sup>-Y<sub>0.5</sub>U<sub>0.5</sub>Ti<sub>2</sub>O<sub>6</sub>) and calcium uranate (U<sup>6+</sup>-CaUO<sub>4</sub>). Y<sub>0.5</sub>U<sub>0.5</sub>Ti<sub>2</sub>O<sub>6</sub> was produced according to the method described by James *et al.*<sup>11</sup> The edge position was determined to be the maximum of the first derivative of the absorption spectrum, the average U oxidation state was determined by performing a linear regression of first derivative energies with respect to standards of known oxidation state.

Incident ( $I_0$ ) and transmitted ( $I_t$ ) X-ray intensities were measured using ion chambers, energy calibration was performed using XANES spectra measured with a reference ion chamber ( $I_r$ ) of a standard placed after the transmission ion chamber in the beam path. Fluorescence mode measurements were made using a four element vortex Si-drift detector. XANES spectra were measured from 30 eV below the edge of interest to 250 eV above. A Si (311) monochromator was used to tune the energy of incident photons giving an energy resolution of  $\pm 0.3$  eV. Data reduction and XANES analysis were performed using the program Athena.<sup>15,16</sup>

## 2.4 Micro-focus X-ray absorption spectroscopy

To determine the U oxidation state exclusively in the brannerite phase, in the presence of accessory phases, samples were studied using micro-focus X-ray absorption spectroscopy at beamline X05LA, Swiss Light Source, Paul Scherrer Institute, Switzerland. Samples were mounted in cold setting resin before being thin-sectioned and mounted on a Spectrasil slide. For measurement, samples were mounted on a motorised  $x$ - $y$ - $z$  stage to allow scanning of the sample in the beam and a spot size of approximately 1  $\mu$ m<sup>2</sup> was used.

To aid in the selection of regions of interest, 30  $\mu$ m<sup>2</sup> fluorescence maps were produced by rastering the sample in the beam at an energy of 17 200 eV. X-ray fluorescence was measured using a Si drift detector (KETEK) mounted 45° to the incident beam. XRF maps were produced by windowing specific regions of the fluorescence spectrum corresponding to the emission lines of U, Gd and Ti. Points of interest for XANES study were then selected on the basis of relative intensities of Gd, Ti and U and knowledge of the respective phase assemblages and elemental partitioning of the samples from prior SEM-EDX analysis. Multiple XANES spectra per sample were measured from 30 eV below the U L-III edge to 250 eV above and then averaged, photon energy was tuned using a double crystal Si (111) monochromator. Again, data reduction and XANES analysis were performed using the program Athena.<sup>15,16</sup> The average uranium oxidation state in the brannerite phase was determined by performing linear regression of the energy value at half the edge step with respect to standards of known oxidation state.

# 3 Results and discussion

## 3.1 Powder X-ray diffraction

All samples produced were characterised by powder X-ray diffraction and sharp reflections indicative of prototypical brannerite were observed in all cases. Other, secondary phases, were observed dependent on processing atmosphere and



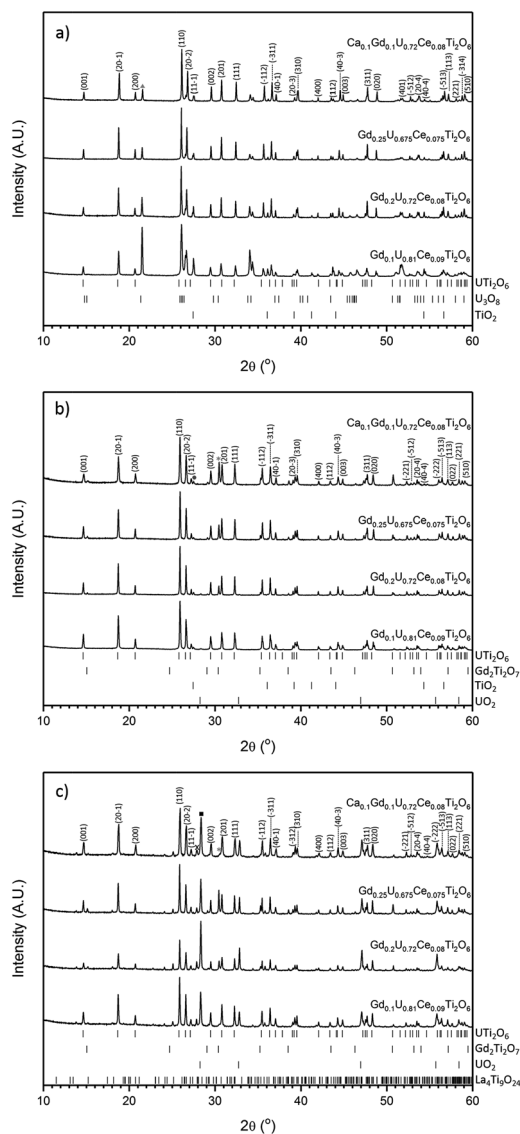


Fig. 1 Powder X-ray diffraction results for compositions sintered under atmosphere: (a) air, (b) Ar and (c) 5%  $\text{H}_2/\text{N}_2$ . Major reflections of secondary phases are indicated by symbols: Triangle- $\text{U}_3\text{O}_8$ ; Circle- $\text{TiO}_2$  (rutile); Square- $\text{UO}_2$ ; Asterisk- $\text{Gd}_2\text{Ti}_2\text{O}_7$  and X- $\text{La}_4\text{Ti}_9\text{O}_{24}$ . Reference patterns were obtained from the ICSD database ( $\text{UTi}_2\text{O}_6$ -ICSD 201342,  $\text{Gd}_2\text{Ti}_2\text{O}_7$ -ICSD 167918,  $\text{U}_3\text{O}_8$ -ICSD 28137,  $\text{TiO}_2$  (rutile)-ICSD 33837,  $\text{UO}_2$ -ICSD 246851,  $\text{La}_4\text{Ti}_9\text{O}_{24}$ -ICSD 80052).

composition. Samples sintered in air contained three phases: brannerite,  $\text{U}_3\text{O}_8$  and rutile ( $\text{TiO}_2$ ); these results are in agreement with those reported by previous studies.<sup>4,5,10,12,13</sup> As can be seen in Fig. 1a, as the level of Gd substitution increased the major peaks associated with  $\text{U}_3\text{O}_8$  decreased, this indicates that the formation of the brannerite phase in air is stabilised by the addition of Gd.

Samples sintered in Ar were found to contain a mixture of prototypical brannerite, rutile and a pyrochlore phase, see Fig. 1b. Considering the solid solution limits quoted by James and Watson (2002) for brannerites in the series  $\text{Gd}_x\text{U}_{1-x}\text{Ti}_2\text{O}_6$  produced under similar conditions,  $0 < x < 0.45$ , these results are unexpected. Unlike samples sintered in air, increased substitution of Gd was seen to have a detrimental effect on the phase assemblage with the relative proportion of the pyrochlore phase showing a concomitant increase.

Samples sintered in 5%  $\text{H}_2/\text{N}_2$ , see Fig. 1c, were found to contain brannerite,  $\text{UO}_2$ , a pyrochlore phase and a rare-earth rich titanate phase related to the  $\text{La}_4\text{Ti}_9\text{O}_{24}$  structure. A similar titanate phase has previously been found to form in  $\text{CeTi}_2\text{O}_6$  ceramics when sintered in Ar and has also been observed in brannerite-based ceramics by Stefanovskiy *et al.*<sup>17</sup> As with samples produced in inert atmospheres, increased substitution of Gd led to an increase in the intensities attributed to the pyrochlore phase.

Although there was not significant variation in unit cell volume between different compositions produced in the same atmosphere; there is clear variation between samples produced in different atmospheres (Table 1). Samples produced in air were found to have the smallest unit cells and those produced in 5%  $\text{H}_2/\text{N}_2$  the largest. Considering the ionic radii of  $\text{U}^{4+}$ ,  $\text{U}^{5+}$  and  $\text{U}^{6+}$  in octahedral coordination (0.89, 0.76 and 0.73 Å respectively), these results are consistent with the incorporation of more highly oxidised U in samples sintered in air and the retention of  $\text{U}^{4+}$  in samples produced in 5%  $\text{H}_2/\text{N}_2$ .

### 3.2 Scanning electron microscopy-energy dispersive X-ray spectroscopy (SEM-EDX)

Scanning electron microscopy was used to examine the phase distribution in sintered samples. In agreement with XRD data, brannerite was observed in all cases, with differing accessory

Table 1 Refined lattice parameters of synthesised brannerites

Nominal composition	Atmosphere	$a$ (Å)	$b$ (Å)	$c$ (Å)	$\beta$ (°)	$V$ (Å <sup>3</sup> )
$\text{Gd}_{0.1}\text{U}_{0.81}\text{Ce}_{0.09}\text{Ti}_2\text{O}_6$	Air	9.8172(2)	3.7390(1)	6.9196(2)	118.554(1)	253.997(2)
$\text{Gd}_{0.25}\text{U}_{0.675}\text{Ce}_{0.075}\text{Ti}_2\text{O}_6$	Air	9.8210(2)	3.7370(1)	6.9101(1)	118.607(1)	253.611(2)
$\text{Gd}_{0.25}\text{U}_{0.675}\text{Ce}_{0.075}\text{Ti}_2\text{O}_6$	Air	9.8207(1)	3.7371(1)	6.9099(1)	118.607(1)	253.599(1)
$\text{Ca}_{0.1}\text{Gd}_{0.1}\text{U}_{0.72}\text{Ce}_{0.08}\text{Ti}_2\text{O}_6$	Air	9.8145(2)	3.7346(1)	6.9027(1)	118.482(1)	253.007(2)
$\text{Gd}_{0.1}\text{U}_{0.81}\text{Ce}_{0.09}\text{Ti}_2\text{O}_6$	Ar	9.8192(1)	3.7617(1)	6.9253(1)	118.807(1)	255.802(1)
$\text{Gd}_{0.2}\text{U}_{0.72}\text{Ce}_{0.08}\text{Ti}_2\text{O}_6$	Ar	9.8215(2)	3.7612(1)	6.9240(1)	118.799(1)	255.779(2)
$\text{Gd}_{0.25}\text{U}_{0.675}\text{Ce}_{0.075}\text{Ti}_2\text{O}_6$	Ar	9.8208(2)	3.7510(1)	6.9219(1)	118.797(1)	255.598(2)
$\text{Ca}_{0.1}\text{Gd}_{0.1}\text{U}_{0.72}\text{Ce}_{0.08}\text{Ti}_2\text{O}_6$	Ar	9.8210(6)	3.7660(2)	6.9293(4)	118.825(1)	256.284(6)
$\text{Gd}_{0.1}\text{U}_{0.81}\text{Ce}_{0.09}\text{Ti}_2\text{O}_6$	5% $\text{H}_2/\text{N}_2$	9.8197(2)	3.7695(1)	6.9297(2)	118.864(1)	256.504(2)
$\text{Gd}_{0.2}\text{U}_{0.72}\text{Ce}_{0.08}\text{Ti}_2\text{O}_6$	5% $\text{H}_2/\text{N}_2$	9.8286(5)	3.7702(2)	6.9324(4)	118.867(3)	256.884(5)
$\text{Gd}_{0.25}\text{U}_{0.675}\text{Ce}_{0.075}\text{Ti}_2\text{O}_6$	5% $\text{H}_2/\text{N}_2$	9.8251(3)	3.7686(1)	6.9292(2)	118.867(1)	256.565(3)
$\text{Ca}_{0.1}\text{Gd}_{0.1}\text{U}_{0.72}\text{Ce}_{0.08}\text{Ti}_2\text{O}_6$	5% $\text{H}_2/\text{N}_2$	9.8192(2)	3.7693(1)	6.9294(1)	118.867(1)	256.468(2)



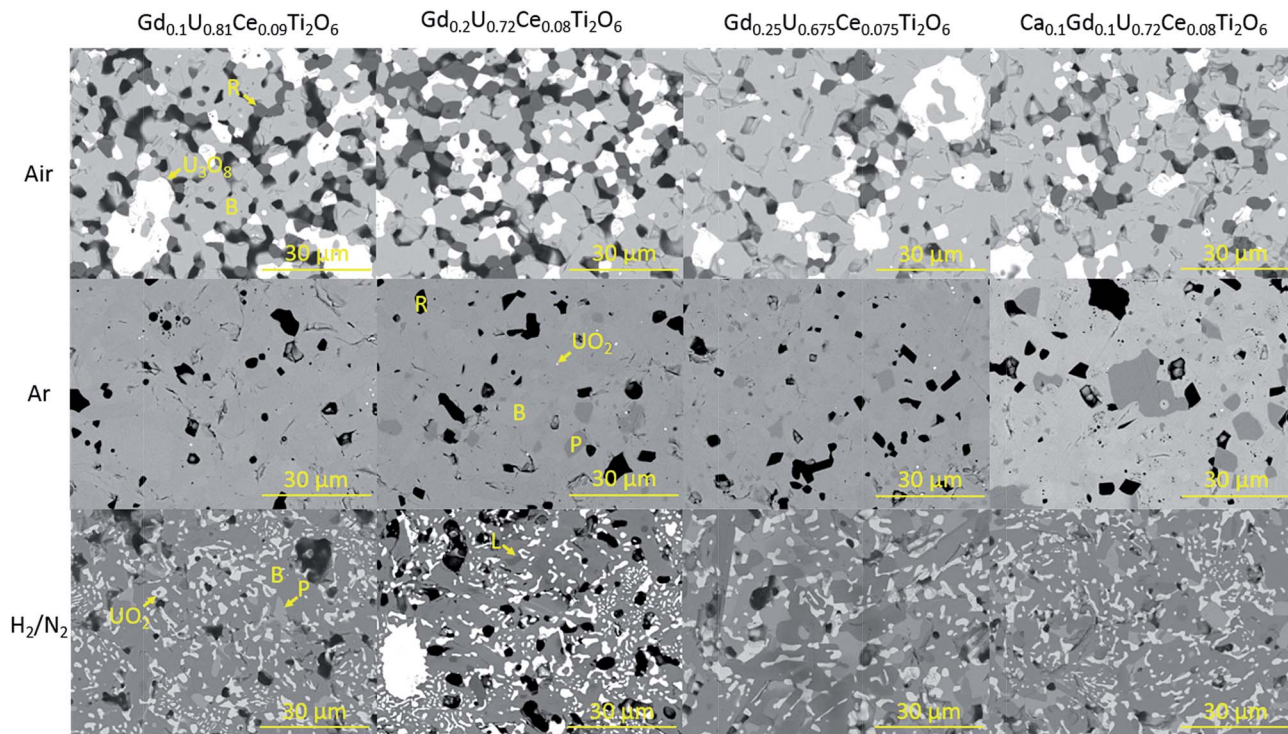


Fig. 2 Representative backscattered electron images of sintered brannerites. B-brannerite, R-rutile, P-pyrochlore, L-Lan<sub>4</sub>Ti<sub>9</sub>O<sub>24</sub>.

phases dependent upon processing atmosphere. Representative backscattered electron images of sintered brannerites are shown in Fig. 2.

Three distinct phases were formed when samples were synthesised in air: brannerite, U<sub>3</sub>O<sub>8</sub> and rutile (TiO<sub>2</sub>). Significant porosity was observed throughout all compositions, this is in agreement with the porosity observed by Vance *et al.* for samples synthesised under similar conditions.<sup>4</sup>

The phase distribution observed in samples sintered in argon was markedly different to that of samples sintered in air. In agreement with XRD results, there are several phases present within the samples; predominantly brannerite, rutile and

pyrochlore with some retained UO<sub>2</sub>. As can be seen in Fig. 2, although there is no evidence of pyrochlore formation in the Gd<sub>0.1</sub>U<sub>0.81</sub>Ce<sub>0.09</sub>Ti<sub>2</sub>O<sub>6</sub> composition, pyrochlore formation was observed for all other compositions. These results are in contrast to those reported by Vance *et al.* and James and Watson who found that substituted Gd formed a solid solution up to a limit of 0.45 formula units when Gd<sub>x</sub>U<sub>1-x</sub>Ti<sub>2</sub>O<sub>6</sub> brannerites were produced in an inert atmosphere.<sup>4,5</sup> Bailey *et al.* found that substitution of Gd in the system Gd<sub>x</sub>U<sub>1-x</sub>Ti<sub>2</sub>O<sub>6</sub> led to the formation of a parasitic pyrochlore phase at a substitution level as low as 0.2 formula units,<sup>12</sup> these results are consistent with those presented in this study.

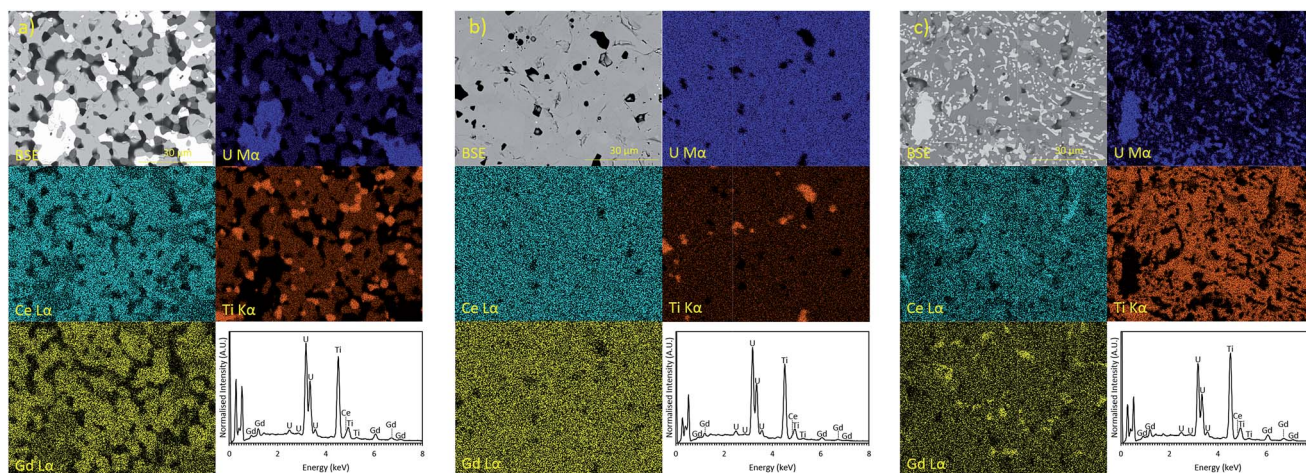


Fig. 3 EDX spectra and elemental partitioning observed in Gd<sub>0.1</sub>U<sub>0.81</sub>Ce<sub>0.09</sub>Ti<sub>2</sub>O<sub>6</sub> synthesised in: (a) air; (b) Argon and (c) 5% H<sub>2</sub>/N<sub>2</sub>.



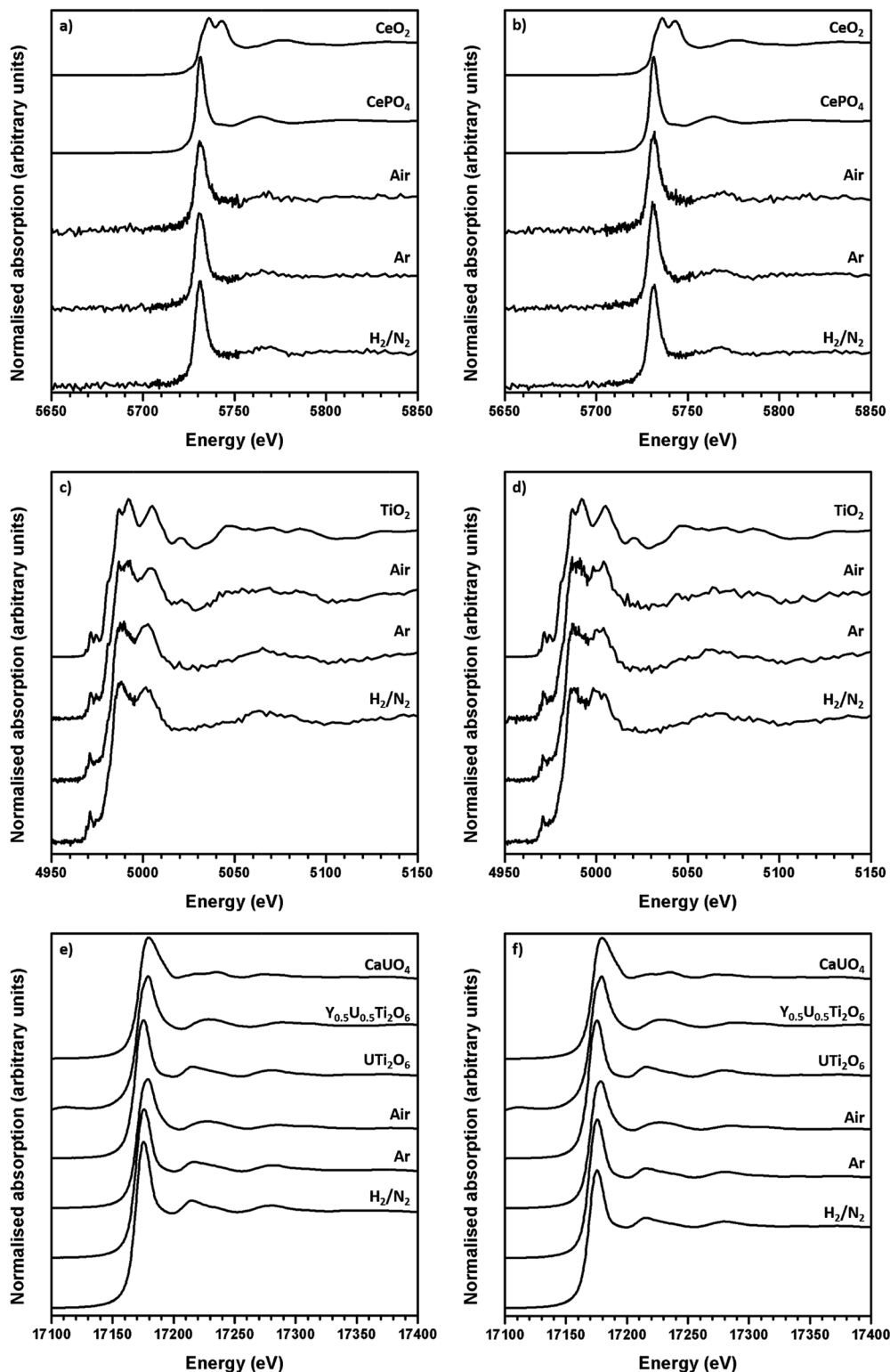


Fig. 4 Representative XANES spectra of synthesised brannerites. (a) Ce  $L_{III}$  edge  $Gd_{0.1}U_{0.81}Ce_{0.1}Ti_2O_6$ ; (b) Ce  $L_{III}$  edge  $Ca_{0.1}Gd_{0.1}U_{0.72}Ce_{0.08}Ti_2O_6$ ; (c) Ti K edge  $Gd_{0.1}U_{0.81}Ce_{0.1}Ti_2O_6$  and (d) Ti K edge  $Ca_{0.1}Gd_{0.1}U_{0.72}Ce_{0.08}Ti_2O_6$ ; (e) U  $L_{III}$  edge  $Gd_{0.1}U_{0.81}Ce_{0.1}Ti_2O_6$  and (f) U  $L_{III}$  edge  $Ca_{0.1}Gd_{0.1}U_{0.72}Ce_{0.08}Ti_2O_6$ .

Heat treatment of samples in a 5%  $H_2/N_2$  atmosphere was found to result in the formation of brannerite, pyrochlore and a rare earth titanate phase along with the retention of  $UO_2$  throughout the samples.

From EDX analysis, it is evident that Gd and Ce are preferentially incorporated in the brannerite phase when samples are produced in an oxidising environment, Fig. 3a. Increased substitution of Gd may lead to the formation of single phase



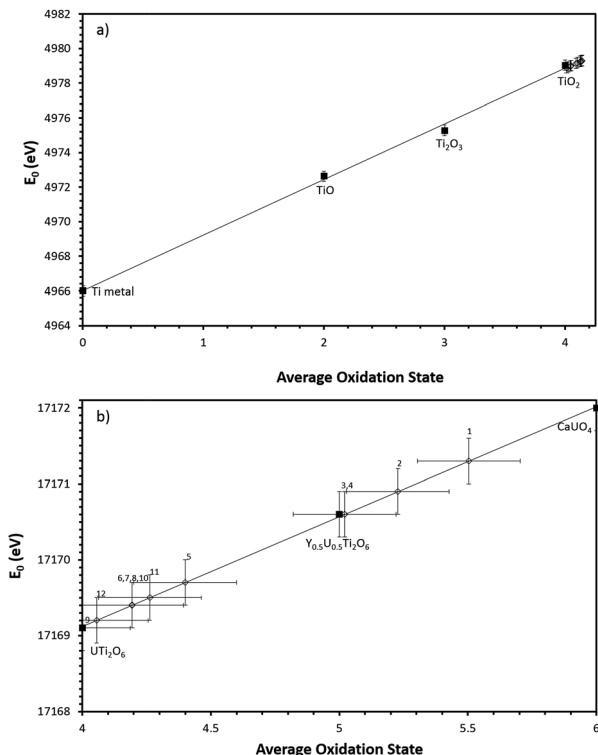


Fig. 5 (a) Linear regression of Ti K edge  $E_0$  values with respect to Ti standards. (b) Linear regression of U L-III edge  $E_0$  values with respect to U standards. Numbers refer to corresponding composition no. in Table 2. Black squares denote standards, open diamonds denote samples.

brannerite, however, the level of substitution required to achieve the desired phase assemblage would have a negative impact on the waste loading of a final wasteform.

Samples produced in an Ar atmosphere were found to exhibit different partitioning behaviour; as can be seen in Fig. 3b, Gd is clearly enriched in the pyrochlore phase and Ti is enriched in the rutile phase. Cerium does not clearly partition to either the brannerite or pyrochlore phase. However, the removal of Gd from the brannerite by the parasitic formation of pyrochlore may have a negative impact on the criticality performance of a final wasteform.

Samples synthesised in a reducing 5%  $H_2/N_2$  atmosphere, Fig. 3c, exhibited similar elemental partitioning to those synthesised in an Ar atmosphere however; it is clear that a greater proportion of the U inventory is retained as  $UO_2$ . Although there is some local enrichment visible in the EDX map, Ce does not show clear partitioning into any one phase.

### 3.3 Bulk X-ray absorption spectroscopy

The average oxidation state of Ti, Ce and U in the synthesised brannerites were determined by X-ray absorption spectroscopy near edge spectroscopy (XANES). Fig. 4 shows representative Ce L-III, Ti K and U L-III edge XANES data.

Ti K-edge XANES data show that the predominant oxidation state of Ti in all samples is  $Ti^{4+}$ , see Fig. 4c, d and 5a, as the white line positions ( $E_0 = 4979.0 \pm 0.3$  eV) and pre-edge features are similar in character to the  $TiO_2$  standard.

Table 2 Average U oxidation state of synthesised brannerites as determined by linear regression with respect to standards

Sample no.	Nominal composition	Atmosphere	Oxidation state
1	$Gd_{0.1}U_{0.81}Ce_{0.09}Ti_2O_6$	Air	5.5 ( $\pm 0.2$ )
2	$Gd_{0.2}U_{0.72}Ce_{0.08}Ti_2O_6$	Air	5.2 ( $\pm 0.2$ )
3	$Gd_{0.25}U_{0.675}Ce_{0.075}Ti_2O_6$	Air	5.0 ( $\pm 0.2$ )
4	$Ca_{0.1}Gd_{0.1}U_{0.72}Ce_{0.08}Ti_2O_6$	Air	5.0 ( $\pm 0.2$ )
5	$Gd_{0.1}U_{0.81}Ce_{0.09}Ti_2O_6$	Ar	4.4 ( $\pm 0.2$ )
6	$Gd_{0.2}U_{0.72}Ce_{0.08}Ti_2O_6$	Ar	4.2 ( $\pm 0.2$ )
7	$Gd_{0.25}U_{0.675}Ce_{0.075}Ti_2O_6$	Ar	4.2 ( $\pm 0.2$ )
8	$Ca_{0.1}Gd_{0.1}U_{0.72}Ce_{0.08}Ti_2O_6$	Ar	4.2 ( $\pm 0.2$ )
9	$Gd_{0.1}U_{0.81}Ce_{0.09}Ti_2O_6$	5% $H_2/N_2$	4.0 ( $\pm 0.2$ )
10	$Gd_{0.2}U_{0.72}Ce_{0.08}Ti_2O_6$	5% $H_2/N_2$	4.2 ( $\pm 0.2$ )
11	$Gd_{0.25}U_{0.675}Ce_{0.075}Ti_2O_6$	5% $H_2/N_2$	4.3 ( $\pm 0.2$ )
12	$Ca_{0.1}Gd_{0.1}U_{0.72}Ce_{0.08}Ti_2O_6$	5% $H_2/N_2$	4.1 ( $\pm 0.2$ )

This indicates that the oxidation state of Ti remains unchanged relative to the initial  $TiO_2$  precursor and is insensitive to both composition and processing atmosphere.

Ce L-III edge XANES data show that the position of the absorption edge and post-edge oscillations of Ce in synthesised brannerites are similar in character to the  $CePO_4$  standard (5725.0 eV). This indicates that the cerium has been reduced from  $Ce^{4+}$  to  $Ce^{3+}$  during synthesis. As can be seen, this reduction occurs regardless of processing atmosphere or composition and it is consistent with results of previous studies involving the substitution of Ce into the brannerite structure.<sup>13,17</sup>

As the Ti and Ce XANES data show, the oxidation states of Ce and Ti in the synthesised brannerites are insensitive to both processing atmosphere and stoichiometry. In contrast, it was found that the average U oxidation state was strongly affected by the processing atmosphere.

Samples synthesised in air exhibited an absorption edge and post-edge oscillations indicative of a mixed  $U^{5+/6+}$  oxidation

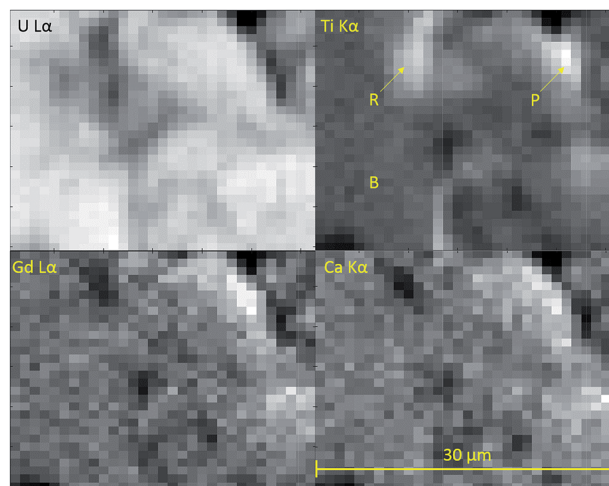


Fig. 6 Fluorescence maps of  $Ca_{0.1}Gd_{0.1}U_{0.72}Ce_{0.08}Ti_2O_6$  sintered in an argon atmosphere. Each pixel represents  $1 \mu m^2$ . Lighter colours indicate higher X-ray fluorescence intensity, darker colours indicate lower intensity. B-brannerite, P-pyrochlore and R-rutile.



**Table 3** Oxidation state of uranium in the brannerite phase as found by micro-focus XAS and linear regression with respect to standards

Sample no.	Nominal composition	Atmosphere	Oxidation state
1	Gd <sub>0.1</sub> U <sub>0.81</sub> Ce <sub>0.09</sub> Ti <sub>2</sub> O <sub>6</sub>	Air	5.0 (±0.2)
2	Gd <sub>0.2</sub> U <sub>0.72</sub> Ce <sub>0.08</sub> Ti <sub>2</sub> O <sub>6</sub>	Air	4.6 (±0.2)
3	Gd <sub>0.25</sub> U <sub>0.675</sub> Ce <sub>0.075</sub> Ti <sub>2</sub> O <sub>6</sub>	Air	4.6 (±0.2)
4	Ca <sub>0.1</sub> Gd <sub>0.1</sub> U <sub>0.72</sub> Ce <sub>0.08</sub> Ti <sub>2</sub> O <sub>6</sub>	Air	5.2 (±0.2)
5	Gd <sub>0.1</sub> U <sub>0.81</sub> Ce <sub>0.09</sub> Ti <sub>2</sub> O <sub>6</sub>	Ar	4.5 (±0.2)
6	Gd <sub>0.2</sub> U <sub>0.72</sub> Ce <sub>0.08</sub> Ti <sub>2</sub> O <sub>6</sub>	Ar	4.5 (±0.2)
7	Gd <sub>0.25</sub> U <sub>0.675</sub> Ce <sub>0.075</sub> Ti <sub>2</sub> O <sub>6</sub>	Ar	4.5 (±0.2)
8	Ca <sub>0.1</sub> Gd <sub>0.1</sub> U <sub>0.72</sub> Ce <sub>0.08</sub> Ti <sub>2</sub> O <sub>6</sub>	Ar	4.6 (±0.2)
9	Gd <sub>0.1</sub> U <sub>0.81</sub> Ce <sub>0.09</sub> Ti <sub>2</sub> O <sub>6</sub>	5% H <sub>2</sub> /N <sub>2</sub>	4.4 (±0.2)
10	Gd <sub>0.2</sub> U <sub>0.72</sub> Ce <sub>0.08</sub> Ti <sub>2</sub> O <sub>6</sub>	5% H <sub>2</sub> /N <sub>2</sub>	4.1 (±0.2)
11	Gd <sub>0.25</sub> U <sub>0.675</sub> Ce <sub>0.075</sub> Ti <sub>2</sub> O <sub>6</sub>	5% H <sub>2</sub> /N <sub>2</sub>	4.5 (±0.2)
12	Ca <sub>0.1</sub> Gd <sub>0.1</sub> U <sub>0.72</sub> Ce <sub>0.08</sub> Ti <sub>2</sub> O <sub>6</sub>	5% H <sub>2</sub> /N <sub>2</sub>	4.4 (±0.2)

state whereas samples synthesised under Ar or 5% H<sub>2</sub>/N<sub>2</sub> possessed features indicative of mixed U<sup>4+/5+</sup> oxidation states. Table 2 shows the average U oxidation state for the synthesised brannerites, as determined by linear regression with respect to standards (Fig. 5b). It is clear that processing atmosphere has a strong influence on the average oxidation state of U. However, comparison between different compositions processed in the same atmosphere does not reveal a strong compositional influence.

The presence of minor U-bearing accessory phases such as U<sub>3</sub>O<sub>8</sub> and UO<sub>2</sub> means that, although indicative, the bulk U oxidation state is not representative of the oxidation state of U in the brannerite phase. As a result, the oxidation state of U in the brannerite phase was subject to further investigation by micro-focus XAS.

### 3.4 Micro-focus X-ray absorption spectroscopy

Micro-focus X-ray spectroscopy was used to determine the oxidation state of U in the brannerite phase. XRF maps were

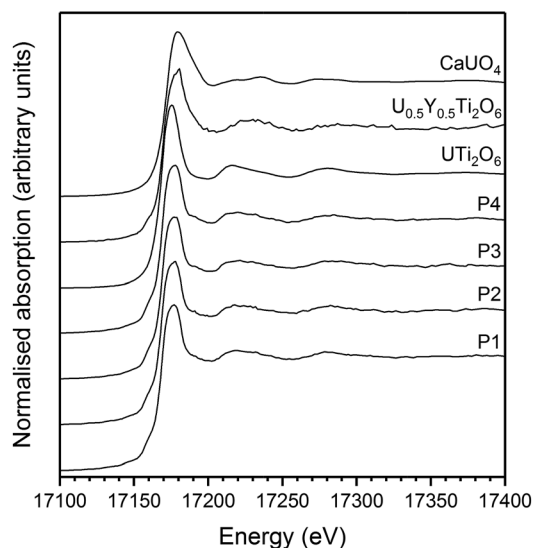


**Fig. 7** Example U L-III edge  $\mu$ -focus XANES for Gd<sub>0.1</sub>U<sub>0.81</sub>Ce<sub>0.09</sub>Ti<sub>2</sub>O<sub>6</sub> synthesised in argon. P1–4 indicate individual spectra taken from separate points.

**Table 4** Comparison of nominal composition and determined average composition of brannerites synthesised in argon atmosphere

Nominal composition	Determined average composition
Gd <sub>0.1</sub> U <sub>0.81</sub> Ce <sub>0.09</sub> Ti <sub>2</sub> O <sub>6</sub>	(Gd <sub>0.09±0.01</sub> U <sub>0.76±0.04</sub> Ce <sub>0.04±0.01</sub> Ti <sub>2.00±0.03</sub> O <sub>6</sub> )
Gd <sub>0.2</sub> U <sub>0.72</sub> Ce <sub>0.08</sub> Ti <sub>2</sub> O <sub>6</sub>	(Gd <sub>0.17±0.01</sub> U <sub>0.71±0.03</sub> Ce <sub>0.05±0.01</sub> Ti <sub>2.00±0.03</sub> O <sub>6</sub> )
Gd <sub>0.25</sub> U <sub>0.675</sub> Ce <sub>0.075</sub> Ti <sub>2</sub> O <sub>6</sub>	(Gd <sub>0.21±0.03</sub> U <sub>0.66±0.03</sub> Ce <sub>0.04±0.01</sub> Ti <sub>2.00±0.06</sub> O <sub>6</sub> )
Ca <sub>0.1</sub> Gd <sub>0.1</sub> U <sub>0.72</sub> Ce <sub>0.08</sub> Ti <sub>2</sub> O <sub>6</sub>	(Ca <sub>0.02±0.02</sub> Gd <sub>0.09±0.02</sub> U <sub>0.79±0.02</sub> Ce <sub>0.03±0.01</sub> Ti <sub>2.00±0.05</sub> O <sub>6</sub> )

used to determine which regions of the sample were brannerite and which were secondary phases, example maps are shown in Fig. 6. Rutile and pyrochlore phases were easily distinguished by a strong Ti K $\alpha$  emission, together with Gd L $\alpha$  or Ca L $\alpha$  emission respectively. U<sub>3</sub>O<sub>8</sub> and UO<sub>2</sub> were distinguished by the absence of Gd L $\alpha$ , Ca L $\alpha$  and Ti K $\alpha$  emission.

U oxidation states, as determined by linear regression with respect to standards, are given in Table 3. Example micro-focus spectra are shown in Fig. 7. A general trend may be observed when comparing the effect of processing atmosphere on the U oxidation state; samples sintered in air had the highest U oxidation state, samples sintered in a reducing atmosphere had the lowest; and samples produced in inert conditions were intermediate between the two extremes. The oxidation of U to higher oxidation states was expected in order to compensate for the incorporation of Ca, Ce and Gd and is in agreement with the results reported by Vance *et al.*<sup>4</sup> The relatively high oxidation state observed in samples sintered in air may be explained by the large amount of U<sub>3</sub>O<sub>8</sub> present in the bulk of the sample: as Gd is incorporated in the brannerite phase and a substantial amount of U is incorporated in U<sub>3</sub>O<sub>8</sub>, the relative proportion of Gd to U in the brannerite phase is higher than in the target composition; consequently, U contained within the brannerite phase must oxidise further to compensate for the relative increase in Gd concentration.

### 3.5 Charge balance mechanism

Combining the results of microfocus XANES with those of SEM-EDX and bulk XANES, a credible charge balance mechanism was derived. Assuming that oxygen is fully stoichiometric, the A-site is cation deficient and incorporates a small proportion of Ti. The charge balance mechanism is therefore hypothesised to be a combination of A-site vacancies and the oxidation of U<sup>4+</sup> to higher oxidation states. Assuming this charge balance mechanism, the average composition closely follows that of the nominal, batched composition (Table 4) and is consistent with the secondary phases observed by SEM-EDX.

## 4 Conclusions

Brannerite compositions have been synthesised under oxidising, inert and reducing atmospheres. Characterisation by XRD and SEM-EDX has shown that the final phase assemblage and



elemental partitioning of brannerite wastefroms is affected by both processing atmosphere and stoichiometry. The most favourable phase assemblages were produced processing in an argon atmosphere. Increasing substitution of Gd and Ca was found to have a negative impact on the resultant phase assemblage of samples produced in inert atmospheres. The most favourable phase assemblage was produced for the target stoichiometry  $\text{Gd}_{0.1}\text{U}_{0.81}\text{Ce}_{0.09}\text{Ti}_2\text{O}_6$  when sintered in argon. Under these conditions Ce was incorporated into the brannerite phase indicating a promising route for immobilisation of expected MOX residue compositions. As the MOX compositions investigated in this study were at the upper bounds of expected Pu concentration for light water reactor fuels, it would be reasonable to assume that immobilisation of lower concentrations of Pu would not result in significant deviation from the outcomes of this study. Combined bulk and micro-focus XANES have established the oxidation states of Ti, Ce and U in synthesised brannerites. Combination of XANES and SEM-EDX data indicates a charge balance mechanism that uses a combination of U oxidation and A-site vacancies to achieve charge neutrality. It is clear that, in order to produce an optimised wastefrom, careful consideration must be given to both the processing conditions and system stoichiometry.

## Conflicts of interest

There are no conflicts of interest to declare.

## Acknowledgements

UK EPSRC is thanked for providing studentship and fellowship for DJB through the Nuclear FiRST Doctoral Training Centre and EPSRC Doctoral Prize Fellowship (Grant EP/G037140/1, EP/M026566/1 and EP/R512175/1). Use of the National Synchrotron Light Source, Brookhaven National Laboratory, was supported by the U.S. Department of Energy, Office of Science, Office of Basic Energy Sciences, under Contract No. DE-AC02-98CH10886. Access to the Swiss Light Source, Paul Scherrer Institute, Villigen, Switzerland, was supported by the TALISMAN collaborative project, with co-funding from the European Commission under the Euratom Research and Training Programme on Nuclear Energy, within the 7<sup>th</sup> Framework programme (grant agreement 323300). NCH is grateful to

the Royal Academy of Engineering and Nuclear Decommissioning Authority for funding. We thank Hands on Thin Sections Ltd. for preparation of the thin section specimens. This research was performed in part at the MIDAS Facility, at the University of Sheffield, which was established with support from the Department of Energy and Climate Change.

## Notes and references

- 1 Nuclear Decommissioning Authority, *Progress on approaches to the management of separated plutonium*, 2014.
- 2 N. C. Hyatt, *Energy Policy*, 2017, **101**, 303–309.
- 3 J. T. Szymanski and J. D. Scott, *Can. Mineral.*, 1982, **20**, 271–279.
- 4 E. R. Vance, J. N. Watson, M. L. Carter, R. A. Day and B. D. Begg, *J. Am. Ceram. Soc.*, 2001, **44**, 141–144.
- 5 M. James and J. N. Watson, *J. Solid State Chem.*, 2002, **165**, 261–265.
- 6 F. X. Zhang, M. Lang, Z. Liu and R. C. Ewing, *J. Solid State Chem.*, 2011, **184**, 2834–2839.
- 7 G. R. Lumpkin, *J. Nucl. Mater.*, 2001, **289**, 136–166.
- 8 Y. Zhang, G. R. Lumpkin, H. Li, M. G. Blackford, M. Colella, M. L. Carter and E. R. Vance, *J. Nucl. Mater.*, 2006, **350**, 293–300.
- 9 M. C. Stennett, C. L. Freeman, A. S. Gandy and N. C. Hyatt, *J. Solid State Chem.*, 2012, **192**, 172–178.
- 10 J. E. Patchett and E. W. Nuffield, *Can. Mineral.*, 1960, **6**, 483–490.
- 11 M. James, M. L. Carter and J. N. Watson, *J. Solid State Chem.*, 2003, **174**, 329–333.
- 12 D. J. Bailey, M. C. Stennett and N. C. Hyatt, *Procedia Chem.*, 2016, **21**, 371–377.
- 13 D. J. Bailey, M. C. Stennett and N. C. Hyatt, *MRS Adv.*, 2016, **2**, 557–562.
- 14 P. D. Wilson, *The Nuclear Fuel Cycle: From Ore to Waste*, Oxford University Press, Oxford, 1st edn, 1996.
- 15 B. Ravel and M. Newville, *J. Synchrotron Radiat.*, 2005, **12**, 537–541.
- 16 B. Ravel and M. Newville, *Phys. Scr.*, 2005, 1007.
- 17 S. V. Stefanovsky, S. V. Yudinsev, A. A. Shiryaev, V. Y. Murzin and A. L. Trigub, *J. Eur. Ceram. Soc.*, 2017, **37**, 771–777.



**7. A new approach to the immobilisation of  
Tc and Pu: co-disposal in a zirconolite  
ceramic matrix**

# A new approach to the immobilisation of Tc and Pu: co-disposal in a zirconolite ceramic matrix

*D. J. Bailey<sup>1</sup>, S. M. Lawson<sup>1</sup>, S. K. Sun<sup>1</sup>, M. C. Stennett<sup>1</sup> & N. C. Hyatt<sup>1</sup>*

1- Immobilisation Science Laboratory, Department of Materials Science and Engineering, University of Sheffield, United Kingdom

## Abstract

**Technetium and plutonium are both problematic long-lived radionuclides produced as a result of nuclear power generation. These long-lived radionuclides require disposal in a robust and durable wastefrom. Co-immobilisation of these radionuclides in a ceramic wastefrom is attractive as they are problematic for vitrification and it would reduce demand on a future geological disposal facility. A range of zirconolite ceramics were produced *via* an oxide route using the surrogates Mo and Ce with a view to the co-immobilisation of Tc and Pu. The resultant materials were characterised by XRD, SEM-EDX, TEM and XAS. Final phase assemblage was found to be affected by target stoichiometry, Ca precursor used, processing temperature and processing atmosphere. Results indicate that, with proper optimisation of processing conditions and target stoichiometry, the co-immobilisation of Tc and Pu can be achieved.**

## Introduction

Energy generation by means of nuclear fission results in the production of significant amounts of both plutonium and technetium. Although Pu is currently considered to be a zero value asset by the UK government, it could potentially be designated as waste in the future. There are also numerous plutonium residues, unsuitable for MOX production, that require disposal [1]. The long-lived radiotoxicity of both plutonium and technetium ( $^{239}\text{Pu}$   $t_{1/2} = 24000$  years,  $^{99}\text{Tc}$   $t_{1/2} = 211000$  years) necessitate their isolation from the biosphere and eventual disposal in a robust host matrix. Technetium and plutonium are both problematic nuclides with respect to vitrification with limited solubility in borosilicate glasses [2]. Consequently, immobilisation in a ceramic wastefrom, where higher waste loadings may be possible, is attractive. Routing technetium and plutonium for disposal in separate wastefroms would require not only development of two separate wastefroms but would also place greater demand on a geological disposal facility resulting in a concomitant increase in disposal costs. For these reasons the prospect of co-immobilisation of both Pu and Tc in a robust host matrix is attractive.

A proposed ceramic wastefrom for the disposal of plutonium is zirconolite,  $\text{CaZrTi}_2\text{O}_7$  [3]–[5]. Zirconolite is the target actinide bearing component of Synroc formulations and has previously been synthesised *via* both alkoxide and oxide routes [6]–[8]. The zirconolite structure is a derivative of the pyrochlore structure and comprises alternating layers of  $\text{TiO}_6$  octahedra in a hexagonal tungsten bronze array (HTB) and Zr and Ca in seven and eight-fold coordination respectively [9], [10]. Ti is situated in three separate sites; two fully occupied octahedral sites and a half-occupied trigonal bi-pyramidal site. There are several known polytypes of zirconolite including monoclinic, trigonal and orthorhombic symmetries (2M, 4M, 3T, 6T and 3O) [11], [12]. The various polytypes arise as a result differences in the stacking order of the

TiO<sub>6</sub> layers and may be affected by substitutions on the Ca and Zr sites and synthesis conditions, including oxygen fugacity and temperature [4], [9], [12].

Natural zirconolite samples have been found to accommodate and retain actinides despite metamictisation and several previous studies have investigated the incorporation and retention of actinides (U, Np, Pu, Cm) in synthetic zirconolites [3], [4], [13]–[15]. Pu has previously been shown to readily substitute into the zirconolite structure with the crystallographic site occupied by the Pu ion being dependent on Pu valence, processing conditions and the designed stoichiometry [13].

Tc has previously been successfully incorporated into the zirconolite-related pyrochlore structure in the Tc (IV) oxidation state [16]. The 4d<sup>3</sup> electron configuration of Tc(IV) suggests a strong preference for octahedral co-ordination in oxides (associated with a crystal field stabilisation energy) and the ionic radius of Tc<sup>4+</sup> is similar to Ti<sup>4+</sup> (0.785 cf. 0.745 Å) it should therefore be feasible to substitute Tc for Ti in the CaZrTi<sub>2</sub>O<sub>7</sub> system [17]. Samples have been successfully produced by high temperature treatment of oxide precursors under vacuum [18]. The relatively low volatilisation temperature of Tc<sub>2</sub>O<sub>7</sub> (311 °C [2]) complicates the processing of Tc bearing ceramics and it is important to maintain proper redox control to ensure the more thermally stable TcO<sub>2</sub> (slight volatility above 900 °C, no decomposition up to 1100 °C [19]) is retained.

This study was conceived to investigate the possibility of co-immobilisation of Pu and Tc in a zirconolite matrix by synthesising zirconolites in the Ca<sub>1-x/2</sub>Zr<sub>1-x/2</sub>Ce<sub>x</sub>Ti<sub>2-x</sub>Mo<sub>x</sub>O<sub>7</sub> series (x = 0.1, 0.2, 0.3) using Ce (III/IV) and Mo (IV) as structural analogues for Pu (III/IV) and Tc (IV), respectively. Zirconolites were formulated with the intention of Ce (III/IV) substitution on both the Ca and Zr sites, respectively; this solid solution mechanism has been characterised for Pu in previous investigations [13].

## Experimental

Zirconolites were prepared by solid state reaction between ZrO<sub>2</sub>, CaCO<sub>3</sub>, MoO<sub>2</sub>, CeO<sub>2</sub> and TiO<sub>2</sub> precursors. Precursors were mixed with isopropanol to form a slurry and milled for five periods of three minutes at 500 rpm, changing the direction of milling with each period, using a Fritsch Pulverisette 6. The milled slurry was dried overnight and sintered pellets were produced by uniaxially pressing batched powders in a hardened steel die (10 mm diameter) and sintering under atmosphere (argon or 5% H<sub>2</sub>/N<sub>2</sub>) for 12 hours at temperatures of 1200, 1250, 1300, 1350 and 1400 °C. Hot isostatically pressed zirconolite samples were produced by HIPing in 316 stainless steel tubes at a temperature of 1250 °C and overpressure of 100 MPa for four hours. To ensure a dense, HIPed product, the generation of gas must be minimised, consequently, CaCO<sub>3</sub> was replaced by CaTiO<sub>3</sub> to avoid the generation of CO<sub>2</sub> caused by thermal decomposition.

The microstructure of synthesised zirconolites were characterised by scanning electron microscopy (SEM) in combination with energy dispersive X-ray spectroscopy (EDX) using a Hitachi TM3030 SEM equipped with a Bruker Quantax EDX. An accelerating voltage of 15 kV was used. EDX data were processed using Bruker Quantax software. Sectioned zirconolites were prepared for SEM analysis by mounting in cold setting resin and polishing with SiC paper and progressively finer diamond pastes to an optical finish (1µm). Samples were sputter coated with carbon to reduce surface charging effects.

Samples were prepared for TEM analysis by grinding in a pestle and mortar followed by suspension. Ground powders were added to a glass vial containing acetone, the vial was then placed in an ultrasonic bath and sonicated to suspend fine particles. A holey copper grid was washed through the suspended fines and the adhered particles were then studied. Electron diffraction patterns were taken using a Philips EM420 transmission electron microscope.

Mass loss during synthesis was investigated by thermogravimetric analysis using a Netzsch TG449 F3 Jupiter. Samples were heated at a rate of 20 °Cmin<sup>-1</sup> in an argon atmosphere up to a temperature of 1450 °C, and changes in mass recorded.

Samples were studied using X-ray absorption near edge spectroscopy (XANES) to find the average oxidation state of Mo. Samples were measured at the Mo K-edge (20000 eV) using a conventional XAS setup at beamline BL-27b, Photon Factory, High Energy Accelerator Research Organization, Japan [20]. Samples were prepared for XAS analysis by homogeneously mixing ground, reacted powders with polyethylene glycol and uniaxially pressing to form 13 mm diameter pellets of approximately one absorption length.

Incident ( $I_0$ ) and transmitted ( $I_t$ ) X-ray intensities were measured using ionisation chambers. Energy calibration was performed by measuring a Mo foil. XANES spectra were measured from 30 eV below the edge of interest to 250 eV above. A Si (111) double crystal monochromator was used to tune the energy of incident photons giving an energy resolution of  $\pm 0.3$  eV. Data reduction and XANES analysis were performed using the program Athena [21], [22]. The edge position was determined to be the energy at  $\mu = 0.8$  of the absorption spectrum to avoid interference from pre-edge features as described by Farges et al [23]. The average Mo oxidation state was determined by performing a linear regression of first derivative energies with respect to standards of known oxidation state- MoO<sub>2</sub> (Mo IV), SrHoMoO<sub>6</sub> (Mo V) and MoO<sub>3</sub> (Mo VI).

## Results and discussion

### *Cold uniaxially pressed zirconolites*

The results of powder X-ray diffraction showed that the resultant phase assemblage was dependant on processing atmosphere, temperature, composition and the initial Ca precursor, as shown in Figures 1 and 2. Samples sintered at lower temperatures were found to form a greater amount of the perovskite phase than those reacted at higher temperatures. It is believed that this is due to the refractory nature of zirconium (IV) oxide, with higher reaction temperatures providing more favourable kinetics. Increasing the waste loading was found to result in increased formation of perovskite and retention of zirconium oxide. It can be seen in Figures 1 and 2 that the calcium precursor also affects the final phase assemblage. Using CaTiO<sub>3</sub> as the precursor was found to result in increased formation of the target zirconolite phase however, this influence was less strong at higher synthesis temperatures. The improvement of zirconolite yield when using CaTiO<sub>3</sub> may indicate that zirconolite formation proceeds *via* the formation of a CaTiO<sub>3</sub> intermediate and subsequent diffusion of ZrO<sub>2</sub>, a similar phenomenon was observed by Gilbert (2014) for zirconolites formed using molten salt synthesis [24]. The processing atmosphere was found to have a similar influence to Ca precursor; at lower synthesis temperatures, sintering under a reducing atmosphere (5 % H<sub>2</sub>/N<sub>2</sub>), produced a greater proportion of zirconolite than sintering in an inert atmosphere (Ar). At higher temperatures this trend was found to reverse and sintering under an inert atmosphere produced a more

favourable phase assemblage than sintering in a reducing atmosphere. Stennett et al (2017) found that it was possible to synthesise single phase molybdenum-doped zirconolites ( $\text{CaZrTi}_{2-x}\text{Mo}_x\text{O}_7$ ,  $x = 0.0 - 0.4$ ) by sintering at a temperature of 1400 °C, however, the proposed mechanism of eventual Mo incorporation was *via* a  $\text{CaMoO}_4$  intermediate, of which there was no evidence found by XRD in the current study [25]. Considering the absence of XRD reflections indicative of the 4M polytype, it was concluded that the zirconolite produced was of the 2M polytype, this was confirmed by TEM.

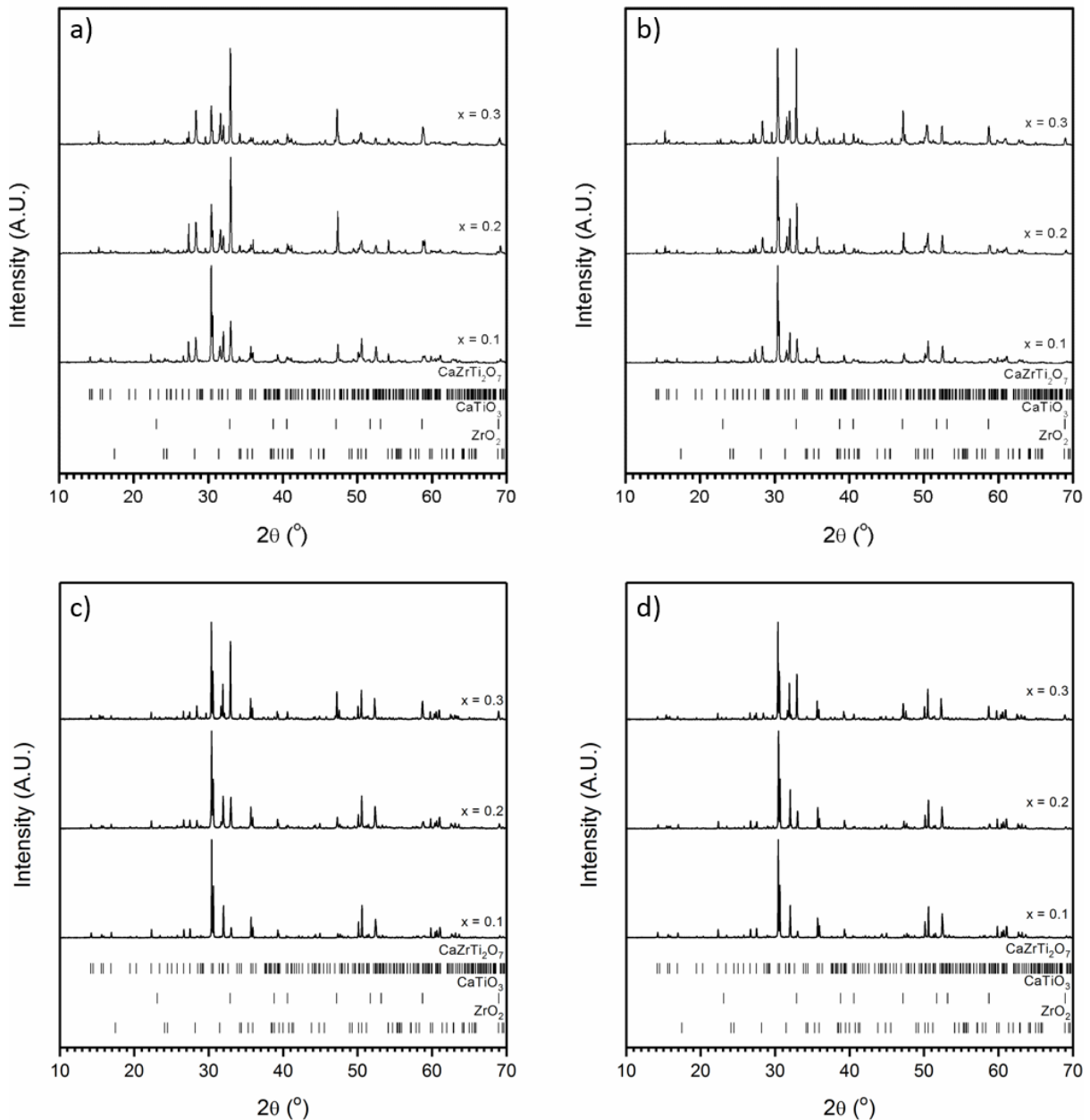


**Figure 1:** The effect of temperature, composition and Ca precursor on the formation of  $\text{Ca}_{1-x/2}\text{Zr}_{1-x/2}\text{Ce}_x\text{Ti}_{2-x}\text{Mo}_x\text{O}_7$  zirconolites ( $x = 0.1, 0.2$  and  $0.3$ ) in an argon atmosphere. a) 1200 °C,  $\text{CaCO}_3$ ; b) 1200 °C,  $\text{CaTiO}_3$ ; c) 1400 °C,  $\text{CaCO}_3$  and d) 1400 °C,  $\text{CaTiO}_3$ .

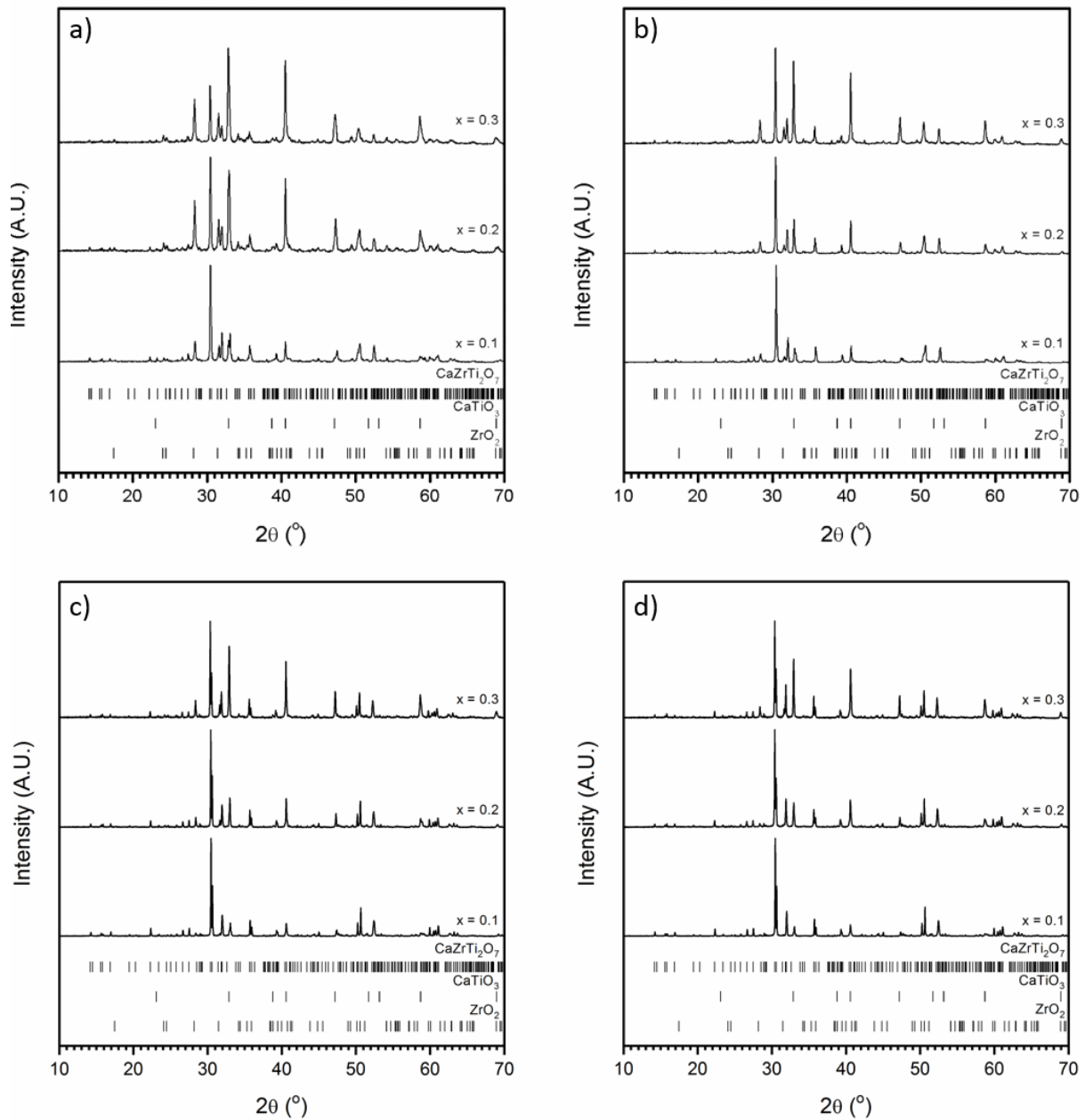


**Figure 2:** The effect of temperature, composition and Ca precursor on the formation of  $\text{Ca}_{1-x/2}\text{Zr}_{1-x/2}\text{Ce}_x\text{Ti}_{2-x}\text{Mo}_x\text{O}_7$  zirconolites ( $x = 0.1, 0.2$  and  $0.3$ ) in a 5 %  $\text{H}_2/\text{N}_2$  atmosphere. a) 1200 °C,  $\text{CaCO}_3$ ; b) 1200 °C,  $\text{CaTiO}_3$ ; c) 1400 °C,  $\text{CaCO}_3$  and d) 1400 °C,  $\text{CaTiO}_3$ .

SEM analysis of the synthesised zirconolites found that the heat treated pellets were poorly sintered, see Figure 3. Zirconolite was observed throughout the samples with regions of  $\text{CaTiO}_3$  and  $\text{ZrO}_2$  in agreement with XRD. Notably, although not evident in the XRD results, Mo metal was observed distributed throughout samples. Mo-free zirconolites processed under comparable conditions (16hr in Ar) by Vance et al (2002) [4] produced more dense material and, it is therefore hypothesised that the relatively poor sintering observed in this study is a result of Mo volatilisation.

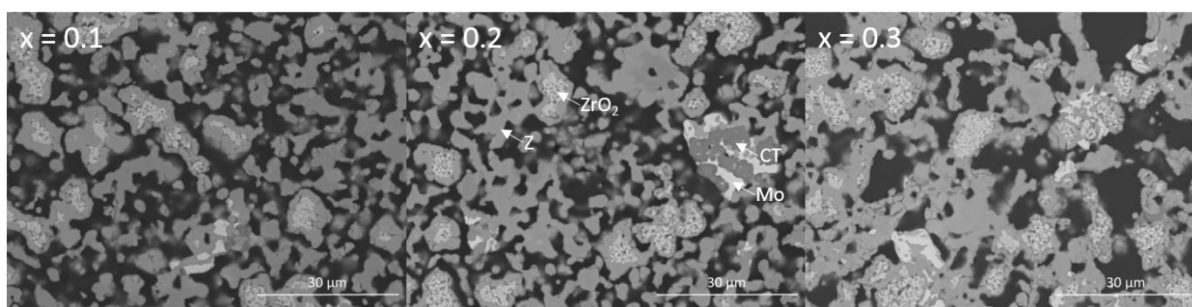


**Figure 3:** Representative electron micrographs of  $\text{Ca}_{1-x/2}\text{Zr}_{1-x/2}\text{Ce}_x\text{Ti}_{2-x}\text{Mo}_x\text{O}_7$  zirconolites sintered at 1200 °C for 12 hours in argon ( $x = 0.1, 0.2$  and  $0.3$ ). Z = zirconolite, Mo = Molybdenum metal and CT =  $\text{CaTiO}_3$ .

The results of thermogravimetric analysis of zirconolites during synthesis in an Ar atmosphere are summarised in **Table 1**. The large initial mass loss observed in  $\text{CaCO}_3$  containing precursors ( $T \leq 950$  °C) was attributed to the decomposition of the carbonate and release of  $\text{CO}_2$ . Increasing substitution of  $\text{CeO}_2$  for  $\text{CaCO}_3$  and  $\text{ZrO}_2$  was found to result in decreased weight loss and is therefore consistent with decomposition of  $\text{CaCO}_3$ , see Table 1. A second weight loss event was evident at temperatures  $> 950$  °C; this weight loss increased progressively with increasing substitution of Ce and Mo and is believed to be as a result of the volatilisation of Mo. Repetition of these analyses using zirconolite precursors that replaced  $\text{CaCO}_3$  with  $\text{CaTiO}_3$  found that, as expected, mass loss was greatly reduced by eliminating the thermal decomposition of  $\text{CaCO}_3$ . It was also found that the use of  $\text{CaTiO}_3$  precursors resulted in an decrease in the mass loss observed during the high temperature phase of the heat treatment ( $T > 950$  °C).

**Table 1:** Mass losses during thermogravimetric analysis of  $\text{Ca}_{1-x/2}\text{Zr}_{1-x/2}\text{Ce}_x\text{Ti}_{2-x}\text{Mo}_x\text{O}_7$  zirconolites (% ,  $\pm 0.005$  %).

x	Ca precursor	Mass loss 1 (< 950 °C)	Mass loss 2 (> 950 °C)
0.1	$\text{CaCO}_3$	10.67	0.34
0.2	$\text{CaCO}_3$	9.20	0.54
0.3	$\text{CaCO}_3$	8.10	0.64
0.1	$\text{CaTiO}_3$	0.43	0.03
0.2	$\text{CaTiO}_3$	0.61	0.10
0.3	$\text{CaTiO}_3$	0.70	0.11

### *Hot uniaxially pressed zirconolites*

To resolve the issue of Mo volatility, a suite of samples were hot isostatically pressed (HIPed). During HIPing, the samples were hermetically sealed within stainless steel tubing, thus eliminating the problem of Mo volatility. Figure 4 shows the resultant powder X-ray diffraction profiles of HIPed zirconolites and Figure 5 shows representative micrographs of their microstructures. The observed phase assemblages were highly similar to that of cold

uniaxially pressed samples (CUPed), with increasing waste loading resulting in increased formation of the parasitic  $\text{CaTiO}_3$  phase. Considering the results observed for CUPed zirconolites, an increased processing temperature would likely result in reduced production of the perovskite phase and increased formation of zirconolite, this would require processing in an alternative can material to the 316 stainless steel used e.g. Ni. The resultant consolidated zirconolites showed markedly less porosity and improved sintering compared to those produced by cold pressing and sintering, as can be seen in Figure 5.

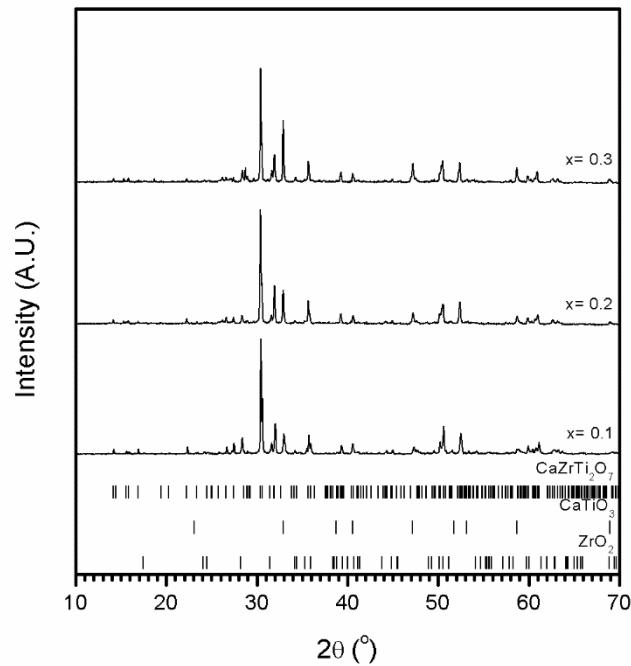


**Figure 4:** X-ray diffraction profiles of HIPed  $\text{Ca}_{1-x/2}\text{Zr}_{1-x/2}\text{Ce}_x\text{Ti}_{2-x}\text{Mo}_x\text{O}_7$  zirconolites ( $x = 0.1$ ,  $0.2$  and  $0.3$ ).  $\text{CaZrTi}_2\text{O}_7$ -ICSD 72888,  $\text{CaTiO}_3$ - ICSD 94568 and  $\text{ZrO}_2$ - ICSD 41572.

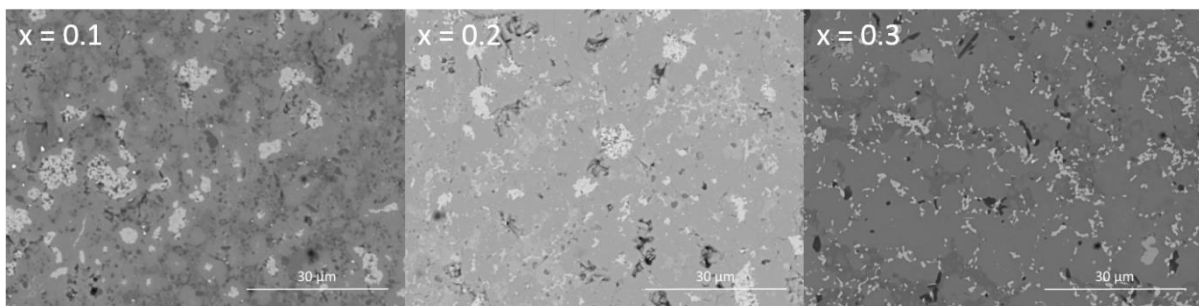


**Figure 5:** Representative backscattered electron micrographs of HIPed zirconolite formulations.

Study of elemental distribution by SEM-EDX (Figure 6 and Table 2 and 3) confirmed the formation of the  $\text{CaTiO}_3$  phase and retention of  $\text{ZrO}_2$ . It was found that Mo was incorporated in the zirconolite and perovskite phases and was also present throughout the sample as metallic Mo inclusions (as shown by the high Z contrast). The presence of reduced, metallic Mo is similar to observations from previous studies of Tc incorporation into Synroc and rutile [26], [27]. Ce was incorporated into the target zirconolite phase and the secondary perovskite phase

as can be seen in Tables 2 and 3. The partitioning of Ce to the perovskite phase could prove problematic in a final Pu wastefrom as, despite its relatively high tolerance to  $\alpha$ -recoil damage, perovskite has proven to be less durable than other host phases, i.e. zirconolite. This highlights the importance of the control of crystal chemistry. It is hypothesised that the apparent excess of positive charge in both the zirconolite and perovskite phases is offset by either the presence of cation vacancies, as suggested by Begg et al (1998) [28], or the reduction of Ce, Mo or Ti.

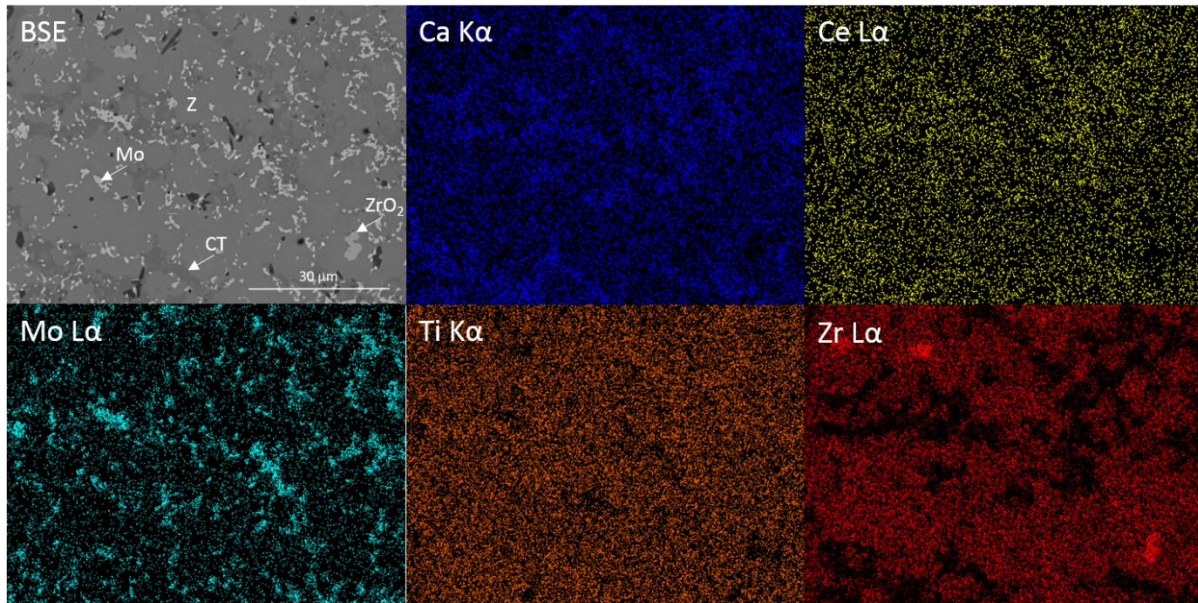


**Figure 6:** Elemental partitioning of HIPed  $(Ca_{0.85}Ce_{0.15})(Zr_{0.85}Ce_{0.15})Ti_{1.7}Mo_{0.3}O_7$  zirconolite. Z = zirconolite, Mo = Molybdenum metal and CT =  $CaTiO_3$ .

**Table 2:** Comparison of nominal composition and determined average composition synthesised by hot isostatic pressing.

Nominal composition	EDX composition
$(Ca_{0.95}Ce_{0.05})(Zr_{0.95}Ce_{0.05})Ti_{1.9}Mo_{0.1}O_7$	$Ca_{0.98\pm 0.08}Zr_{0.89\pm 0.26}Ce_{0.05\pm 0.02}Ti_{1.95\pm 0.18}Mo_{0.05\pm 0.02}O_7$
$(Ca_{0.9}Ce_{0.1})(Zr_{0.9}Ce_{0.1})Ti_{1.8}Mo_{0.2}O_7$	$Ca_{1.02\pm 0.09}Zr_{1.06\pm 0.12}Ce_{0.08\pm 0.02}Ti_{1.92\pm 0.12}Mo_{0.08\pm 0.04}O_7$
$(Ca_{0.85}Ce_{0.15})(Zr_{0.85}Ce_{0.15})Ti_{1.7}Mo_{0.3}O_7$	$Ca_{1.03\pm 0.07}Zr_{1.12\pm 0.13}Ce_{0.18\pm 0.06}Ti_{1.85\pm 0.18}Mo_{0.15\pm 0.03}O_7$

**Table 3:** Determined average composition of perovskite phase in hot isostatically pressed  $Ca_{1-x/2}Zr_{1-x/2}Ce_xTi_{2-x}Mo_xO_7$  zirconolites.

x	EDX composition
0.1	$Ca_{0.61\pm 0.03}Zr_{0.09\pm 0.01}Ce_{0.04\pm 0.01}Mo_{0.03\pm 0.01}Ti_{1.00\pm 0.03}O_3$
0.2	$Ca_{0.67\pm 0.02}Zr_{0.1\pm 0.01}Ce_{0.17\pm 0.02}Mo_{0.05\pm 0.01}Ti_{1.00\pm 0.03}O_3$
0.3	$Ca_{0.62\pm 0.03}Zr_{0.08\pm 0.01}Ce_{0.21\pm 0.01}Mo_{0.04\pm 0.01}Ti_{1.00\pm 0.05}O_3$

### *Transmission electron microscopy (TEM)*

Electron diffraction patterns of synthesised zirconolites were acquired to confirm the zirconolite polytype formed. In agreement with XRD results, electron diffraction patterns were found to index to the zirconolite 2M structure. The formation of the 4M polytype was not evident at the levels of substitution studied in this investigation. It remains possible that increased substitution on the A-site would lead to a change in symmetry, as observed by Vance *et al* (2002)[4].

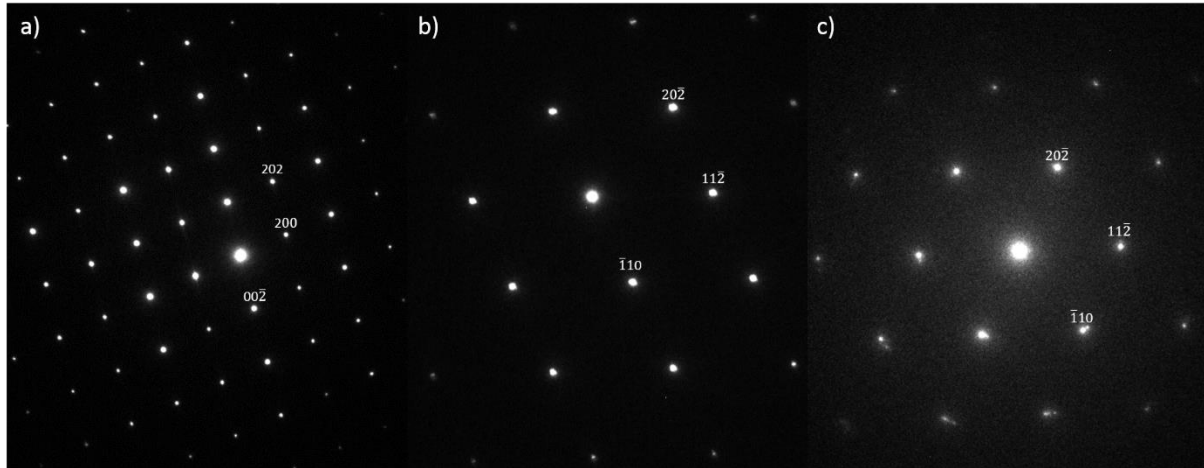


**Figure 7:** Zone axis electron diffraction patterns of  $(\text{Ca}_{0.9}\text{Ce}_{0.1})(\text{Zr}_{0.9}\text{Ce}_{0.1})\text{Ti}_{1.8}\text{Mo}_{0.2}\text{O}_7$  synthesised under different processing conditions: a) HIP [010], b) Argon atmosphere [111] and c) 5 %  $\text{H}_2/\text{N}_2$  atmosphere [111]. Indexed in the C12/c1 space group.

### *X-ray absorption spectroscopy (XAS)*

Mo compounds exhibit a pre-edge feature  $\sim 20\text{-}30$  eV before the main absorption edge. The pre-edge feature is related electronic transitions from 1s to 4d states for Mo in addition to quadrupolar 1s to 4d and dipolar 1s to 2p transitions to Mo or O nearest neighbours. The intensity of the pre-edge feature increases as the 4d states become emptier hence the pre-edge feature is especially intense for Mo (VI) compounds when Mo is in a non-centrosymmetric site. The pre-edges of Mo (IV) or Mo (V) compounds are difficult to resolve and often appear as a shoulder on the main absorption edge [23]. The edge position itself has been shown to follow a linear trend with the oxidation state of Mo by Farges *et al* [23]. Mo speciation was determined by XAS and linear regression with respect to standards, see Figure 8 and 9. Results are summarised in Table 4.

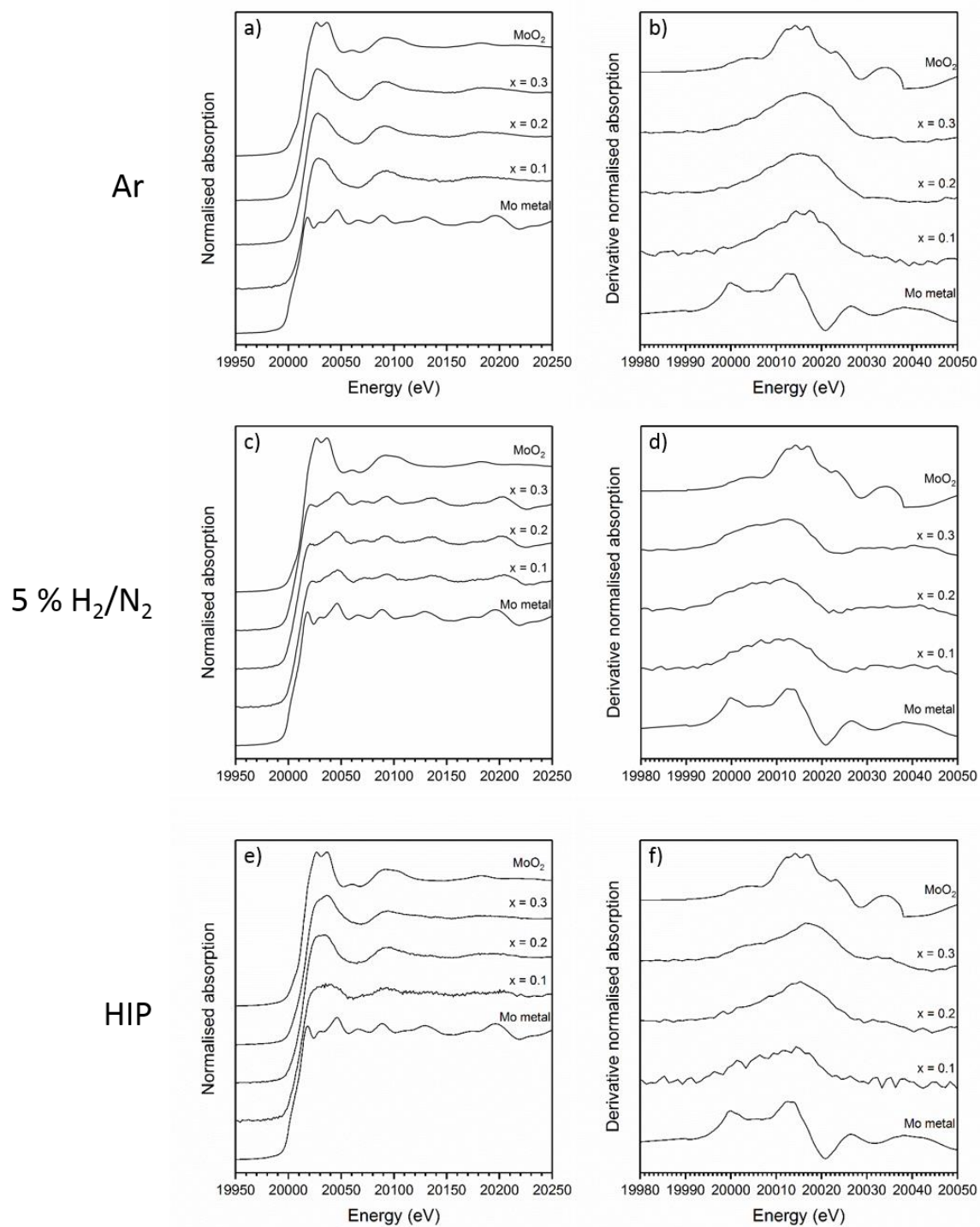


**Figure 8:** Mo K-edge XANES and derivative XANES of  $\text{Ca}_{1-x/2}\text{Zr}_{1-x/2}\text{Ce}_x\text{Ti}_{2-x}\text{Mo}_x\text{O}_7$  zirconolites synthesised in Ar and 5 %  $\text{H}_2/\text{N}_2$  atmospheres or consolidated by HIP: a) Ar XANES; b) Ar derivative XANES; c) 5%  $\text{H}_2/\text{N}_2$  XANES; d) 5 %  $\text{H}_2/\text{N}_2$  derivative XANES; e) HIP XANES and f) HIP derivative XANES.

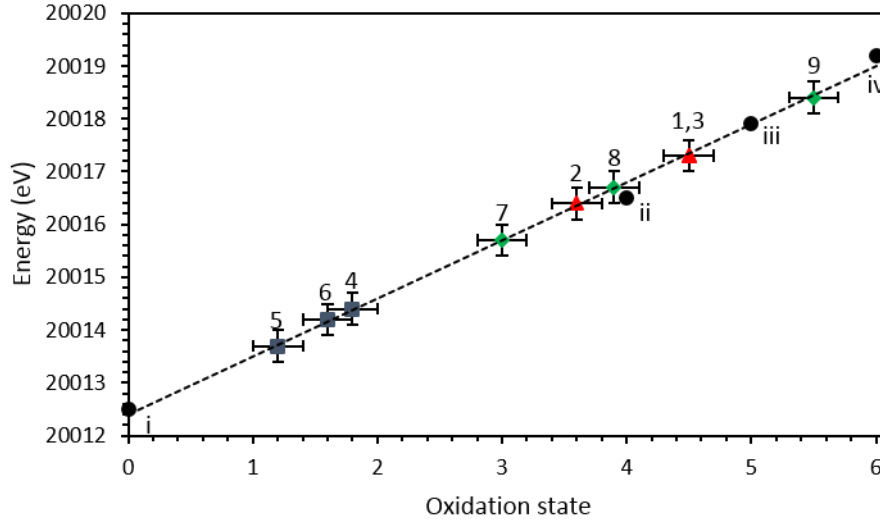


**Figure 9:** Linear regression of Mo K edge  $E_0$  values with respect to Mo standards. Black circles denote standards: i) Mo metal, ii)  $\text{MoO}_2$ , iii)  $\text{Sr}_2\text{HoMoO}_6$  and iv)  $\text{MoO}_3$ . Red triangles denote samples sintered in argon, blue squares denote samples sintered in 5 %  $\text{H}_2/\text{N}_2$  and green diamonds denote samples consolidated by HIP. Numbers refer to corresponding Sample no. in Table 5.

**Table 4:** Average Mo oxidation state of synthesised zirconolites as determined by linear regression with respect to standards.

Sample no.	Nominal composition	Atmosphere	$E_0$ (eV, $\pm 0.3$ )	Mean OS ( $\pm 0.2$ )
1	$(\text{Ca}_{0.95}\text{Ce}_{0.05})(\text{Zr}_{0.95}\text{Ce}_{0.05})\text{Ti}_{1.9}\text{Mo}_{0.1}\text{O}_7$	Ar	20017.3	4.5
2	$(\text{Ca}_{0.9}\text{Ce}_{0.1})(\text{Zr}_{0.9}\text{Ce}_{0.1})\text{Ti}_{1.8}\text{Mo}_{0.2}\text{O}_7$	Ar	20016.4	3.6
3	$(\text{Ca}_{0.85}\text{Ce}_{0.15})(\text{Zr}_{0.85}\text{Ce}_{0.15})\text{Ti}_{1.7}\text{Mo}_{0.3}\text{O}_7$	Ar	20017.3	4.5
4	$(\text{Ca}_{0.95}\text{Ce}_{0.05})(\text{Zr}_{0.95}\text{Ce}_{0.05})\text{Ti}_{1.9}\text{Mo}_{0.1}\text{O}_7$	5 % $\text{H}_2/\text{N}_2$	20014.4	1.8
5	$(\text{Ca}_{0.9}\text{Ce}_{0.1})(\text{Zr}_{0.9}\text{Ce}_{0.1})\text{Ti}_{1.8}\text{Mo}_{0.2}\text{O}_7$	5 % $\text{H}_2/\text{N}_2$	20013.7	1.2
6	$(\text{Ca}_{0.85}\text{Ce}_{0.15})(\text{Zr}_{0.85}\text{Ce}_{0.15})\text{Ti}_{1.7}\text{Mo}_{0.3}\text{O}_7$	5 % $\text{H}_2/\text{N}_2$	20014.2	1.6
7	$(\text{Ca}_{0.95}\text{Ce}_{0.05})(\text{Zr}_{0.95}\text{Ce}_{0.05})\text{Ti}_{1.9}\text{Mo}_{0.1}\text{O}_7$	HIP	20015.7	3
8	$(\text{Ca}_{0.9}\text{Ce}_{0.1})(\text{Zr}_{0.9}\text{Ce}_{0.1})\text{Ti}_{1.8}\text{Mo}_{0.2}\text{O}_7$	HIP	20016.7	3.9
9	$(\text{Ca}_{0.85}\text{Ce}_{0.15})(\text{Zr}_{0.85}\text{Ce}_{0.15})\text{Ti}_{1.7}\text{Mo}_{0.3}\text{O}_7$	HIP	20018.4	5.5

Processing conditions were found to have a strong influence on Mo speciation. As can be seen in Figure 8, samples sintered in Ar were found to have edge positions and post-edge oscillations typical of Mo (IV) whereas samples sintered in 5%  $\text{H}_2/\text{N}_2$  were found to be more typical of Mo metal. Samples prepared by HIP were found to have edge positions and post-edge features that indicated a mixture of metallic Mo and Mo (IV) however, with increasing substitution of Mo for Ti, it was noted that the edge position progressively shifted to higher energies. This may be attributable to the incorporation and stabilisation of higher Mo oxidation states in the

perovskite phase [29], the proportion of which also increases with increasing Mo substitution as shown in Figure 4. Although Mo was added as Mo (IV) it is possible that the Mo was oxidised by redox coupling with either Ce ( $\text{Ce (IV)} + \text{Mo (IV)} \rightarrow \text{Ce (III)} + \text{Mo (V/VI)}$ ), Ti ( $\text{Ti (IV)} + \text{Mo (IV)} \rightarrow \text{Ti (III)} + \text{Mo (V/VI)}$ ) or a combination of the two. The absence of a strong pre-edge feature in the measured spectra indicates that any Mo incorporated is unlikely to be Mo (VI) and more likely Mo (IV/V).

## Conclusions

Target zirconolite compositions were synthesised under Ar, 5%  $\text{H}_2/\text{N}_2$  and also by hot isostatic pressing. Zirconolite was formed in all cases with accompanying secondary phases. Zirconolite yield was found to be affected by processing atmosphere, temperature, total substitution of Mo and Ce and the initial Ca precursor used. Using  $\text{CaTiO}_3$  as the Ca precursor was found to improve the final phase assemblage and reduce the weight loss due to Mo volatilisation. Achieving dense materials by traditional CUPing methods proved difficult as high temperature treatment exacerbated the problems of Mo volatilisation but sintering at lower temperatures was found to result in greatly decreased yields of zirconolites. HIPing was found to produce the most dense material and, with optimisation of the can material and redox conditions, would provide the best route for the co-immobilisation of Tc and Pu in a zirconolite matrix. Ce was observed in both the target zirconolite phase and secondary perovskite phase highlighting the importance of achieving the full reaction of precursors and the elimination of secondary phases. The partitioning behaviour of Mo was found to vary with processing atmosphere. When processed under Ar, Mo was found to remain in the Mo (IV) oxidation state and was partitioned to the zirconolite phase. Processing under 5%  $\text{H}_2/\text{N}_2$  was found to result in Mo being reduced to Mo metal and encapsulated. Hot isostatic pressing of zirconolite batches yielded a mixture Mo metal, Mo (IV) and higher Mo oxidation states. It is hypothesised that the higher Mo oxidation states are stabilised by incorporation into the secondary perovskite phase.

## Acknowledgements

DJB and SML are funded by the Engineering, Physical Sciences Research Council *via* the Nuclear FiRST Doctoral Training Centre. NCH is grateful to the Royal Academy of Engineering and Nuclear Decommissioning Authority for funding. This research was performed in part at the MIDAS Facility, at the University of Sheffield, which was established with support from the Department of Energy and Climate Change.

## References

- [1] N. C. Hyatt, "Plutonium management policy in the United Kingdom: The need for a dual track strategy," *Energy Policy*, vol. 101, pp. 303-309, 2017.
- [2] I. W. Donald, *Waste immobilization in glass and ceramic based hosts*. Chichester: John Wiley & Sons, Ltd., 2010.
- [3] E. R. Vance, C. J. Ball, R. A. Day, K. L. Smith, M. G. Blackford, and P. J. Angel, "Actinide and rare earth incorporation into zirconolite," *J. Alloys Compd.*, vol. 214, pp. 406–409, 1994.

- [4] E. R. Vance, G. R. Lumpkin, M. L. Carter, D. J. Cassidy, C. J. Ball, R. A. Day, and B. D. Begg, "Incorporation of Uranium in Zirconolite ( $\text{CaZrTi}_2\text{O}_7$ )," *J. Am. Ceram. Soc.*, vol. 59, no. 187500, pp. 1853–1859, 2002.
- [5] W. J. Weber, R. C. Ewing, C. R. A. Catlow, T. Diaz de la Rubia, L. W. Hobbs, C. Kinoshita, H. Matzke, A. T. Motta, M. Nastasi, E. K. H. Salje, E. R. Vance, and S. J. Zinkle, "Radiation effects in crystalline ceramics for the immobilization of high-level nuclear waste and plutonium," *J. Mater. Res.*, vol. 13, no. 6, pp. 1434–1484, 1998.
- [6] E. R. Vance, C. J. Ball, M. G. Blackford, D. J. Cassidy, and K. L. Smith, "Crystallisation of zirconolite from an alkoxide precursor," *J. Nucl. Mater.*, vol. 175, no. 1–2, pp. 58–66, 1990.
- [7] A. E. Ringwood, S. E. Kesson, N. G. Ware, W. Hibberson, and A. Major, "Immobilisation of high level nuclear reactor wastes in SYNROC," *Nature*, vol. 278, no. 5701, pp. 219–223, Mar. 1979.
- [8] A. E. Ringwood, K. D. Reeve, D. M. Levins, and E. J. Ramm, "Synroc," in *Radioactive Waste Forms for the Future*, R. C. Ewing and W. Lutze, Eds. New York: North Holland Physics Publishing, 1988, pp. 233–335.
- [9] T. J. White, "The microstructure and microchemistry of synthetic zirconolite, zirkelite and related phases," *Am. Mineral.*, vol. 69, pp. 1156–1172, 1984.
- [10] T. J. White, R. L. Segall, J. L. Hutchinson, and J. C. Barry, "Polytypic behaviour of zirconolite," *Proceeds R. Soc. London A*, no. 392, pp. 343–358, 1984.
- [11] R. Giere and P. Stille, Eds., *Energy, waste and the environment: a geochemical perspective*. London: Geological Society.
- [12] P. Bayliss, F. Mazzi, R. Munno, and T. J. White, "Mineral nomenclature : zirconolite," *Mineral. Mag.*, vol. 53, no. December, pp. 565–569, 1989.
- [13] B. D. Begg, E. R. Vance, and S. D. Conradson, "The incorporation of plutonium and neptunium in zirconolite and perovskite," *J. Alloys Compd.*, vol. 271–273, pp. 221–226, 1998.
- [14] F. Mazzi and R. Munno, "Calciobetafite (new mineral of the pyrochlore group) and related minerals from Campi Flegrei, Italy: crystal structures of polymignyte and zirkelite: comparison with pyrochlore and zirconolite.," *Am. Mineral.*, vol. 68, no. 1–2, pp. 262–276, 1983.
- [15] G. R. Lumpkin, K. L. Smith, M. G. Blackford, R. Giere, and C. Terry Williams, "Determination of 25 elements in the complex oxide mineral zirconolite by analytical electron microscopy," *Micron*, vol. 25, no. 6, pp. 581–587, 1994.
- [16] S. A. Luksic, B. J. Riley, M. Schweiger, and P. Hrma, "Incorporating technetium in minerals and other solids: A review," *J. Nucl. Mater.*, vol. 466, pp. 526–538, 2015.
- [17] R. D. Shannon, "Revised Effective Ionic Radii and Systematic Studies of Interatomic Distances in Halides and Chalcogenides," *Acta Crystallogr.*, vol. 32, pp. 751–767, 1976.
- [18] T. Hartmann, A. J. Alaniz, and D. J. Antonio, "Fabrication and Properties of Technetium-bearing Pyrochlores and Perovskites as Potential Waste Forms," *Procedia Chem.*, vol. 7, pp. 622–628, 2012.

- [19] O. Muller, "Crystal Chemistry of Some Technetium-Containing Oxides," *J. Inorg. Nucl. Chem.*, vol. 26, no. 1962, pp. 2075–2086, 1964.
- [20] H. Konishi, A. Yokoya, H. Shiwaku, H. Motohashi, T. Makita, Y. Kashihara, S. Hashimoto, T. Harami, H. Maeta, H. Maezawa, S. Asaoka, N. Kanaya, K. Ito, N. Usami, and K. Kobayashi, "Synchrotron radiation beamline to study radioactive Photon Factory materials at the," *Nucl. Instruments Methods Phys. Res. A*, vol. 372, pp. 322–332, 1996.
- [21] B. Ravel and M. Newville, "ATHENA, ARTEMIS, HEPHAESTUS: Data analysis for X-ray absorption spectroscopy using IFEFFIT," in *Journal of Synchrotron Radiation*, 2005, vol. 12, no. 4, pp. 537–541.
- [22] B. Ravel and M. Newville, "ATHENA and ARTEMIS Interactive Graphical Data Analysis using IFEFFIT," *Phys. Scr.*, p. 1007, 2005.
- [23] F. Farges, R. Siewert, G. E. J. Brown, and A. Guesdon, "Structural Environments Around Molybdenum in Silicate Glasses and Melts. I. Influence of Composition and Oxygen Fugacity On the Local Structure of Molybdenum," *Can. Mineral.*, vol. 44, pp. 731–753, 2006.
- [24] M. R. Gilbert, "Molten Salt Synthesis of Zirconolite Polytypes," *Mater. Res. Soc. Symp. Proc.*, vol. 1665, pp. 325–330, 2014.
- [25] M. C. Stennett, T. Lee, D. J. Bailey, E. V. Johnstone, J. Heo, and N. C. Hyatt, "Ceramic Immobilization Options for Technetium," *MRS Adv.*, pp. 7–12, 2017.
- [26] K. P. Hart, E. R. Vance, R. A. Day, B. D. Begg, P. J. Angel, and A. Jostons, "Immobilization of separated Tc and Cs/Sr in Synroc," *Mater. Res. Soc. Symp. Proc.*, vol. 412, pp. 281–287, 1996.
- [27] E. R. Vance, K. P. Hart, M. L. Carter, M. J. Hambley, R. A. Day, and B. D. Begg, "Further studies of Synroc immobilisation of HLW sludges and Tc for Hanford tank waste remediation," *Mater. Res. Soc. Symp. Proc.*, vol. 506, pp. 289–293, 1998.
- [28] B. D. Begg, E. R. Vance, and G. R. Lumpkin, "Charge Compensation and the Incorporation of Cerium in Zirconolite and Perovskite," *Mater. Res. Soc. Symp. Proc.*, vol. 506, pp. 79–86, 1998.
- [29] A. F. Fuentes, M. Garza-García, J. I. Escalante-García, G. Mendoza-Suárez, K. Boulahya, and U. Amador, "Synthesis and structural characterization of  $\text{Ba}(\text{Ln}_{2/3}^{\text{III}}\text{B}_{1/3}^{\text{VI}})\text{O}_3$  ( $\text{Ln}^{\text{III}} = \text{Dy}, \text{Gd}$  and  $\text{Sm}$ ;  $\text{B}^{\text{VI}} = \text{Mo}$  or  $\text{W}$ ) complex perovskites," *J. Solid State Chem.*, vol. 175, no. 2, pp. 299–305, 2003.

**8. A Synchrotron X-ray Spectroscopy  
Study of Titanium Co-ordination in  
Explosive Melt Glass Derived From the  
Trinity Nuclear Test**

# A Synchrotron X-ray Spectroscopy Study of Titanium Co-ordination in Explosive Melt Glass Derived From the Trinity Nuclear Test

D.J. Bailey<sup>a,\*</sup>, M.C. Stennett<sup>a</sup>, B. Ravel<sup>b</sup>, D.E. Crean<sup>a</sup> and N.C. Hyatt<sup>a</sup>

Received 16th January 2017,  
Accepted 00th January 20xx

DOI: 10.1039/x0xx00000x

[www.rsc.org/](http://www.rsc.org/)

The speciation of Ti in trinitite, the explosive melt glass derived from the Trinity Test of 16<sup>th</sup> of July 1945, was investigated by X-ray absorption spectroscopy (XAS). Ti K-edge XANES showed that Ti was present in the Ti (IV) oxidation state for all samples. Fitting of pre-edge features by Gaussian functions and comparison with standards of known Ti coordination revealed significant variation in Ti coordination environment between samples. The variation of Ti coordination may be attributed to several factors including specific local chemistry and thermal histories of samples, in keeping with the highly heterogeneous microstructure of trinitite and the arkosic sand source material.

## 1.0 Introduction

Trinitite is an explosive melt glass derived from the Trinity Test that took place on the 16<sup>th</sup> of July, 1945 at the White Sands Missile Range, New Mexico. The Trinity Test was the first detonation of a nuclear weapon and utilised a plutonium core and an implosion mechanism to achieve criticality.

The extreme heat generated by the resultant explosion (estimated average  $T = 8,430$  K, estimated extreme  $T = 3 \times 10^7$  K<sup>1,2</sup>) melted or vapourised the vicinal desert sand and support structures. Rapid heating and cooling by afterwinds (estimated fireball duration  $\sim 3.1$  s<sup>-1</sup>) resulted in the formation of a glassy product. The dominant morphology of trinitite specimens is 1–3 cm thick, green, glassy fragments with a smooth upper surface and a rough undulating lower surface.

Although predominantly green, high concentrations of elements, such as copper and iron, can change the colour of trinitite, resulting in 'red' and 'black' trinitite respectively. The majority of trinitite composition is drawn from minerals in the surrounding desert sand including: quartz (SiO<sub>2</sub>), microcline (KAlSi<sub>3</sub>O<sub>8</sub>), albite (NaAlSi<sub>3</sub>O<sub>8</sub>), muscovite ((KF)<sub>2</sub>(Al<sub>2</sub>O<sub>3</sub>)<sub>3</sub>(SiO<sub>2</sub>)<sub>6</sub>(H<sub>2</sub>O)), actinolite (Ca<sub>2</sub>(Mg,Fe)<sub>5</sub>Si<sub>8</sub>O<sub>22</sub>(OH)<sub>2</sub>) and calcite (CaCO<sub>3</sub>)<sup>3</sup>. The inclusion of minority minerals such as titaniferous magnetite, rutile and barite has also been reported<sup>4,5</sup>.

The speciation and coordination of titanium in silicate melts has been found to be affected by the thermal history of the melt as well as other factors including composition and pressure during melting. Previous studies have used X-ray absorption

spectroscopy (XAS) to determine the speciation of Fe in trinitite<sup>6</sup>. This study presents the novel speciation of Ti in trinitite as determined by XAS.

## 2.0 Materials and Methods

### 2.1 Trinitite samples and preparation

Trinitite specimens were supplied by the Mineral Research Company (one large 12 g piece and several small  $\sim 1$ g fragments) and the US Army (small  $\sim 0.25$ g fragments recovered from a sand grab sample obtained from the Trinity Test Site on the White Sands Missile Range)<sup>5</sup>. The trinitite fragments had a variety of morphologies, but were consistent in appearance to previously studied examples<sup>1,3,4</sup>. Also consistent with previously studied samples, numerous vesicles are observed from gas bubbles present in the melt.

Samples were prepared for bulk XAS by powdering aliquots from six small fragments. The powders were homogeneously mixed with polyethylene glycol and pressed to form 13 mm diameter pellets. The thin section sample was prepared from the large trinitite specimen by sectioning and polishing to a  $\sim 30$   $\mu$ m thickness. The specimen was sectioned vertically to preserve the smooth top and rough bottom of the sample in cross section, and was mounted in cold setting resin on a Spectrasil (Triad Scientific) fused quartz slide.

The average composition of the desert sand and trinitite was found by dissolving 0.5 g aliquots of representative material in hydrofluoric acid and then quantifying the constituents by inductively coupled plasma mass spectrometry (ICP-MS). The compositions quoted are limited to components with abundance  $\geq 0.01$  wt%.

Elemental distribution within trinitite samples were studied by SEM-EDX using a Hitachi TM3030 electron microscope and equipped with a Bruker Quantax EDX detector. EDX data were analysed using Bruker Quantax software. Samples were

<sup>a</sup> Immobilisation Science Laboratory, Department of Materials Science and Engineering, University of Sheffield, United Kingdom.  
E-mail: [d.j.bailey@sheffield.ac.uk](mailto:d.j.bailey@sheffield.ac.uk)

<sup>b</sup> National Institute of Standards and Technology, 100 Bureau Drive, Gaithersburg MD 20899, USA.

prepared for SEM analysis by mounting in cold setting resin and polishing to an optical finish (1  $\mu\text{m}$ ) using SiC paper and progressively finer diamond pastes. Samples were sputter coated with carbon to reduce surface charging effects.

Gamma spectroscopy was used to characterise radionuclides contained within the remaining trinitite fragment samples using a Canberra BEGe detector. Spectra were gathered for 12 hours and the energy resolution of the detector was  $\pm 0.15$  keV.

## 2.2 XAS Measurements

Samples were measured at the Ti K-edge using a conventional XAS setup at beamline X23A2, of the now decommissioned National Synchrotron Light Source, Brookhaven National Laboratory. Transmission mode measurements of the prepared samples were made alongside Ti standards ( $\text{TiO}$ ,  $\text{Ti}_2\text{O}_3$ ,  $\text{TiO}_2$  and  $\text{CaTiO}_3$ ). Incident ( $I_0$ ) and transmitted ( $I_t$ ) X-ray intensities were measured using ion chambers, energy calibration was performed with respect to XAS spectra measured with a reference ion chamber ( $I_r$ ) of a Ti foil placed after the transmission ion chamber in the beam path. Two different regions of the same thin section were measured in fluorescence mode. Fluorescence mode measurements were made using a four element Si drift detector. XAS spectra were measured from 30 eV below the Ti K-edge to 250 eV above, using a Si (311) monochromator. Data reduction and XANES analysis were performed using the program Athena<sup>7,8</sup>.

Fits to Ti pre-edge data of trinitite samples and standards were performed in the energy range 4965–4975 eV (0.3 eV energy resolution) to derive average oxidation state and co-ordination environment information<sup>9</sup>. The XANES spectra were fitted following the method proposed by Waychunas, such fitting permitting direct comparison with other data gathered in previous studies regarding Ti co-ordination in minerals and glass melts<sup>9–14</sup>. Data were normalised to a unit edge step using the Athena software package<sup>7</sup>, and the rising edge background was fit using an arctangent function over the energy range 4960–5040 eV, as described previously<sup>15</sup>. Gaussian components were then fit to the data to describe the components of the pre-edge features. The height and position of the weighted mean centroids of the functions were taken to be representative of the pre-edge feature.

## 3.0 Results and Discussion

The composition of trinitite samples and desert sand, as found by ICP-MS, are shown in Table 1. As can be understood from Table 1, trinitite is primarily an alkali / alkaline earth aluminosilicate glass with considerable FeO and  $\text{TiO}_2$  additions. The ratio of non-bridging oxygens to tetrahedrally coordinated cations, NBO/T<sup>16</sup>, is indicative of the connectivity of the glass network; a high NBO/T value would indicate a highly modified glass network with lower connectivity. Although there is not gross compositional variation between the two trinitite samples, a notable difference in NBO/T, calculated using Equation 1, was observed between the two trinitite samples.

**Table 1:** Composition of trinitite and desert sand wt% by oxide (estimated error in initial measurement  $\pm 2\%$ ). Fe is known to be in the  $\text{Fe}^{2+}$  oxidation state. Results are restricted to major elements (0.01 wt%), full ICP-MS results are available in the supplementary material.

Oxide	Desert Sand	Sample 1	Sample 2
$\text{SiO}_2$	71.33	69.99	70.54
$\text{Al}_2\text{O}_3$	10.24	12.13	10.06
$\text{CaO}$	7.58	7.04	8.16
$\text{K}_2\text{O}$	6.86	3.89	4.19
$\text{FeO}$	0.7	2.72	2.87
$\text{Na}_2\text{O}$	2.62	2.12	2.03
$\text{MgO}$	0.22	1.15	1.11
$\text{TiO}_2$	0.04	0.49	0.5
$\text{BaO}$	0.09	0.08	0.08
$\text{ZrO}_2$	0.10	0.08	0.14
$\text{P}_2\text{O}_5$	0.08	0.15	0.13
$\text{MnO}$	0.02	0.06	0.07
$\text{SrO}$	0.03	0.03	0.04
$\text{PbO}$	0.02	0.00	0.01
$\text{CeO}_2$	0.03	0.01	0.01
$\text{SO}_4$	0.02	0.01	0.01
$\text{V}_2\text{O}_5$	0.00	0.01	0.01
$\text{Cr}_2\text{O}_3$	0.00	0.01	0.01
Other	0.02	0.03	0.03
Total	100.00	100.00	100.00
NBO/T	N/A	0.22	0.29

$$\text{Equation 1} \quad \text{NBO/T} = \frac{(2(\text{RO} + \text{R}_2\text{O}) - 2\text{R}_2\text{O}_3)}{\text{RO}_2 + 2\text{R}_2\text{O}_3}$$

Radionuclides contained within the trinitites were characterised by gamma spectroscopy. The resultant spectrum is shown in Figure 1. As can be seen, the trinitite samples clearly contain

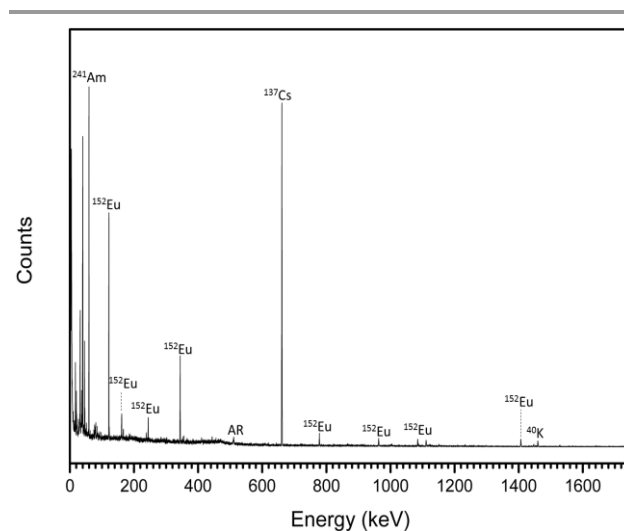


**Figure 1:** Gamma spectrum of representative trinitite fragments. AR = annihilation radiation caused by interaction of positrons and electrons ( $E = 511$  keV).

$^{241}\text{Am}$ ,  $^{137}\text{Cs}$  and  $^{152}\text{Eu}$  indicating that the samples are the result of the detonation of a Pu-based fission device <sup>17</sup>.

Previous studies have shown that trinitite is chemically inhomogeneous and actually comprises several glasses of varying composition and grains of unmelted, shock amorphised minerals <sup>5,18,19</sup>. The results of SEM-EDX analysis of a representative sample are shown in Figures 2 and 3 (Further EDX maps and spectra are available in the supplementary material). As can be seen, elemental distribution varies across the sample with several distinct glasses: a high silica glass, an

aluminium rich glass, a calcium rich glass and an alkali / alkaline earth aluminosilicate glass. Ti is present throughout the sample and, as evident in Figure 2, local chemistry varies significantly. Spot EDX analysis (see Figure 3) confirmed the variation in local chemistry as observed in Figure 2. Point 1 is evidently a region highly enriched in Ti relative to the rest of the glass and Point 2 is likely a grain of melted quartz. Points 3, 4, 5 and 6 are more

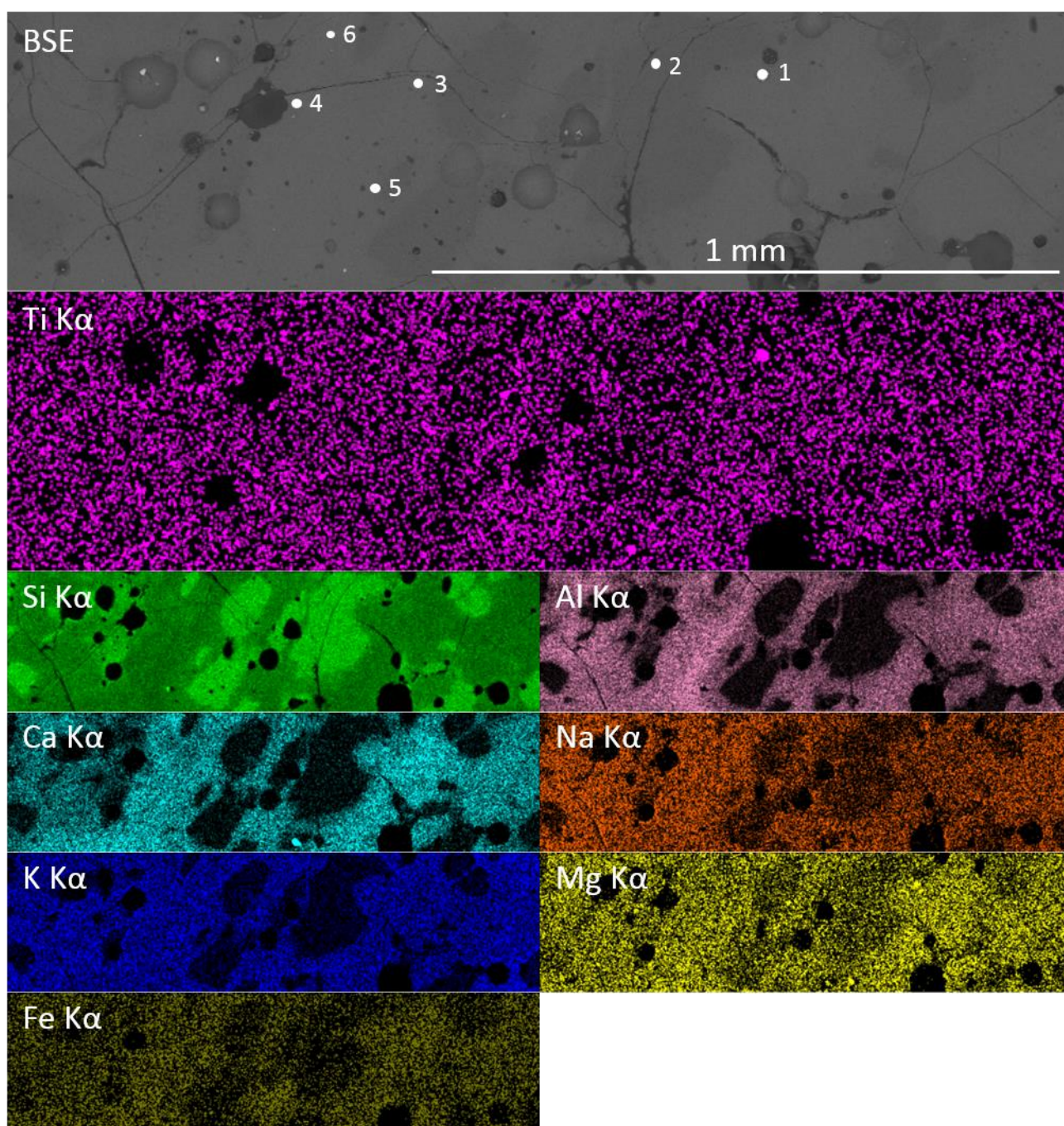


Figure 2: Elemental distribution within a representative sample of trinitite as determined by SEM-EDX.

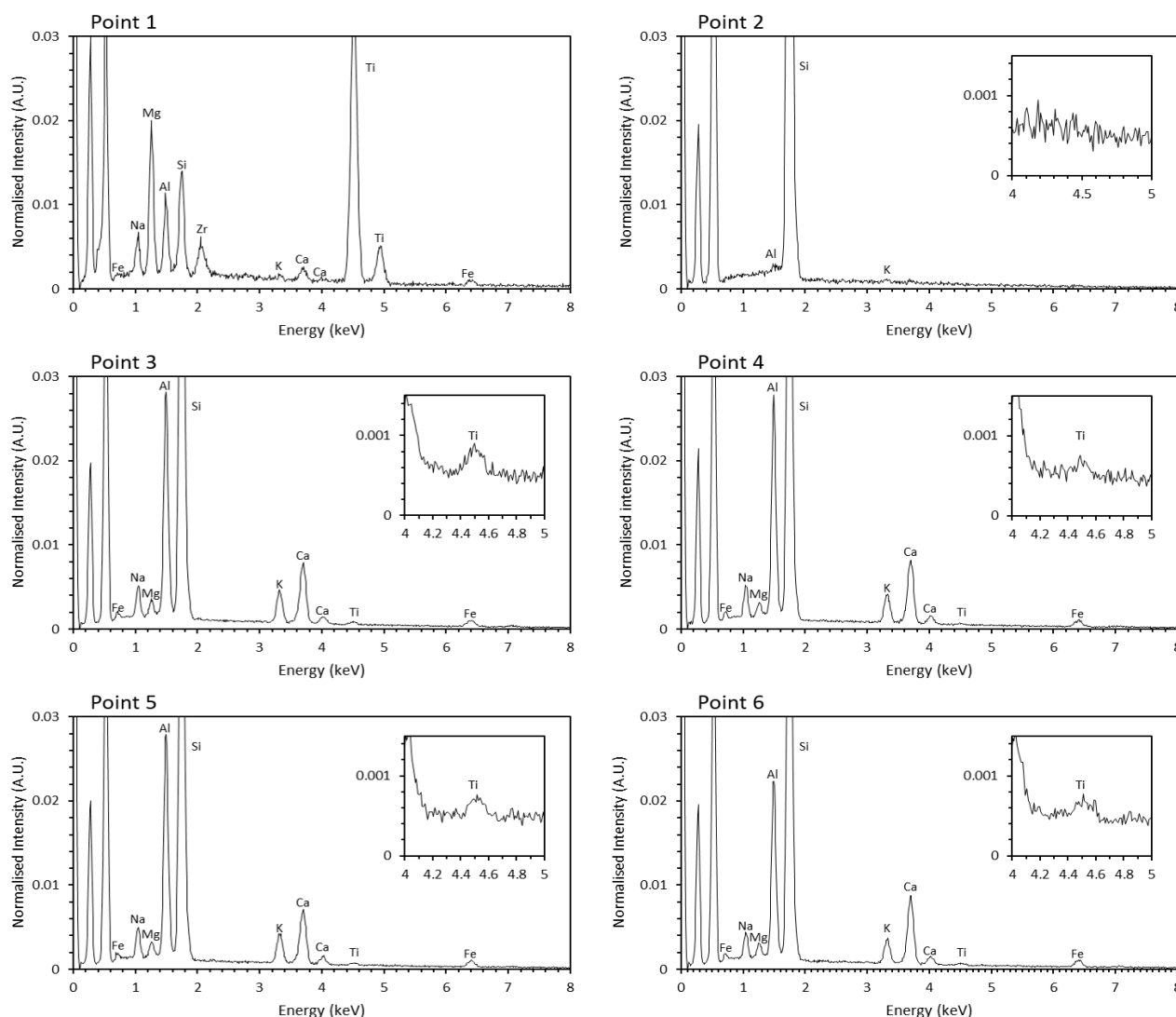


Figure 3: Point EDX spectra of locations denoted in Figure 2. Inset, magnified Ti section of the spectra.

similar in their composition however, it is apparent that there is local variation; for example, Point 6 is clearly enriched in Ca compared to Points 3, 4 and 5. Local chemistry has previously been shown to affect the co-ordination of Ti in silicate melts and it is therefore possible to conclude that it is likely that Ti exists in several different co-ordination environments throughout the measured samples<sup>20</sup>.

Figure 4a shows the measured XANES spectra of the trinitite, desert sand samples and standards (TiO, Ti<sub>2</sub>O<sub>3</sub> and CaTiO<sub>3</sub>). Figure 3b shows a detailed view of the pre-edge region of the XANES spectra in Figure 3a.

Ti K-edge XANES data show that the predominant oxidation state of Ti in all samples is Ti (IV), average for Ti (IV) standards  $E_0 = 4984.1 \pm 0.3$  eV, desert sand  $E_0 = 4984.3 \pm 0.3$  eV and average trinitite  $E_0 = 4983.0$  eV  $\pm 0.3$  eV (standard deviation = 0.4). This indicates that the oxidation state of Ti remains unchanged relative to that in the geological source material and is

insensitive to the blast conditions. The trinitite samples, desert sand and the reference standards exhibit a distinct pre-edge feature at  $\sim 18 \pm 3$  eV before the edge step<sup>11</sup>. The pre-edge feature is attributed to transitions from Ti 1s to bound Ti 3d/O 2p molecular orbitals. A 1s to 3d transition is forbidden due to dipole selection rules ( $\Delta l = \pm 1$ ) however, this rule is relaxed when Ti is located in a non-centrosymmetric co-ordination environment and p-d mixing occurs<sup>9</sup>. Waychunas and Farges have both demonstrated that the pre-edge position and intensity are a direct function of p-d mixing and consequently indicative of the Ti co-ordination environment<sup>9,11</sup>. As can be seen from Figure 4b, there is significant variation in the position and height of the pre-edge features indicating the existence of differing Ti co-ordination environments. Damping of the post-edge XANES features in the trinitite samples studied (see Figure 4a) is a result of random phase decoherence and multiple

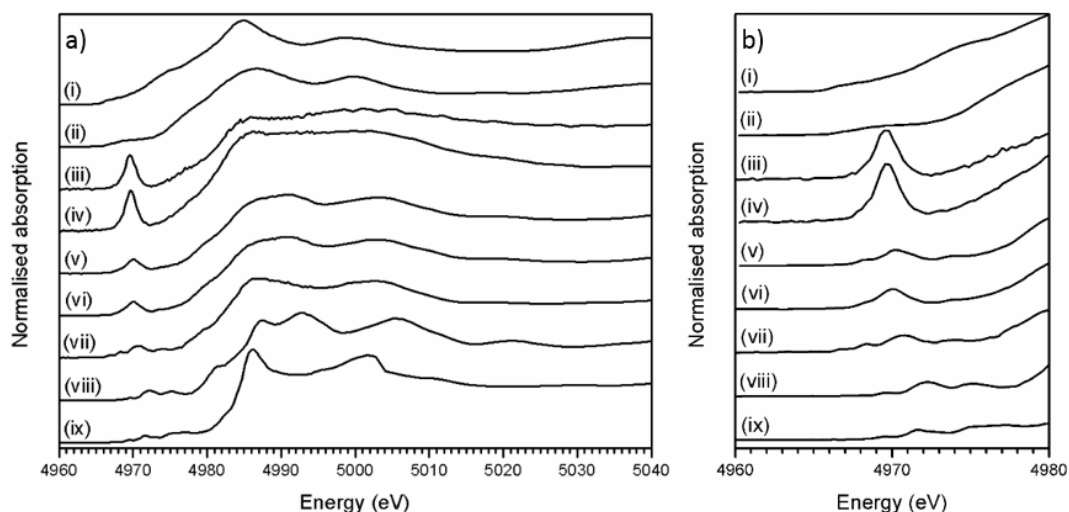


**Figure 4:** (a) Ti K-edge XANES spectra of trinitite samples, sand and standards; (b) detail of pre-edge XANES features. TiO (i), Ti<sub>2</sub>O<sub>3</sub> (ii), Thin Section 1 (iii), Bulk Sample 1 (iv), Thin Section 2 (v), Bulk Sample 2 (vi), Desert Sand (vii), TiO<sub>2</sub> (viii) and CaTiO<sub>3</sub> (ix). Note the shift in pre-edge feature position for trinitite samples relative to the TiO<sub>2</sub> and CaTiO<sub>3</sub> standards. Thin Section 1 and Thin Section 2 are different regions of the same thin section sample (Thin Section 1 is ~14.7 mm closer to the top edge of the sample).

scattering paths and is symptomatic of atomic disorder, typical of glasses.

The measured XANES spectra were fitted according to the method used by Waychunas<sup>9</sup>. Gaussian functions were fitted to the pre-edge envelope and the height and position of the weighted mean centroids of these functions were taken to represent the overall height and energy of the pre-edge feature. Fitted values are given in Table 2, an example fit is shown in Figure 5.

Figure 6 shows the correlation of pre-edge height and energy with co-ordination environment of Ti bearing standards (solid diamonds) and that of tektites (solid triangles) as reported by Farges et al<sup>10,14</sup> together with data from the current study (open circles). Distinct zones exist for 4, 5 and 6- fold Ti co-ordination with adjacent regions assigned from analysis of mechanical mixture of titanium compounds with Ti in different site geometries i.e. a mixture of 4 and 6-fold co-ordination<sup>10</sup>.

The determined pre-edge height and energy of Ti in CaTiO<sub>3</sub> (4,971.6 eV, 0.11) is identical to that reported in previous investigations (4,971.6 eV, 0.11; Point 7, Figure 6), it was therefore concluded that the measured data were consistent with the literature and it was possible to compare our data with that of previously reported standards measured using

comparable X-ray optics<sup>11</sup>. As can be seen in Figure 5, the Trinitite samples have a range of average Ti co-ordination environments.

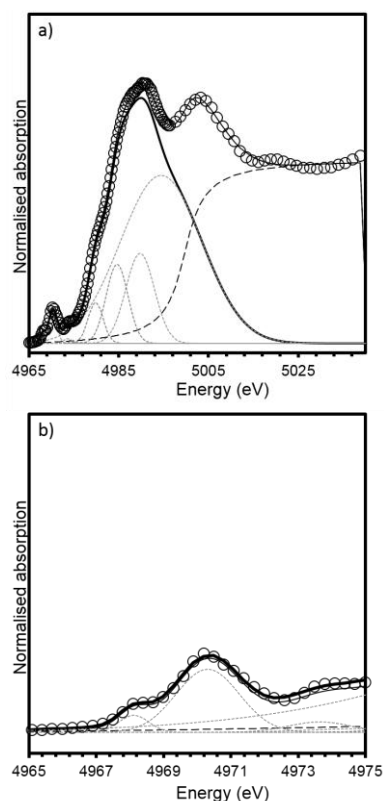


**Figure 5:** Fitting of XANES features for bulk trinitite sample measured in fluorescence mode, using a combination of Gaussian and arctangent functions (grey lines); data are shown by open symbols, fit is shown by a solid black line; methodology follows that of Waychunas<sup>9</sup>.

**Table 2:** Normalised pre-edge height and energies of fitted Ti XANES spectra

Sample	Energy (eV)	Normalised Pre-edge height
Thin Section 1	4969.6	0.56
Bulk Sample 1	4969.6	0.58
Thin Section 2	4970.2	0.21
Bulk Sample 2	4970.5	0.17
Desert Sand	4971.1	0.18
TiO <sub>2</sub>	4971.5	0.11
CaTiO <sub>3</sub>	4971.6	0.11
Precision	± 0.3	± 0.03

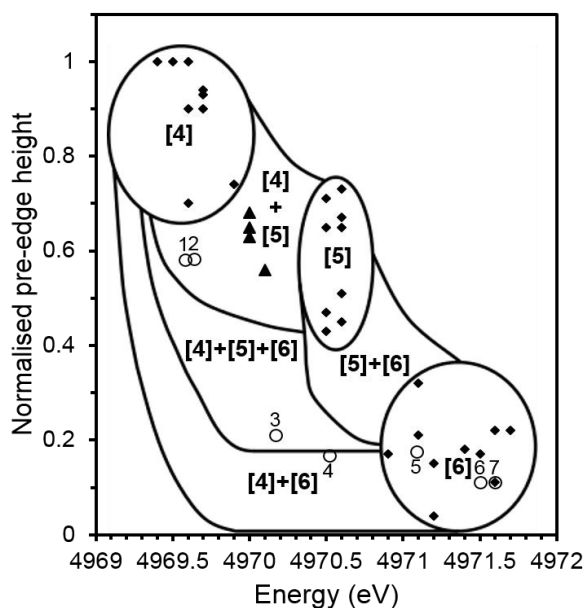


**Figure 6:** Ti co-ordination environment as speculated by pre-edge energy position and normalised height of pre-edge feature in Ti K edge XANES. Solid squares show data for mineral standards from previous studies<sup>11</sup>; solid triangles show data for tektites from previous studies<sup>14</sup> and open circles show data from this study for: Thin Section 1 (1), Bulk Sample 1 (2), Thin Section 2 (3), Bulk Sample 2 (4), Desert Sand (5), TiO<sub>2</sub> (6) and CaTiO<sub>3</sub> (7). Adapted from Farges (1997)<sup>14</sup>.

Thin Section 1 and Bulk Sample 1 (data points 1 and 2, respectively) lie within the region associated with mixed four and five-fold co-ordinate Ti. Thin Section 2 (data point 3) lies in the region associated with mixed four, five and six-fold co-ordination, Bulk Sample 2 (data point 4) contains a mixture of four and six-fold Ti. The sand sample (data point 5) is located within the six-fold co-ordinated region indicating that the average co-ordination of Ti before the blast was six-fold, consistent with the reported presence of rutile [5], [6].

The region occupied by Thin Section 1 and Bulk Sample 1 is also that occupied by the tektites studied by Farges et al.<sup>14</sup> Tektites are natural glasses formed by the impact of extra-terrestrial bodies and the melting of vicinal materials and it has previously been observed that trinitite is similar in morphology to some tektites<sup>21</sup>. A study of natural glasses and tektites by Farges et al (1997) found that the dominant co-ordination environment of Ti is five-fold in silicate melts, however, there is a significant amount of four-fold Ti in the most polymerised systems such as rhyolitic glasses and tektites. The co-ordination environment of Ti has been found to be strongly dependent on the ratio of Ti to non-bonding oxygens with glasses of lower ratios, such as tektites (NBO/T = 0.08-0.13), yielding more four and five-fold Ti<sup>14</sup>. This would suggest that the trinitite of Thin Section 1 and Bulk Sample 1 is more highly polymerised than the trinitite of Thin Section 2 and Bulk Sample 2. This possibility is supported by the observed variation of NBO/T between the trinitite samples studied by ICP-MS, as shown in Table 1.

Ti coordination in synthetic, natural and impact glasses is known to be influenced by glass composition, pressure and the rate at which the glass is cooled<sup>13,20,22</sup>. The chemical inhomogeneity of trinitite may explain the observed variation in Ti coordination. Trinitite composition is drawn from a range of

minerals including alkali and alkaline earth bearing feldspars and, due to insufficient equilibration time, there is significant variation in the concentrations of these elements within specimens<sup>5,18</sup>. Dingwell et al found that Ti in alkaline earth bearing silicates had a higher average coordination number than Ti in alkali silicates<sup>20</sup>. SEM-EDX analysis (see Figure 2) has shown that local chemistry varies significantly across trinitite samples and, consequently, it is possible that Thin Section 2 and Bulk Sample 2 may contain a higher relative concentration of alkaline earth cations and hence have Ti in a higher average coordination number. High pressure has also been found to increase the coordination of Ti in melts<sup>22</sup>, possibly indicating variation in pressure conditions during trinitite formation. Additionally, Ti coordination may be affected by the cooling rate from the melt temperature to ambient temperature<sup>13</sup>. Comparisons of quenched and unquenched melts found that observed pre-edge height was greater in quenched samples, indicating retention of a greater degree of four-fold Ti. The higher normalised height and lower energy position of the pre-edge features of Bulk Sample 1 relative to Bulk Sample 2 may show that it was cooled more rapidly and retained a greater proportion of four-fold Ti. Another possibility that may explain the variation observed between the bulk samples is that Bulk Sample 2 was under greater pressure than Bulk Sample 1 at the time of formation and as result formed a greater degree of six-fold coordinated Ti. Cooling rate considerations were found to not apply to the two thin section measurements. Figure 6 shows the pre-edge feature associated with the location of Thin Section 1 (within the thin section specimen interior) is consistent with a lower average Ti co-ordination number compared to the pre edge feature corresponding to location of Thin Section 2 (near the upper surface of the thin section specimen interior). If this Trinitite were formed in a single major deposition event, the exterior would be expected to have cooled more rapidly due to afterwinds that followed the blast, resulting in a lower average co-ordination number for Ti at the surface, compared to the interior. Depletion of alkalis from the surface, by volatilisation, would result in a lower NBO/T ratio, and a lower average Ti co-ordination number relative to the interior. This is contrary to our observation, but could be rationalised by the local variation in chemical composition being of crucial importance, or a hybrid formation mechanism in which the quench rate of the surface-formed material exceeded that of the precipitated material. Further multi-element micro-focus XAS and XRF studies of this material would assist in understanding the spatial variation in Ti speciation as a function of the local chemical composition.

#### 4.0 Conclusions

The speciation of Ti in trinitite was investigated by X-ray absorption spectroscopy. Ti was consistently present in the Ti (IV) oxidation state however, the coordination environment was found to be inhomogeneous. The variation in Ti coordination could be as a result of numerous factors with variations in local chemistry, network polymerisation and thermal history all possible contributors. The variation

observed in this study is reflective of the diverse source material and extreme formation conditions of trinitite and serves to highlight the highly heterogeneous nature of melt material produced by nuclear weapons tests. Nevertheless, further micro-focus XAS and XRF studies of Trinitites, linking element speciation to spatial disposition and local chemistry, may shed further light on the formation mechanism of this fascinating material.

## Acknowledgements

UK EPSRC is thanked for providing studentship for DJB and DEC through the Nuclear FIRST Doctoral Training Centre (Grant EP/G037140/1). Use of the National Synchrotron Light Source, Brookhaven National Laboratory, was supported by the U.S. Department of Energy, Office of Science, Office of Basic Energy Sciences, under Contract No. DE-AC02-98CH10886. NCH is grateful to the Royal Academy of Engineering and Nuclear Decommissioning Authority for funding. This research was performed in part at the MIDAS Facility, at the University of Sheffield, which was established with support from the Department of Energy and Climate Change. We are grateful to the Public Affairs Office of the White Sands Missile Range for provision of a sand grab sample from the Trinity Test Site. We thank Michelle Higgins of the Open University for preparation of the thin section specimen and Neil Bramall of the University of Sheffield for ICP-MS analyses. The contribution of DEC to this study was undertaken in partial fulfilment of the requirements of Doctor of Philosophy in 2013.

## Notes and references

§The Trinity Test Site was declared a national historic landmark in 1975 and it is illegal to remove material from this location. The sand grab sample used in this study was kindly provided by the Public Affairs Office of the White Sands Missile Range

- 1 R. E. Hermes and W. B. Strickfaden, *Nucl. Weapons J.*, 2005, **2**, 2–7.
- 2 F. Belloni, J. Himbert, O. Marzocchi and V. Romanello, *J. Environ. Radioact.*, 2011, **102**, 852–862.
- 3 N. Eby, R. Hermes, N. Charnley and J. Smoliga, *Geol. Today*, 2010, **26**, 180–185.
- 4 A. J. Fahey, C. J. Zeissler, D. E. Newbury, J. Davis and R. M. Lindstrom, *Proc. Natl. Acad. Sci. U. S. A.*, 2010, **107**, 20207–12.
- 5 G. N. Eby, N. Charnley, D. Pirrie, R. Hermes, J. Smoliga and G. Rollinson, *Am. Mineral.*, 2015, **100**, 427–441.
- 6 G. Giuli, G. Pratesi, S. G. Eeckhout, C. Koeberl and E. Paris, in *Large Meteorite Impacts and Planetary Evolution IV: Geological Society of America Special Paper 465*, eds. R. L. Gibson and W. U. Reimold, 2010, pp. 653–660.
- 7 B. Ravel and M. Newville, *Phys. Scr.*, 2005, 1007.
- 8 B. Ravel and M. Newville, in *Journal of Synchrotron Radiation*, 2005, vol. 12, pp. 537–541.
- 9 G. A. Waychunas, *Am. Mineral.*, 1987, **72**, 89–101.
- 10 F. Farges, *Am. Mineral.*, 1997, **82**, 36–43.
- 11 F. Farges, G. E. Brown and J. J. Rehr, *Geochim. Cosmochim. Acta*, 1996, **60**, 3023–3038.
- 12 F. Farges, G. E. Brown, A. Navrotsky, H. Gan and J. J. Rehr, *Geochim. Cosmochim. Acta*, 1996, **60**, 3039–3053.
- 13 F. Farges, G. E. Brown, A. Navrotsky, H. Gan and J. R. Rehr, *Geochim. Cosmochim. Acta*, 1996, **60**, 3055–3065.
- 14 F. Farges and G. E. Brown, *Geochim. Cosmochim. Acta*, 1997, **61**, 1863–1870.
- 15 D. P. Reid, M. C. Stennett, B. Ravel, J. C. Woicik, N. Peng, E. R. Maddrell and N. C. Hyatt, *Nucl. Instruments Methods Phys. Res. Sect. B Beam Interact. with Mater. Atoms*, 2010, **268**, 1847–1852.
- 16 S. Amma, M. T. Lanagan, S. H. Kim and C. G. Pantano, *J. Am. Ceram. Soc.*, 2016, **99**, 1239–1247.
- 17 P. P. Parekh, T. M. Semkow, M. a. Torres, D. K. Haines, J. M. Cooper, P. M. Rosenberg and M. E. Kitto, *J. Environ. Radioact.*, 2006, **85**, 103–120.
- 18 E. Staritzky, *Thermal effects of atomic bomb explosions on soils at Trinity and Eniwetok*, 1950.
- 19 C. Ross, *Am. Mineral.*, 1948, 360–362.
- 20 D. B. Dingwell, E. Paris, F. Seifert, A. Mottana and C. Romano, *Phys. Chem. Miner.*, 1994, **21**, 501–509.
- 21 T. E. Bunch, R. E. Hermes, a. M. T. Moore, D. J. Kennett, J. C. Weaver, J. H. Wittke, P. S. DeCarli, J. L. Bischoff, G. C. Hillman, G. a. Howard, D. R. Kimbel, G. Kletetschka, C. P. Lipo, S. Sakai, Z. Revay, a. West, R. B. Firestone and J. P. Kennett, *Proc. Natl. Acad. Sci.*, 2012, **109**, E1903–E1912.
- 22 E. Paris, D. B. Dingwell, F. A. Seifert, A. Mottana and C. Romano, *Phys. Chem. Miner.*, 1994, **21**, 510–515.

## 9. Summary

This chapter will summarise and discuss the main findings of the work produced in the course of this thesis.

### **9.1. Chapter 4: Synthesis and characterisation of the hollandite solid solution $\text{Ba}_{1.2-x}\text{Cs}_x\text{Fe}_{2.4-x}\text{Ti}_{5.6+x}\text{O}_{16}$ for partitioning and conditioning of radiocaesium**

This chapter investigated the potential use of hollandite ceramics for the immobilisation of separated caesium. Although archetypal SYNROC hollandite contains Al on the B-site, this study investigated the potential use of Fe as the B-site species and the effect of Cs-loading on the structural environment of Fe in the hollandite structure. Samples were characterized by XRD, SEM-EDX, XRF, Mössbauer spectroscopy and XAS.

Analysis of synthesised samples found that the addition of increasing amounts of caesium resulted in the transformation of the hollandite unit cell from the monoclinic form to a tetragonal unit cell. Increasing the substitution was observed to result in the expansion of the unit cell as determined by Le Bail refinement of XRD data. XRF analysis of sintered samples found that, although Cs content increased, the amount of Cs present in the final sample was lower than the target stoichiometry; this was attributed to volatilisation of Cs during high temperature synthesis. The volatilisation of Cs was also found to affect the microstructure of synthesised samples; extensive porosity was observed throughout samples. The oxidation state and local co-ordination chemistry of Fe were studied by both XAS and Mössbauer spectroscopy. Fe was determined to be in the Fe (III) oxidation state and in six-fold coordination in all samples and it was therefore concluded that the Cs-loading had no effect on the oxidation state and coordination of Fe.

This work has demonstrated that it is possible to produce hollandite wastefoms for the immobilisation of separated Cs using iron as a B-site species. The use of only Fe and Ti as B-site species is novel and comparable waste loading to previous studies has been achieved. These wastefoms could be applied to Cs separated from HLW raffinate using the FPEX or CCD processes.

Future work on this system, and other hollandite systems, should focus on improving the synthesis of the target hollandite phase, specifically minimising the volatilisation of caesium during synthesis. Improving the retention of caesium during synthesis will allow an effective solid solution limit of Cs in the  $\text{Ba}_{1.2-x}\text{Cs}_x\text{Fe}_{2.4-x}\text{Ti}_{5.6+x}\text{O}_{16}$  system to be determined thereby giving an upper bound to the possible waste loading in a Fe hollandite wastefrom. This could possibly be achieved *via* the use of hot isostatic pressing to eliminate volatilisation however, it is worth noting that any reduction of Fe by can materials, e.g. steel, may affect the charge balance mechanism of the system. In order for these hollandites to be considered as a wastefrom, their dissolution performance must either be comparable or superior to that of current HLW glasses/SYNROC, it would therefore be prudent to investigate the durability of these materials using standard tests to allow comparison e.g. PCT-B and MCC-1.

## **9.2. Chapter 5: An investigation of iodovanadinite wastefroms for the immobilisation of radio-iodine and technetium**

This chapter investigated the potential use of iodovanadinite ceramics for the immobilisation of iodine. This study investigated both the sole immobilisation of iodine and the co-immobilisation of iodine and technetium. Mo was used as a structural surrogate of Tc. Samples were synthesised by HIP and characterized using XRD, SEM-EDX and TGA-MS. The effect if overpressure during HIPing was also investigated

The main finding of this investigation was that the choice of iodine precursor is highly important. When  $\text{PbI}_2$  was used as a precursor it was found that it was possible to form the target iodovanadinite phase. Substituting  $\text{AgI}$  for  $\text{PbI}_2$  was found to have a negative effect on the observed phase assemblage.  $\text{AgI}$  did not react and form the target phase; it was instead found to melt and sit between grains of the other materials in the batch. As two out of three sections of this study used  $\text{AgI}$  as a major iodine source it was not possible to meet the initial aims of the study. Despite these problems this study did find that it was possible to synthesise iodovanadinite directly from the constituent iodide and oxide precursors by hot isostatic pressing and that increased overpressure during HIPing yielded more dense products. It was also observed that a solid solution exists between  $\text{Ba}_3(\text{VO}_4)_2$  and  $\text{Pb}_3(\text{VO}_4)_2$ .

This work has found a novel synthesis route for processing iodovanadinite wasteforms. The ability to synthesise and consolidate iodovanadinite from precursors in a single step offers the potential for significant cost savings. The issue of iodine precursor has also highlighted that any immobilisation of Ag-based iodine scrubbing materials would require an additional processing step to convert AgI to a more suitable form. These wasteforms may be applied to future fuel cycles wherein dilution and dispersal of radioiodine is forbidden.

Future experiments should attempt the synthesis of the original target phases using an iodine source other than AgI e.g.  $\text{PbI}_2$ . The solid solution of  $\text{Ba}_3(\text{VO}_4)_2$ - $\text{Pb}_3(\text{VO}_4)_2$  should also be investigated further to determine if a solid solution limit exists between the two and whether these compounds possess any properties that may be exploited.

### **9.3. Chapter 6: Synthesis and characterisation of brannerite compositions $(\text{U}_{0.9}\text{Ce}_{0.1})_{1-x}\text{M}_x\text{Ti}_2\text{O}_6$ ( $\text{M} = \text{Gd}^{3+}, \text{Ca}^{2+}$ ) for the immobilisation of MOX residues**

This chapter describes the formulation and characterisation of novel brannerite compositions for the disposal of mixed oxide fuel residues. The study used the archetypal brannerite stoichiometry,  $\text{UTi}_2\text{O}_6$ , as a starting point and adjusted it to contain 10 % substitution of Pu for U (Ce was used as a structural surrogate) along with varying substitution of neutron absorbing and charge balancing species (Ca and Gd). Samples were produced by traditional solid state synthesis and characterised by XRD, SEM-EDX, bulk XANES and micro-focus XANES.

Both the processing atmosphere and target stoichiometry were found to affect the final phase assemblage. Processing samples in air was found to result in the formation of brannerite along with rutile and  $\text{U}_3\text{O}_8$ ; the proportion of brannerite was found to increase with increased Gd content as this stabilised the higher oxidation states of U in the brannerite structure. When processing samples in an argon atmosphere the reverse was found; increasing Gd content was found to result in a decrease in the amount of brannerite formed. This was attributed to the formation of a parasitic pyrochlore phase. A similar pattern was observed to occur when samples were processed in a 5 %  $\text{H}_2/\text{N}_2$  atmosphere with an additional rare-earth rich parasitic phase ( $\text{La}_4\text{Ti}_9\text{O}_{24}$ ) and retention of a large

amount of  $\text{UO}_2$  observed. The average oxidation states of U, Ce and Ti were determined by XAS to allow the derivation of a possible charge balance mechanism. It was found that Ce was reduced from Ce (IV) to Ce (III) and that Ti remained as Ti (IV) in all cases. U oxidation was found to vary with processing atmosphere. The presence of U-bearing accessory phases necessitated the use of  $\mu$ -focus XAS to determine the oxidation state of U in the brannerite phase. It was found that U oxidation state was highest in brannerites sintered in air and lowest in those sintered in 5 %  $\text{H}_2/\text{N}_2$ . A charge balance mechanism of oxidation of U to higher oxidation states (U V/VI) combined with A-site vacancies was hypothesised.

This investigation has demonstrated that it is feasible to produce brannerite wasteforms for the disposal of MOX residues. It has shown that it is possible to incorporate both Ce (as a Pu surrogate) and Gd (as a neutron absorber) in a brannerite wasteform with U oxidising to act as a charge balancing species. The necessity of close control of target stoichiometry and processing conditions has also been highlighted. These wasteforms may be applied to a closed fuel cycle involving the recycle of Pu and U as mixed oxide fuel.

This work could be developed further by refining the target stoichiometry and processing conditions to achieve single phase material. The most promising route appears to be an argon/inert atmosphere combined with low Gd content ( $< 0.2$  f.u.). Another possibility would be to synthesise the samples *via* HIP, however, depending on can material, this could result in a change in synthesis conditions necessitating adjustment of the target composition. The durability of these materials should also be assessed to be sure that they are comparable to other proposed wasteforms.

#### **9.4. Chapter 7: A new approach to the immobilisation of Tc and Pu: co-disposal in a zirconolite ceramic matrix**

This chapter describes the investigation of novel zirconolite compositions designed for the co-disposal of Pu and Tc. The study used Ce and Mo as structural surrogates for Pu and Tc, respectively and targeted co-substitution of Ce for Ca and Zr and Mo for Ti. Samples were produced by both traditional solid state synthesis and hot isostatic pressing. Materials were characterised by XRD, SEM-EDX, TEM, XANES and TGA-MS.

XRD analysis of samples found that zirconolite was formed in all cases along with secondary  $\text{CaTiO}_3$ , acting as an intermediate phase, and retained  $\text{ZrO}_2$ . After comparison of XRD and SEM-EDX results of materials produced over a range of temperatures, it was concluded that the process was complicated by the volatilisation of molybdenum during high temperature processing and the relatively refractory nature of the  $\text{ZrO}_2$  precursor. Processing at lower temperatures retained more molybdenum, however, there was less reaction of  $\text{ZrO}_2$  and a greater proportion of intermediate  $\text{CaTiO}_3$  was observed. The volatilisation of molybdenum during synthesis was confirmed by TGA-MS whereby the mass loss observed at temperatures  $> 950\text{ }^\circ\text{C}$  was observed to follow an increasing trend with increasing waste loading. The waste-loading was found to have an effect on the observed phase assemblage with increased loading resulting in the formation of a greater proportion of  $\text{CaTiO}_3$  and  $\text{ZrO}_2$ . Processing atmosphere was also found to affect the observed phase assemblage with a temperature dependent effect also observed. An inert atmosphere was found to produce a more favourable phase assemblage at  $1,400\text{ }^\circ\text{C}$  whereas a reducing atmosphere ( $5\text{ }\% \text{ H}_2/\text{N}_2$ ) produced the most favourable phase assemblage at  $1,200\text{ }^\circ\text{C}$ . A suite of samples were synthesised *via* HIP to eliminate the problem of molybdenum volatilisation. HIP consolidated samples were found to have greatly improved density and waste loading was found to have a similar effect on the observed phase assemblage, a considerable proportion of metallic Mo was also observed in these samples. It is worth noting that synthesis temperatures were limited to  $1250\text{ }^\circ\text{C}$  when HIPing because stainless steel was used as the can material. Electron diffraction, performed using TEM, found that waste loading and processing method did not have an effect on the unit cell symmetry, all samples were found to form the zirconolite 2M polytype. The average oxidation state of Mo was determined by XANES analysis and found to be strongly affected by processing atmosphere. Samples sintered in reducing conditions had the lowest Mo oxidation state; samples sintered in inert conditions were relatively similar to the initial  $\text{MoO}_2$  precursor and HIPed samples were found to follow an increasing trend with increased waste loading.

This study has demonstrated that it is possible to incorporate Ce and Mo, and therefore possibly Pu and Tc, into the zirconolite structure. It has also highlighted that control of processing conditions and processing method are important to the final observed phase

assemblage. These wastefoms may be applied to future fuel cycles where separated plutonium and technetium are considered as waste.

Further work on this project should focus on the investigation of alternative Zr precursors or synthesis routes to produce a more reactive material that will form at lower temperatures. This may include the replacement of  $ZrO_2$  or a shift to an alkoxide-nitrate/sol-gel route. Alternatively, if a more suitable, high temperature HIP can material can be used it may be possible to synthesise single phase material by HIPing the same precursor materials at a higher temperature. Another avenue of investigation would be to study the substitution of actual Pu and Tc into the system, however, this would come with considerable costs and radiation safety considerations.

## **9.5. Chapter 8: A Synchrotron X-ray Spectroscopy Study of Titanium Co-ordination in Explosive Melt Glass Derived From the Trinity Nuclear Test**

This chapter describes the characterisation and determination of Ti local chemistry in trinitite, an explosive melt glass derived from the first atomic bomb test. Ti coordination in synthetic, natural and impact glasses is known to be affected by glass composition, pressure and cooling rate; the coordination of Ti in trinitite therefore offers insight into the formation conditions during the explosion- an area of much debate. Representative samples of trinitite were characterised by ICP-MS, gamma spectroscopy, SEM-EDX and XANES.

ICP-MS analysis found that the trinitite was an alkali-alkaline earth aluminosilicate with considerable additions of Fe and Ti. Gamma spectroscopy confirmed the presence of  $^{241}Am$ ,  $^{137}Cs$  and  $^{152}Eu$ , consistent with the detonation of a Pu based bomb. SEM-EDX found that the trinitite was not a homogeneous but a mixture of at least four distinct glasses- an alkali-alkaline earth aluminosilicate glass, a high Al glass, a high Ca glass and a high Si glass. Ti was found throughout these glasses and it was concluded that the local chemistry of Ti varied across the samples. Analysis of Ti XANES and the associated pre-edge features found that Ti was present as Ti (IV) and that the co-ordination varied, as would be expected given the local chemistry observed by SEM-EDX.

This work is the first study to investigate the chemistry of Ti in trinitite and has determined the average oxidation state and local chemistry of Ti in trinitite. It has shown that, due to the heterogeneous nature of trinitite, Ti coordination varies throughout trinitite.

Further investigation of this material could involve the use of EPMA and micro-focus XAS and XRF to determine a more precise local chemistry and XAS spectra for specific regions. Other elements present in trinitite, e.g. Fe, could also be probed in a similar manner to elucidate further knowledge regarding the structure and formation of these materials.

## References- Chapters 1-3

- [1] D. Bodansky, *Nuclear Energy: Principles, Practices, and Prospects*, 2nd ed. New York: Springer, 1997.
- [2] W. D. Loveland, D. J. Morrissey, and G. T. Seaborg, *Modern Nuclear Chemistry*. Hoboken: John Wiley & Sons, Ltd., 2005.
- [3] W. N. Association, “Nuclear Power Reactors.” [Online]. Available: <http://www.world-nuclear.org/information-library/nuclear-fuel-cycle/nuclear-power-reactors/nuclear-power-reactors.aspx>. [Accessed: 03-Jan-2017].
- [4] IAEA, “The Database on Nuclear Power Reactors,” *Power Reactor Information System*. 2016.
- [5] P. D. Wilson, *The Nuclear Fuel Cycle: From Ore to Waste*, 1st ed. Oxford: Oxford University Press, 1996.
- [6] J. Bruno and R. C. Ewing, “Spent Nuclear Fuel,” *Elements*, vol. 2, no. 6, pp. 343–349, 2006.
- [7] J. J. Laidler, “GNEP Spent Fuel Processing ; Waste Streams and Disposition Options,” 2007, pp. 1–15.
- [8] J. Law, D. Peterman, C. Riddle, D. Meikrantz, and T. Todd, “Advances in Development of the Fission Product Extraction Process for the Separation of Cesium and Strontium from Spent Nuclear Fuel,” in *Proceedings of the 11th International Conference on Environmental Remediation and Radioactive Waste Management (ICEM 2007)*, 2007.
- [9] J. D. Law, K. N. Brewer, R. S. Herbst, T. A. Todd, and D. J. Wood, “Development and demonstration of solvent extraction processes for the separation of radionuclides from acidic radioactive waste,” *Waste Manag.*, vol. 19, no. 1, pp. 27–37, Feb. 1999.
- [10] G. F. Vandegrift, M. C. Regalbuto, S. B. Aase, H. A. Arafat, A. J. Bakel, D. L. Bowers, J. P. Byrnes, M. A. Clark, J. W. Emery, J. R. Falkenberg, A. V. Gelis, L. D. Hafenrichter, R. A. Leonard, C. Pereira, K. J. Quigley, Y. Tsai, M. H. Vander Pol, and J. J. Laidler, “Lab-Scale Demonstration of the UREX+ Process,” in *WM’04 Conference*, 2004.
- [11] K. M. Goff, J. C. Wass, K. C. Marsden, and G. M. Teske, “Processing of Used Nuclear Fuel,” *World Nucl. Assoc.*, vol. 43, no. January, pp. 335–342, 2011.

- [12] M. L. Carter, A. L. Gillen, K. Olufson, and E. R. Vance, "HIPed tailored hollandite waste forms for the immobilization of radioactive Cs and Sr," *J. Am. Ceram. Soc.*, vol. 92, pp. 1112–1117, 2009.
- [13] E. R. Vance, J. Davis, K. Olufson, I. Chironi, I. Karatchevtseva, and I. Farnan, "Candidate waste forms for immobilisation of waste chloride salt from pyroprocessing of spent nuclear fuel," *J. Nucl. Mater.*, vol. 420, no. 1–3, pp. 396–404, Jan. 2012.
- [14] National Research Council, *Disposition of High-Level Waste and Spent Nuclear Fuel: The Continuing Societal and Technical Challenges*, 1st ed. Washington: National Academy Press, 2001.
- [15] United Kingdom Nirex Ltd., "The viability of a phased geological repository concept for the long-term management of the UK's radioactive waste," 2003.
- [16] *Convention on the Prevention of Marine Pollution by Dumping Wastes and Other Matter*. 1972.
- [17] *The Antarctic Treaty*. 1959.
- [18] *Treaty on principles governing the activities of states in the exploration and use of outer space, including the moon and other celestial bodies*. 1967.
- [19] F. G. F. Gibb, "High-temperature, very deep, geological disposal: A safer alternative for high-level radioactive waste?," *Waste Manag.*, vol. 19, no. 3, pp. 207–211, 1999.
- [20] Nuclear Decommissioning Authority, "Geological Disposal: Generic Disposal Facility Designs," 2010.
- [21] J. T. Carter, R. Kehrman, and T. Hayes, "A generic salt repository for waste from a spent nuclear fuel recycle facility," Aiken, 2011.
- [22] T. W. Hicks, M. J. White, and P. J. Hooker, "Role of Bentonite in Determination of Thermal Limits on Geological Facility Design," 2009.
- [23] R. A. Wigeland, T. H. Bauer, T. H. Fanning, and E. E. Morris, "Separations and transmutation criteria to improve utilization of a geologic repository," *Nucl. Technol.*, vol. 154, no. 1, pp. 95–106, 2006.
- [24] W. Callister and D. Rethwisch, "Structures and properties of ceramics," in *Materials science and engineering: an introduction*, 7th ed., New York: John Wiley & Sons, Ltd., 2007.
- [25] I. W. Donald, *Waste immobilization in glass and ceramic based hosts*. Chichester: John Wiley & Sons, Ltd., 2010.

- [26] L. P. Hatch, "Ultimate Disposal of Radioactive Wastes," *Am. Sci.*, vol. 41, no. 3, pp. 410–421, 1953.
- [27] G. J. McCarthy, "High level waste ceramics: Materials considerations, process simulation, and product characterization," *Nuclear Technology*, vol. 32, no. 1. pp. 92–105, 1977.
- [28] K. L. Smith, G. R. Lumpkin, M. G. Blackford, R. a. Day, and K. P. Hart, "The durability of synroc," *J. Nucl. Mater.*, vol. 190, pp. 287–294, 1992.
- [29] R. C. Ewing and W. Lutze, "High-level nuclear waste immobilization with ceramics," *Ceram. Int.*, vol. 17, pp. 287–293, 1991.
- [30] A. E. Ringwood, S. E. Kesson, N. G. Ware, W. Hibberson, and A. Major, "Immobilisation of high level nuclear reactor wastes in SYNROC," *Nature*, vol. 278, no. 5701, pp. 219–223, Mar. 1979.
- [31] A. E. Ringwood, S. E. Kesson, N. G. Ware, W. O. Hibberson, and A. Major, "The SYNROC process: A geochemical approach to nuclear waste immobilization.," *Geochem. J.*, vol. 13, no. 4, pp. 141–165, 1979.
- [32] B. D. Begg and E. R. Vance, "The incorporation of cerium in zirconolite," *Mater. Res. Soc. Symp. Proc.*, vol. 465, pp. 333–340, 1997.
- [33] E. R. Vance, G. R. Lumpkin, M. L. Carter, D. J. Cassidy, C. J. Ball, R. A. Day, and B. D. Begg, "Incorporation of Uranium in Zirconolite ( $\text{CaZrTi}_2\text{O}_7$ )," *J. Am. Ceram. Soc.*, vol. 59, no. 187500, pp. 1853–1859, 2002.
- [34] B. D. Begg, R. A. Day, and A. Brownscombe, "Structural Effect of Pu Substitutions on the Zr-Site in Zirconolite," *Mater. Res. Soc. Symp. Proc.*, vol. 663, pp. 1–8, 2017.
- [35] E. R. Vance, B. D. Begg, R. A. Day, and C. J. Ball, "Zirconolite-Rich Ceramics for Actinide Wastes," *Mater. Res. Soc. Symp. Proc.*, vol. 353, pp. 767–774, 1995.
- [36] B. D. Begg, E. R. Vance, and B. A. Hunter, "Zirconolite transformation under reducing conditions," *J. Mater. Res.*, vol. 13, no. 11, pp. 3181–3190, 1998.
- [37] E. R. Vance, M. W. A. Stewart, and S. A. Moricca, "Progress at ANSTO on SYNROC," *Journal of the Australian Ceramic Society*, vol. 50, no. 1. Australasian Ceramic Society, pp. 38–48, 2014.
- [38] K. P. Hart, E. R. Vance, R. A. Day, B. D. Begg, P. J. Angel, and A. Jostons, "Immobilization of separated Tc and Cs/Sr in Synroc," *Mater. Res. Soc. Symp. Proc.*, vol. 412, pp. 281–287, 1996.

- [39] H. Li, Y. Zhang, P. J. McGlenn, S. Moricca, B. D. Begg, and E. R. Vance, "Characterisation of stainless steel-synroc interactions under hot isostatic pressing (HIPing) conditions," *J. Nucl. Mater.*, vol. 355, no. 1–3, pp. 136–141, 2006.
- [40] L. A. Bursill and D. J. Smith, "Electron irradiation effects in (Cs,Ba)-hollandites," *J. Solid State Chem.*, vol. 69, no. 2, pp. 343–354, 1987.
- [41] T. Murakami, "Microstructure of SYNROC," *Nucl. Chem. Waste Manag.*, vol. 5, no. 4, pp. 269–278, 1985.
- [42] E. R. Vance, J. N. Watson, M. L. Carter, R. A. Day, and B. D. Begg, "Crystal Chemistry and Stabilization in Air of Brannerite,  $UTi_2O_6$ ," *J. Am. Ceram. Soc.*, vol. 44, pp. 141–144, 2001.
- [43] V. Aubin, D. Caurant, D. Gourier, N. Baffier, S. Esnouf, and T. Advocat, "Radiation Effects on Hollandite Ceramics developed for Radioactive Cesium Immobilization," *Mater. Res. Soc. Symp. Proc.*, vol. 792, pp. 1–7, 2004.
- [44] A. Y. Leinekugel-le-Cocq, P. Deniard, S. Jobic, R. Cerny, F. Bart, and H. Emerich, "Synthesis and characterization of hollandite-type material intended for the specific containment of radioactive cesium," *J. Solid State Chem.*, vol. 179, pp. 3196–3208, 2006.
- [45] F. Angeli, P. McGlenn, and P. Frugier, "Chemical durability of hollandite ceramic for conditioning cesium," *J. Nucl. Mater.*, vol. 380, pp. 59–69, 2008.
- [46] M. L. Carter, E. R. Vance, D. R. G. Mitchell, J. V. Hanna, Z. Zhang, and E. Loi, "Fabrication, characterization, and leach testing of hollandite,  $(Ba,Cs)(Al,Ti)_2Ti_6O_{16}$ ," *J. Mater. Res.*, vol. 17, no. January, pp. 2578–2589, 2002.
- [47] Y. Zhang, M. W. A. Stewart, H. Li, M. L. Carter, E. R. Vance, and S. Moricca, "Zirconolite-rich titanate ceramics for immobilisation of actinides - Waste form/HIP can interactions and chemical durability," *J. Nucl. Mater.*, vol. 395, no. 1–3, pp. 69–74, 2009.
- [48] E. R. Vance, C. J. Ball, R. A. Day, K. L. Smith, M. G. Blackford, and P. J. Angel, "Actinide and rare earth incorporation into zirconolite," *J. Alloys Compd.*, vol. 214, pp. 406–409, 1994.
- [49] B. D. Begg, E. R. Vance, and S. D. Conradson, "The incorporation of plutonium and neptunium in zirconolite and perovskite," *J. Alloys Compd.*, vol. 271–273, pp. 221–226, 1998.

- [50] A. Bohre and O. P. Shrivastava, “Crystallographic evaluation of sodium zirconium phosphate as a host structure for immobilization of cesium and strontium,” *Int. J. Appl. Ceram. Technol.*, vol. 10, pp. 552–563, 2013.
- [51] R. Roy, E. R. Vance, and J. Alamo, “[NZZ], a new radiophase for ceramic nuclear waste forms,” *Mater. Res. Bull.*, vol. 17, no. c, pp. 585–589, 1982.
- [52] L. J. Yang, S. Komarneni, and R. Roy, “Titanium Phosphate (NTP) Waste Form,” in *Advances in Ceramics*, vol. 8, pp. 255–262, 1984.
- [53] L. J. Yang, S. Komarneni, and R. Roy, “Leach Resistance of NZZ Waste Form,” in *Advances in Ceramics*, vol. 8, pp. 377–384, 1984.
- [54] E. Du Fou de Kerdaniel, N. Clavier, N. Dacheux, O. Terra, and R. Podor, “Actinide solubility-controlling phases during the dissolution of phosphate ceramics,” *J. Nucl. Mater.*, vol. 362, pp. 451–458, 2007.
- [55] O. Terra, N. Dacheux, N. Clavier, R. Podor, and F. Audubert, “Preparation of optimized uranium and thorium bearing brabantite or monazite/brabantite solid solutions,” *J. Am. Ceram. Soc.*, vol. 91, pp. 3673–3682, 2008.
- [56] N. C. Hyatt, M. C. Stennett, S. G. Fiddy, J. S. Wellings, S. S. Dutton, E. R. Maddrell, A. J. Connelly, and W. E. Lee, “Synthesis and characterisation of transition metal substituted barium hollandites,” *Mater. Res. Soc. Symp. Proc.*, vol. 932, 2006.
- [57] M. L. Carter, E. R. Vance, and H. Li, “Hollandite-rich Ceramic Melts for the Immobilisation of Cs,” *Mater. Res. Soc. Symp. Proc.*, vol. 807, pp. 1–6, 2004.
- [58] V. Aubin-Chevaldonnet, D. Caurant, a. Dannoux, D. Gourier, T. Charpentier, L. Mazerolles, and T. Advocat, “Preparation and characterization of (Ba,Cs)(M,Ti)<sub>8</sub>O<sub>16</sub> (M = Al<sup>3+</sup>, Fe<sup>3+</sup>, Ga<sup>3+</sup>, Cr<sup>3+</sup>, Sc<sup>3+</sup>, Mg<sup>2+</sup>) hollandite ceramics developed for radioactive cesium immobilization,” *J. Nucl. Mater.*, vol. 366, pp. 137–160, 2007.
- [59] V. Aubin-Chevaldonnet, D. Caurant, D. Gourier, T. Charpentier, and S. Esnouf, “Synthèse et stabilité sous irradiation électronique d’une céramique Ba<sub>1.16</sub>Al<sub>2.32</sub>Ti<sub>5.68</sub>O<sub>16</sub> de structure hollandite envisagée pour le confinement de césium radioactif,” *Comptes Rendus Chim.*, vol. 12, pp. 1079–1092, 2009.
- [60] N. Nguyen, A. Ducouret, F. Studer, V. Aubin, D. Caurant, D. Gourier, and J. M. Costantini, “Defects induced by electron irradiation in hollandite ceramics, specific radioactive cesium-host wastefoms: A <sup>57</sup>Fe Mössbauer study,” *Hyperfine Interact.*, vol. 166, no. 1–4, pp. 489–493, 2005.
- [61] A. Byström and A. M. Byström, “The crystal structure of hollandite, the related

manganese oxide minerals, and  $\alpha$ - $\text{MnO}_2$ ,” *Acta Crystallogr.*, vol. 3, no. 2, pp. 146–154, 1950.

- [62] A. E. Ringwood, K. D. Reeve, D. M. Levins, and E. J. Ramm, “Synroc,” in *Radioactive Waste Forms for the Future*, R. C. Ewing and W. Lutze, Eds. New York: North Holland Physics Publishing, 1988, pp. 233–335.
- [63] W. Sinclair, G. M. McLaughlin, and a. E. Ringwood, “The structure and chemistry of a barium titanate hollandite-type phase,” *Acta Crystallogr. Sect. B Struct. Crystallogr. Cryst. Chem.*, vol. 36, no. 12, pp. 2913–2918, 1980.
- [64] S. E. Kesson and T. J. White, “Radius ratio tolerance factors and the stability of hollandites,” *J. Solid State Chem.*, vol. 63, pp. 122–125, 1986.
- [65] A. F. Reid and A. E. Ringwood, “Six-coordinate silicon: High pressure strontium and barium aluminosilicates with the hollandite structure,” *J. Solid State Chem.*, vol. 1, no. 1, pp. 6–9, 1969.
- [66] B. J. Riley, J. D. Vienna, D. M. Strachan, J. S. McCloy, and J. L. Jerden, “Materials and processes for the effective capture and immobilization of radioiodine: A review,” *J. Nucl. Mater.*, vol. 470, pp. 307–326, 2016.
- [67] R. T. Jubin, S. H. Bruffey, and K. K. Patton, “Expanded analysis of hot isostatic pressed iodine-loaded silver-exchanged mordenite,” 2014.
- [68] F. Audubert, J. Carpenaa, J. L. Lacoutb, and F. Tetard, “Elaboration of an iodine-bearing apatite iodine diffusion into a  $\text{Pb}_3(\text{VO}_4)_2$  matrix,” *Solid State Ionics*, vol. 95, pp. 113–119, 1997.
- [69] M. S. Schriewer and W. Jeitschko, “Preparation and Crystal Structure of Isotypic Orthorhombic Sr Perrhenate Halides  $\text{Sr}_5(\text{ReO}_5)_3\text{X}$  ( $\text{X} = \text{Cl}, \text{Br}, \text{I}$ ) and Structure Refinement of the Related Hexagonal Apatite-like Compound  $\text{Ba}_5(\text{ReO}_5)_3\text{Cl}$ ,” *J. Solid State Chem.*, vol. 107, pp. 1–11, 1993.
- [70] F. Audubert, J.-M. Savariault, and J.-L. Lacout, “Pentalead tris(vanadate) iodide, a defect vanadinite-type compound,” *Acta Crystallogr. Sect. C Cryst. Struct. Commun.*, vol. 55, no. 3, pp. 271–273, 1999.
- [71] N. C. Hyatt, “Plutonium management policy in the United Kingdom: The need for a dual track strategy,” *Energy Policy*, vol. 99, 2016.
- [72] Nuclear Decommissioning Authority, “Plutonium: Credible options analysis (Gate A),” 2010.
- [73] B. B. Ebbinghaus and O. H. Krikorian, “Ternary Phase Diagrams that Relate to the Plutonium Immobilization Ceramic,” 2001.

- [74] F. J. Ryerson and B. Ebbinghaus, "Pyrochlore-Rich Titanate Ceramics for the Immobilization of Plutonium : Redox Effects on Phase Equilibria in Cerium- and Thorium- Substituted Analogs," 2000.
- [75] F. J. Ryerson, B. Ebbinghaus, and O. Kirkorian, *Saturation of Impurity-Rich Phases in a Cerium-Substituted Pyrochlore-Rich Titanate Ceramic : Part 1 . Experimental Results*. 2000.
- [76] J. T. Szymanski and J. D. Scott, "A Crystal Structure Refinement of Synthetic Brannerite,  $UTi_2O_6$  , and Its Bearing on Rate of Alkaline-Carbonate Leaching of Brannerite in Ore," *Can. Mineral.*, vol. 20, pp. 271–279, 1982.
- [77] M. James and J. N. Watson, "The Synthesis and Crystal Structure of Doped Uranium Brannerite Phases  $U_{1-x}M_xTi_2O_6$  ( $M=Ca^{2+}$ ,  $La^{3+}$ , and  $Gd^{3+}$ )," *J. Solid State Chem.*, vol. 165, pp. 261–265, 2002.
- [78] F. X. Zhang, M. Lang, Z. Liu, and R. C. Ewing, "Phase stability of some actinides with brannerite structure at high pressures," *J. Solid State Chem.*, vol. 184, no. 11, pp. 2834–2839, 2011.
- [79] T. J. White, "The microstructure and microchemistry of synthetic zirconolite , zirkelite and related phases," *Am. Mineral.*, vol. 69, pp. 1156–1172, 1984.
- [80] T. J. White, R. L. Segall, J. L. Hutchinson, and J. C. Barry, "Polytypic behaviour of zirconolite," *Proceeds R. Soc. London A*, no. 392, pp. 343–358, 1984.
- [81] R. Giere and P. Stille, Eds., *Energy, waste and the environment: a geochemical perspective*. London: Geological Society.
- [82] P. Bayliss, F. Mazzi, R. Munno, and T. J. White, "Mineral nomenclature : zirconolite," *Mineral. Mag.*, vol. 53, no. December, pp. 565–569, 1989.
- [83] F. Mazzi and R. Munno, "Calciobetafite (new mineral of the pyrochlore group) and related minerals from Campi Flegrei, Italy: crystal structures of polymignyte and zirkelite: comparison with pyrochlore and zirconolite.," *Am. Mineral.*, vol. 68, no. 1–2, pp. 262–276, 1983.
- [84] G. R. Lumpkin, K. L. Smith, M. G. Blackford, R. Giere, and C. Terry Williams, "Determination of 25 elements in the complex oxide mineral zirconolite by analytical electron microscopy," *Micron*, vol. 25, no. 6, pp. 581–587, 1994.
- [85] O. Muller, "Crystal Chemistry of Some Technetium- Containing Oxides," *J. Inorg. Nucl. Chem.*, vol. 26, no. 1962, pp. 2075–2086, 1964.

- [86] S. A. Luksic, B. J. Riley, M. Schweiger, and P. Hrma, "Incorporating technetium in minerals and other solids: A review," *J. Nucl. Mater.*, vol. 466, pp. 526–538, 2015.
- [87] D. D. Keiser Jr, D. P. Abraham, and J. W. Richardson Jr, "Influence of technetium on the microstructure of a stainless steel - zirconium alloy," *J. Nucl. Mater.*, vol. 277, pp. 333–338, 2000.
- [88] M. Y. Khalil and W. B. White, "Magnesium Titanate Spinel: A Ceramic Phase for Immobilization of Technetium-99 from Radioactive Wastes," *J. Am. Ceram. Soc.*, vol. 66, no. 10, pp. c197–c198, 1983.
- [89] ASTM, "Standard Test Methods for Determining Chemical Durability of Nuclear, Hazardous, and Mixed Waste Glasses and Multiphase Glass Ceramics : The Product Consistency Test ( PCT )," *Standard*, vol. C 1285-02.
- [90] ASTM, "Standard Test Method for Static Leaching of Monolithic Waste Forms for Disposal of Radioactive Waste," *Standard*, vol. C 1220-98.
- [91] M. V. Zamoryanskaya and B. E. Burakov, "Feasibility limits in using cerium as a surrogate for plutonium incorporation in zircon, zirconia and pyrochlore," *Materials Research Society, Symposium Proceedings*, vol. 663. pp. 301–306, 2001.
- [92] M. N. Rahaman, "Ceramic processing and sintering," *Int. Mater. Rev.*, vol. 41, pp. 36–37, 1996.
- [93] W. D. Kingery, H. K. Bowen, and D. N. Uhlmann, *Introduction to Ceramics*, 2nd ed. John Wiley & Sons, Ltd., 1976.
- [94] H. V Atkinson and S. Davies, "Fundamental Aspects of Hot Isostatic Pressing : An Overview," *Metall. Mater. Trans. A Phys. Metall. Mater. Sci.*, vol. 31A, no. December, pp. 2000–2981, 2000.
- [95] A. R. West, *Basic solid state chemistry*, 2nd ed. Chichester: John Wiley & Sons, Ltd., 1999.
- [96] H. M. Rietveld, "A profile refinement method for nuclear and magnetic structures," *J. Appl. Crystallogr.*, vol. 2, pp. 65–71, 1969.
- [97] B. D. Cullity and S. R. Stock, *Elements of X-ray Diffraction*, 3rd ed. Upper Saddle River: Prentice Hall, 2001.
- [98] S. Calvin, *XAFS for Everyone*. Boca Raton: CRC Press, 2013.

- [99] S. D. Kelly, D. Hesterberg, and B. Ravel, "Analysis of Soils and Minerals Using X-ray Absorption Spectroscopy," *Rev. Mineral. Geochemistry*, no. 5, pp. 387-464, 2008.
- [100] B. Ravel and M. Newville, "ATHENA, ARTEMIS, HEPHAESTUS: Data analysis for X-ray absorption spectroscopy using IFEFFIT," in *Journal of Synchrotron Radiation*, 2005, vol. 12, no. 4, pp. 537-541.
- [101] B. Ravel and M. Newville, "ATHENA and ARTEMIS Interactive Graphical Data Analysis using IFEFFIT," *Phys. Scr.*, p. 1007, 2005.
- [102] P. J. Goodhew, J. Humphreys, and R. Beanland, *Electron microscopy and analysis*, 3rd ed. London: Taylor and Francis, 2001.
- [103] L. Reimer, *Scanning electron microscopy: Physics of image formation and microanalysis*, 2nd ed. Berlin: Springer, 1998.
- [104] B. Fultz and J. Howe, *Transmission Electron Microscopy and Diffractometry of Materials*, 3rd ed. Berlin: Springer, 2008.
- [105] R. L. Mössbauer, "Kernresonanzfluoreszenz von Gammastrahlung in Ir191," *Zeitschrift für Phys.*, vol. 151, no. 2, pp. 124-143, 1958.
- [106] M. D. Dyar, D. G. Agresti, M. W. Schaefer, C. a. Grant, and E. C. Sklute, "Mössbauer Spectroscopy of Earth and Planetary Materials," *Annu. Rev. Earth Planet. Sci.*, vol. 34, no. 1, pp. 83-125, 2006.
- [107] D. G. Rancourt and K. Lagarec, "Recoil, Mössbauer Spectral Analysis Software for Windows." 1998.
- [108] G. Gilmore, *Practical gamma-ray spectrometry*, 2nd ed. Chichester: John Wiley & Sons, Ltd., 1996.
- [109] P. Gabbot, Ed., *Principles and Applications of Thermal Analysis*. Oxford: Blackwell Publishing, 2008.
- [110] S. Tamari, "Optimum design of the constant-volume gas pycnometer for determining the volume of solid particles," *Meas. Sci. Technol.*, vol. 15, pp. 549-558, 2004.

# Appendices

## Table of Figures

<b>Figure 2.1:</b> Yield of fission fragments as a function of atomic mass number $A$ for thermal fission of $^{235}\text{U}$ (in percent per fission). Taken from Bodansky (1997) [1].	6
<b>Figure 2.2:</b> Neutron-induced fission cross section of $^{235}\text{U}$ and $^{238}\text{U}$ as a function of neutron energy, $E_n$ . Taken from Loveland, Morrissey and Seaborg (2005) [2].	7
<b>Figure 2.3:</b> A schematic of an Advanced Gas-cooled Reactor (AGR) [3].	8
<b>Figure 2.4:</b> A schematic of a Pressurised Water Reactor (PWR) [3].	9
<b>Figure 2.5:</b> Schematic illustration of the microstructure of spent fuel, showing the distribution of actinides and fission products following burn up in a reactor. From Bruno and Ewing (2006)[6].	12
<b>Figure 2.6:</b> Outline of UREX + 1a process [7].	15
<b>Figure 2.7:</b> Simplified diagram of a Geological Disposal Facility	28
<b>Figure 2.8:</b> Crystal structure of hollandite. Blue = Ti and red = Ba/Cs. Oxygen has been omitted for clarity	33
<b>Figure 2.9:</b> Structure of the iodovanadinite unit cell. Orange = V, Grey = Pb. Iodine resides in the tunnel sites but has been omitted for clarity.	34
<b>Figure 2.10:</b> Brannerite crystal structure. Blue = Ti, yellow = U.	36
<b>Figure 2.11:</b> Zirconolite crystal structure. Blue = Ti, yellow = Ca and green = Zr.	37
<b>Figure 2.12:</b> Hexagonal tungsten bronze array of $\text{TiO}_6$ octahedra.	37
<b>Figure 3.1:</b> Six distinct mechanisms can contribute to the sintering of a consolidated mass of crystalline particles: (1) surface diffusion, (2) lattice diffusion from the surface, (3) vapour transport, (4) grain boundary diffusion, (5) lattice diffusion from the grain boundary, and (6) plastic flow. Only mechanisms 1 to 3 lead to densification, but all cause the necks to grow and so influence the rate of densification. Adapted from Rahaman (1996) [92].	35
<b>Figure 3.2:</b> Schematic of the hot isostatic pressing process:	37
<b>Figure 3.3:</b> HIP sample preparation station	37
<b>Figure 3.4:</b> HIP unit	38
<b>Figure 3.5:</b> Schematic of small-scale HIP tube.	39

<b>Figure 3.6:</b> HIP canister schematic. ....	40
<b>Figure 3.7:</b> Derivation of Bragg's Law .....	42
<b>Figure 3.8:</b> Bragg-Brentano parafocussing geometry as used in Bruker D2 Phaser.....	43
<b>Figure 3.9:</b> A typical XRD pattern of an alumino titanate hollandite ( $\text{Ba}_{1.2}\text{Al}_{2.4}\text{Ti}_{5.6}\text{O}_{16}$ ) measured using Cu $K\alpha$ radiation.....	45
<b>Figure 3.10:</b> A typical transmission XAS spectrum (Fe K-edge, $\text{Ba}_{1.2}\text{Fe}_{2.4}\text{Ti}_{5.6}\text{O}_{16}$ ), indicating the 'white line' and the XANES and EXAFS regions. ....	47
<b>Figure 3.11:</b> Airy rings resulting from the diffraction of a laser beam by small apertures: a) 75 $\mu\text{m}$ and b) 100 $\mu\text{m}$ . Taken from Goodhew (2001) [102].....	49
<b>Figure 3.12:</b> Schematic diagram of an analogue scanning electron microscope. Taken from Goodhew (2001) [102].....	50
<b>Figure 3.13:</b> Origin and information depth of secondary electrons (SE), backscattered electrons (BSE), Auger electrons (AE) and X-ray quanta (X) in the diffusion cloud of electron range $R$ for normal incidence of the primary electrons (PE). Adapted from Reimer (1998) [103].....	52
<b>Figure 3.14:</b> Schematic of a transmission electron microscope. Taken from Fultz et al (2008) [104]. ....	54
<b>Figure 3.15:</b> Ideal resonant absorption. $E_0$ is the difference in energy between the ground and excited states. Taken from Dyar et al (2006) [106].....	56
<b>Figure 3.16:</b> Typical hyperfine parameters for Fe bearing minerals. Taken from Dyar et al (2006) [106]. ....	59
<b>Figure 3.17:</b> A schematic of a constant volume gas pycnometer. Adapted from Tamari (2004) [110] .....	62

## Published Papers

**Note:** The following works are either open access or have been reproduced with the publisher's permission. A DOI link to the original published material has been included.

D. J. Bailey, M. C. Stennett, and N. C. Hyatt, "Synthesis and Characterization of Brannerite Wasteforms for the Immobilization of Mixed Oxide Fuel Residues," *Procedia Chem.*, vol. 21, pp. 371–377, 2016. DOI: 10.1557/adv.2016.631

D. J. Bailey, M. C. Stennett, and N. C. Hyatt, "Synthesis and Characterization of Brannerite Compositions for MOX Residue Disposal," *MRS Adv.*, vol. 2, pp. 557-562, 2016. DOI: 10.1016/j.proche.2016.10.052

C. L. Corkhill, D. E. Crean, D. J. Bailey, C. Makepeace, M. C. Stennett, R. Tappero, D. Grolimund, N. C. Hyatt, "Multi-scale investigation of uranium attenuation by arsenic at an abandoned uranium mine," *Nature Materials and Degradation*, vol. 1, pp. 1-7, 2017. DOI: 10.1038/s41529-017-0019-9

E. V. Jonhstone, D. J. Bailey, M. C. Stennett, J. Heo and N. C. Hyatt, "On the existence of  $\text{AgM}_9(\text{VO}_4)_6\text{I}$  ( $\text{M}=\text{Ba}, \text{Pb}$ )," *RSC Adv.*, vol. 7(77), pp. 49004-49009, 2017. DOI: 10.1039/C7RA09313F

S. T. Barlow, D. J. Bailey, A. J. Fisher, M. C. Stennett, C. L. Corkhill, and N. C. Hyatt, "Synthesis of simulant 'lava-like' fuel containing materials (LFCM) from the Chernobyl reactor Unit 4 meltdown," *MRS Adv.*, vol. 2, pp. 609-614, 2016. DOI: 10.1557/adv.2016.642

C. L. Corkhill, D. J. Bailey, F. Y. Tocino, M. C. Stennett, J. A. Miller, J. L. Provis, K. P. Travis, and N. C. Hyatt, "Role of Microstructure and Surface Defects on the Dissolution Kinetics of  $\text{CeO}_2$ , a  $\text{UO}_2$  Fuel Analogue," *ACS Appl. Mater. Interfaces*, vol. 8, pp. 10562-10571, 2016. DOI: 10.1021/acsami.5b11323

M. C. Stennett, T. Lee, D. J. Bailey, E. V. Johnstone, J. Heo, and N. C. Hyatt, "Ceramic Immobilization Options for Technetium," *MRS Adv.*, vol. 2, pp. 753–758, 2017. DOI: 10.1557/adv.2017.268

N. C. Hyatt, C. L. Corkhill, D. J. Bailey, A. J. Fisher, and R. J. Hand, "Comment on 'Preliminary assessment of modified borosilicate glasses for chromium and ruthenium immobilization', by Farid and Rahman," *Mater. Chem. Phys.*, vol. 192, pp. 29–32, 2017. DOI: 10.1016/j.matchemphys.2016.12.071

C. Corkhill, E. Myllykyla, D. J. Bailey, S. M. Thornber, J. Qi, P. Maldonado, M. C. Stennett, A. Hamilton, and N. C. Hyatt, "The contribution of energetically reactive surface features to the dissolution of  $\text{CeO}_2$  and  $\text{ThO}_2$  analogues for spent nuclear fuel microstructures," *ACS Appl. Mater. Interfaces*, vol. 6, pp. 12279-12289, 2014. DOI: 10.1021/am5018978



5th International ATALANTE Conference on Nuclear Chemistry for Sustainable Fuel Cycles

## Synthesis and characterization of brannerite wastefoms for the immobilization of mixed oxide fuel residues

D. J. Bailey<sup>a\*</sup>, M. C. Stennett<sup>a</sup> & N. C. Hyatt<sup>a</sup>

<sup>a</sup>*Immobilisation Science Laboratory, Department of Materials Science and Engineering, University of Sheffield, Sheffield, S1 3JD, United Kingdom*

---

### Abstract

A possible method for the reduction of civil Pu stockpiles is the reuse of Pu in mixed oxide fuel (MOX). During MOX fuel production, residues unsuitable for further recycle will be produced. Due to their high actinide content MOX residues require immobilization within a robust host matrix. Although it is possible to immobilize actinides in vitreous wastefoms; ceramic phases, such as brannerite ( $UTi_2O_6$ ), are attractive due to their high waste loading capacity and relative insolubility. A range of uranium brannerites, formulated  $Gd_xU_{1-x}Ti_2O_6$ , were prepared using a mixed oxide route. Charge compensation of divalent and trivalent cations was expected to occur via the oxidation of  $U^{4+}$  to higher valence states ( $U^{5+}$  or  $U^{6+}$ ).  $Gd^{3+}$  was added to act as a neutron absorber in the final Pu bearing wastefom. X-ray powder diffraction of synthesised specimens found that phase distribution was strongly affected by processing atmosphere (air or Ar). In all cases prototypical brannerite was formed accompanied by different secondary phases dependent on processing atmosphere. Microstructural analysis (SEM) of the sintered samples confirmed the results of the X-ray powder diffraction. The preliminary results presented here indicate that brannerite is a promising host matrix for mixed oxide fuel residues.

© 2016 The Authors. Published by Elsevier B.V. This is an open access article under the CC BY-NC-ND license (<http://creativecommons.org/licenses/by-nc-nd/4.0/>).

Peer-review under responsibility of the organizing committee of ATALANTE 2016

*Keywords:* Brannerite, X-ray diffraction, nuclear waste immobilization, mixed oxide fuel

---

---

\* Corresponding author. Tel.: +44 (0) 1142 225973.  
E-mail address: [dbailey2@sheffield.ac.uk](mailto:dbailey2@sheffield.ac.uk)

## 1. Introduction

Several countries have large stockpiles of plutonium. A possible method for the reduction of Pu stockpiles is the use of mixed oxide fuel (MOX) to produce power in civilian, thermal nuclear reactors. Mixed oxide fuels are composed of a mixture of uranium and plutonium oxides, typically 90-95 % U and 5 - 10% Pu<sup>(1)</sup>. Although highly recyclable, some residues arising from the production of MOX fuels will eventually require disposal. Ceramic phases are particularly attractive for actinide bearing wastes due to their ability to incorporate a high actinide waste loadings. Brannerite,  $UTi_2O_6$ , is a monoclinic phase with space group  $C2/m$  commonly found as an accessory mineral in uranium deposits and multiphase ceramic wasteforms designed for disposal of actinide bearing wastes<sup>(2,3)</sup>. The brannerite structure consists of layers of  $TiO_6$  octahedra with larger cations located between the layers, natural brannerites exhibit considerable chemical flexibility with elements such as Ca, Y, Pb, Ce and Th being incorporated on the U site and Fe, Si and Al substituting on the Ti site. Although natural samples are often found to be completely metamict, the presence of brannerite in vial sediments after the weathering of host rocks indicates that brannerites possess sufficient aqueous durability for consideration as potential host matrices for actinide bearing wastes<sup>(4,5)</sup>.

In this study, the production of brannerites suitable for MOX disposal was investigated by synthesising brannerites with a range of Gd contents ( $Gd_xU_{1-x}Ti_2O_6$ ) under different atmospheres in an attempt to find a suitable baseline composition and processing conditions. Previous studies have shown that although synthesis of stoichiometric brannerite requires inert conditions it is possible to stabilize the brannerite structure in air by the addition of dopants (Ca, La, Gd)<sup>(6-8)</sup>.

## 2. Materials and methods

### 2.1. Materials synthesis

Brannerites with composition  $Gd_xU_{1-x}Ti_2O_6$  were synthesised via the oxide route under oxidizing or inert atmospheres (air or argon). Waste loadings were varied across the compositions with varying levels of Gd added to act as a neutron absorber for the final Pu bearing wasteform ( $x = 0.1, 0.2$  and  $0.3$ ). Charge balancing of trivalent cations was expected to occur via the oxidation of U(IV) to higher oxidation states (U(V), U(VI)) as observed in previous investigations<sup>(7,8)</sup>.

Stoichiometric amounts of oxide precursors ( $UO_2$ ,  $Gd_2O_3$ ,  $TiO_2$ ) were mixed with isopropanol to form a slurry and ball milled using a Fritsch Pulverisette 23 for five minutes at a frequency of 30 Hz. The milled slurry was then dried in an oven. Sintered pellets were produced by uniaxially pressing 0.6 g of material in a hardened steel die with a load of 2 tons to form a green body followed by reaction under flowing air or argon at 1320 °C for 24 hours.

### 2.2. Materials characterization

Sintered brannerites were ground and characterized by x-ray powder diffraction using a Bruker D2 Phaser in Bragg-Brentano geometry with a Cu source and Ni foil  $K\beta$  filter. Lattice parameters were found by performing a Le Bail refinement of the data.

Microstructure and phase distribution of sintered pellets was investigated by scanning electron microscopy and energy dispersive x-ray spectroscopy (SEM-EDX) using a Hitachi TM3030 SEM equipped with a Bruker Quantax EDX detector. Samples were prepared for SEM analysis by mounting in cold setting resin and polishing with progressively finer SiC paper and diamond pastes to an optical finish (1  $\mu m$ ). Samples were sputter coated with carbon to reduce surface charging effects.

### 3. Results and discussion

#### 3.1. Air sintered samples

All synthesised brannerites were characterized by powder x-ray diffraction and scanning electron microscopy. X-ray diffraction found sharp peaks indicative of prototypical brannerite for all compositions. The secondary phases  $U_3O_8$  and rutile ( $TiO_2$ ) were also observed and found to vary with the level of Gd substitution, see Figure 1. As Gd substitution was increased the relative intensities of  $U_3O_8$  and rutile decreased whereas the intensity of the brannerite peaks was found to increase indicating a higher yield of brannerite. The brannerite microstructure observed by scanning electron microscopy closely matched that indicated by x-ray diffraction. As can be seen in Figure 2, the relative proportions of brannerite,  $U_3O_8$  and rutile vary with the level of Gd substitution. As Gd substitution increases, the amount of brannerite formed increases and the amount of  $U_3O_8$  and rutile present decreases, in agreement with XRD data.

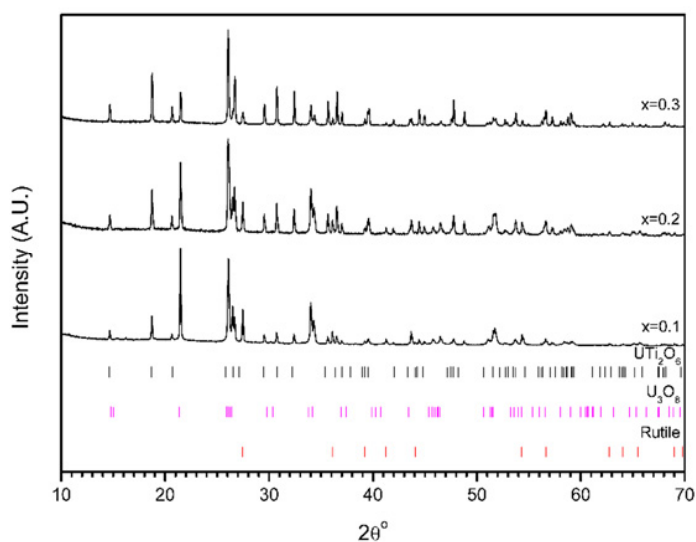


Figure 1: X-ray powder diffraction data for  $Gd_xU_{1-x}Ti_2O_6$  compositions sintered in air at 1320 °C

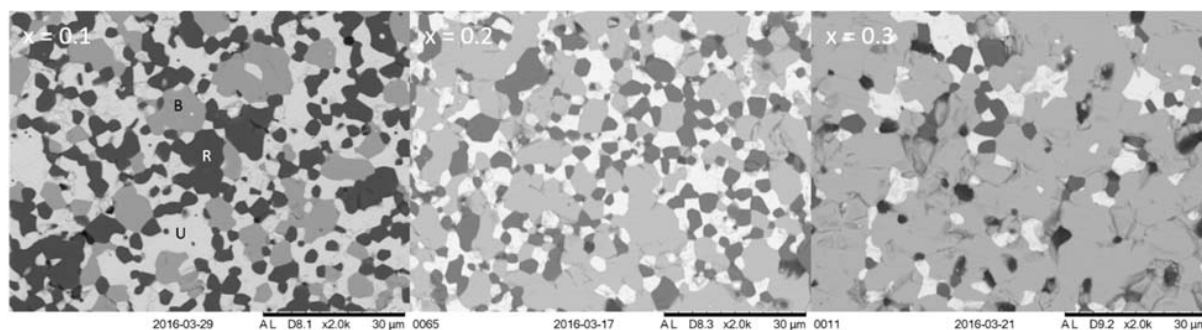


Figure 2: Representative backscattered electron images for  $Gd_xU_{1-x}Ti_2O_6$  compositions sintered in air at 1320 °C.  
B = Brannerite, R = Rutile, U =  $U_3O_8$ .

Sintering samples in air was found to result in the formation of three distinct phases; brannerite,  $U_3O_8$  and rutile ( $TiO_2$ ). Patchett and Nuffield (1960) found that sintering stoichiometric brannerite batches in air results in the formation of rutile and  $U_3O_8$  (6); it would therefore appear that the addition of Gd stabilizes the formation of the brannerite phase in air. These results are in agreement with both Vance et al (2001) and James and Watson (2002) who also found that Gd stabilized the formation of brannerite in air and that Gd-substituted brannerites with  $x \leq 0.3$  formed a mixture of brannerite,  $U_3O_8$  and rutile (7,8).

SEM-EDX was used to study the elemental distribution of brannerites synthesised in air, typical results are shown in Figure 3. Uranium was found to be localised in the  $U_3O_8$  and brannerite phases with no incorporation apparent within regions identified as rutile. Similar to U, Ti was found to be localized in the rutile and brannerite phases with no incorporation apparent within regions identified as  $U_3O_8$ . Gd was found to be present throughout the samples but is preferentially incorporated into the brannerite phase and not the  $U_3O_8$  or rutile phases.

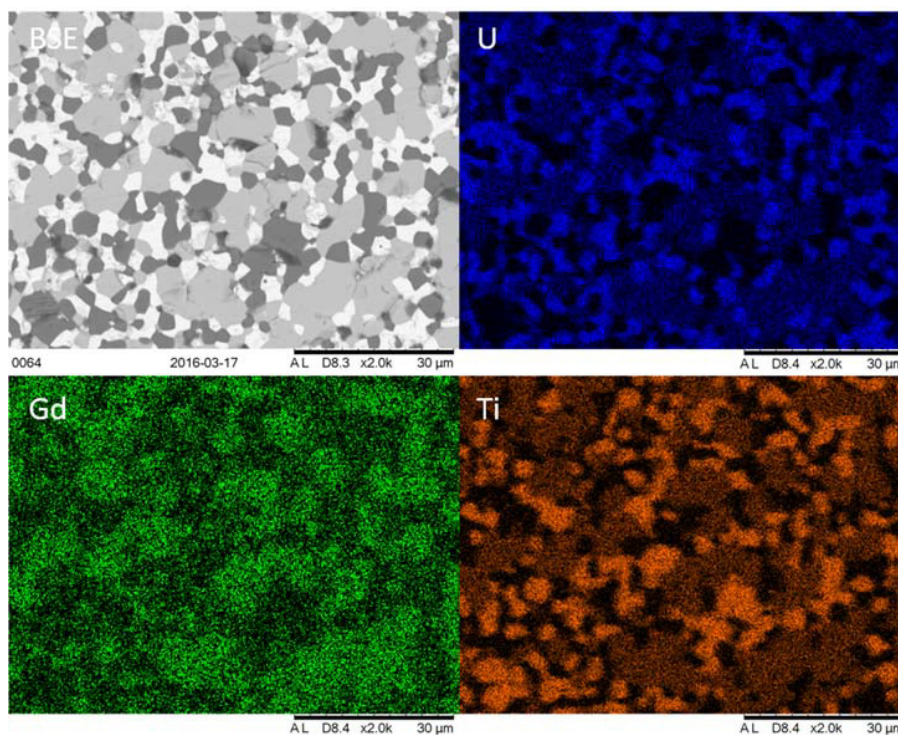


Figure 3: Representative backscattered electron image and EDX maps of U, Gd and Ti for  $Gd_{0.2}U_{0.8}Ti_2O_6$  sintered in air at 1320 °C.

### 3.2. Air sintered samples

Sintering samples under an argon atmosphere resulted in a different phase assemblage to that observed for air fired samples. When analysed by XRD, sharp peaks indicative of prototypical brannerite were found in all cases however, it was found that the level of Gd substitution affected the final phase assemblage. As shown in figure 4, samples with  $x = 0.1$  were found to form near single phase brannerite, inclusions of unreacted  $UO_2$  and rutile were also observed. Samples with  $x = 0.2$  or  $0.3$  did not show evidence of retained  $UO_2$  but were instead found to contain an additional pyrochlore phase (major peaks evident at approximately 15, 31 and 39 °2 $\theta$ ) and minor inclusions of rutile. Considering the relative intensities of the pyrochlore peaks observed, it would appear that increasing Gd substitution simply results in the formation of a greater amount of the pyrochlore phase. Multiple heat treatments at 1320 °C and duplicated experiments at 1400 °C, see Figure 5, did not result in more favourable phase assemblages indicating that the observed phase assemblages are most likely not a result of kinetic factors and more likely the result of compositional effects. These results are supported by the microstructures observed by electron microscopy.

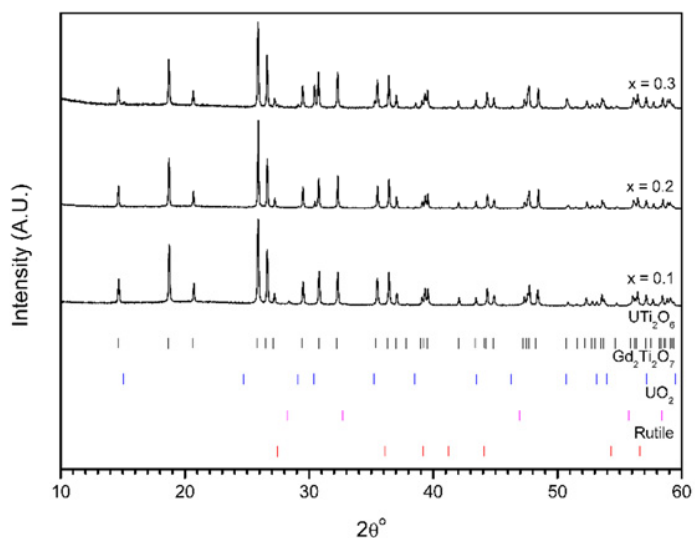


Figure 4: X-ray powder diffraction data for  $Gd_xU_{1-x}Ti_2O_6$  compositions sintered in argon at 1320 °C

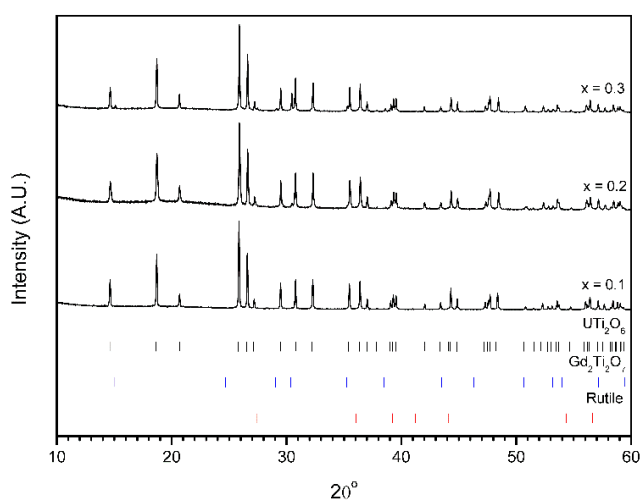
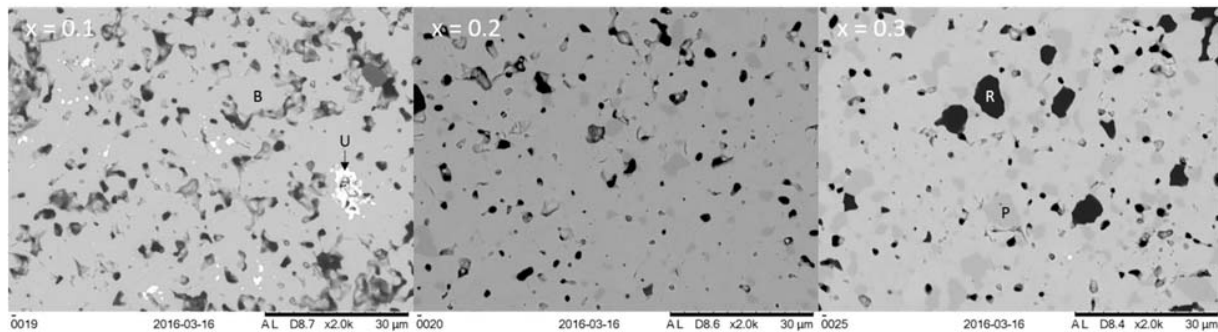
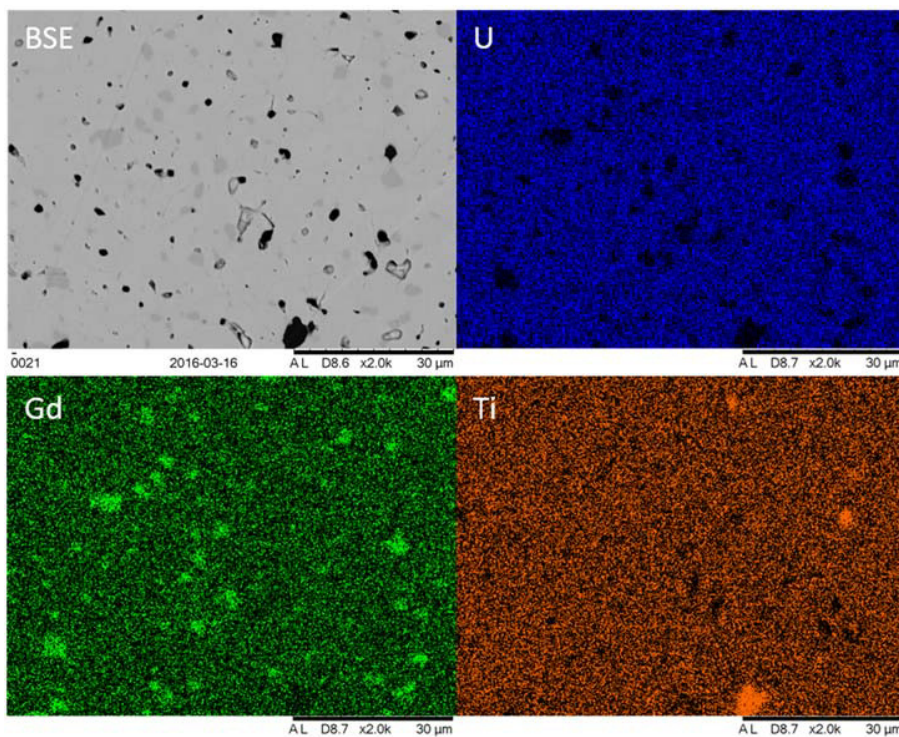


Figure 5: X-ray powder diffraction data for  $Gd_xU_{1-x}Ti_2O_6$  compositions sintered in argon at 1400 °C

The refined lattice parameters, see Table 1, suggest that despite increasing amounts of Gd being added to the initial batch; no extra Gd is incorporated into the brannerite structure with increasing Gd substitution. Considering the respective ionic radii of U(IV) and Gd (III) in six-fold co-ordination (0.89 and 0.938 Å<sup>(9)</sup>); it would be expected that the incorporation of increasing amounts of Gd would result in an increase in the lattice parameters of the unit cell, as can be seen there is no notable variation in the lattice parameters with respect to Gd substitution.

Table 1: Refined lattice parameters for the  $\text{Gd}_x\text{U}_{1-x}\text{Ti}_2\text{O}_6$  compositions sintered in inert atmospheres

x	a	b	c	$\beta$
0.1	9.8199(2)	3.7648(1)	6.9232(1)	118.841(1)
0.2	9.8190(2)	3.7591(1)	6.9170(1)	118.794(1)
0.3	9.8203(2)	3.7592(1)	6.9176(1)	118.787(1)

Figure 6: Representative backscattered electron images for  $\text{Gd}_x\text{U}_{1-x}\text{Ti}_2\text{O}_6$  compositions sintered in air at 1320 °C. B = Brannerite, P = Pyrochlore, R = Rutile, U =  $\text{UO}_2$ .Figure 7: Representative backscattered electron image and EDX maps of U, Gd and Ti for  $\text{Gd}_{0.2}\text{U}_{0.8}\text{Ti}_2\text{O}_6$  sintered in argon at 1320 °C.

As can be seen in Figure 6, increasing Gd substitution leads to the formation of greater amounts of a secondary phase, this was determined to be the pyrochlore phase found by x-ray diffraction.

Figure 7 shows the typical elemental distribution of Gd-substituted brannerites with  $x \geq 0.2$  synthesised under inert atmospheres. As can be seen, although brannerite is present as a majority phase, the secondary pyrochlore phase is present throughout the sample. Gd is present throughout the sample however, the concentration of Gd within the pyrochlore phase may result in decreased criticality performance for a final wasteform.

The results reported in this study are in contrast to those reported by both Vance et al (2001) and James and Watson (2002)<sup>(7,8)</sup>. The solid solution limit of Gd in brannerite synthesized in Ar quoted by James and Watson,  $0 < x < 0.45$ , does not correlate with the observations from this work which indicate that the solubility limit of Gd is  $< 0.2$  formula units. These findings are clearly evidenced by the X-ray diffraction and scanning electron microscopy data.

#### 4. Conclusions

This study has found that the synthesis of brannerite compositions for MOX residue disposal requires careful control of the system stoichiometry and processing conditions. Sintering material in air produces an unfavourable mixture of brannerite,  $U_3O_8$  and rutile. Increasing substitution of Gd for U improves the final observed phase assemblage. However, in order to achieve a single phase wasteform, the level of substitution would have to be such that the final waste loading of any wasteform would be significantly reduced. When brannerites are synthesised in inert atmospheres, the level of Gd substitution has been shown to have a strong effect on the final phase assemblage. Substitution of  $\geq 0.2$  formula units of Gd results in the formation of a parasitic pyrochlore phase that preferentially incorporates Gd.

Although this study has investigated the synthesis of Gd substituted uranium brannerites, the behaviour of plutonium in a final wasteform remains uncertain. Further investigation using either a surrogate, e.g. Ce, or plutonium is necessary to be certain of the solid state chemistry of a final MOX wasteform.

#### Acknowledgements

UK EPSRC is thanked for providing studentship for DJB through the Nuclear FiRST Doctoral Training Centre (Grant EP/G037140/1). NCH is grateful to the Royal Academy of Engineering and Nuclear Decommissioning Authority for funding. This research was performed in part at the MIDAS Facility, at the University of Sheffield, which was established with support from the Department of Energy and Climate Change.

#### References

1. Wilson PD. The Nuclear Fuel Cycle: From Ore to Waste. 1st ed. Oxford: Oxford University Press; 1996. 323 p.
2. Szymanski J. T., Scott J. D. A Crystal Structure Refinement of Synthetic Brannerite,  $UTi_2O_6$ , and Its Bearing on Rate of Alkaline-Carbonate Leaching of Brannerite in Ore. *Can Mineral.* 1982;**20**:271–9.
3. Ryerson FJ, Ebbinghaus B. Pyrochlore-Rich Titanate Ceramics for the Immobilization of Plutonium: Redox Effects on Phase Equilibria in Cerium- and Thorium- Substituted Analogs. 2000.
4. Zhang Y, Lumpkin GR, Li H, Blackford MG, Colella M, Carter ML, et al. Recrystallisation of amorphous natural brannerite through annealing: The effect of radiation damage on the chemical durability of brannerite. *J Nucl Mater.* 2006;**350**:293–300.
5. Lumpkin GR. Alpha-decay damage and aqueous durability of actinide host phases in natural systems. *J Nucl Mater.* 2001;**289**(1-2):136–66.
6. Patchett JE, Nuffield EW. THE SYNTHESIS AND CRYSTALLOGRAPHY OF BRANNERITE, [PART] 10 OF STUDIES OF RADIOACTIVE COMPOUNDS. *Can Mineral.* 1960;**6**:483–90.
7. Vance ER, Watson JN, Carter ML, Day R a, Begg BD. Crystal Chemistry and Stabilization in Air of Brannerite,  $UTi_2O_6$ . *J Am Ceram Soc.* 2001;**44**:141–4.
8. James M, Watson JN. The Synthesis and Crystal Structure of Doped Uranium Brannerite Phases  $U_{1-x}M_xTi_2O_6$  ( $M=Ca^{2+}$ ,  $La^{3+}$ , and  $Gd^{3+}$ ). *J Solid State Chem.* 2002;**165**:261–5.
9. Shannon RD. Revised Effective Ionic Radii and Systematic Studies of Interatomic Distances in Halides and Chalcogenides. *Acta Crystallogr.* 1976;**32**:751–67.

## Synthesis and Characterization of Brannerite Compositions for MOX Residue Disposal

D.J. Bailey<sup>1\*</sup>, M.C. Stennett<sup>1</sup> and N.C. Hyatt<sup>1</sup>

<sup>1</sup>Immobilisation Science Laboratory, Department of Materials Science and Engineering, University of Sheffield, Mappin Street, Sheffield, S1 3JD, United Kingdom

### ABSTRACT

Due to their high actinide content MOX residues require immobilization within a robust host matrix. Although it is possible to immobilize actinides in vitreous wasteforms; ceramic phases, such as brannerite ( $UTi_2O_6$ ), are attractive due to their high waste loading capacity and relative insolubility. Brannerites  $Gd_{0.1}U_{0.9}Ti_2O_6$ ,  $Ce_{0.1}U_{0.9}Ti_2O_6$  and  $Gd_{0.1}U_{0.81}Ce_{0.09}Ti_2O_6$  were prepared using an oxide route. Charge compensation of trivalent cations was expected to occur via the oxidation of U (IV) to higher valence states (U (V) or U (VI)). Gd was added to act as a neutron absorber in the final Pu bearing wasteform and Ce was used as a structural surrogate for Pu. X-ray absorption spectroscopy showed that Ce (IV) was reduced to Ce (III) in all cases. X-ray powder diffraction of synthesized specimens found that the final phase assemblage was strongly affected by processing atmosphere (air or argon). Prototypical brannerite was formed in all compositions, secondary phases observed were found to vary according to processing atmosphere and stoichiometry. Microstructural analysis (SEM) of the sintered samples confirmed the results of the X-ray powder diffraction.

### INTRODUCTION

The accumulation of plutonium stockpiles as a result of civil reprocessing of spent nuclear fuel (SNF) presents a significant proliferation risk [1]. As a result, the reduction of Pu stockpiles is an issue of great importance. A possible method for the reduction of Pu stockpiles is re-use of Pu in mixed oxide fuel (MOX) to generate electricity. MOX fuels are composed of a mixture of uranium and plutonium oxides, typically 90-95 % U and 5 - 10% Pu [2]. Residues arising from the production of MOX fuels will require disposal and, consequently, require the design of a robust host matrix. Ceramic phases are particularly attractive for actinide-bearing wastes due to their ability to incorporate high actinide waste loadings. Brannerite,  $UTi_2O_6$ , is particularly attractive due to its high actinide content (~ 55 wt% U). A monoclinic phase with space group  $C2/m$ , brannerite is often an accessory mineral in uranium deposits and multiphase ceramic wasteforms for disposal of actinide-rich wastes [3], [4]. The brannerite structure consists of layers of  $TiO_6$  octahedra with larger cations, also in octahedral co-ordination, located between the layers. Naturally occurring brannerites have been shown to be chemically flexible with elements such as Ca, Y, Pb, Ce and Th incorporated on the A site (U) and Fe, Si and Al substituting on the B site (Ti)[5], [6]. Although natural samples are often found to be completely metamict, the presence of brannerite in alluvial sediments after the weathering of host rocks indicates that brannerites possess sufficient aqueous durability for consideration as potential host matrices for MOX residues[5]–[7]. Previous work has found that the Pu surrogate Ce forms an isostructural brannerite phase  $Ce_{0.975}Ti_2O_{5.95}$  and that Pu readily substitutes into the brannerite structure [8], [9]. This study was therefore conceived to investigate the possibility of using brannerite as a crystalline host phase for the disposal of MOX fuel residues.

## EXPERIMENT

### Materials synthesis

Brannerites with composition  $\text{Gd}_{0.1}\text{U}_{0.9}\text{Ti}_2\text{O}_6$ ,  $\text{Ce}_{0.1}\text{U}_{0.9}\text{Ti}_2\text{O}_6$  and  $\text{Gd}_{0.1}\text{U}_{0.81}\text{Ce}_{0.09}\text{Ti}_2\text{O}_6$  were synthesized via the oxide route under oxidizing or inert atmospheres (air or argon). Gd was added to act as a neutron absorber for the final Pu bearing wasteform. Ce was added to act as a surrogate for Pu. Charge balancing of trivalent cations was expected to occur via the oxidation of U(IV) to higher oxidation states (U(V), U(VI)) as observed in previous investigations [9], [10], [12].

Stoichiometric amounts of oxide precursors ( $\text{UO}_2$ ,  $\text{Gd}_2\text{O}_3$ ,  $\text{CeO}_2$  and  $\text{TiO}_2$ ) were mixed with isopropanol to form a slurry and ball milled using a Fritsch Pulverisette 23 for five minutes at a frequency of 30 Hz. The milled slurry was then dried in an oven. Sintered pellets were produced by uniaxially pressing 0.6 g of material in a hardened steel die with a load of 2 tons to form a green body followed by reaction under flowing air or argon at 1320 °C for 24 hours.

### Materials characterization

Sintered brannerites were ground and characterized by X-ray powder diffraction using a Bruker D2 Phaser in Bragg-Brentano geometry using Cu K $\alpha$  radiation (1.5418 Å). A Ni foil was used to filter Cu K $\beta$  radiation.

Microstructure and phase distribution of sintered pellets was investigated by scanning electron microscopy and energy dispersive X-ray spectroscopy (SEM-EDX) using a Hitachi TM3030 SEM equipped with a Bruker Quantax EDX detector. Samples were prepared for SEM analysis by mounting in cold setting resin and polishing with progressively finer SiC paper and diamond pastes to an optical finish (1  $\mu\text{m}$ ). Samples were sputter coated with carbon to reduce surface charging effects.

Average cerium oxidation state was determined by X-ray absorption near edge spectroscopy (XANES) at the Ce L-III edge (5723 eV) and comparison with standards of known oxidation state:  $\text{CePO}_4$  (Ce (III)) and  $\text{CeO}_2$  (Ce (IV)). Measurements were made using beamline X23A2, National Synchrotron Lightsource, Brookhaven National Laboratory. Samples were prepared for XAS analysis by grinding and homogeneously mixing reacted powders with polyethylene glycol and uniaxially pressing to form 13 mm diameter. Incident ( $I_0$ ) X-ray intensities were measured using an ion chamber. Ce edge fluorescence was measured using a four element Si-drift detector. XANES spectra were measured from 30 eV below the edge of interest to 250 eV above. A Si (311) monochromator was used to tune the energy of incident photons giving an energy resolution of  $\pm 0.3$  eV. Data reduction and XANES analysis were performed using the program Athena [11].

## DISCUSSION

### Powder X-ray diffraction

All synthesized brannerites were characterized by powder X-ray diffraction. Results of X-ray diffraction analysis showed sharp reflections indicative of prototypical brannerite for all compositions, as shown in Figure 1.

When sintered in air,  $\text{U}_3\text{O}_8$  and rutile ( $\text{TiO}_2$ ) were also observed, see Figure 1a. For samples substituted with only Ce or Gd, the most intense peaks were found to be those of  $\text{U}_3\text{O}_8$  indicating that  $\text{U}_3\text{O}_8$  was the major crystalline phase in these samples. Co-substitution of Gd and Ce resulted

in a relative decrease in the intensity of peaks attributed to  $U_3O_8$  and rutile indicating a higher yield of the target brannerite phase.

Sintering in argon yielded a different phase assemblage with brannerite found to be the major crystalline phase and  $UO_2$  and rutile ( $TiO_2$ ) observed as secondary phases, see Figure 1b.

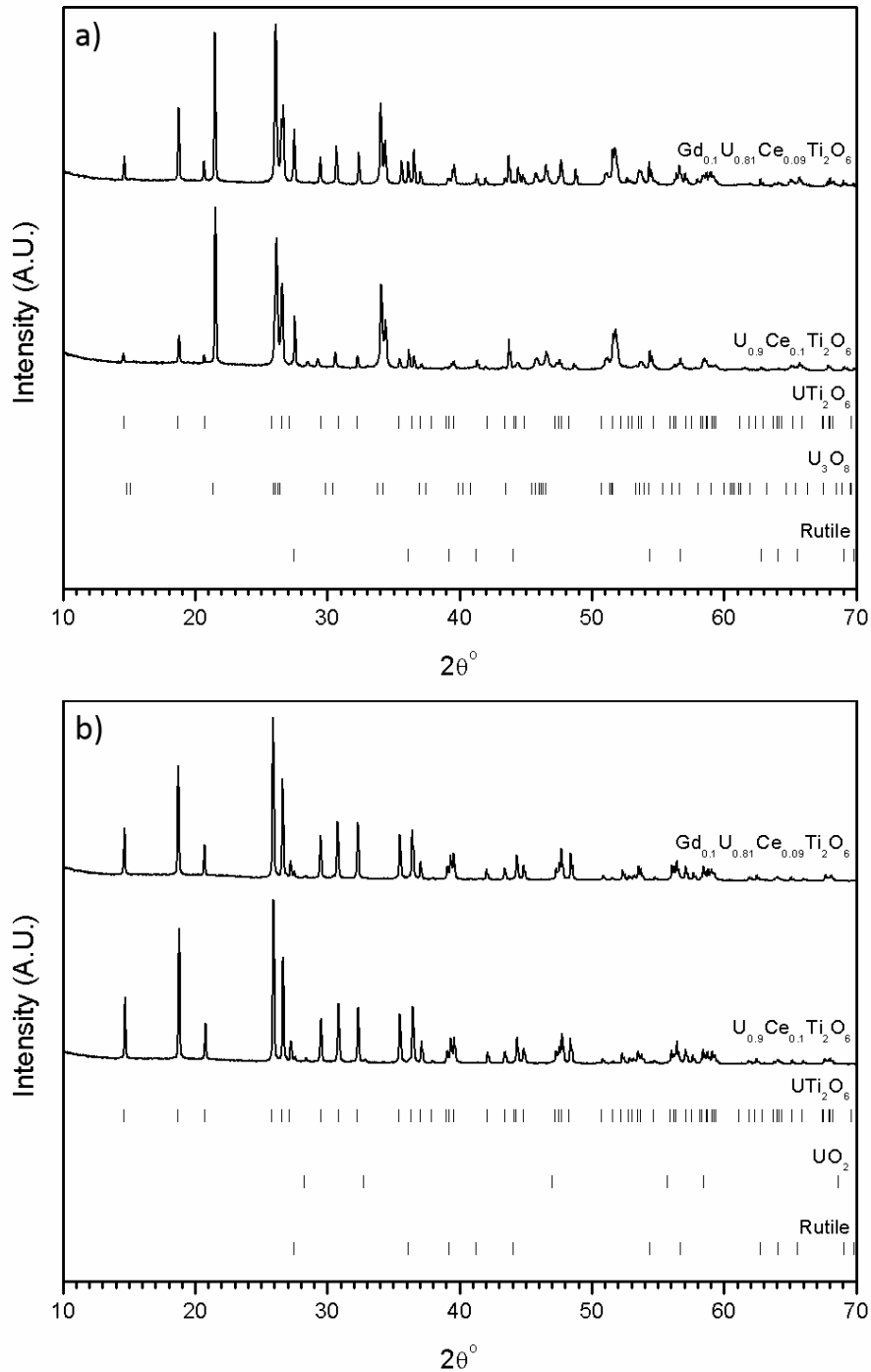


**Figure 1:** Powder X-ray diffraction results for synthesized brannerite compositions sintered in a) Air and b) Argon.

## SEM-EDX

Scanning electron microscopy was used to examine the microstructure of sintered samples. In agreement with XRD data, brannerite was observed in all cases with differing accompanying phases present dependent upon processing atmosphere. The brannerite microstructures observed by scanning electron microscopy closely matched those indicated by X-ray diffraction.

Sintering samples in air was shown to result in the formation of three distinct phases: brannerite,  $U_3O_8$  and rutile ( $TiO_2$ ), see Figure 2. Patchett and Nuffield (1960) found that sintering stoichiometric brannerite batches (i.e.  $UTi_2O_6$ ) in air resulted in the formation of rutile and  $U_3O_8$  [12]; it would therefore appear that the addition of Gd or Ce stabilizes the formation of brannerite in air. This is in agreement with previous studies of Gd substitution in brannerite that have found that Gd stabilized the formation of brannerite in air and that Gd-substituted brannerites with  $x \leq 0.3$  formed a mixture of brannerite,  $U_3O_8$  and rutile [9], [10], [13].

Sintering samples in an argon atmosphere was found to result in near single phase brannerite with minor inclusions of rutile and  $UO_2$  for samples containing Gd or Ce only. Co-substitution of Gd and Ce resulted in the formation of an additional pyrochlore structured phase with the Gd being preferentially incorporated into the pyrochlore, see Figure 3 and Figure 4. These results are similar to those described by Bailey et al (2016), who found that increasing substitution of Gd in the  $Gd_xU_{1-x}Ti_2O_6$  system led to the formation of a pyrochlore phase that preferentially incorporated Gd [13].

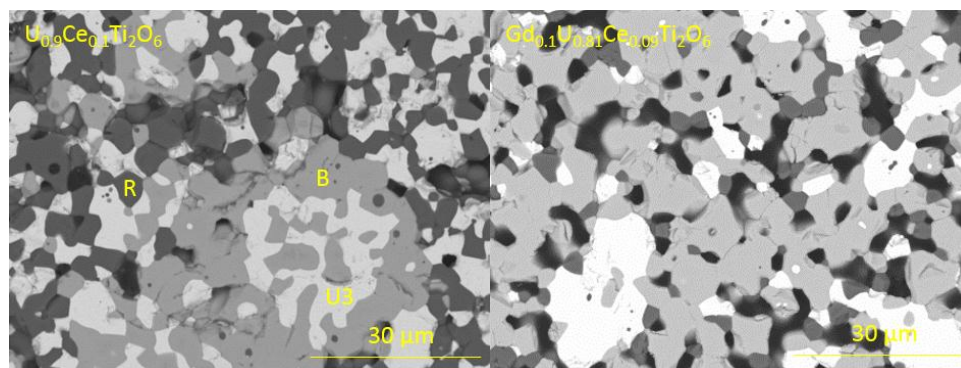


**Figure 2:** Back-scattered electron images of brannerite compositions sintered in air. R = Rutile, B = Brannerite and U3 =  $U_3O_8$ . Results for  $Gd_{0.1}U_{0.9}Ti_2O_6$  not shown.

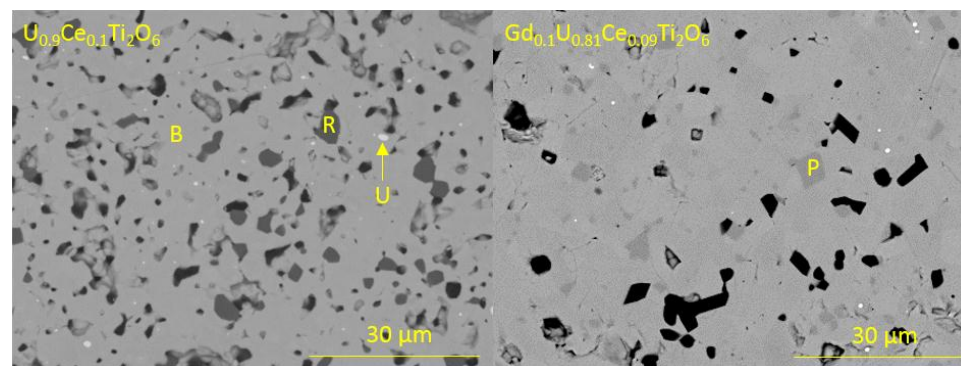


**Figure 3:** Back-scattered electron images of brannerite compositions sintered in argon. R = Rutile, B = Brannerite, U =  $UO_2$  and P = Pyrochlore. Results for  $Gd_{0.1}U_{0.9}Ti_2O_6$  not shown.

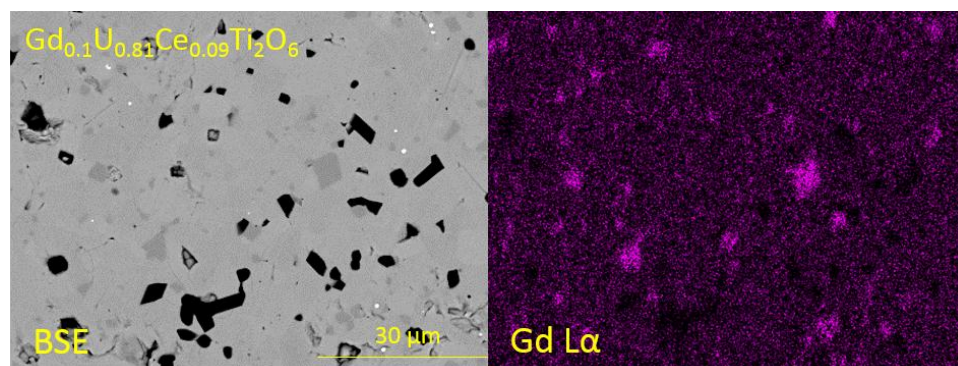


**Figure 4:** Relative enrichment of Gd in the pyrochlore phase relative to the bulk brannerite phase.

### Ce XANES

Ce L-III edge XANES spectra allow straightforward fingerprinting of Ce oxidation state. Comparison of spectra edge shifts, white line positions and post-edge oscillations of Ce in synthesized brannerites to standards shows that the dominant Ce oxidation state is Ce (III). This indicates that the cerium has been reduced from Ce (IV) to Ce (III) during synthesis. This reduction occurs regardless of processing atmosphere or composition. The reduction of Ce (IV) to Ce (III) during processing aids in the explanation of the relative increase of brannerite in samples synthesized in air and the formation of the pyrochlore phase for co-substituted samples sintered in Ar. Ce (III) acts as an additional charge compensating species allowing the incorporation of a larger amount of oxidized U (U (V)/U(VI)) to be incorporated into the brannerite structure and subsequent increase in brannerite yield, similar to the results of previous studies concerning the substitution of Gd [9], [10], [13].

### CONCLUSIONS

This study has found that the synthesis of brannerite compositions for MOX residue disposal requires careful control of the system stoichiometry and processing conditions. Cerium is auto-reduced regardless of processing atmosphere and stoichiometry. Sintering material in air produced a mixture of brannerite,  $U_3O_8$  and rutile. Increasing addition of charge compensating species ( $Ce^{3+}$  and  $Gd^{3+}$ ) resulted in the formation of a greater amount of the target brannerite phase. When brannerites were synthesized in inert atmospheres, near single phase brannerite was produced for substitution of either Gd or Ce only. Co-substitution of Gd and Ce results in the formation of a parasitic pyrochlore phase that preferentially incorporates Gd. An investigation of Pu substitution is underway using the General Utility Lattice Program to determine whether Pu incorporation into the brannerite structure is more energetically favorable as Pu (III) or Pu (IV).

### ACKNOWLEDGMENTS

UK EPSRC is thanked for providing studentship for DJB through the Nuclear FiRST Doctoral Training Centre (Grant EP/G037140/1). NCH is grateful to the Royal Academy of Engineering

and Nuclear Decommissioning Authority for funding. Use of the National Synchrotron Light Source, Brookhaven National Laboratory, was supported by the U.S. Department of Energy, Office of Science, Office of Basic Energy Sciences, under Contract No. DE-AC02-98CH10886. This research was performed in part at the MIDAS Facility, at the University of Sheffield, which was established with support from the Department of Energy and Climate Change.

## REFERENCES

- [1] N. C. Hyatt, "Plutonium management policy in the United Kingdom: The need for a dual track strategy," *Energy Policy*, **99**, (In press, 2016).
- [2] P. D. Wilson, *The Nuclear Fuel Cycle: From Ore to Waste*, 1st ed (Oxford University Press, Oxford, 1996).
- [3] J. T. Szymanski and J. D. Scott, "A Crystal Structure Refinement of Synthetic Brannerite,  $UTi_2O_6$ , and Its Bearing on Rate of Alkaline-Carbonate Leaching of Brannerite in Ore," *Can. Mineral.*, **20**, 271–279 (1982).
- [4] F. J. Ryerson and B. Ebbinghaus, "Pyrochlore-Rich Titanate Ceramics for the Immobilization of Plutonium: Redox Effects on Phase Equilibria in Cerium- and Thorium- Substituted Analogs," Lawrence Livermore National Laboratory Report, UCRL-ID-139092 (2000).
- [5] Y. Zhang, G. R. Lumpkin, H. Li, M. G. Blackford, M. Colella, M. L. Carter, and E. R. Vance, "Recrystallisation of amorphous natural brannerite through annealing: The effect of radiation damage on the chemical durability of brannerite," *J. Nucl. Mater.*, **350**, 293–300 (2006).
- [6] F. A. Charalambous, R. Ram, M. I. Pownceby, J. Tardio, and S. K. Bhargava, "Chemical and microstructural characterisation studies on natural and heat treated brannerite samples," *Miner. Eng.*, **39**, 276–288 (2012).
- [7] G. R. Lumpkin, "Alpha-decay damage and aqueous durability of actinide host phases in natural systems," *J. Nucl. Mater.*, **289** (1–2), 136–166 (2001).
- [8] M. C. Stennett, C. L. Freeman, A. S. Gandy, and N. C. Hyatt, "Crystal structure and non-stoichiometry of cerium brannerite:  $Ce_{0.975}Ti_2O_{5.95}$ ," *J. Solid State Chem.*, **192**, 172–178 (2012).
- [9] E. R. Vance, J. N. Watson, M. L. Carter, R. A. Day, and B. D. Begg, "Crystal Chemistry and Stabilization in Air of Brannerite,  $UTi_2O_6$ ," vol. 44, pp. 141–144, 2001.
- [10] M. James and J. N. Watson, "The Synthesis and Crystal Structure of Doped Uranium Brannerite Phases  $U_{1-x}M_xTi_2O_6$  ( $M=Ca^{2+}$ ,  $La^{3+}$ , and  $Gd^{3+}$ )," *J. Solid State Chem.*, **165**, 261–265 (2002).
- [11] B. Ravel and M. Newville, "ATHENA, ARTEMIS, HEPHAESTUS: Data analysis for X-ray absorption spectroscopy using IFEFFIT," *Journal of Synchrotron Radiation*, **12** (4), 537–541 (2005).
- [12] J. E. Patchett and E. W. Nuffield, "Studies of Radioactive Compounds X- The Synthesis and Crystallography of Brannerite," *Can. Mineral.*, **6**, 483–490 (1960).
- [13] D. J. Bailey, M. C. Stennett, and N. C. Hyatt, "Synthesis and Characterization of Brannerite Wasteforms for the Immobilization of Mixed Oxide Fuel Residues," *Procedia Chem.*, **21**, 371–377 (2016).

## ARTICLE OPEN

## Multi-scale investigation of uranium attenuation by arsenic at an abandoned uranium mine, South Terras

Claire L. Corkhill<sup>1</sup>, Daniel E. Crean<sup>2</sup>, Daniel J. Bailey<sup>1</sup>, Carmen Makepeace<sup>1</sup>, Martin C. Stennett<sup>1</sup>, Ryan Tappero<sup>3</sup>, Daniel Grolimund<sup>4</sup> and Neil C. Hyatt<sup>1</sup>

Detailed mineralogical analysis of soils from the UK's historical uranium mine, South Terras, was performed to elucidate the mechanisms of uranium degradation and migration in the 86 years since abandonment. Soils were sampled from the surface (0–2 cm) and near-surface (25 cm) in two distinct areas of ore processing activities. Bulk soil analysis revealed the presence of high concentrations of uranium (<1690 p.p.m.), arsenic (1830 p.p.m.) and beryllium (~250 p.p.m.), suggesting pedogenic weathering of the country rock and ore extraction processes to be the mechanisms of uranium ore degradation. Micro-focus XRF analysis indicated the association of uranium with arsenic, phosphate and copper;  $\mu$ -XRD data confirmed the presence of the uranyl-arsenate minerals metazeunerite ( $\text{Cu}(\text{UO}_2)_2(\text{AsO}_4)_2 \cdot 8\text{H}_2\text{O}$ ) and metatorbernite ( $\text{Cu}(\text{UO}_2)_2(\text{PO}_4)_2 \cdot 8\text{H}_2\text{O}$ ) to be ubiquitous. Our data are consistent with the solid solution of these two uranyl-mica minerals, not previously observed at uranium-contaminated sites. Crystallites of uranyl-mica minerals were observed to coat particles of jarosite and muscovite, suggesting that the mobility of uranium from degraded ores is attenuated by co-precipitation with arsenic and phosphate, which was not previously considered at this site.

*npj Materials Degradation* (2017)1:19; doi:10.1038/s41529-017-0019-9

## INTRODUCTION

The UK's most important uranium-producing mine, South Terras, is located in the St. Austell District of Cornwall (SW England, Supplementary Fig. 1), which operated between 1873 and 1930. The primary ore, pitchblende (primarily  $\text{UO}_2$  and  $\text{U}_3\text{O}_8$ ), is associated with late stage metamorphism related to the St. Austell granitic intrusion, formed 225 Ma.<sup>1</sup> Secondary uranium-ores of torbernite ( $\text{Cu}(\text{UO}_2)_2(\text{PO}_4)_2 \cdot 12\text{H}_2\text{O}$ ) and autunite ( $\text{Ca}(\text{UO}_2)_2(\text{PO}_4)_2 \cdot 12\text{H}_2\text{O}$ ) formed 60 Ma.<sup>2,3</sup> In the 57 year period of operation before closure, South Terras produced 736 tonnes of uranium.<sup>1</sup> The discovery of radium, in 1911, focused mining operations on the uranium spoil heaps at the site, which were investigated by Marie Curie.<sup>1</sup> The tailings were reworked to extract radium through  $\text{BaSO}_4$  recovery methods.<sup>1</sup>

South Terras has been considered to be a "natural laboratory" for the environmental degradation and behaviour of naturally occurring radionuclides.<sup>4–6</sup> Previous investigations have attempted to elucidate the degradation process of uranium ores and the subsequent transport of uranium from the spoil heaps into the River Fal (Supplementary Fig. 1). Currently, two key hypotheses remain open: i) small uranium-rich particles are transported from the sediments to the stream<sup>6</sup> and/or; ii) uranyl-phosphate or uranyl-carbonate species are transported by groundwater.<sup>4,7</sup> To accurately predict the U(VI) transport processes with reactive transport models, detailed understanding of uranium ore degradation mechanisms and uranium speciation, from the macro-scale to the micro-scale, is necessary. We present the results of a detailed multi-modal micro-focus X-ray fluorescence spectroscopy and diffraction characterisation of South

Terras soils, complemented with macro-scale analyses, and reveal the presence of important phases not previously considered in uranium speciation models of the site, which may influence the long-term release of uranium from the soils. This study contributes to the management of legacy uranium contamination at sites with a complex industrial history.

## RESULTS

## Bulk soil properties

XRD analysis revealed the ubiquitous presence of muscovite ( $\text{KAl}_2(\text{AlSi}_3\text{O}_{10})(\text{OH})_2$ ), quartz ( $\text{SiO}_2$ ) and jarosite ( $\text{KFe}_3(\text{OH})_6(\text{SO}_4)_2$ ) (Supplementary Fig. 2), in agreement with previous analysis of soils from South Terras.<sup>5,6</sup> Additional goethite ( $\text{FeO}(\text{OH})$ ) and the zeolite, montesommaite ( $(\text{K},\text{Na})_9\text{Al}_9\text{Si}_{23}\text{O}_{64} \cdot 10\text{H}_2\text{O}$ ), were identified at the Ochre Works (OW) location, reflecting the different ore degradation mechanisms at this sample location.

Uranium-containing, sub-micron phases with a platy morphology were observed to coat the surfaces of lower z-contrast (i.e., not uranium-containing) particles. Figure 1 shows an example of this morphology in particles from 25 cm depth (Dressing Floor (DF) location). Elemental mapping analysis confirmed the presence of uranium, which was found to occur in association with arsenic, copper and phosphorus (Fig. 1). The underlying particle contained silicon, aluminium, sulphur and iron, which is in agreement with the XRD identification of muscovite and jarosite.

<sup>1</sup>Department of Materials Science and Engineering, NucleUS Immobilisation Science Laboratory, The University of Sheffield, Sheffield, UK; <sup>2</sup>Atomic Weapons Establishment plc, Aldermaston, Berkshire RG7 4PR, UK; <sup>3</sup>Photon Sciences Directorate, Brookhaven National Laboratory, Upton, NY, USA and <sup>4</sup>Swiss Light Source, Paul Scherrer Institute, Villigen 5232, Switzerland

Correspondence: Claire L. Corkhill (c.corkhill@sheffield.ac.uk) or Neil C. Hyatt (n.c.hyatt@sheffield.ac.uk)

Received: 6 June 2017 Revised: 24 September 2017 Accepted: 29 September 2017

Published online: 14 December 2017

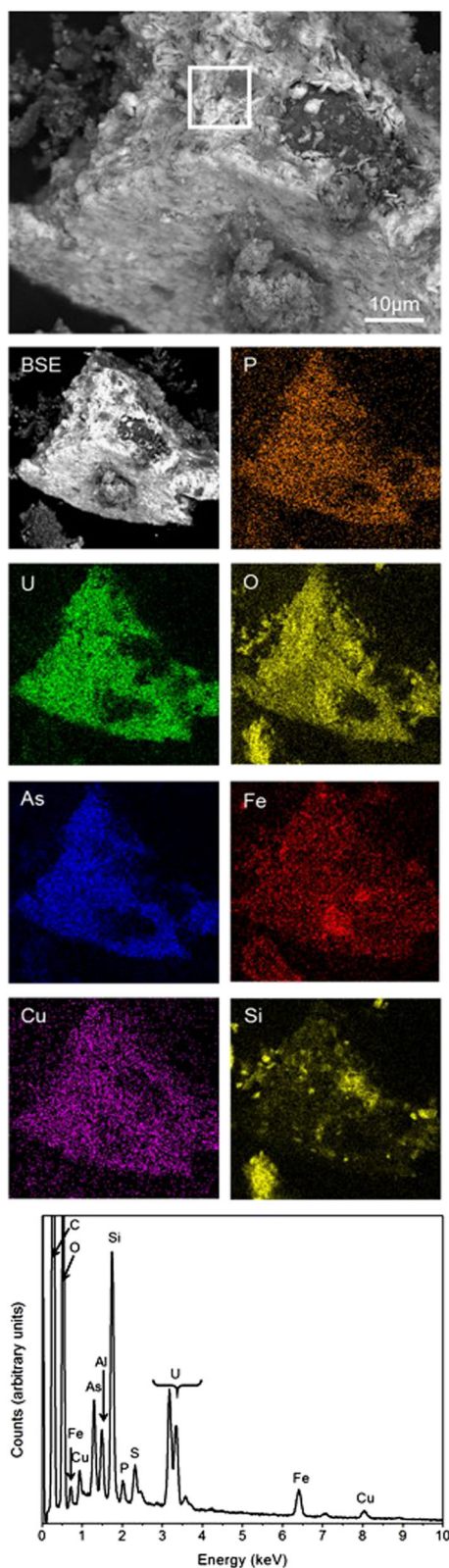


**Fig. 1** SEM and EDX analysis of a uranium-bearing particle in soil from the Dressing Floor location (25 cm), showing the uranium morphology and distribution of associated elements. EDX spectrum summed from map taken in the ROI indicated by the white square box

**Table 1.** Concentration of selected elements in South Terras soil locations, derived from total acid digest (residual fraction, Supplementary Table 2) and ICP-AES analysis

	Elemental concentration (p.p.m.)		
	Ochre Works 0–2 cm	Dressing Floor 25 cm	Dressing Floor 0–2 cm
Be	$(2.43 \pm 0.07) \times 10^2$	$(2.49 \pm 0.07) \times 10^2$	$(2.78 \pm 0.08) \times 10^2$
P	$(1.22 \pm 0.73) \times 10^3$	$(7.18 \pm 0.63) \times 10^2$	$(1.35 \pm 0.02) \times 10^3$
V	$(1.81 \pm 0.05) \times 10^2$	$(9.20 \pm 0.30) \times 10^1$	$(6.70 \pm 0.02) \times 10^1$
Cu	$(3.15 \pm 0.12) \times 10^2$	$(5.00 \pm 0.02) \times 10^2$	$(5.18 \pm 0.07) \times 10^2$
As	$(1.83 \pm 0.03) \times 10^3$	$(3.28 \pm 0.06) \times 10^3$	$(2.00 \pm 0.01) \times 10^3$
Pb	$(1.22 \pm 0.05) \times 10^3$	$(1.17 \pm 0.02) \times 10^3$	$(2.87 \pm 0.14) \times 10^3$
U	$(1.11 \pm 0.09) \times 10^2$	$(1.69 \pm 0.37) \times 10^3$	$(3.66 \pm 0.07) \times 10^2$

Note: Error estimates are  $\pm 1$  standard deviation of replicate (10) analysis. See Supplementary Table 1, for all elemental analysis

#### Total acid digest analysis

Uranium concentrations, shown in Table 1, ranged from  $111 \pm 9$  p.p.m. to  $1690 \pm 370$  p.p.m. The uranium concentration in soils taken at 25 cm (DF location) was significantly higher than the two surface (0–2 cm) soils. Significant concentrations of arsenic were observed, ranging from  $1830 \pm 30$  p.p.m. to  $3280 \pm 60$  p.p.m., consistent with the mining activities at the site and also with pedogenesis of the country rock, which has been reported to contain the arsenate minerals scorodite ( $\text{FeAsO}_4 \cdot 2\text{H}_2\text{O}$ ) and pharmacosiderite  $[(\text{AsO}_4)_3(\text{OH})_3 \cdot 6\text{H}_2\text{O}]$ .<sup>3</sup> Average stream water concentrations of arsenic in the vicinity of South Terras were recently determined as 99 p.p.m. by the TELLUS airborne geophysical survey,<sup>8</sup> which is significantly above the World Health Organisation drinking water limit of 0.1 p.p.m.<sup>9</sup> To our knowledge, despite detailed investigation of uranium at the site, the migration of arsenic to the River Fal has not previously been investigated.

Notably high beryllium concentrations were observed, at  $\sim 250$  p.p.m., across the site (Table 1). The average crustal abundance of beryllium is 3 p.p.m., but in areas of pegmatitic igneous activity, soil concentrations can be elevated. Previously, beryllium has been identified in the St. Austell area, occurring in minerals such as danalite  $[(\text{Fe}_4(\text{Be}_3\text{Si}_3\text{O}_{12})\text{S}]$ , phenacite ( $\text{Be}_2\text{SiO}_4$ ) and bertrandite ( $\text{Be}_4\text{Si}_2\text{O}_7(\text{OH})_2$ ).<sup>2</sup> Although beryllium minerals were not identified in the present study, to our knowledge, elevated soil concentrations of beryllium at South Terras have not previously been reported.

#### Sequential extraction analysis

The fraction of uranium determined in each extraction step, expressed as a percent of the total digest concentration (Table 1), is shown in Fig. 2. The greatest proportion of uranium was located in the residual and recalcitrant fractions, followed by the oxidisable fraction. The lowest proportion was observed in the reducible and exchangeable fractions. Elements that showed similar behaviour to uranium were arsenic, phosphorus and copper (Supplementary Fig. 3), suggesting that uranium is closely associated with these elements, in agreement with EDX analysis (Fig. 1).

#### Micro-focus analysis of major uranium particles

To obtain a positive identification of the form of uranium present in South Terras soils, a combination of  $\mu$ -XRF and  $\mu$ -XRD analyses were performed. Micro-XRF was used to identify U-enriched particles and phase identification was subsequently performed by  $\mu$ -XRD. Large uranium-bearing particles in all South Terras soils were associated with copper and arsenic, as shown by  $\mu$ -XRF maps (Fig. 3a). Micro-XRD analysis of particles from 25 cm (DF location,

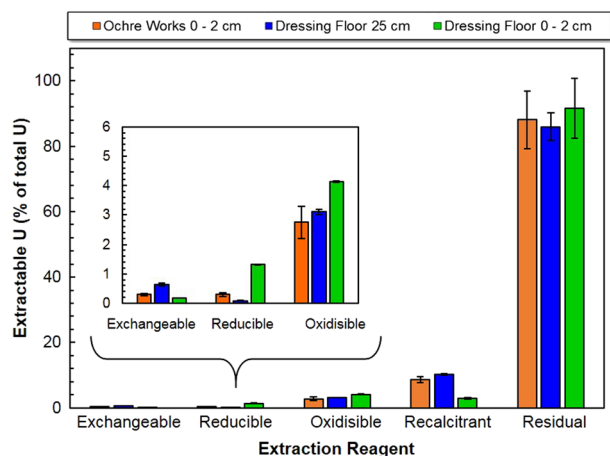


**Fig. 2** Fractionation of uranium between defined classifications for three soils at the South Terras site. Total elemental concentrations are given in Table 1. Error bars are one standard deviation of multiple (ten) replicates

Fig. 3b) is consistent with the structure of the uranyl mica family of minerals (space group P4/nz), which have a characteristic layered structure with alternating sheets of  $[(\text{UO}_2)(\text{XO}_4)]^{-1}$ , where X=P, As and hydrated  $\text{Cu}^{2+}$  cations.<sup>10</sup> A number of compounds with the A  $(\text{UO}_2)_2(\text{XO}_4)_2 \cdot n\text{H}_2\text{O}$  structure exist, where A=Ca, Ba, Mg,  $\text{Cu}^{2+}$ ,  $\text{Ni}^{2+}$ ,  $\text{Pb}^{2+}$ ,  $\text{Fe}^{2+}$  including: metaautunite ( $\text{Ca}(\text{UO}_2)_2(\text{PO}_4)_2 \cdot 8\text{H}_2\text{O}$ ), a partially-dehydrated counterpart of the secondary South Terras uranium-ores, autunite; metatorbernite ( $\text{Cu}(\text{UO}_2)_2(\text{PO}_4)_2 \cdot 8\text{H}_2\text{O}$ ), and the arsenic end-member of the same family, metazeunerite ( $\text{Cu}(\text{UO}_2)_2(\text{AsO}_4)_2 \cdot 8\text{H}_2\text{O}$ ).

Rietveld analysis of the micro-XRD pattern in Fig. 3b gives lattice parameters of  $a = 6.992(1) \text{ \AA}$ ,  $c = 17.318(4) \text{ \AA}$  and a lattice volume of  $846.77(1) \text{ \AA}^3$ . These lattice parameters, combined with the significant concentration of As measured by  $\mu$ -XRF, are suggestive of the presence of the copper and arsenic-bearing uranyl-mica, metazeunerite. However, EDX maps also suggest the presence of P (Fig. 1), which was not measured in the  $\mu$ -XRF analysis due to the imposed energy cut-off; the refined lattice parameters and volume fall between those of metazeunerite and the phosphate end-member of the same family, metatorbernite ( $a = 7.1094(1)$ ,  $c = 17.146(1)$  and  $v = 866.620(1) \text{ \AA}^3$  for metazeunerite, and  $a = 6.9756(5)$ ,  $c = 17.349(2)$  and  $v = 844.184(3) \text{ \AA}^3$  for metatorbernite).<sup>11</sup> Owing to the similar thermochemical radii of P and As (2.38  $\text{ \AA}$  and 2.48  $\text{ \AA}$  for phosphate and arsenate, respectively),<sup>12</sup> it is feasible that a solid solution of divalent interlayer anions exists between metazeunerite and metatorbernite.<sup>13</sup> The refined lattice parameters are closer in dimension to metazeunerite, therefore arsenic is expected to dominate over phosphorus in this solid solution of  $\text{Cu}(\text{UO}_2)_2(\text{AsO}_4)_{2-x}(\text{PO}_4)_x \cdot 8\text{H}_2\text{O}$ . Assuming the solid solution to follow Vegard's Law, our unit cell volume suggests ~18% solid solution of metatorbernite in metazeunerite. Metatorbernite has previously been reported to sequester uranium at other uranium-contaminated sites such as Hanford (USA)<sup>14-17</sup> and has also been reported to occur at South Terras<sup>3</sup>. Although the occurrence of metazeunerite at South Terras has been previously inferred,<sup>18</sup> to our knowledge, this study provides conclusive and verifiable evidence for this phase at the site, and indeed for any studied uranium-contaminated vadose sediments.<sup>14-17</sup>

In the  $\mu$ -XANES analysis of the copper, uranium, arsenic particle shown in Fig. 3a, the reduced intensity of the white line, and the presence of a shoulder feature (labelled 'A', Fig. 3c) confirms that uranium is present as the uranyl ( $\text{UO}_2^{2+}$ ) species, consistent with the presence of (a solid solution of) metazeunerite and metatorbernite. This feature is absent in compounds that do not contain the uranyl moiety. With reference to the measured

uranium standards, which display a linear relationship between the uranium  $L_{III}$ -edge position and the oxidation state in the range U(IV) to U(VI) (Supplementary Fig. 4), the sample particle composed of metazeunerite and metatorbernite demonstrates a mean uranium oxidation state of  $5.9 \pm 0.4$  (Table 2).

#### Micro-focus analysis of minor uranium particles

Particles with uranium fluorescence counts one order of magnitude lower than observed in Fig. 3a were investigated. Co-location of uranium with rubidium, known to be present in high concentrations in the Cornubian granites, and often substituted for potassium in minerals such as muscovite,<sup>19</sup> necessitated a two-step analysis due to the closely overlapping fluorescence lines of U  $L\alpha_1$  (13.614 keV) and Rb  $K\alpha_1$  (13.396 keV), as illustrated in Fig. 4a. The difference in X-ray absorption at an incident energy above the U  $L_{III}$  edge ( $E_0 = 17.200 \text{ keV}$ , Fig. 4b) to that below the U  $L_{III}$  edge ( $E_0 = 16.900 \text{ keV}$ ) served to distinguish concentrations of uranium from rubidium (Fig. 4c). Areas with an intensity  $< 0$  in Fig. 4c are related to rubidium, due to a reduction in the rubidium absorption cross section as the incident photon energy is increased, while those with an intensity  $> 0$  are related to uranium, due to the excitation of the  $L_{III}$  edge exclusively at the higher energy.  $\mu$ -XRD analysis of the point identified in Fig. 4c, belonging to a particle from 0–2 cm DF location, revealed the presence of quartz, plumbogjarosite ( $\text{PbFe}^{3+}_6(\text{SO}_4)_2(\text{OH})_{12}$ ), muscovite ( $\text{KAl}_2(\text{Si}_3\text{Al})\text{O}_{10}(\text{OH})_2$ ) and kaolinite ( $\text{Al}_2\text{Si}_2\text{O}_5(\text{OH})_4$ ). No reflections for uranium-bearing minerals could be fit to the data. In their study of uranium at the Hanford site, Catalano et al.<sup>14</sup> similarly found non-crystalline uranium bound to phyllosilicates. The mean uranium oxidation state in particles from this location ranged from  $5.0 \pm 0.4$  to  $6.0 \pm 0.4$  (Table 2, Supplementary Fig. 4); the partially reduced state may arise from reduction of uranium to  $\text{U}_3\text{O}_8$  by Fe(II), e.g., in chlorite phyllosilicates.

The phases metatorbernite ( $\text{Cu}(\text{UO}_2)_2(\text{PO}_4)_2 \cdot 8\text{H}_2\text{O}$ ), jarosite ( $\text{KFe}_3(\text{OH})_6(\text{SO}_4)_2$ ) and akaganeite ( $\beta\text{-FeOOH}$ ) were observed in soils from 25 cm DF location (Supplementary Fig. 5a–c). The presence of metatorbernite, in this case isolated from metazeunerite, confirms the prevalence of uranyl-mica minerals in South Terras soils. The presence of iron-bearing jarosite and akaganeite are in agreement with EDX observations shown in Fig. 1, where uranium-bearing crystallites coat an iron-bearing particle. Micro-XANES analysis of metatorbernite gave a mean oxidation state of  $5.7 \pm 0.4$  (Table 2, Supplementary Fig. 4). An additional uranyl-mica phase, parsonite [ $\text{Pb}_2(\text{UO}_2)(\text{PO}_4)_2 \cdot 2\text{H}_2\text{O}$ ]; PDF 00-012-0259], was observed in particles of this sample, with a mean uranium oxidation state of  $5.7 \pm 0.4$  (Table 2, Supplementary Fig. 4).

Uranium-bearing particles sampled from the Ochre Works location were identified as metavanuralite ( $\text{Al}(\text{UO}_2)_2(\text{VO}_4)_2(\text{OH}) \cdot 8\text{H}_2\text{O}$ ) (Supplementary Fig. 5d–f). This mineral was found to be closely associated with vanadyl goethite [ $(\text{Fe},\text{V})\text{OOH}$ ]; and muscovite–paragonite ( $\text{NaK}_3(\text{Al}_{12}\text{Si}_{12}\text{O}_{40}(\text{OH})_8$ ). Metavanuralite, space group P1, is an uncommon uranyl mineral in the St. Austell region and, to our knowledge, has not previously been reported at South Terras. The archetypal location is the Mounana mine, Gabon, where it occurs as elongated crystals that form as crusts on goethite.<sup>20,21</sup> Due to the historical processing of iron ore at South Terras, the presence of goethite is not unexpected. Micro-XANES analysis of metavanuralite revealed a mean uranium oxidation state of  $5.6 \pm 0.4$  (Table 2, Supplementary Fig. 4).

## DISCUSSION

The degradation of uraninite ore in vadose zone soils typically involves the formation of hydrated uranium oxides, uranyl-silicates, uranyl-carbonates and uranyl-phosphates.<sup>22</sup> Soluble uranyl ions can migrate from the primary ore body and other uranyl-bearing phases may be formed. At South Terras, ore

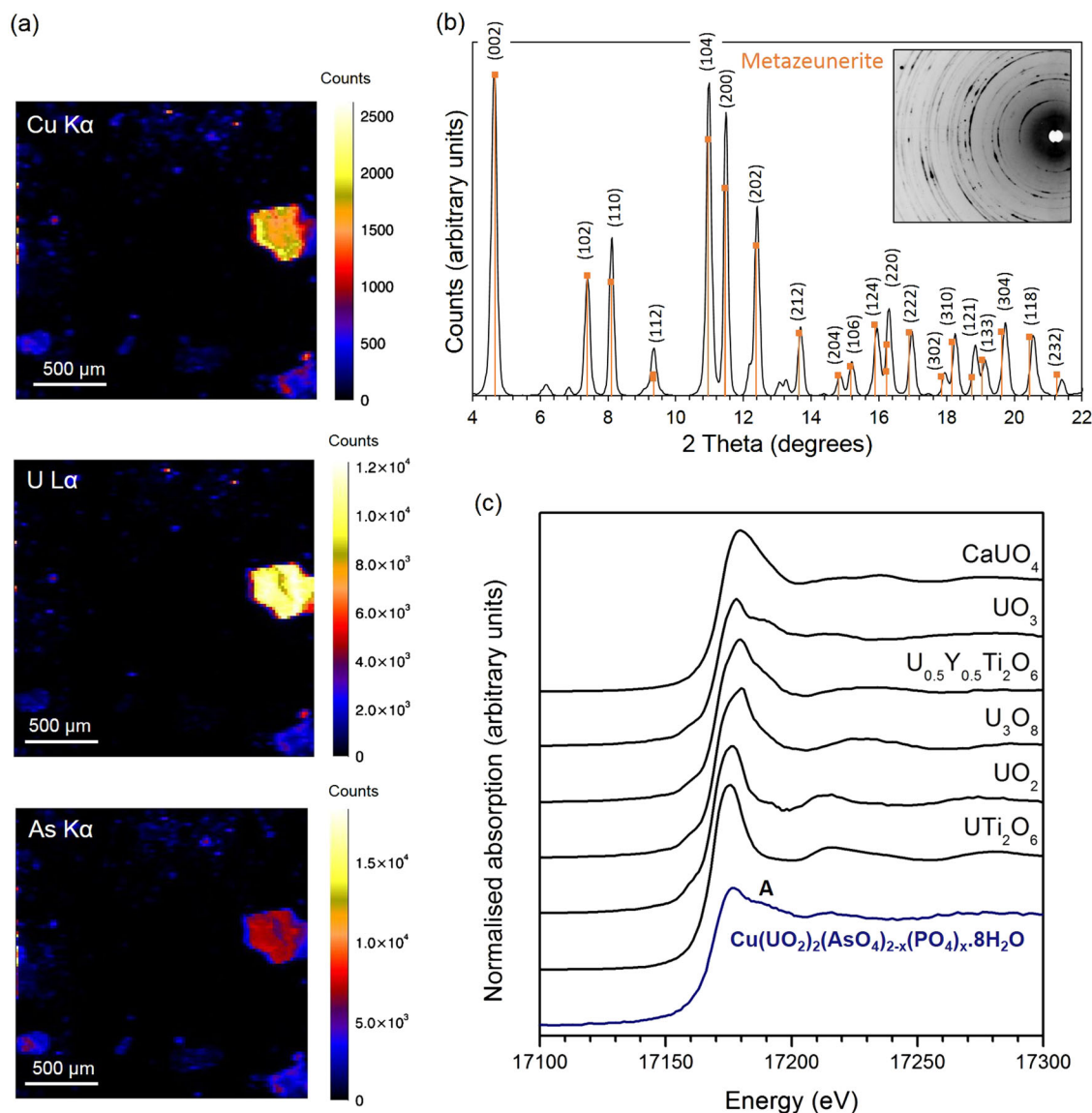


**Fig. 3** Analysis of particles from 25 cm at the Dressing Floor (DF) location using **a**  $\mu$ -XRF mapping, revealed the association of uranium with copper and arsenic; **b**  $\mu$ -XRD analysis confirmed a uranyl-mica structure similar to both metazeunerite ( $\text{Cu}(\text{UO}_2)_2(\text{AsO}_4)_2 \cdot 8\text{H}_2\text{O}$ ) [PDF 00-004-0108] and metatorbernite ( $\text{Cu}(\text{UO}_2)_2(\text{PO}_4)_2 \cdot 8\text{H}_2\text{O}$ ) [PDF 00-008-0309]; and **c**  $\mu$ -XANES spectra taken at the U L<sub>III</sub> edge revealed an oxidation state predominantly of U(VI) when compared with known uranium-oxide standards. e.g.<sup>30</sup>

extraction processes and natural weathering of the country rock led to the proliferation of other elements during degradation, particularly arsenic and beryllium, which were found in significant concentrations (Table 1). The major uranium-bearing phases identified (across two sample locations and multiple sampling depths; 15 samples and at least three particles per sample) were the copper-bearing uranyl-arsenate and uranyl-phosphate phases, metazeunerite, metatorbernite, and their solid solution, in contrast to previous supposition.<sup>4–6,23</sup> The mechanism of uranium attenuation in these uranyl-micas is evident in Fig. 1; re-precipitation of mobile uranium, with arsenate and phosphate, as metazeunerite, metatorbernite, and their solid solution, is demonstrated by the presence of a copper, arsenic, phosphorus and uranium-bearing ‘crust’ coating the surfaces of silicon, aluminium, sulphur and iron-bearing minerals, for example, muscovite or jarosite.

Significantly, our data indicate that metazeunerite and metatorbernite were found to occur in solid solution, which has not been previously observed at other uranium-contaminated sites where uranyl-micas are present.<sup>14–17</sup> Owing to the higher solubility

of uranyl-phosphate minerals compared with uranyl-arsenates (with solubility products of  $10^{-12.8}$  and  $10^{-49.2}$  for metatorbernite and metazeunerite, respectively),<sup>24</sup> it might be expected that arsenate end-members of this mineral family would dominate over the phosphate end-members, which is indeed observed in the Rietveld analysis of data shown in Fig. 3b, and composition inferred from interpolation of the unit cell volume of the end members. Remarkably, as a result of the complex environmental conditions brought about by the combined degradation of uranium ores and granitic lithologies at South Terras, arsenic contamination aids the attenuation of uranium through direct precipitation of metazeunerite—metatorbernite solid solution.

Metazeunerite and metatorbernite were found to be particularly concentrated at a depth of 25 cm (DF location), as highlighted by the high fractions of “recalcitrant and residual” copper, uranium, arsenic and phosphorus in the sequential extraction (Fig. 2, Supplementary Fig. 3). Indeed, concentrations of uranium were one order of magnitude greater at this depth (Table 1). This may be due to the presence of relatively undisturbed mine spoil at

**Table 2.** Mean oxidation state of uranium-bearing particles identified at South Terras, determined from the first derivative of the position of the uranium L<sub>III</sub>-edge absorption spectrum, compared with the average oxidation state of U(IV–VI) compounds with similar chemical environments

Location	Phase identified	Mean oxidation state
Ochre works, 0–2 cm	Metavanuralite (Al(UO <sub>2</sub> ) <sub>2</sub> (VO <sub>4</sub> ) <sub>2</sub> (OH)·8H <sub>2</sub> O)	5.6 ± 0.4
Dressing floor, 25 cm	Meta(zeunerite/torbernite) solid solution (Cu(UO <sub>2</sub> ) <sub>2</sub> (AsO <sub>4</sub> ) <sub>2-x</sub> (PO <sub>4</sub> ) <sub>x</sub> ·8H <sub>2</sub> O)	5.9 ± 0.4
Dressing floor, 25 cm	Metatorbernite (Cu(UO <sub>2</sub> ) <sub>2</sub> (PO <sub>4</sub> ) <sub>2</sub> ·8H <sub>2</sub> O)	5.7 ± 0.4
Dressing floor, 25 cm	Parsonite (Pb <sub>2</sub> (UO <sub>2</sub> )(PO <sub>4</sub> ) <sub>2</sub> ·2H <sub>2</sub> O)	5.7 ± 0.4
Dressing floor, 0–2 cm	Non-crystalline uranium	6.0 ± 0.4
Dressing floor, 0–2 cm	Non-crystalline uranium	5.0 ± 0.4

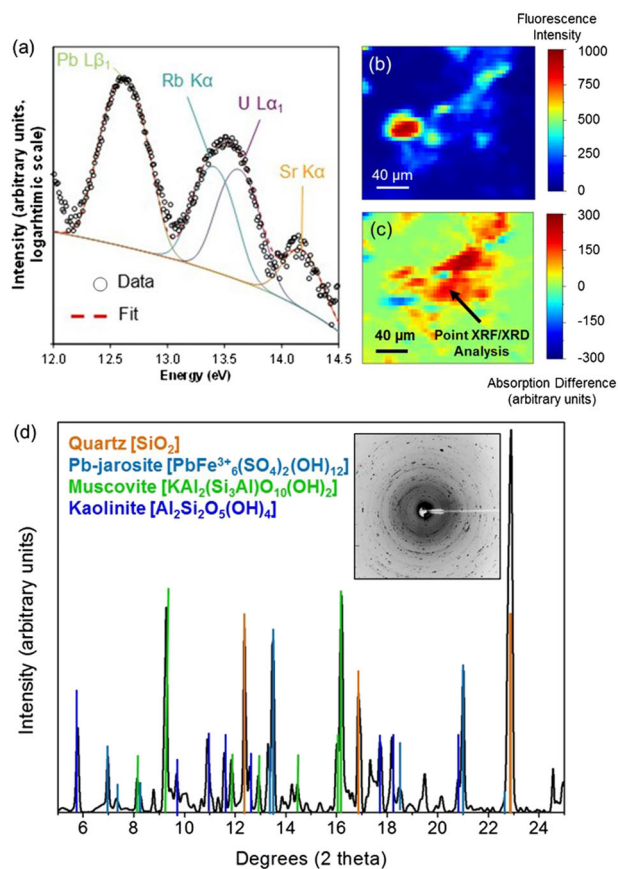


**Fig. 4** Micro-focus analysis of soil sample from the Dressing Floor location at 0–2 cm depth **a** illustrative Gaussian fits to the  $\mu$ -XRF spectrum demonstrates the overlap between Rb K $\alpha$  and U L $\alpha$ 1 fluorescence lines; **b**  $\mu$ -XRF map of soil particles recording intensity above the U L<sub>III</sub> edge ( $E_0 = 17.2$  keV); **c** ratio of the  $\mu$ -XRF intensity at, and below ( $E_0 = 16.9$  keV) the U L<sub>III</sub> edge; areas with intensity > 0 can be distinguished as containing uranium; and **d**  $\mu$ -XRD analysis of uranium-rich point in (c), with patterns for quartz [PDF 04-016-2085], plumbojarosite [PDF 00-018-0698], muscovite [PDF 01-082-3731] and kaolinite [PDF 04-010-4800]

depth, or due to aqueous downward transport and precipitation of uranium, arsenic and phosphorous; either possibility confirms the potential for the entrapped micron-sized particles of metazeunerite/metatorbernite to control the long-term release of uranium at the site. At the surface, the speciation of uranium was markedly different; non-crystalline species with variable oxidation state dominated the DF location. The surface soils were enriched in phosphorus compared to at depth, by one order of magnitude (Table 1) and the sequential extraction showed that

fractionally more uranium was associated with the reducible fraction at the surface than at depth (Fig. 2). This indicates that uranyl-phosphates, likely bound to iron-bearing phases, may be present at the surface, however the presence of uranyl-carbonates or uranyl species bound to organics cannot be ruled out. Nevertheless, it seems likely that the surface fraction of uranium shows a higher mobility than that associated with metazeunerite and metatorbernite, sequestered at depth.

Interestingly, there was a clear difference in the uranium concentration and mineralogy at the Ochre Works and Dressing Floor areas of comparable depths; uranyl mica phases were ubiquitous in the samples taken from the Dressing Floor (at all depths sampled), while the soils from the Ochre works area exhibited much lower uranium content, which was associated with oxidised iron and vanadium (Table 2, Supplementary Fig. 4). These differences are clearly associated with the different degradation mechanisms of uranium arising from different ore processing methods; chemical extraction at the Dressing Floor location, and smelting at the Ochre Works location. With the predominant groundwater flow direction from the Dressing Floor towards the Ochre Works and the River Fal,<sup>4,23</sup> the absence of significant uranium content in the Ochre Works indicates the potential efficacy of the uranyl-micas for attenuation of uranium at the site.

Sequestration of uranium in complex mineralogical assemblages at South Terras is the result of a set of rather unique geological conditions. To identify this remediation mechanism at other sites, where arsenic and uranium are key co-contaminants, further detailed mineralogical assessments are required. These should be considered as an essential input to understand the ultimate environmental fate of degraded uranium ore.

## METHODS

### Site and soil sampling

South Terras is located in the St. Austell District of Cornwall (SW England, Supplementary Fig. 1a) where uranium mining operations were performed near Tolgarrick Mill (Supplementary Fig. 1b). The location is a Site of Special Scientific Interest (SSSI) with restricted access. Detailed site information regarding the geology, stratigraphy and spatial variations in soil, groundwater and stream water chemistry (e.g., cation concentrations and pH) are given by Read et al.,<sup>4</sup> Sideeg et al.,<sup>5</sup> and Hooker et al.<sup>23</sup> Two well-documented sites, the Ochre Works (OW) and Dressing Floor (DF) locations, were selected for investigation (Supplementary Fig. 1b) to understand how ore processing influenced the degradation of uranium ore and subsequent uranium speciation in the soil. The former is where iron-ore was once smelted and the latter is where uranium-ore and mine spoil processing occurred.<sup>1</sup> Spoil processing involved sequential chemical treatments using HCl, H<sub>2</sub>SO<sub>4</sub>, BaSO<sub>4</sub>, NaHCO<sub>3</sub>, NH<sub>4</sub>, NaOH and hydrobromic acid<sup>1</sup>. The site is heavily vegetated, with a surface dark-brown mineral/organic soil horizon (0–15 cm, Supplementary Fig. 1c), beneath which lays mine spoil interspersed with a hematitic sand (to ~50 cm)<sup>6</sup>. These sequences are underlain by kaolinitic clay.<sup>24</sup> A series of samples, taken from locations 10–20 m apart, were collected, by hand, at the surface (0–2 cm depth) from both sample locations, and at a shallow depth (25 cm) at the DF location.

### Soil preparation and bulk characterisation

Soils were dried in air and sieved to a particle size of <300 µm, removing organic litter. Thinly spread soils were screened to localise radioactive particles for further analysis using autoradiography (Packard Instant Imager). Portions of soil containing radioactive 'hotspots' were collected onto adhesive carbon tabs for SEM analysis or kapton tape for synchrotron analyses. Back scattered electron imaging was performed using a Hitachi TM3030 with an accelerating voltage of 15 kV with coupled EDX analysis using a Quantax 70 EDX detector. Samples were analysed in variable pressure mode (no coating required). Bulk XRD analysis was performed using a Bruker D2 Phaser diffractometer, operating in reflection mode at 40 kV and 30 mA with Cu K $\alpha$  radiation. Data were acquired between 5 < 2 $\theta$  < 60° at 2° min<sup>-1</sup> and a step size of 0.02°.

### $\mu$ -XRF, $\mu$ -XRD and $\mu$ -XANES analysis

Synchrotron radiation micro-focus analyses were conducted at the now decommissioned X27A beamline at the National Synchrotron Light Source (NSLS, USA) and at the microXAS (X05LA) beamline at the Swiss Light Source (SLS). At NSLS, the soil particles, mounted between two films of kapton tape, were oriented at 45° to the direction of x-ray propagation and raster scanned through the micro-focused x-ray beam (spot size of  $\sim 7 \times 14$  µm). X-ray fluorescence (XRF) was measured using a four-element silicon drift detector (Hitachi) mounted at 90° to the incident x-ray beam direction. Uranium L<sub>III</sub>-edge ( $E_0 = 17.166$  keV)  $\mu$ -XANES (X-ray Absorption Near-Edge Structure) spectra were recorded in fluorescence mode by monitoring the U L $\alpha_1$  emission (13.614 keV). Two-dimensional micro-x-ray diffraction ( $\mu$ -XRD) measurements were acquired using a CCD camera (Bruker SMART 1500) positioned 235 mm behind the sample and calibrated to an alumina Al<sub>2</sub>O<sub>3</sub> standard (NIST SRM676a)<sup>25</sup>. At a monochromatic beam energy of 17.200 keV, the wavelength was 0.7093 Å.

At SLS,  $\mu$ -XAS data were collected according to the methodology detailed by Crean et al.<sup>25,26</sup> The monochromatic beam energy was identical to NSLS. Fluorescence  $\mu$ -XANES spectra of uranium standards (UTi<sub>2</sub>O<sub>6</sub>, UO<sub>2</sub>, U<sub>0.5</sub>Y<sub>0.5</sub>Ti<sub>2</sub>O<sub>6</sub>, U<sub>3</sub>O<sub>8</sub>, UO<sub>3</sub> and CaUO<sub>4</sub>) were measured to aid interpretation.

### Sequential extraction

A modified version of the Community Bureau of Reference (BCR) scheme,<sup>27</sup> previously applied to uranium speciation in soils,<sup>28,29</sup> was used. The distribution of uranium was defined in five phases: exchangeable, reducible, oxidisable and recalcitrant and residual. A separate aliquot was digested in aqua regia/HF to determine the concentration of each element in the soil. The residual fraction represents the elemental concentration of the total digest, less the elemental concentration of the other extraction steps combined. The extraction and digest reagents and procedure are summarised in Supplementary Table 2. Ten replicate experiments using 0.5 g soil were analysed, in addition to duplicate blanks. After each extraction step, samples were centrifuged (3000 r.p.m., 15 min), the supernatant removed and acidified with concentrated HNO<sub>3</sub>. All extract solutions were analysed for major and minor elements by ICP-AES (Spectro Ciros Vision).

### Data availability

The data that support the findings of this study are available from the corresponding author upon reasonable request.

### ACKNOWLEDGEMENTS

The authors wish to acknowledge Natural England and the St. Stephen Estate for granting access to the South Terras SSSI. We wish to thank Mr. Neil Bramall and Mrs. Irene Johnson for technical support. We acknowledge support from the UK Government Department of Energy and Climate Change, through the award of the MIDAS Collaboratory, for analytical equipment. Portions of this work were performed at Beamline X27A, NSLS, Brookhaven National Laboratory. X27A is supported in part by the U.S. Department of Energy (DOE)—Geosciences (DE-FG02-92ER14244 to The University of Chicago—CARS). Use of the NSLS was supported by the DOE, Office of Science, under Contract No. DE-AC02-98CH10886. Access to the Swiss Light Source, Paul Scherrer Institute, Villigen, Switzerland, was supported by the TALISMAN collaborative project, with co-funding from the European Commission under the Euratom Research and Training Programme on Nuclear Energy, within the 7th Framework programme (grant agreement 323300). We wish to acknowledge EPSRC for the award of an ECR Fellowship (EP/N017374/1), and for funding on the Nuclear

FIRST CDT (EP/G037140/1). Thanks are given to Dr. Eric Pierce for his help in improving the manuscript through the review process.

### AUTHOR CONTRIBUTIONS

All authors provided substantial contributions to conception of the research performed, or the acquisition, analysis or interpretation of the data; they drafted or revised the manuscript; approved the final version and; are accountable for the accuracy and integrity of the data and its interpretation.

### ADDITIONAL INFORMATION

**Supplementary information** accompanies the paper on the *npj Materials Degradation* website (<https://doi.org/10.1038/s41529-017-0019-9>).

**Competing interests:** The authors declare no competing financial interests.

**Publisher's note:** Springer Nature remains neutral with regard to jurisdictional claims in published maps and institutional affiliations.

### REFERENCES

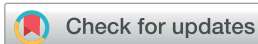
- Smale, C. V. Cornwall's premier uranium and radium mine. *J. Royal Inst. Cornwall* **184**, 304–322 (1992).
- Collins, J. H. Observations on the West of England Mining Region. *Trans. Royal Geol. Soc. Cornwall* (1912).
- Dines, H. G. The metalliferous mining region of South West England. *Mem. Geol. Surv. Great Brit.* **2**, 541–543 (1956).
- Read, D., Hooker, P. J., Ivanovich, M. & Milodowski, A. E. A natural analogue study of an abandoned uranium mine in Cornwall, England. *Radiochim. Acta* **52/53**, 349–356 (1991).
- Sideeg, S. M., Bryan, N. D. & Livens, F. R. Behaviour and mobility of U and Ra in sediments near an abandoned uranium mine, Cornwall, UK. *Environ. Sci. Proc. Impact.* **17**, 235–245 (2015).
- Moliner-Martinez, Y., Campins-Falco, P., Worsfold, P. J. & Keith-Roach, M. The impact of a disused mine on uranium transport in the River Fal, South West England. *J. Environ. Monitoring* **6**, 907–913 (2004).
- Pablo, J. D. et al. The oxidative dissolution mechanism of uranium dioxide. I. The effect of temperature in hydrogen carbonate medium. *Geochim. Cosmochim. Acta* **63**, 3097–3103 (1999).
- Beamish, D., Howard, A. S., Ward, E. K., White, J. & Young M. E. Tellus South West airborne geophysical data. Natural Environment Research Council, British Geological Survey Report OR/14/014 (2014).
- Middleton, D. R. S. et al. Urinary arsenic profiles reveal exposures to inorganic arsenic from private drinking water supplies in Cornwall, UK. *Sci. Rep.* **6**, 25656 (2016).
- Hanic, F. The crystal structure of meta-zeunerite Cu(UO<sub>2</sub>)<sub>2</sub>(AsO<sub>4</sub>)<sub>2</sub>·8H<sub>2</sub>O. *Czech J. Phys. B.* **10**, 169–181 (1960).
- Locock, A. J. & Burns, P. C. Crystal structures and synthesis of the copper-dominant members of the autunite and meta-autunite groups: torbernite, zeunerite, metatorbernite and metazeunerite. *Can. Min.* **41**, 489–502 (2003).
- Da Silva, J. R. R. & Williams, R. J. P. (eds) *The Biological Chemistry of the Elements: The Inorganic Chemistry of Life* (Oxford University Press, 1997).
- Locock, A. J. & Burns, P. C. Monovalent cations in structures of the meta-autunite group. *Can. Min.* **42**, 973–996 (2004).
- Catalano, J. G. et al. Changes in uranium speciation through a depth sequence of contaminated handford sediments. *Environ. Sci. Technol.* **40**, 2517–2524 (2006).
- Arai, Y., Marcus, M. A., Tamura, N., Davis, J. A. & Zachara, J. M. Spectroscopic evidence of uranium bearing precipitates in vadose zone sediments at the Hanford 300-Area site. *Environ. Sci. Technol.* **41**, 4633–4639 (2007).
- Singer, D. M., Zachara, J. M. & Brown, G. E. Jr. Uranium speciation as a function of depth in contaminated Hanford sediments—A micro-XRF, micro-XRD and micro-and bulk-XAFS study. *Environ. Sci. Technol.* **43**, 630–636 (2009).
- Stubbs, J. E. et al. Newly recognised hosts for uranium in the Hanford site vadose zone. *Geochim. Cosmochim. Acta* **73**, 1563–1576 (2009).
- Purvis, O. W., Bailey, E. H., McLean, J., Kasama, T. & Williamson, B. J. *Geomicrobiol. J.* **21**, 159–167 (2004).
- Stone, M. The tregonning granite: petrogenesis of Li-mica granites in the Cornubian batholith. *Miner. Mag.* **56**, 141–155 (1992). 383.
- Cesbron, F. Nouvelles donnees sur la vanuralite. Existence de la metavanuralite. *Bull. Soc. Fr. Minér. Cristallogr.* **93**, 242–248 (1970).
- Lauf, R. J. *Mineralogy of uranium and thorium* (Schiffer Publishing, 2016).
- Frondel, C. Study of uranium minerals: gummite. *Bull. Geol. Soc. Am.* **63**, 1252–1253 (1952).

23. Hooker, P. J. et al. *A radionuclide migration study at the disused South Terras uranium mine*, Cornwall. DOE Report WE/89/13 (1989).
24. Vochten, R. & Goeminne, A. Synthesis, crystallographic data, solubility and electrokinetic properties of meta-zeunerite, meta-kirchheimerite and nickel-uranylarsenate. *Phys. Chem. Miner.* **11**, 95–100 (1984).
25. Crean, D. E. et al. Microanalytical X-ray imaging of depleted uranium speciation in environmentally aged munitions residues. *Environ. Sci. Technol.* **48**, 1467–1474 (2014).
26. Crean, D. E. et al. Expanding the nuclear forensic toolkit: chemical profiling of uranium ore concentrate particles by synchrotron X-ray microanalysis. *RSC Adv.* **5**, 87908–87918 (2015).
27. Ure, A. M., Quevauviller, P., Muntau, H. & Griepink, B. Speciation of heavy metals in soils and sediments. An account of the improvement and harmonisation of extraction techniques undertaken under the auspices of the BCR of the commission of the european communities. *Int. J. Environ. Anal. Chem.* **51**, 135–151 (1993).
28. Oliver, I. W., Graham, M. C., MacKenzie, A. B., Ellam, R. M. & Farmer, J. G. Distribution and partitioning of depleted uranium (DU) in soils at weapons test ranges—investigations combining the BCR extraction scheme and isotopic analysis. *Chemosphere* **72**, 932–939 (2008).
29. Crean, D. E. et al. Remediation of soils contaminated with particulate depleted uranium by multi-stage chemical extraction. *J. Haz. Mater.* **263**, 382–390 (2013).
30. Pierce, E. M., Icenhower, J. P., Serne, R. J. & Catalano, J. G. Experimental determination of  $UO_{2(cr)}$  dissolution kinetics: Effects of solution saturation state and pH. *J. Nucl. Mater.* **345**, 206–218 (2005).



**Open Access** This article is licensed under a Creative Commons Attribution 4.0 International License, which permits use, sharing, adaptation, distribution and reproduction in any medium or format, as long as you give appropriate credit to the original author(s) and the source, provide a link to the Creative Commons license, and indicate if changes were made. The images or other third party material in this article are included in the article's Creative Commons license, unless indicated otherwise in a credit line to the material. If material is not included in the article's Creative Commons license and your intended use is not permitted by statutory regulation or exceeds the permitted use, you will need to obtain permission directly from the copyright holder. To view a copy of this license, visit <http://creativecommons.org/licenses/by/4.0/>.

© The Author(s) 2017



## On the existence of $\text{AgM}_9(\text{VO}_4)_6\text{I}$ ( $\text{M} = \text{Ba}, \text{Pb}$ )<sup>†</sup>

Cite this: *RSC Adv.*, 2017, 7, 49004

E. V. Johnstone,<sup>a</sup> D. J. Bailey,<sup>a</sup> M. C. Stennett,<sup>a</sup> J. Heo<sup>bc</sup> and N. C. Hyatt<sup>\*a</sup>

The syntheses of the reported compounds  $\text{AgM}_9(\text{VO}_4)_6\text{I}$  ( $\text{M} = \text{Ba}, \text{Pb}$ ) were reinvestigated. Stoichiometric amounts of  $\text{AgI}$  with either  $\text{M}_3(\text{VO}_4)_2$  ( $\text{M} = \text{Ba}, \text{Pb}$ ) or  $\text{PbO}$  and  $\text{V}_2\text{O}_5$  were reacted in the solid-state at elevated temperatures in air or in flame-sealed quartz vessels. The resulting products were characterized by X-ray diffraction, scanning electron microscopy with energy dispersive X-ray analysis, and thermal analyses. Results show that, for all reaction conditions, the target  $\text{AgM}_9(\text{VO}_4)_6\text{I}$  ( $\text{M} = \text{Ba}, \text{Pb}$ ) phases could not be isolated. Instead, heterogeneous phase distributions of primarily  $\text{M}_3(\text{VO}_4)_2$  ( $\text{M} = \text{Ba}, \text{Pb}$ ) and  $\text{AgI}$  were obtained. These findings demonstrate that  $\text{AgI}$  incorporation into single phase, iodine-deficient apatite derivatives for the immobilization of iodine-129 are not feasible under such conditions. This conclusion is important for the conditioning of iodine-129 in advanced reprocessing flowsheets, where iodine is typically sequestered as  $\text{AgI}$ .

Received 22nd August 2017  
 Accepted 4th October 2017

DOI: 10.1039/c7ra09313f

[rsc.li/rsc-advances](http://rsc.li/rsc-advances)

## Introduction

A myriad of apatite ( $\text{A}_{10}(\text{BO}_4)_6\text{X}_2$ ) and apatite supergroup phases, such as hedyphane, belovite, britholite, and ellestadite groups, are found as naturally occurring minerals, a testament to their chemically robust character.<sup>2</sup> Because the apatite phase and those similar to it are capable of structurally substituting a host of different cation (A and B sites) and anion variants (X site), they are ideal synthetic templates for the immobilization of chemically complex radioactive wastes. Previous studies have already shown that an assortment of fission products (*e.g.*,  $\text{Cs}^+$ ,  $\text{Sr}^{2+}$ ,  $\text{Ag}^+$ ,  $\text{Eu}^{2+}$ ,  $\text{Ln}^{3+}$ ,  $\text{I}^-$ ),<sup>3,4</sup> actinide components (*e.g.*,  $\text{Th}^{4+}$ ,  $\text{U}^{4+}$ ,  $\text{U}^{6+}$ ),<sup>5</sup> and other process additives or corrosion products (*e.g.*,  $\text{Na}^+$ ,  $\text{Co}^{2+}$ ,  $\text{Pb}^{2+}$ ,  $\text{F}^-$ ,  $\text{Cl}^-$ ) can be integrated into the apatite structure for purposes of nuclear waste disposal.<sup>6,7</sup>

Due to its volatile nature and radiotoxicity, radioiodine, *e.g.*,  $^{129}\text{I}$  and  $^{131}\text{I}$ , has been a long-standing problem in terms of its containment during reprocessing and disposal in nuclear fuel cycles.<sup>8</sup> In particular, because of its long half-life,  $^{129}\text{I}$  ( $t_{1/2} = 15.7 \times 10^6$  y) must be properly treated in order to minimize its long-term accumulation and effect on the environment.<sup>9</sup> Radioiodine is of concern due to its environmental dispersal during nuclear reprocessing,<sup>10</sup> accidents,<sup>11,12</sup> and weapons testing.<sup>13</sup> Current regulatory practices overseeing reprocessing utilize

dispersion and dilution of  $^{129}\text{I}$  with natural  $^{127}\text{I}$  to reduce its impact on the biosphere.<sup>14</sup> However, it is possible that future reprocessing and waste schemes will focus on its capture and disposal, where a range of robust treatments and waste forms will be necessary for its management.<sup>8</sup>

Specifically, of these materials, iodoapatite phases, such as  $\text{M}_{10}(\text{VO}_4)_6\text{I}_2$  ( $\text{M} = \text{Ba}, \text{Pb}$ ), have been suggested as possible waste forms for radioiodine, and, in particular, the Pb variant has been the topic of many recent studies.<sup>15–23</sup> Using a variation of these  $\text{M}_{10}(\text{VO}_4)_6\text{I}_2$  host phases, the synthesis and characterization of the compounds  $\text{AgBa}_9(\text{VO}_4)_6\text{I}$  and  $\text{AgPb}_9(\text{VO}_4)_6\text{I}$  were reported using  $\text{AgI}$  as an iodine source.<sup>1</sup> The use of  $\text{AgI}$  as the iodine carrier is attractive because this compound is formed in the spent nuclear fuel and occurs in various stages of reprocessing, such as during fuel dissolution, where it comprises a part of the undissolved solids (UDS),<sup>24–26</sup> and in the dissolver off-gas capture of gaseous iodine with solid  $\text{Ag}$  or  $\text{AgNO}_3$ -loaded sorbents (*e.g.*, zeolite, alumina, or silica).<sup>8</sup>

The aim of this study was to synthesize compounds  $\text{AgM}_9(\text{VO}_4)_6\text{I}$  ( $\text{M} = \text{Ba}, \text{Pb}$ ) and investigate the feasibility of  $\text{AgI}$  incorporation and retention into these matrices. Batched powders corresponding to  $\text{AgM}_9(\text{VO}_4)_6\text{I}$  ( $\text{M} = \text{Ba}, \text{Pb}$ ) were reacted using standard solid-state ceramic syntheses in air and in sealed quartz vessels at elevated temperatures. The resulting materials were studied using X-ray diffraction, microscopy, and thermal analysis techniques. However, as reported herein, our attempts to synthesize “ $\text{AgBa}_9(\text{VO}_4)_6\text{I}$ ” and “ $\text{AgPb}_9(\text{VO}_4)_6\text{I}$ ” for further investigation proved unsuccessful, with no evidence for the formation of compounds of this stoichiometry incorporating  $\text{AgI}$ . Nevertheless, our X-ray diffraction data are in good agreement with those published previously for these hypothesized compounds, which on careful inspection, show the phase assemblage to comprise the  $\text{M}_3(\text{VO}_4)_2$  and  $\text{AgI}$  starting

<sup>a</sup>University of Sheffield, Materials Science and Engineering Department, Sheffield, S10 2TN, UK. E-mail: erikjohnstone@gmail.com

<sup>b</sup>Department of Materials Science and Engineering, Pohang University of Science and Technology (POSTECH), Pohang, Gyeongbuk 790-784, South Korea

<sup>c</sup>Division of Advanced Nuclear Engineering, Pohang University of Science and Technology (POSTECH), Pohang, Gyeongbuk 790-784, South Korea

<sup>†</sup> Electronic supplementary information (ESI) available: Synthesis, PXRD, and SEM/EDX of “ $\text{AgPb}_9(\text{VO}_4)_6\text{I}$ ” from  $\text{PbO}$ ,  $\text{V}_2\text{O}_5$ , and  $\text{AgI}$ . Additional PXRD figures, SEM images, EDX spectra, and TG-DTA measurements for “ $\text{AgM}_9(\text{VO}_4)_6\text{I}$  ( $\text{M} = \text{Pb}, \text{Ba}$ )”. See DOI: 10.1039/c7ra09313f



materials, as also evidenced by scanning electron microscopy/energy dispersive X-ray analysis.

## Experimental

### Synthesis of $\text{AgM}_9(\text{VO}_4)_6\text{I}$ ( $\text{M} = \text{Ba}, \text{Pb}$ )

Stoichiometric amounts of  $\text{M}_3(\text{VO}_4)_2$  ( $\text{M} = \text{Ba}, \text{Pb}$ ) and  $\text{AgI}$ , were batched to yield a final reacted composition of  $\text{AgM}_9(\text{VO}_4)_6\text{I}$  ( $\text{M} = \text{Ba}, \text{Pb}$ ). The batched powders were pulverized and mixed as a slurry with isopropanol in an agate mortar and pestle. After drying, the resulting powders were pressed at 2 tonnes into  $\sim 250$  mg, 6 mm disk pellets. Pellets were reacted in air in a box furnace or under vacuum in flame-sealed quartz tubes (10 mm O.D., 8 mm I.D., 180 length) in an alumina tube furnace at  $700^\circ\text{C}$  for 5 h. Because preparations of  $\text{Pb}_{10}(\text{VO}_4)_6\text{I}_2$  have also been reported starting with the component oxides, additional reactions for the Pb series were also performed using the same synthetic procedure with  $\text{PbO}$ ,  $\text{V}_2\text{O}_5$ , and  $\text{AgI}$  as starting materials; characterization of these materials are reported in the ESI.†

### Characterization techniques

Powder X-ray diffraction (PXRD) was performed on a Bruker D2 Phaser system operating with Ni filtered Cu  $K\alpha$  radiation and a position sensitive detector. Samples were pulverized with an agate mortar and pestle and dispersed on a low-background silicon holder. Measurements were made from  $10^\circ < 2\theta < 70^\circ$  with a step size of 0.02 increments at scan rate of  $1.0 \text{ min}^{-1}$ . Phase analysis was completed using DiffraSuite Eva V.3 (Bruker) and Rietveld refinements were performed using Topas V.4.2 (Bruker). Scanning electron microscopy (SEM) (Hitachi-TM3030) and energy-dispersive X-ray spectroscopy (EDX) (Quantax 70) measurements were performed at an accelerating voltage of 15 keV with backscattered electron (BSE) detection. Pieces of reacted pellets were cold-mounted in an epoxy resin and polished to  $1 \mu\text{m}$  using SiC grit paper and diamond polishing paste with a polishing cloth. Thermal gravimetric (TG) and differential thermal analysis (DTA) measurements (Netzsch Jupiter STA 449F3) of powdered samples were performed under flowing  $\text{Ar}(\text{g})$  in an alumina crucible with a scan rate of  $10^\circ\text{C min}^{-1}$  from 30 to  $1150^\circ\text{C}$ .

## Results and discussion

### Synthesis and formation of “ $\text{AgPb}_9(\text{VO}_4)_6\text{I}$ ”

Powders of  $\text{Pb}_3(\text{VO}_4)_2$  and  $\text{AgI}$  were batched and reacted using standard solid-state ceramic techniques. The combined starting materials produced yellow-white powders before reacting. After pressing into pellets and reacting, the resulting pellets were dark grey-blue and produced pale yellow to yellow-brown powders upon grinding. For reactions performed in quartz tubes, no apparent sublimation of iodine from the reacted pellet was observed at the cooler end of the tube.

The PXRD patterns of “ $\text{AgPb}_9(\text{VO}_4)_6\text{I}$ ” are shown in Fig. 1. The PXRD patterns of the resulting products were similar, irrespective of sealed tube or open reaction conditions. Phase

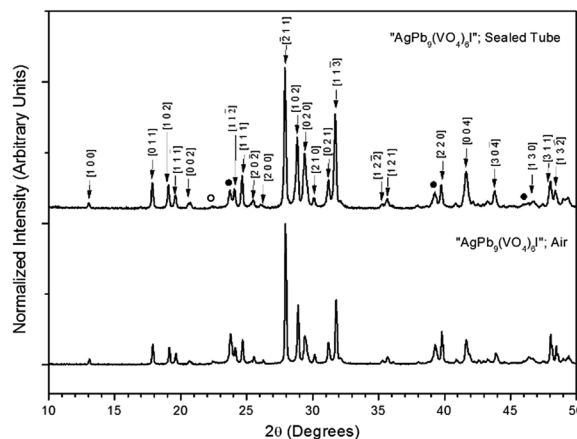


Fig. 1 PXRD patterns of “ $\text{AgPb}_9(\text{VO}_4)_6\text{I}$ ” treated at  $700^\circ\text{C}$  for 5 h in either air or a sealed quartz tube. Markers indicate peaks assigned to the  $\beta\text{-Pb}_3(\text{VO}_4)_2$  (labelled (hkl) Miller indices),  $\gamma\text{-AgI}$  (●), and  $\beta\text{-AgI}$  (○) phases.

analysis of each pattern identified  $\beta\text{-Pb}_3(\text{VO}_4)_2$  (monoclinic  $P12_1/c1$ ) and  $\beta/\gamma\text{-AgI}$  (hexagonal  $P6_3mc$ /cubic  $F\bar{4}3m$ , respectively) as the primary phases. Additionally, the  $\text{Pb}_{9.85}(\text{VO}_4)_6\text{I}_{1.7}$  (hexagonal  $P6_3/m$ ) phase was identified, as a minor component, in the “ $\text{AgPb}_9(\text{VO}_4)_6\text{I}$ ” sample reacted in a sealed tube. The formation of  $\text{Pb}_{9.85}(\text{VO}_4)_6\text{I}_{1.7}$  is hypothesised to be a result of the decomposition of  $\text{AgI}$  to yield  $\text{Ag}$  metal and  $\text{I}_2$ , and subsequent reaction of the latter with  $\beta\text{-Pb}_3(\text{VO}_4)_2$ .

Rietveld fitting of X-ray diffraction data of “ $\text{AgPb}_9(\text{VO}_4)_6\text{I}$ ” was effectively achieved assuming a mixture of  $\beta\text{-Pb}_3(\text{VO}_4)_2$ ,  $\gamma\text{-AgI}$ , and  $\text{Pb}_{9.85}(\text{VO}_4)_6\text{I}_{1.7}$  as shown in Fig. 2; the refined phase fractions were  $70 \pm 5\%$ ,  $8 \pm 1\%$ , and  $22 \pm 5\%$ , respectively. The phase fraction of  $\beta\text{-AgI}$  was determined to be  $< 1\%$ . Although the crystal structure of “ $\text{AgPb}_9(\text{VO}_4)_6\text{I}$ ” was stated to be of monoclinic symmetry, no space group was determined, but the

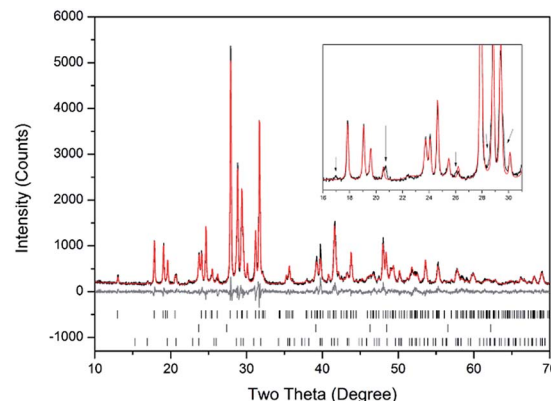


Fig. 2 Rietveld analysis of PXRD data of “ $\text{AgPb}_9(\text{VO}_4)_6\text{I}$ ” reacted at  $700^\circ\text{C}$  in a sealed quartz tube; the data are shown in black, the fit is shown in red, and the difference plot in grey. Tick marks show allowed reflections of  $\beta\text{-Pb}_3(\text{VO}_4)_2$  (upper ticks),  $\gamma\text{-AgI}$  (middle ticks), and  $\text{Pb}_{9.85}(\text{VO}_4)_6\text{I}_{1.7}$  (bottom ticks). Inset: Rietveld fit without the  $\text{Pb}_{9.85}(\text{VO}_4)_6\text{I}_{1.7}$  phase showing consequent reflection misfits, highlighted by black arrows.



**Table 1** Crystal system and unit cell parameters reported for “AgPb<sub>9</sub>(VO<sub>4</sub>)<sub>6</sub>I”, and those determined in this study by Rietveld analysis for β-Pb<sub>3</sub>(VO<sub>4</sub>)<sub>2</sub> as well as reported literature values for β-Pb<sub>3</sub>(VO<sub>4</sub>)<sub>2</sub> (ref. 26) and Pb<sub>9.85</sub>(VO<sub>4</sub>)<sub>6</sub>I<sub>1.7</sub> (ref. 16)

	“AgPb <sub>9</sub> (VO <sub>4</sub> ) <sub>6</sub> I” <sup>1</sup>	β-Pb <sub>3</sub> (VO <sub>4</sub> ) <sub>2</sub> in “AgPb <sub>9</sub> (VO <sub>4</sub> ) <sub>6</sub> I” this study	β-Pb <sub>3</sub> (VO <sub>4</sub> ) <sub>2</sub> [ref. 27]	Pb <sub>9.85</sub> (VO <sub>4</sub> ) <sub>6</sub> I <sub>1.7</sub> [ref. 17]
Crystal system	Monoclinic (NR <sup>a</sup> )	Monoclinic <i>P12<sub>1</sub>/c1</i>	Monoclinic <i>P12<sub>1</sub>/c1</i>	Hexagonal <i>P6<sub>3</sub>/m</i>
<i>a</i> (Å)	7.509	7.518 (1)	7.514	10.422
<i>b</i> (Å)	6.097	6.072 (1)	6.107	—
<i>c</i> (Å)	9.268	9.555 (1)	9.526	7.467
α (°)	90	90	90	90
β (°)	111.8	115.3 (3)	115.2	90
γ (°)	90	90	90	120

<sup>a</sup> Not reported.

compound was reported not to adopt an apatite related structure.<sup>1</sup> Inspection of Table 1 shows the reported unit cell parameters of “AgPb<sub>9</sub>(VO<sub>4</sub>)<sub>6</sub>I” to be close to those determined for β-Pb<sub>3</sub>(VO<sub>4</sub>)<sub>2</sub>, the major phase identified in our reaction product, which adopts the monoclinic space group *P12<sub>1</sub>/c1*. The PXRD patterns acquired here for “AgPb<sub>9</sub>(VO<sub>4</sub>)<sub>6</sub>I” in both open and closed systems are comparable to those reported by Uno *et al.* for “AgPb<sub>9</sub>(VO<sub>4</sub>)<sub>6</sub>I”.<sup>1</sup> In these PXRD patterns, reflections are evident at  $2\theta = 23.7^\circ$ ,  $39.3^\circ$  and  $46.4^\circ$ , which may be attributed to γ-AgI (indexed (*hkl*) as (111), (022) and (113)), as highlighted in Fig. 1 here. These same reflections are apparent, but unindexed, in Fig. 1 of Uno *et al.*<sup>1</sup> These data suggest that the compound identified by Uno *et al.* as “AgPb<sub>9</sub>(VO<sub>4</sub>)<sub>6</sub>I” was, in fact, β-Pb<sub>3</sub>(VO<sub>4</sub>)<sub>2</sub>.

In order to further investigate the product phase assemblage and element distribution, sectioned pieces of the reacted pellets were mounted into an epoxy resin, polished, and characterized using SEM/EDX. In Fig. 3, the SEM image and corresponding EDX element distribution maps for V, Ag, I, and Pb are shown for “AgPb<sub>9</sub>(VO<sub>4</sub>)<sub>6</sub>I” reacted at 700 °C in a sealed quartz tube. From the BSE imaging, at least two primary phases were identified, distinguished according to contrast. Element

distribution maps further support this conclusion, with association of Ag and I in one phase, and association of Pb and V in a second phase. In accordance with the PXRD data, these two phases can be interpreted as the AgI and β-Pb<sub>3</sub>(VO<sub>4</sub>)<sub>2</sub> phases, respectively. EDX analyses (Fig. S3†) of individual β-Pb<sub>3</sub>(VO<sub>4</sub>)<sub>2</sub> grains demonstrated the absence of measurable iodine concentration. The apparent weak iodine signal associated with β-Pb<sub>3</sub>(VO<sub>4</sub>)<sub>2</sub> grains in Fig. 3 is attributed to the background X-ray emission in the I *Lα* energy window (*i.e.*, no discernible I *Lα* emission line was observed in the corresponding EDX spectra). Small inclusions of Ag metal were also identified in the microstructure of this “AgPb<sub>9</sub>(VO<sub>4</sub>)<sub>6</sub>I” sample (Fig. S4†); this phase was not clearly evident in the associated PXRD data due to reflection overlap from compounds with more complex and lower symmetry structures. The presence of Ag metal supports a hypothesised mechanism of Pb<sub>9.85</sub>(VO<sub>4</sub>)<sub>6</sub>I<sub>1.7</sub> *via* decomposition of AgI, liberating I<sub>2</sub> which subsequently reacts with β-Pb<sub>3</sub>(VO<sub>4</sub>)<sub>2</sub>. It was not possible to conclusively identify the minor Pb<sub>9.85</sub>(VO<sub>4</sub>)<sub>6</sub>I<sub>1.7</sub> phase in the microstructure by BSE imaging. Using well-established formulations,<sup>28</sup> the BSE coefficients for β-Pb<sub>3</sub>(VO<sub>4</sub>)<sub>2</sub> and Pb<sub>10</sub>(VO<sub>4</sub>)<sub>6</sub>I<sub>2</sub> were estimated as  $\eta = 0.2903$  and  $\eta = 0.3064$ , respectively, yielding a difference in

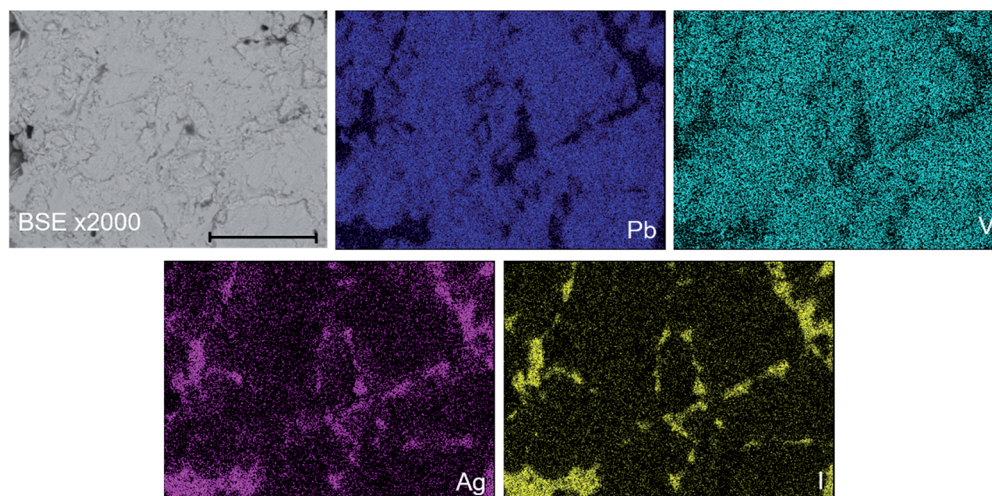


**Fig. 3** BSE SEM image at  $\times 2000$  magnification (scale bar length = 30  $\mu\text{m}$ ) and EDX map of Pb (blue), V (teal), I (yellow), and Ag (pink) present in “AgPb<sub>9</sub>(VO<sub>4</sub>)<sub>6</sub>I” reacted at 700 °C for 5 h in a sealed quartz tube.



**Table 2** Elemental analyses (wt%) as determined by EDX (Meas.) for "AgM<sub>9</sub>(VO<sub>4</sub>)<sub>6</sub>I" (M = Pb, Ba) reacted at 700 °C for 5 h in sealed quartz tubes in comparison with the reported literature<sup>1</sup> (Lit.) and stoichiometric (Stoich.) values

Element	"AgPb <sub>9</sub> (VO <sub>4</sub> ) <sub>6</sub> I"			"AgBa <sub>9</sub> (VO <sub>4</sub> ) <sub>6</sub> I"		
	Elemental wt%			Elemental wt%		
	Stoich.	Lit. <sup>1</sup>	Meas.	Stoich.	Lit. <sup>1</sup>	Meas.
Ag	3.87	4.33	5.3 ± 0.2	4.99	3.30	5.7 ± 0.2
Pb	66.86	64.14	62 ± 2	—	—	—
Ba	—	—	—	57.21	62.67	56 ± 1
V	10.96	15.02	10.8 ± 0.3	14.15	15.83	14.2 ± 0.4
O	13.77	11.48	14 ± 2	17.77	12.24	18 ± 2
I	4.55	5.03	7.9 ± 0.3	5.87	4.61	6.1 ± 0.2

contrast of 5%. Such a small difference in contrast, which would be further reduced by non-stoichiometry in the apatite phase, is acknowledged to make differentiation of the two phases challenging.<sup>28</sup> Nevertheless, by forming a Red – Green – Blue colour map from the EDX signals associated with the Pb M $\alpha$ , I L $\alpha$  and V K $\alpha$  signals, it was possible to identify small white regions that afforded EDX spectra exhibiting X-ray emission lines characteristic of all three elements, but excluding Ag L $\alpha$  emission lines (Fig. S5†). These regions were identified as the Pb<sub>9.85</sub>(VO<sub>4</sub>)<sub>6</sub>I<sub>1.7</sub> component required to adequately fit X-ray diffraction data in Fig. 1. The elemental analysis of the whole field of view in Fig. 3 is displayed in Table 2; the determined average composition is comparable with the expected and reported composition for the "AgPb<sub>9</sub>(VO<sub>4</sub>)<sub>6</sub>I" phase.

TG-DTA analysis (Fig. S6†) of "AgPb<sub>9</sub>(VO<sub>4</sub>)<sub>6</sub>I" reacted at 700 °C for 5 h, in a sealed tube, is characterized with significant weight loss shown in the TG curve beginning at ~630 °C continuing up to ~1100 °C. Uno *et al.* reported "AgPb<sub>9</sub>(VO<sub>4</sub>)<sub>6</sub>I" to be stable up to ~677 °C,<sup>1</sup> which is broadly consistent with the weight loss data obtained in this study. In accordance with the SEM and XRD data, this thermal behaviour can be associated

with the melting and iodine release/decomposition of AgI and Pb<sub>9.85</sub>(VO<sub>4</sub>)<sub>6</sub>I<sub>1.7</sub> within the matrix. Additionally, a DTA signal was observed at ~150 °C, which was indicative of the  $\beta/\gamma \rightarrow \alpha$  phase transformation of AgI,<sup>29</sup> confirming the presence of this compound.

### Synthesis and formation of "AgBa<sub>9</sub>(VO<sub>4</sub>)<sub>6</sub>I"

Powders of Ba<sub>3</sub>(VO<sub>4</sub>)<sub>2</sub> and AgI were batched and reacted using standard solid-state ceramic techniques. The combined starting materials produced pale yellow powders, before reacting. After pressing into pellets and reacting, the resulting pellets were pale yellow with small dark inclusions, and yielded pale and canary yellow powders for those reacted in sealed tubes or air, respectively. For reactions performed in quartz tubes, no apparent sublimation of iodine from the reacted pellet was observed at the cooler end of the tube. The PXRD patterns of "AgBa<sub>9</sub>(VO<sub>4</sub>)<sub>6</sub>I" reacted in air and a sealed tube are shown in Fig. 4. The PXRD patterns of the resulting products were similar, irrespective of sealed tube or open reaction conditions. Phase analysis of each PXRD pattern identified major phases: Ba<sub>3</sub>(VO<sub>4</sub>)<sub>2</sub> (trigonal R $\bar{3}m$ ) and  $\beta/\gamma$ -AgI (hexagonal P6<sub>3</sub>mc/cubic F43m, respectively). Rietveld fitting of X-ray diffraction data of "AgBa<sub>9</sub>(VO<sub>4</sub>)<sub>6</sub>I" was effectively achieved assuming a mixture of Ba<sub>3</sub>(VO<sub>4</sub>)<sub>2</sub>,  $\gamma$ -AgI, and  $\beta$ -AgI, as shown in Fig. 5; the refined phase fractions were 92 ± 1%, 7 ± 1%, and 1.0 ± 0.1%, respectively.

Note, that although the crystal structure of "AgBa<sub>9</sub>(VO<sub>4</sub>)<sub>6</sub>I" was stated to be of rhombohedral symmetry, no space group was determined, and the compound was reported not to adopt an apatite related structure. Inspection of Table 3 shows the reported unit cell parameters of "AgBa<sub>9</sub>(VO<sub>4</sub>)<sub>6</sub>I" to be close to those determined for Ba<sub>3</sub>(VO<sub>4</sub>)<sub>2</sub>, the major phase in our reaction product, which adopts the trigonal space group R $\bar{3}/m$ .<sup>30</sup> The PXRD patterns acquired here for "AgBa<sub>9</sub>(VO<sub>4</sub>)<sub>6</sub>I" in both open and closed systems are comparable to those reported in the by Uno *et al.* for this purported phase.<sup>1</sup> In these PXRD patterns,

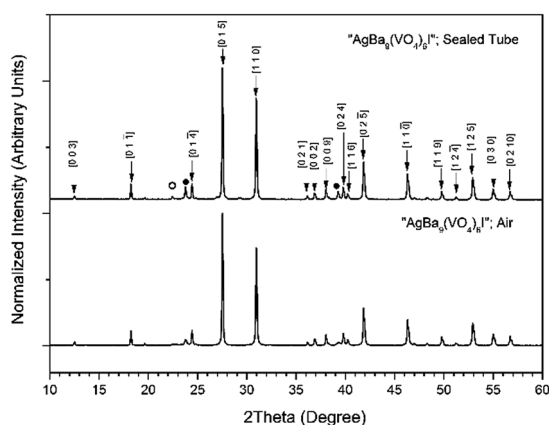


**Fig. 4** PXRD patterns of "AgBa<sub>9</sub>(VO<sub>4</sub>)<sub>6</sub>I" treated at 700 °C for 5 h in either air or a sealed quartz tube. Markers indicate peaks assigned to the Ba<sub>3</sub>(VO<sub>4</sub>)<sub>2</sub> (labelled *hkl* Miller indices),  $\beta$ -AgI (○), and  $\gamma$ -AgI (●) phases.

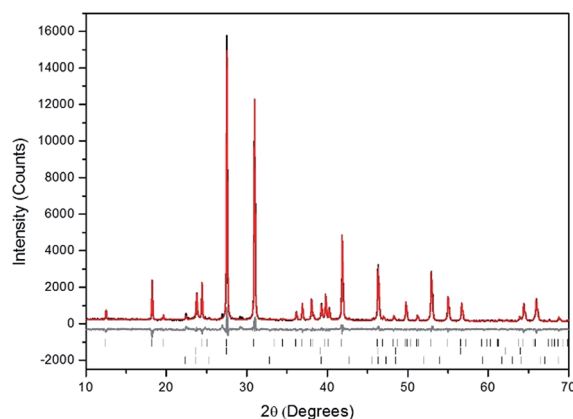


**Fig. 5** Rietveld analysis of PXRD data of "AgBa<sub>9</sub>(VO<sub>4</sub>)<sub>6</sub>I" (black) fit reacted at 700 °C in a sealed quartz tube; the data are shown in black, the fit is shown in red, and the difference plot in grey. Tick marks show allowed reflections of Ba<sub>3</sub>(VO<sub>4</sub>)<sub>2</sub> (upper ticks) and  $\gamma$ -AgI (middle ticks), and  $\beta$ -AgI (lower ticks).



**Table 3** Crystal system and lattice parameters reported<sup>1</sup> for “AgBa<sub>9</sub>(VO<sub>4</sub>)<sub>6</sub>I” and those determined in this study by Rietveld analysis of Ba<sub>3</sub>(VO<sub>4</sub>)<sub>2</sub>

	“AgBa <sub>9</sub> (VO <sub>4</sub> ) <sub>6</sub> I” <sup>1</sup>	Ba <sub>3</sub> (VO <sub>4</sub> ) <sub>2</sub> in “AgBa <sub>9</sub> (VO <sub>4</sub> ) <sub>6</sub> I” this study	Ba <sub>3</sub> (VO <sub>4</sub> ) <sub>2</sub> [ref. 30]
Crystal system	Rhombohedral (NR <sup>a</sup> )	Trigonal $R\bar{3}/m$	Trigonal $R\bar{3}/m$
<i>a</i> (Å)	7.846	7.857 (1)	7.837
$\alpha$ (°)	43.22	43.2 (1)	43.14

<sup>a</sup> Not reported.

reflections are evident at  $2\theta = 23.7^\circ$  and  $39.3^\circ$ , which may be attributed to  $\gamma$ -AgI (indexed as (111) and (022)) and  $2\theta = 22.4^\circ$  to  $\beta$ -AgI (indexed as (010)), as highlighted in Fig. 5 here. These reflections are also apparent but unindexed in Fig. 1 of Uno *et al.*<sup>1</sup> These data suggest that the compound identified by Uno *et al.* as “AgBa<sub>9</sub>(VO<sub>4</sub>)<sub>6</sub>I” was, in fact, Ba<sub>3</sub>(VO<sub>4</sub>)<sub>2</sub>.

The phase assemblage and element distribution for “AgBa<sub>9</sub>(VO<sub>4</sub>)<sub>6</sub>I” was similar to that observed in the Pb counterpart. In Fig. 6, the BSE-SEM image and corresponding EDX maps for V, Ba, I, and Ag are presented for “AgBa<sub>9</sub>(VO<sub>4</sub>)<sub>6</sub>I” reacted at 700 °C in a sealed quartz tube. From the BSE image, two major phases were identified, based on their differentiated contrasts. Element distribution maps were consistent with the BSE images, with a notable association of Ag and I in one phase and Ba and V in a second phase (Fig. S7†). These two phases can be interpreted as the AgI and Ba<sub>3</sub>(VO<sub>4</sub>)<sub>2</sub> phases, respectively, identified by PXRD. Elemental analysis (Table 2) of the entire field of view in Fig. 6, yielded an elemental composition consistent with that of “AgBa<sub>9</sub>(VO<sub>4</sub>)<sub>6</sub>I” as reported in the literature and determined by the calculated stoichiometry.<sup>1</sup> Once again, this information indicates that AgI incorporation into an apatite or other single phase product was not achieved. Small areas of Ag metal were also identified, indicative of

decomposition of AgI but there was no evidence for the presence of an iodoapatite phase, as in the counterpart Pb system.

The TG-DTA analysis (Fig. S8†) of “AgBa<sub>9</sub>(VO<sub>4</sub>)<sub>6</sub>I” reacted at 700 °C for 5 h in a sealed quartz tube was characterized by a gradual weight loss, beginning at  $\sim 680^\circ\text{C}$  in the TG curve. This is consistent with the reported thermal stability of purported “AgBa<sub>9</sub>(VO<sub>4</sub>)<sub>6</sub>I”, which was stated to decompose above  $\sim 677^\circ\text{C}$ .<sup>1</sup> The  $\beta/\gamma \rightarrow \alpha$  phase transformation of AgI was also identified in the DTA signal occurring at  $\sim 152^\circ\text{C}$ ,<sup>29</sup> a further indication of the presence of unreacted AgI in the sample.

## Conclusions

Syntheses of lead/barium vanadium iodoapatite and Ag-I bearing single phases, *i.e.*, “AgM<sub>9</sub>(VO<sub>4</sub>)<sub>6</sub>I” (M = Ba, Pb) were attempted, but proved unsuccessful, contrary to previous literature reports.<sup>1</sup> Reactions were carried out in either sealed quartz tubes or in air at elevated temperatures, which yielded similar results for each system. Notably, for each system investigated, AgI incorporation into an apatite, apatite-like, or alternative ternary phase was not observed.

In these reactions, AgI was mostly unreactive and found as a secondary phase, responsible for the sequestration of the majority of iodine in the sample. However, lead iodovanadinite was identified in the Pb system from reactions performed in closed environments, most likely due to decomposition of AgI and reaction of liberated iodine with the  $\beta$ -Pb<sub>3</sub>(VO<sub>4</sub>)<sub>2</sub>. These results indicate that the stability and formation of AgI is favoured over the formation of a single phase apatite incorporating both Ag and I. Nevertheless, the observed formation of Pb<sub>9.85</sub>(VO<sub>4</sub>)<sub>6</sub>I<sub>1.7</sub> suggests that AgI may be a suitable substrate for the synthesis of this phase as a sacrificial iodine source with stoichiometric quantities of PbO, V<sub>2</sub>O<sub>5</sub> and Pb<sub>3</sub>(VO<sub>4</sub>)<sub>2</sub>. This hypothesis will be the subject of a future communication.

Furthermore, excluding Ag(IO<sub>3</sub>) and iodargyrite, the terrestrial mineral form of AgI, no other Ag/I-bearing monolith

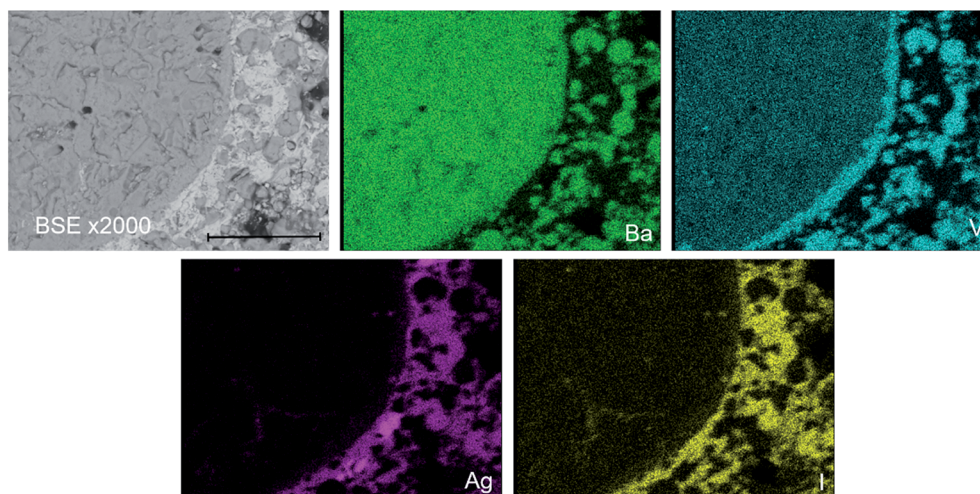


**Fig. 6** BSE-SEM image  $\times 2000$  magnification (scale bar length = 30  $\mu\text{m}$ ) and distribution of V (teal), Ba (green), I (yellow), and Ag (pink) in a sectioned pellet of “AgBa<sub>9</sub>(VO<sub>4</sub>)<sub>6</sub>I” reacted at 700 °C for 5 h in a sealed quartz tube.



phases have been reported.<sup>8,31</sup> However, Ag/lanthanide-containing Pb fluoro- and chloroapatites (*i.e.*,  $\text{Pb}_8\text{AgLn}(\text{PO}_4)_6\text{X}_2$  and  $\text{Pb}_6\text{Ag}_2\text{Ln}_2(\text{PO}_4)_6\text{X}_2$ ; Ln = La, Nd, Eu and X = F, Cl) have been prepared,<sup>3</sup> although no bromo- or iodo-analogues have been reported. Likewise, the endmember compound  $\text{Ag}_2\text{-Pb}_8(\text{PO}_4)_6$  and its analogue  $\text{Ag}_2\text{Pb}_8(\text{AsO}_4)_6$ , which exhibit the apatite structure with fully unoccupied halide channels, have also been synthesized;<sup>32,33</sup> the vanadate-derivative  $\text{Ag}_2\text{Pb}_8(\text{VO}_4)_6$  has yet to be discovered and could give further insight into the nature of these materials.

## Conflicts of interest

There are no conflicts to declare.

## Acknowledgements

The corresponding author (EVJ) would like to thank the Engineering and Physical Sciences Research Council (EPSRC) for the financial support under grant ref. EP/M026566/1. Jong Heo was supported by the National Research Foundation of Korea (NRF) grant funded by the Korean government (MSIT: Ministry of Science and ICT) (NRF-2015M2A7A1000191). Additionally, the authors would like to show gratitude for the financial support concerning the operation of MIDAS facilities at the University of Sheffield by the Department of Energy and Climate Change.

## References

- M. Uno, A. Kosuga, S. Masuo, M. Imamura and S. Yamanaka, *J. Alloys Compd.*, 2004, **384**, 300–302.
- M. Pasero, A. R. Kampf, C. Ferraris, I. V. Pekov, J. Rakovan and T. J. White, *Eur. J. Mineral.*, 2010, **22**, 163–179.
- I. Mayer, A. Semadja and V. J. Weiss, *Solid State Chem.*, 1980, **34**, 223–229.
- I. Mayer, E. Fischbein and S. J. Cohen, *Solid State Chem.*, 1975, **14**, 307–312.
- O. Terra, F. Audubert, N. Dacheux, C. Guy and R. J. Podor, *J. Nucl. Mater.*, 2007, **366**, 70–86.
- J. Wang, *Front. Earth Sci.*, 2015, **3**, 1–11.
- E. E. Jay, P. C. M. Fossati, M. J. D. Rushton and R. W. Grimes, *J. Mater. Chem. A*, 2015, **3**, 1164–1173.
- B. J. Riley, J. D. Vienna, D. M. Strachan, J. S. McCloy and J. L. Jerden Jr, *J. Nucl. Mater.*, 2016, **470**, 307–326.
- X. Hou, V. Hansen, A. Aldahan, G. Possnert, O. C. Lind and G. Lujanienė, *Anal. Chim. Acta*, 2009, **26**, 181–196.
- J. E. Moran, S. Oktay, P. H. Santschi and D. R. Schink, *Environ. Sci. Technol.*, 1999, **33**, 2536–2542.
- Y. Koo, Y. Yang and K. Song, *Prog. Nucl. Energy*, 2014, **74**, 61–70.
- T. Imanaka and H. Koide, *J. Environ. Radioact.*, 1986, **4**, 149–153.
- E. S. Gilbert, R. Tarone and E. J. Ron, *J. Natl. Cancer Inst.*, 1998, **90**, 1654–1660.
- P. D. Wilson, *The Nuclear Fuel Cycle from Ore to Waste*, Oxford University Press, Oxford, 1996.
- M. Uno, M. Shinohara, K. Kurosaki and S. J. Yamanaka, *J. Nucl. Mater.*, 2001, **294**, 119–122.
- F. Lu, T. Yao, Y. Danon, J. Zhou, R. C. Ewing and J. Lian, *J. Am. Ceram. Soc.*, 2015, **98**, 2261–3366.
- F. Audubert, J. M. Savariault and J. L. Lacout, *Acta Crystallogr., Sect. C: Cryst. Struct. Commun.*, 1999, **55**, 271–273.
- F. Lu, T. Yao, J. Xu, S. Scott, Z. Dong, R. C. Ewing and J. Lian, *RSC Adv.*, 2014, **4**, 38718–38725.
- Y. J. Suetsugu, *J. Nucl. Mater.*, 2014, **454**, 223–229.
- M. Zhang, E. R. Maddrell, P. K. Abratis and E. K. H. Salje, *Mater. Sci. Eng., B*, 2007, **137**, 149–155.
- M. Stennett, I. J. Pinnock and N. C. Hyatt, *J. Nucl. Mater.*, 2011, **414**, 352–359.
- T. Yao, S. Scott, G. Xin, F. Lu and J. Lian, *J. Am. Ceram. Soc.*, 2015, **98**, 3733–3739.
- T. Yao, L. Fengyuan, H. Sun, J. Wang, R. C. Ewing and J. Lian, *J. Am. Ceram. Soc.*, 2014, **97**, 2409–2412.
- T. Sakurai, A. Takahashi, N. Ishikawa, Y. Komaki, M. Ohnuki and T. Adachi, *Nucl. Technol.*, 1989, **85**, 206–212.
- T. Sakurai, A. Takahashi, N. Ishikawa, Y. Komaki, M. Ohnuki and T. Adachi, *Nucl. Technol.*, 1992, **99**, 70–79.
- E. C. Buck, E. J. Mausolf, B. K. McNamara, C. Z. Soderquist and J. M. Schwantes, *J. Nucl. Mater.*, 2016, **482**, 229–235.
- P. Garnier, G. Calvarin, J. F. Berar and D. Weigel, *Mater. Res. Bull.*, 1984, **19**, 407–414.
- J. Goldstein, D. E. Newbury, P. Echlin, D. C. Joy, A. D. Romig Jr, C. E. Lyman, C. Fiori and E. Lifshin, *Scanning Electron Microscopy and X-Ray Microanalysis*, Plenum Press, New York and London, 2nd edn, 1992.
- W. A. Bassett and T. Takahashi, *Am. Mineral.*, 1965, **50**, 1576–1594.
- P. Süssse and M. J. Buerger, *Z. Kristallogr.*, 1970, **131**, 161–174.
- L. L. Burger, R. D. Scheele and K. D. Wiemers, *Selection of a Form for Fixation of Iodine-129, PNL-4045*, Battelle Pacific Northwest Laboratory, Richland, WA, 1981.
- G. Engel and H. Jäckle, *Z. Anorg. Allg. Chem.*, 1979, **448**, 71–78.
- R. Ternane, M. Ferid, N. Kbir-Arighuib and M. Trabelsi-Ayedi, *J. Alloys Compd.*, 2000, **308**, 83–86.



## Synthesis of simulatant 'lava-like' fuel containing materials (LFCM) from the Chernobyl reactor Unit 4 meltdown

Sean T. Barlow, Daniel J. Bailey, Adam J. Fisher, Martin C. Stennett, Claire L. Corkhill and Neil C. Hyatt  
Department of Materials Science and Engineering, The University of Sheffield, S1 3JD, UK.

### ABSTRACT

A preliminary investigation of the synthesis and characterization of simulatant 'lava-like' fuel containing materials (LFCM), as low activity analogues of LFCM produced by the melt down of Chernobyl Unit 4. Simulant materials were synthesized by melting batched reagents in a tube furnace at 1500 °C, under reducing atmosphere with controlled cooling to room temperature, to simulate conditions of lava formation. Characterization using XRD and SEM-EDX identified several crystalline phases including  $ZrO_2$ ,  $UO_x$  and solid solutions with spherical metal particles encapsulated by a glassy matrix. The  $UO_x$  and  $ZrO_2$  phase morphology was very diverse comprising of fused crystals to dendritic crystallites from the crystallization of uranium initially dissolved in the glass phase. This project aims to develop simulatant LFCM to assess the durability of Chernobyl lavas and to determine the rate of dissolution, behavior and evolution of these materials under shelter conditions.

### INTRODUCTION

On the 26<sup>th</sup> of April 1986, an accident during an experimental power failure test destroyed Unit 4 of the Chernobyl Nuclear Power Plant, Ukraine. During the accident, temperatures reached in excess of 1600 °C resulting in melting of the nuclear fuel and zirconium cladding [1]. Interaction of the molten fuel mass with the structural materials of the reactor resulted in the formation of several lava-like flows. These lava-like flows formed glassy materials upon cooling in the basement levels beneath the ruined reactor [2]. These so called lava-like fuel containing materials (LFCM) are essentially glass-ceramic composite materials [3]. Accumulations of LFCM are located in numerous sub-reactor rooms beneath Unit 4, amounting to approximately 1250 tons [1]. LFCM masses are primarily brown or black and contain considerable porosity and compositional heterogeneity. However, granulated and pumice-like materials have also been observed. Solidified metallic spheres of varying diameter have been found in brown and black type lavas. Granulated and pumice-like materials are hypothesized to be the result of lava flows interacting with cold water, causing instant foaming and the formation of highly porous material [3].

Following the accident, an interim shelter was constructed to contain the ruined reactor and protect its contents. Although designed to last 30 years, degradation of the shelter structure has led to the ingress of substantial volumes of water. Interaction of water with LFCM within the shelter has caused weathering of substantial portions of the LFCM and formation of numerous secondary uranium compounds, studtite ( $UO_4 \cdot H_2O$ ), rutherfordine ( $UO_2CO_3$ ), schoepite ( $(UO_2)_8O_2(OH)_{12} \cdot 12H_2O$ ) and paulscherrerite ( $UO_2(OH)_2$ ). Constant wetting and drying of LFCM materials and associated secondary uranium mineral phases leads to the formation of fine radioactive aerosol particles; a significant respirable hazard within the shelter and a possible

source of airborne contamination [4], [5]. The study of the alteration of LFCM under shelter conditions is vital to understanding the long term behaviour of these materials, the hazard LFCM presents and the eventual remediation of the site. Due to the large amounts of spent nuclear fuel contained within LFCM, study of actual LFCM is hazardous and not without considerable challenge. Study of low activity simulant LFCM, derived from actual lava compositions, is needed to understand the durability of LFCM materials and to determine the alteration behaviour of these materials. This study was therefore conceived to design and synthesize representative simulant LFCM to allow the behaviour of LFCM to be studied without the additional complications of high radioactivity. The findings of this project could also assist in the development of glass wastefoms in engineered repositories.

## REVIEW OF LFCM AND COMPOSITIONS AS SYNTHETIC TARGETS

Brown LFCM contains metallic iron in the form of spherical droplets within the glass matrix and ~11 wt% uranium. Black LFCM do not contain metallic iron and incorporate less uranium, ~6 wt% [1]. Analysis of LFCM by the Khloplin Radium Institute revealed several crystalline inclusions including non-stoichiometric  $\text{UO}_2$ ,  $\text{ZrO}_2$ , from the fuel cladding materials, and a high uranium zircon phase termed Chernobylite. Dendrite-like inclusions of  $\text{UO}_x + \text{Zr}$  were reported, representing recrystallization of LFCM after cooling, along with phases of a fused morphology from the interaction between droplets of  $\text{UO}_x$  and Zirconium alloy cladding [6]. Compositions of brown and black LFCM have been reported in numerous publications, but each differ with regards to major glass components [1], [3], [7]–[9]. Consequently, averaged compositions were determined and used to produce the simulant materials in this study. Synthesized simulant compositions are shown in Table 1.

**Table 1.** Synthesized LFCM compositions

Component	Brown LFCM (mol%)	Black LFCM (mol%)
$\text{SiO}_2$	65.6	67.9
$\text{CaO}$	7.3	8.2
$\text{ZrO}_2$	3.3	3.0
$\text{Na}_2\text{O}$	5.3	5.8
$\text{BaO}$	0.1	0.1
$\text{Al}_2\text{O}_3$	4.2	5.1
$\text{MnO}$	0.5	0.4
$\text{Fe}_2\text{O}_3$	0.5	-
$\text{MgO}$	10.7	8.4
$\text{UO}_2$	2.5	1.2

## EXPERIMENTAL PROCEDURE

Stoichiometric amounts of  $\text{SiO}_2$  (Lochaline Quartz Sand 99.6%),  $\text{CaCO}_3$  (Fisher 98%),  $\text{ZrO}_2$  (Aldrich 99%),  $\text{Na}_2\text{CO}_3$  (Alfa Aesar 98%),  $\text{BaCO}_3$  (Alfa Aesar 99%),  $\text{Al}(\text{OH})_3$  (Acros 95%),  $\text{Mn}_2\text{O}_3$  (Aldrich 99%),  $\text{Fe/Cr}_{18}/\text{Ni}_{10}/\text{Mo}_3$  (Goodfellow),  $\text{Mg}(\text{OH})_2$  (Sigma-Aldrich 99.9%)

and UO<sub>2</sub> (British Drug Houses) were batched accordingly to produce both black and brown compositions. Batched compositions were carefully mixed prior to melting in an Elite Thermal Systems TSH 15/50/450 tube furnace under flowing H<sub>2</sub>/N<sub>2</sub>. Reducing conditions were utilized to simulate formation conditions during the accident. Samples were melted at 1500 °C and cooled to room temperature at a controlled rate. Initial samples were prone to spontaneous fracturing and an intermediate annealing step was successfully applied to reduce the residual stresses within the glass and obtain monolithic samples.

X-ray powder diffraction (XRD) was performed to determine the crystalline phases present within synthesized materials. Measurements were conducted using a Bruker D2 X-ray diffractometer in reflectance mode over the range  $10^\circ < 2\theta < 60^\circ$  with Cu K $\alpha$  radiation (30 kV, 10 mA). Subsequent data was processed using the Bruker DiffracEva 3.0 software package and the PDF-2 database used for peak identification.

Representative cross-sections of synthesized LFCM were produced by sectioning melted glasses using a Buehler Isomet Low Speed Saw. Crystalline phase assemblage of the cross-sections was studied by scanning electron microscopy (SEM) using a Hitachi TM3030 SEM. Partitioning of key elements within the simulant samples was determined by energy dispersive X-ray spectroscopy (EDX) using a Bruker Quantax EDX system coupled to the SEM. Samples were prepared for SEM-EDX by mounting in cold-setting epoxy resin and polishing with SiC and diamond paste to a 1  $\mu$ m finish. Samples were sputter coated with carbon to avoid surface charge effects.

## RESULTS & DISCUSSION

### LFCM Synthesis

Produced ‘Brown’ and ‘Black’ LFCM compositions formed highly crystalline, glassy products. Brown type simulants were dark brown in color with a cracked and mottled surface with low porosity. Black simulant compositions formed a dark blue glass with a thin pale-blue surface layer that was glassy in appearance. The pale blue colored surface is not reported as present in the actual LFCM samples, found in the Chernobyl sub-reactor rooms, and the bulk was much darker in coloration. However, one particular LFCM variant, termed polychromatic ceramic, located in the upper levels of the destroyed Unit 4, was described as “a sealing-wax brown color with bright blue veinlets” [10]. Overall, the visual appearance of the simulants is comparable with reported LFCM.

### Phase analysis

Results of powder X-ray diffraction analysis showed simulant LFCM to be glassy materials with significant crystalline content, as shown in Figure 1. The strong diffuse intensity is typical of glassy materials and the observed reflections were indexed to zirconium oxide (ZrO<sub>2</sub>), a uranium-zirconium oxide solid solution (U<sub>0.8</sub>Zr<sub>0.2</sub>O<sub>2</sub>) and cristobalite (SiO<sub>2</sub>). Brown compositions were also found to contain a spinel phase, nominally Fe(Fe<sub>1.96</sub>Cr<sub>0.03</sub>Ni<sub>0.01</sub>)O<sub>4</sub>.

The pale blue surface phase observed on black simulant lava was removed and characterized by XRD however no significant difference compared to the bulk was detected. This phase is believed to contain uranium in the U (IV) oxidation state, due to its blue coloration. A full analysis of the average oxidation state within the lavas will be carried out at a later date.

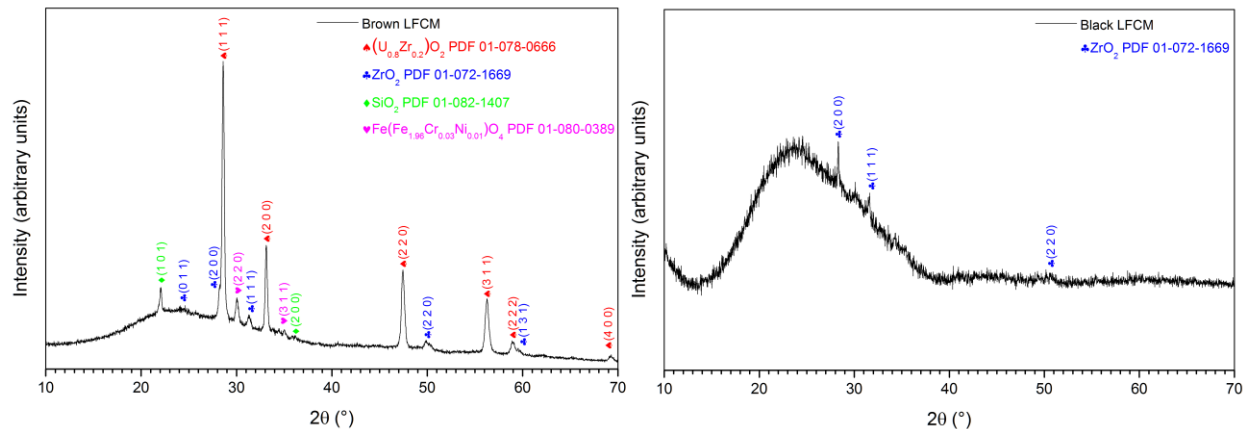


Figure 1. XRD plot of simulant brown (left) and black (right) LFCM

Scanning electron microscopy of black and brown simulant lavas found the microstructure to consist of a majority glass matrix with various minor phases dispersed throughout as distinguished by their contrast. Minor phases rich in U and Zr were present as dendritic and fused crystals. Spherical particles of metal were also found throughout the glass matrix of brown LFCM simulants, likely formed as droplets of molten metal trapped within the glass matrix during melting, as shown in Figure 2. Complementary EDX analysis highlights elemental partitioning with the samples in correspondence with the crystalline phases identified by XRD. EDX maps for the key elements indicate uranium and zirconium are evenly distributed throughout the glass matrix and concentrated within their representative crystal phases as shown in Figure 3.

Comparison of the experimental data presented in this study with the results of analysis of actual LFCM shows good agreement between the simulant and real materials [1], [3], [7]–[9]. Morphology, crystalline content and microstructure were found to be consistent with those observed in actual LFCM samples with the notable exception of the crystalline phase zircon ( $\text{ZrSiO}_4$ ). These results would suggest that, although the simulant materials are a good approximation, further refinement is necessary to produce more representative simulant LFCM.

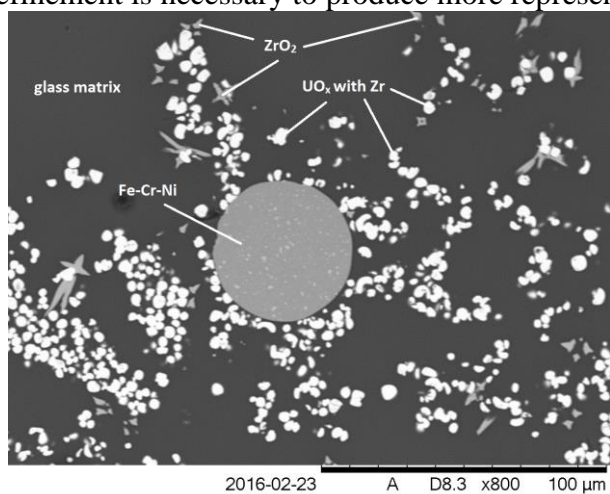


Figure 2. SEM micrograph of simulant brown LFCM labeling the crystalline phases present.

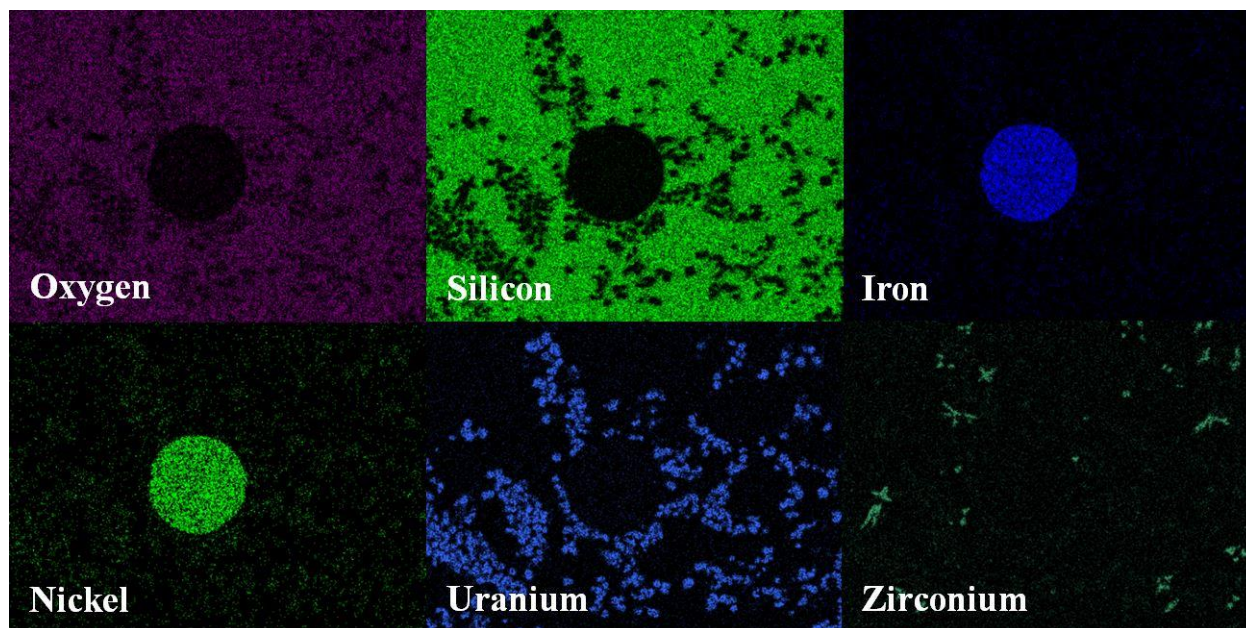


Figure 3. EDS maps of key elements in brown LFCM

### **Further elaboration of simulant LFCM**

The behaviour of LFCM compositions when melting will be further studied by simultaneous thermal analysis (STA). This will allow the glass transition temperature and liquidus temperature of synthesized samples to be determined. The results will allow further refinement of the synthesis process and aid in the production of more representative samples.

The relative durability of simulant LFCM will be studied using standard test protocols to allow direct comparison with both UK and international glass wasteforms for the immobilization of high and intermediate level radioactive waste.

Alteration of samples under simulated shelter conditions, including simulated groundwater and high humidity, will be performed to encourage the formation of secondary uranium phases and allow studying the formation of alteration products observed on actual LFCM samples.

X-ray absorption spectroscopy (XAS) will be implemented to determine the average oxidation state of uranium in synthesized simulants; which is known to have influence on the solubility of U [11]. This will aid in the understanding of U in the dissolution of LFCM.

## **CONCLUSIONS**

This study demonstrates the successful synthesis of simulant ‘lava-like’ fuel containing materials. The morphology and microstructure have both been recreated successfully in the simulant material and the crystalline content has been found to be largely similar with the exception of zircon. Further refinement of the composition and synthesis procedure is ongoing;

production of adjusted LFCM compositions to reproduce the zircon phase is underway with promising results so far.

## ACKNOWLEDGMENTS

The authors would like to thank the EPSRC (Grants EP/G037140/1, EP/N017374/1, EP/L014041/1) for financial support for this research, which was performed at the MIDAS Facility, at the University of Sheffield, established with support from the Department of Energy and Climate Change. We also acknowledge financial support from the EPSRC allocation to University of Sheffield from its Global Challenges Research Fund.

## REFERENCES

- [1] A. Bilyk, A. Novikov, K. Shefer, V. Kashtanov, L. Dodd, and Y. Appolonsky, “‘Shelter’ Object Safety Status Report / Отчет О Состоянии Безопасности Объекта « Укрытие »,” (2008).
- [2] A. S. Baev, Y. A. Teterin, K. E. Ivanov, A. Y. Teterin, and S. A. Bogatov, “X-ray photoelectron Study of the Samples of Fuel Containing Masses Formed as a Result of the Chernobyl Accident,” *Radiochemistry*, vol. 39, no. 2, pp. 169–174, (1997).
- [3] E. M. Pazukhin, “Fuel-Containing Lavas of the Chernobyl NPP 4th Block Topography physicochemical properties and formation scenario,” *Radiochemistry*, vol. 36, no. 2, pp. 109–154, (1994).
- [4] A. A. Borovoi, “Nuclear fuel in the shelter,” *At. Energy*, vol. 100, no. 4, pp. 249–256, (2006).
- [5] I. E. Kuz and V. V Tokarevskii, “Sources and mechanisms of aerosol formation in the Chernobyl ‘Sarcophagus,’” *At. Energy*, vol. 82, no. 2, pp. 130–136, (1997).
- [6] B. E. Burakov, E. B. Anderson, S. I. Shabalev, E. E. Strykanova, S. V. Ushakov, M. Trotabas, J. Y. Blanc, P. Winter, and J. Duco, “The Behavior of Nuclear Fuel in First Days of the Chernobyl Accident,” *Mater. Res. Soc. Symp. Proc.*, vol. 465, no. August, pp. 1297–1308, (1997).
- [7] Y. A. Olkhovyk and M. I. Ojovan, “Corrosion Resistance of Chernobyl NPP Lava Fuel-Containing Masses,” *Innov. Corros. Mater. Sci.*, vol. 5, no. 1, pp. 36–42, (2015).
- [8] A. A. Borovoi, A. S. Lagunencko, and E. M. Pazukhin, “Radiochemical and Selected Physicochemical Characteristics of Lava and Concrete from Subreactor Room no. 304/3 of the Fourth Block of the Chernobyl Nuclear Power Plant and Their Connection with the Accident Scenario,” *Radiochemistry*, vol. 41, no. 2, pp. 197–202, (1999).
- [9] A. A. Shiryaev, I. E. Vlasova, B. E. Burakov, B. I. Ogorodnikov, V. O. Yapaskurt, A. A. Averin, A. V. Pakhnevich, and Y. V. Zubavichus, “Physico-chemical properties of Chernobyl lava and their destruction products,” *Prog. Nucl. Energy*, vol. 92, no. 2016, pp. 104–118, (2016).
- [10] E. M. Pazukhin, A. S. Lagunencko, V. A. Krasnov, and V. V Bil, “Fuel at Upper Levels of the Destroyed Fourth Block of Chernobyl NPP . Refining the Formation Scenario of the Polychromatic Ceramics,” *Radiochemistry*, vol. 48, no. 5, pp. 522–534, (2006).
- [11] E. R. Weiner, *Applications of Environmental Aquatic Chemistry: A Practical Guide*, 3rd ed. CRC Press, (2013).

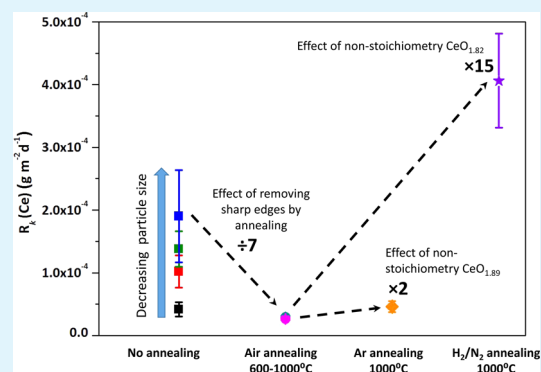
# Role of Microstructure and Surface Defects on the Dissolution Kinetics of CeO<sub>2</sub>, a UO<sub>2</sub> Fuel Analogue

Claire L. Corkhill,\* Daniel J. Bailey, Florent Y. Tocino, Martin C. Stennett, James A. Miller, John L. Provis, Karl P. Travis, and Neil C. Hyatt\*

Immobilisation Science Laboratory, Department of Materials Science and Engineering, The University of Sheffield, Sir Robert Hadfield Building, Mappin Street, Sheffield S1 3JD, U.K.

**ABSTRACT:** The release of radionuclides from spent fuel in a geological disposal facility is controlled by the surface mediated dissolution of UO<sub>2</sub> in groundwater. In this study we investigate the influence of reactive surface sites on the dissolution of a synthesized CeO<sub>2</sub> analogue for UO<sub>2</sub> fuel. Dissolution was performed on the following: CeO<sub>2</sub> annealed at high temperature, which eliminated intrinsic surface defects (point defects and dislocations); CeO<sub>2-x</sub> annealed in inert and reducing atmospheres to induce oxygen vacancy defects and on crushed CeO<sub>2</sub> particles of different size fractions. BET surface area measurements were used as an indicator of reactive surface site concentration. Cerium stoichiometry, determined using X-ray Photoelectron Spectroscopy (XPS) and supported by X-ray Diffraction (XRD) analysis, was used to determine oxygen vacancy concentration. Upon dissolution in nitric acid medium at 90 °C, a quantifiable relationship was established between the concentration of high energy surface sites and CeO<sub>2</sub> dissolution rate; the greater the proportion of intrinsic defects and oxygen vacancies, the higher the dissolution rate. Dissolution of oxygen vacancy-containing CeO<sub>2-x</sub> gave rise to rates that were an order of magnitude greater than for CeO<sub>2</sub> with fewer oxygen vacancies. While enhanced solubility of Ce<sup>3+</sup> influenced the dissolution, it was shown that replacement of vacancy sites by oxygen significantly affected the dissolution mechanism due to changes in the lattice volume and strain upon dissolution and concurrent grain boundary decohesion. These results highlight the significant influence of defect sites and grain boundaries on the dissolution kinetics of UO<sub>2</sub> fuel analogues and reduce uncertainty in the long term performance of spent fuel in geological disposal.

**KEYWORDS:** nuclear fuel, dissolution, defects, oxygen vacancies, grain boundaries



## 1. INTRODUCTION

Spent nuclear fuel is a heterogeneous ceramic material composed primarily of UO<sub>2</sub>, with a minor component of actinides and fission products. The internationally supported strategy for the safe disposal of this nuclear waste material is within a geological disposal facility,<sup>1</sup> where the release of radionuclides to the environment will be dominated by the interaction of the UO<sub>2</sub> matrix with groundwater. To assess the long-term performance of the geological disposal site toward the containment of radionuclides, a safety case is being prepared, which assesses the mechanism and kinetics of fuel dissolution; accordingly, a large number of laboratory experiments have been focused on determining the dissolution kinetics of UO<sub>2</sub> under a wide variety of temperature and redox conditions.<sup>2,3</sup> However, dissolution rates determined from natural uraninite (UO<sub>2</sub>) ore weathering indicate that rates measured in the laboratory are orders of magnitude greater than in nature.<sup>4,5</sup> This phenomenon has been widely considered and is attributed to a number of factors including artifacts of specimen preparation, solution saturation state, and changes in surface area with time.<sup>6</sup> Clearly, it is important to

the development of a robust postclosure safety case for spent fuel disposal that such uncertainty is reduced.

In the current study, we consider the role of “energetically reactive sites”, which contain fewer, and weaker, chemical bonds than those on defect-free surfaces or in the bulk, in the determination of laboratory dissolution rates of spent UO<sub>2</sub> fuel. These sites, which may include natural crystal defects (point defects and dislocations), grain boundaries, or sample preparation-induced artifacts (e.g., polishing scratches or sharp edges on crushed particles), comprise atoms that have greater reactivity than those in the defect-free surfaces or in the bulk, thus may dissolve more rapidly.<sup>7,8</sup> For example, the dissolution of UO<sub>2</sub> and a CeO<sub>2</sub> analogue for UO<sub>2</sub> have been found to be influenced by sample crushing<sup>9,10</sup> and polishing;<sup>11</sup> dissolution rates were overestimated by 3 orders of magnitude due to the reactive surface sites induced through these sample preparation techniques.<sup>11</sup> Natural defects, especially randomly distributed oxygen vacancy defects, dominate the lattice

Received: November 23, 2015

Accepted: March 29, 2016

Published: March 29, 2016

structure of spent  $\text{UO}_2$  fuel, due to the incorporation of trivalent rare earth fission products in the  $\text{UO}_2$  lattice.<sup>12</sup> It has been hypothesized that the presence of such energetically reactive defect sites may influence the dissolution rate.<sup>13–18</sup> However, the extent of such an effect on the overall dissolution rate is difficult to observe when other factors, such as the enhanced solubility of  $\text{U(VI)}$  over  $\text{U(IV)}$ , strongly influence the dissolution behavior. Recent work by the current authors has shown that these seemingly minor features may significantly influence the *initial* dissolution rate of  $\text{UO}_2$  fuel analogues<sup>11,19</sup> and, therefore, should be taken into consideration alongside other important factors (notably oxidation, solubility, and radiolysis) when understanding dissolution mechanisms of spent fuel.

In an attempt to preclude the dominant effects of  $\text{U(IV)}$  oxidation, the high solubility of  $\text{U(VI)}$  and radiolysis on the dissolution kinetics, we here report the role of energetically reactive features on the dissolution of a  $\text{UO}_2$  analogue,  $\text{CeO}_2$ , that was developed to closely resemble the microstructure of  $\text{UO}_2$  fuel.<sup>20</sup> Both  $\text{UO}_2$  and  $\text{CeO}_2$  crystallize in the same fluorite-type structure ( $Fm\bar{3}m$ ) and can be engineered to have similar grain sizes and crystallographically randomly orientated grains. We describe an evaluation of how energetically reactive sites, including intrinsic surface defects and oxygen vacancies, influence dissolution kinetics. Through quantification of these effects, we attempt to improve our understanding of the uncertainties associated with dissolution rates of spent fuel in geological disposal conditions.

## 2. EXPERIMENTAL METHODS

**2.1.  $\text{CeO}_2$  Preparation.** Cerium dioxide monoliths were prepared according to Stennett et al.,<sup>20</sup> at a sintering temperature of 1700 °C. Monoliths were crushed using a percussion mortar and ball mill, sieved to four different size fractions, 25–50  $\mu\text{m}$ , 75–150  $\mu\text{m}$ , 300–600  $\mu\text{m}$ , and 2–4 mm, and washed, all according to ASTM C1285 (the Product Consistency Test).<sup>21</sup> Prior to use, the particles were inspected by Scanning Electron Microscopy (SEM) to ensure no fine particles <1  $\mu\text{m}$  in size remained adhered to particle surfaces. Particles in the size fraction 25–50  $\mu\text{m}$  were subjected to further heat treatment; annealing in air was performed in a standard muffle furnace heated to 300, 400, 600, 800, 1000, and 1250 °C at a ramp rate of 5 °C  $\text{min}^{-1}$  and held for 4 h. Annealing in inert (Ar) and reducing (5%  $\text{H}_2$ /95%  $\text{N}_2$ ) atmospheres was performed in a standard tube furnace, sealed, and purged with gas for 2 h prior to heating to 1000 °C at a ramp rate of 5 °C  $\text{min}^{-1}$  and held for 4 h. Following dissolution, particles were dried by patting with tissue and placed in an inert-atmosphere desiccator prior to analysis.

**2.2. Particle Characterization.** The surface area of each crushed size fraction and the 25–50  $\mu\text{m}$  heat-treated particles was determined using the Brunauer, Emmett, and Teller (BET) method, using a nitrogen adsorbate. Particles were degassed for 3 h at 200 °C and analyzed using a Beckman Coulter SA3100 instrument. The surface oxidation state of annealed particles was determined using a Kratos Axis Ultra X-ray Photoelectron Spectrometer (XPS) with a monochromatic Al  $K\alpha$  source. The spectral intensities recorded were converted to surface oxidation state concentrations by first subtracting a Shirley-type background<sup>22</sup> and then obtaining accurate peak positions by fitting peaks using a mixed Gaussian/Lorentzian line shape. All photoelectron binding energies were referenced to C 1s adventitious contamination peaks at a binding energy of 285 eV.

Powder X-ray Diffraction (XRD) patterns were acquired using a Bruker D2 Phaser diffractometer operating in reflection mode at 30 kV and 10 mA with Cu  $K\alpha_1$  radiation. Data were collected between  $20 < 2\theta < 60^\circ$  at  $2^\circ \text{min}^{-1}$  and a step size of  $0.02^\circ$ . Rietveld analysis of phases identified in the diffraction patterns was performed using the refinement software, Topas (Bruker), and strain was calculated using

the Double-Voigt approach.<sup>23</sup> Secondary electron images of particles were acquired using a Hitachi TM3030 SEM, operating at an accelerating voltage of 15 kV and a working distance of 18 mm.

**2.3.  $\text{CeO}_2$  Dissolution.** Samples of 0.1 g of each size fraction of  $\text{CeO}_2$  particles were placed in 50 mL PTFE vessels, which had been cleaned according to ASTM C1285.<sup>21</sup> Each vessel was filled with 40 mL of 0.01 M  $\text{HNO}_3$  (pH 2.0), sealed, and placed within a Carbolite oven. For 25–50  $\mu\text{m}$   $\text{CeO}_2$  particles with no annealing treatment, experiments were performed at 40, 70, and 90 °C ( $\pm 0.5^\circ\text{C}$ ). All other experiments were performed at 90 ( $\pm 0.5$ ) °C. Each experiment was performed in triplicate with duplicate blanks, and sampling was conducted at regular intervals from 0 to 35 days. During each sampling, an aliquot (1.2 mL) of the supernatant liquid in each vessel was removed and filtered (0.22  $\mu\text{m}$ ) prior to analysis by Inductively Coupled Plasma – Mass Spectroscopy (ICP-MS) (Agilent 4500 Spectrometer). Solution data expressed as the normalized weight loss ( $N_L$ , expressed in  $\text{g m}^{-2}$ ) were calculated from the Ce concentrations after normalization by the surface area  $S$  ( $\text{m}^2$ ) of the sample in contact with the solution (assuming that all the surface is “reactive”) and by the mass loading of the element considered in the solid (i.e.,  $f_i$  is expressed as the ratio between the mass of the considered element and the overall mass of the leached sample), according to eq 1<sup>24,25</sup>

$$N_L(i) = \frac{m_i}{f_i \times S} \quad (1)$$

where  $m_i$  (g) corresponds to the total amount of the element  $i$  measured in the solution.

Derivation of eq 1 as a function of dissolution time gives the normalized dissolution rate of Ce ( $R_L(\text{Ce})$ ), expressed in  $\text{g m}^{-2} \text{d}^{-1}$ <sup>26</sup>

$$\begin{aligned} R_L(\text{Ce}) &= \frac{dN_L(\text{Ce})}{dt} = \frac{1}{f_{\text{Ce}} \times S} \times \frac{dm_{\text{Ce}}}{dt} \\ &= \frac{1}{f_{\text{Ce}} \times S} \times \frac{d}{dt}(C_{\text{Ce}} \times V) \approx \frac{V}{f_{\text{Ce}} \times S} \times \frac{dC_{\text{Ce}}}{dt} \end{aligned} \quad (2)$$

where  $C_{\text{Ce}}$  ( $\text{g L}^{-1}$ ) is the concentration of Ce in solution, and  $V$  (L) is volume of leachate. In this expression, the  $f_{\text{Ce}}$  and  $S$  values are usually assumed to remain almost constant during the leaching experiments, which can be considered as a valid assumption at the beginning of the dissolution tests for powdered samples.

## 3. RESULTS

**3.1. Characterization of Defect Structures in  $\text{CeO}_2$ .** Particles from the 25–50  $\mu\text{m}$  size fraction were annealed in air at temperatures ranging from 300–1250 °C. One sample was analyzed without annealing for comparison. High temperature annealing in air lead to a reduction in surface area, as shown in Figure 1. For example, annealing at 600 °C gave a surface area of  $0.20 \pm 0.01 \text{ m}^2 \text{ g}^{-1}$ , while at 1000 °C the surface area was  $0.11 \pm 0.01 \text{ m}^2 \text{ g}^{-1}$ . We hypothesize that the surface area decrease reflects the removal of “sharp edges” and other intrinsic surface defects in the  $\text{CeO}_2$  particles, during heating. When the annealing temperature was increased to the range 700 to 1250 °C, a sharp drop in surface area was observed. This may be due to agglomeration of particles at these higher temperatures. Dissolution rate investigation was performed on samples annealed at 600 and 1000 °C; both were representative of the removal of “sharp edges” and intrinsic surface defects, but samples annealed at 1000 °C additionally represented particles with a significantly lower surface area.

An attempt to generate oxygen vacancies in particles of  $\text{CeO}_2$  in the 25–50  $\mu\text{m}$  size fraction was made by annealing at 1000 °C in the absence of oxygen (inert or reducing environments). The creation of an oxygen vacancy in  $\text{CeO}_2$  is accompanied by the release of two electrons from lattice  $\text{O}^{2-}$ , resulting in the reduction of  $\text{Ce}^{4+}$  ions to  $\text{Ce}^{3+}$ .<sup>27</sup> Reduction from  $\text{CeO}_2$  to

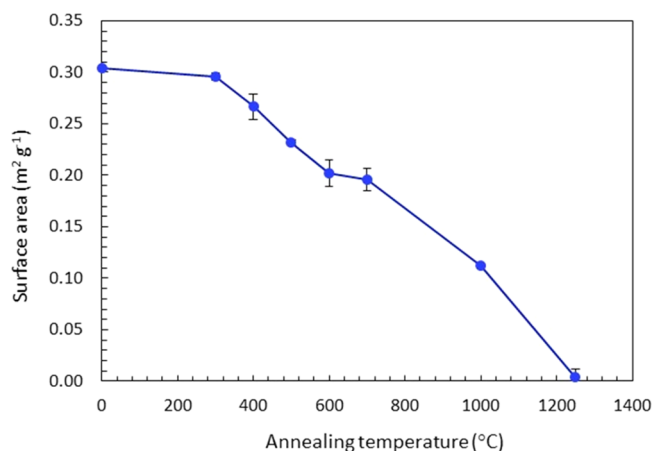


**Figure 1.** Surface area analysis of CeO<sub>2</sub> 25–50 μm particles as a function of annealing temperature, as determined by the BET method. Errors represent 1σ from triplicate samples.

Ce<sub>2</sub>O<sub>3</sub> occurs through the formation of CeO<sub>2-x</sub> intermediate phases;<sup>28</sup> to confirm the presence of oxygen vacancies, the oxidation state of Ce was determined using XPS, shown in Figure 2. Trivalent Ce was identified in the particle surfaces (top ~10 nm), confirming that Ce<sup>4+</sup> reduction to Ce<sup>3+</sup> had

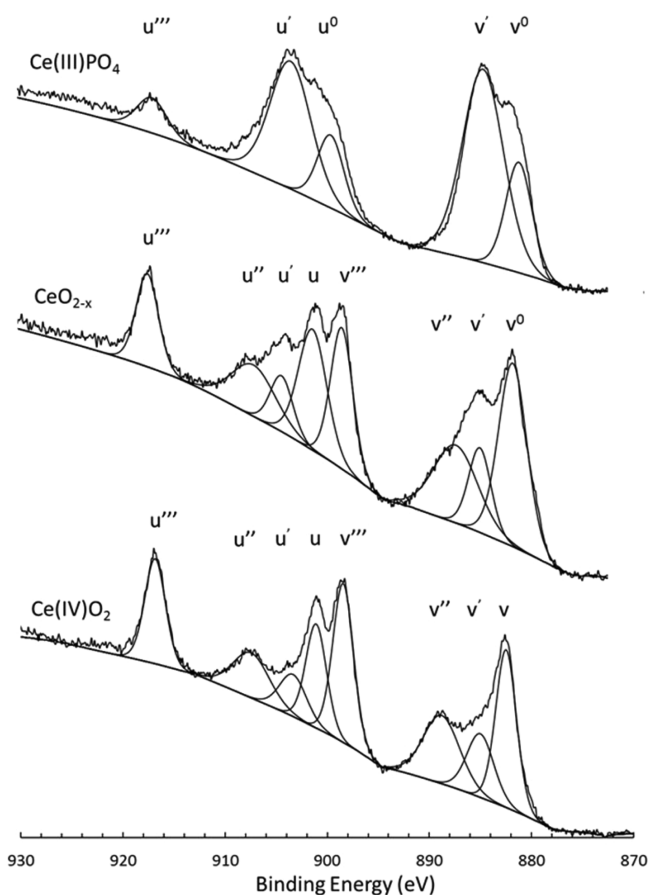


**Figure 2.** X-ray photoelectron oxidation state analysis of CeO<sub>2</sub> annealed under reducing conditions, showing Ce 3d spectra for CeO<sub>2-x</sub> annealed in a reducing (H<sub>2</sub>/N<sub>2</sub>) atmosphere. Standard spectra for Ce<sup>3+</sup>- and Ce<sup>4+</sup>-containing materials are shown for comparison. Peak deconvolution was performed and labeled according to the accepted Burroughs nomenclature<sup>30</sup> for Ce 3d as described in Table 1.

**Table 1.** Experimental Binding Energies and FWHM for Ce 3d Peaks Derived from a CePO<sub>4</sub> Standard and CeO<sub>2</sub> and CeO<sub>2-x</sub> Particles Investigated in the Current Study

Ce 3d peak assignment	oxidation state assignment	binding energy (eV) (±0.1)	fwhm (eV) (±0.05)
v <sup>0</sup>	3+	881.90	3.0
V	3+	882.40	1.8
v'	4+	885.30	4.3
v''	4+	888.40	4.2
v'''	4+	898.50	2.3
u <sup>0</sup>	3+	899.95	3.0
U	3+	901.10	1.8
u'	4+	903.00	4.3
u''	4+	907.60	4.2
u'''	4+	916.80	2.3

occurred. The Ce 3d XPS data were resolved using ten components;<sup>29</sup> Table 1 describes each of the components found in the current study according to the accepted Burroughs nomenclature.<sup>30</sup> These data are in excellent agreement with previously published XPS data for partially reduced CeO<sub>2</sub><sup>31,32</sup> and show that samples annealed in an inert or reducing environment were not fully reduced to Ce<sub>2</sub>O<sub>3</sub> but contained a combination of identifiable contributions from both Ce<sup>3+</sup> and Ce<sup>4+</sup> oxidation states at the sample surface. This indicates the formation of partially reduced CeO<sub>2</sub> with a stoichiometry of CeO<sub>2-x</sub> and the generation of oxygen vacancies. These defects have been previously characterized as Frenkel-type defects.<sup>33</sup>

The fraction of Ce<sup>3+</sup> (denoted α) was determined from Ce 3d peak area analysis, according to eq 3. On the basis that half an oxygen vacancy is formed per Ce<sup>3+</sup> created, the deviation, x, from the ideal oxygen stoichiometry was determined for each sample, as shown in Table 2

$$\alpha = \frac{\text{Ce}^{3+}}{\sum \text{Ce}} \quad (3)$$

**Table 2.** Calculated Surface Stoichiometry and Ce<sup>3+</sup> Fraction (α) of Samples and Standards Investigated in This Study, as Determined from Ce 3d XPS Data<sup>a</sup>

sample treatment	surface stoichiometry	α
Ce(III)PO <sub>4</sub> standard		0.952 ± 0.051
H <sub>2</sub> /N <sub>2</sub> atmosphere 1000 °C	CeO <sub>1.82</sub>	0.370 ± 0.019
Ar atmosphere 1000 °C	CeO <sub>1.89</sub>	0.221 ± 0.011
air 1000 °C	CeO <sub>1.96</sub>	0.080 ± 0.004
air 600 °C	CeO <sub>1.93</sub>	0.143 ± 0.007
air - no annealing	CeO <sub>1.99</sub>	0.021 ± 0.008

<sup>a</sup>Errors quoted for α are standard deviations based upon duplicate XPS scans on each sample.

Annealing in a reducing (H<sub>2</sub>/N<sub>2</sub>) atmosphere resulted in CeO<sub>2-x</sub> with the greatest Ce<sup>3+</sup> fraction (α = 0.370 ± 0.019) and a stoichiometry of CeO<sub>1.82</sub>, while annealing in an inert (Ar) atmosphere gave a higher Ce<sup>3+</sup> fraction than annealing in air under the same conditions (α = 0.221 ± 0.011 and α = 0.080 ± 0.004, respectively). As the Ce<sup>3+</sup> fraction is directly related to the concentration of oxygen vacancies generated, it can be assumed that the oxygen vacancy concentration is proportional to the Ce<sup>3+</sup> fraction of each sample.

The crystal structure of nonstoichiometric CeO<sub>2-x</sub> was determined using X-ray diffraction. Because the samples were

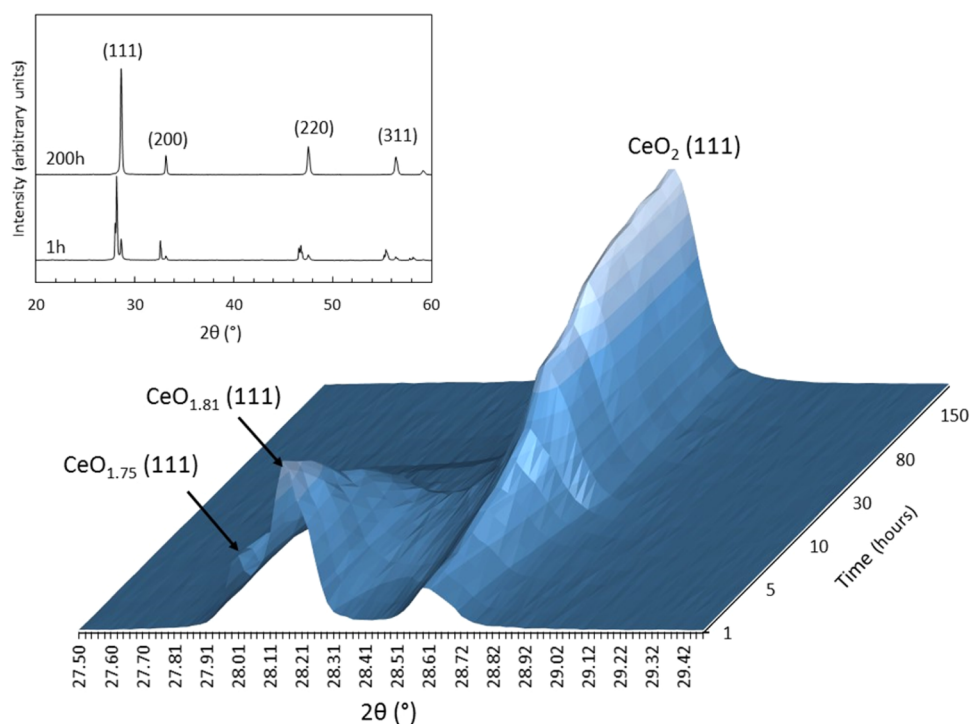


**Figure 3.** X-ray diffraction data for  $\text{CeO}_{2-x}$  formed by annealing  $\text{CeO}_2$  at  $1000\text{ }^\circ\text{C}$  under a reducing atmosphere ( $\text{H}_2/\text{N}_2$ ). XRD patterns were recorded, in air, at regular periods from 0.76 to 200 h after annealing. Correlation of the fluorite lattice parameter with the known oxygen stoichiometry in the  $\text{CeO}_{2-x}$  system<sup>31</sup> allowed diffraction peaks to be identified as  $\text{CeO}_{1.75}$ ,  $\text{CeO}_{1.81}$ , and  $\text{CeO}_2$ . Inset shows full diffraction patterns recorded at 1 h and 200 h, indexing peaks for  $\text{CeO}_2$ .

found to be chemically unstable upon exposure to air, they were loaded into the diffractometer within minutes of being removed from the annealing furnace. By comparison to the known correlation of the fluorite lattice parameter with the oxygen stoichiometry in the  $\text{CeO}_{2-x}$  system,<sup>34</sup> the three main diffraction peaks identified in Figure 3 were assigned to  $\text{CeO}_{1.75}$ ,  $\text{CeO}_{1.81}$ , and  $\text{CeO}_2$ . The second phase is in reasonable agreement with the XPS analysis of this sample, which gave a stoichiometry of  $\text{CeO}_{1.82}$  (Table 2). The  $\text{CeO}_{1.75}$  phase was not identified by XPS; this may be due to the rapid oxidation, as described below. The spatial distribution of the phases within the samples was not investigated, however, since  $\text{Ce}^{3+}$  species have previously been found to accumulate at grain boundaries within partially reduced  $\text{CeO}_2$ ,<sup>35</sup> grain boundaries may host  $\text{CeO}_{1.75}$  and  $\text{CeO}_{1.81}$ . The identification of these phases following annealing in a reducing atmosphere is consistent with the formation of oxygen vacancies.<sup>34</sup>

With prolonged exposure to ambient conditions (air, for up to 200 h), the relative intensity of the peaks assigned to  $\text{CeO}_{1.75}$ ,  $\text{CeO}_{1.81}$ , and  $\text{CeO}_2$  changed (Figure 3). Quantitative Rietveld analysis of the distribution of phases as a function of time is shown in Figure 4. Initially, the sample was composed of  $\sim 15\%$   $\text{CeO}_{1.75}$ ,  $\sim 68\%$   $\text{CeO}_{1.81}$  and  $\sim 16\%$   $\text{CeO}_2$  ( $\pm 1.0\%$ ). After 56 h,  $\text{CeO}_{1.75}$  was no longer observed, and the distribution of phases remained at  $4.5 \pm 0.9\%$   $\text{CeO}_{1.81}$  and  $95.2 \pm 1.3\%$   $\text{CeO}_2$  (Figure 4) until 200 h. The increase in the content of oxygen, corresponding to a decrease in oxygen vacancies, was found to occur at a rate of  $(1.40 \pm 0.14) \times 10^{-3} \text{ mol h}^{-1}$  during the first 24 h of exposure to ambient conditions. This process was associated with a change in the volume of the fluorite unit cell, as calculated from Rietveld-refined lattice parameters. The fluorite unit cell was found to contract, from  $167.62 \pm 3.4 \text{ \AA}^3$  for  $\text{CeO}_{1.75}$  to  $164.97 \pm 3.30 \text{ \AA}^3$  for  $\text{CeO}_{1.81}$  and to  $157.58 \pm$

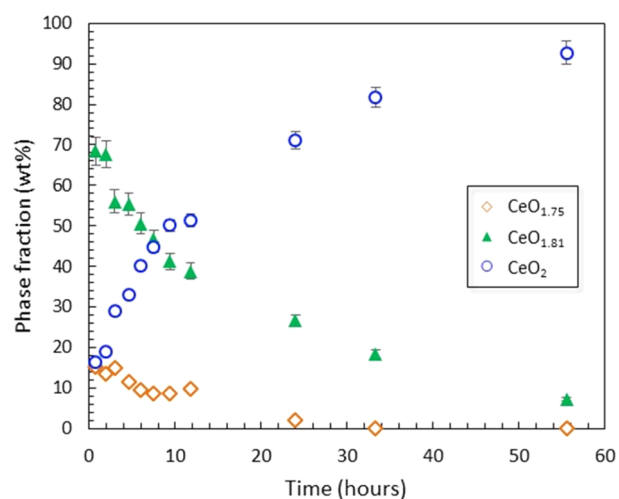


**Figure 4.** Weight fraction of  $\text{CeO}_2$  and  $\text{CeO}_{2-x}$  phases present in a sample of  $\text{CeO}_2$  annealed at  $1000\text{ }^\circ\text{C}$  in a  $\text{H}_2/\text{N}_2$  atmosphere as a function of time, as determined by quantitative Rietveld analysis of powder XRD patterns. After 56 h, there was no further change in the distribution of phases up to 200 h of observation. Errors are  $\pm 3\%$  based on Rietveld analysis methods.

$3.15 \text{ \AA}^3$  for  $\text{CeO}_2$ . This volume reduction is consistent with the oxidation of  $\text{Ce}^{3+}$  to  $\text{Ce}^{4+}$ ;  $\text{Ce}^{3+}$  has a larger ionic radius than  $\text{Ce}^{4+}$  (1.03 and 0.97  $\text{\AA}$ , respectively).<sup>36</sup> Overall, the sample annealed in a  $\text{H}_2/\text{N}_2$  atmosphere underwent a 6% volume contraction within several hours of exposure to oxygen under ambient atmospheric conditions. The lattice strain, as calculated using Rietveld analysis of the  $\text{CeO}_2$  phase, was found to significantly decrease during oxidation, from a value of  $\varepsilon = 0.092 \pm 0.01$  at 2 h to  $\varepsilon = 0.034 \pm 0.01$  after 200 h, consistent

with the observed change in lattice volume. Due to the rapid nature of these chemical and structural changes, all dissolution experiments were performed within 30 min of sample annealing to minimize the effects of air oxidation.

**3.2. CeO<sub>2</sub> Dissolution.** Cerium dioxide dissolution experiments were performed under aggressive conditions (0.01 M HNO<sub>3</sub>, 90 °C) to attain quantitative dissolution kinetic data within several weeks. It has been suggested that reduction of Ce<sup>4+</sup> to Ce<sup>3+</sup> may be induced by nitrous acid (HNO<sub>2</sub>) formed through nitric acid instability at high acidity (>0.5 M);<sup>13</sup> however, this is not expected to influence the dissolution reaction in the current experiments, which were at an acidity much less than 0.5 M.

The dissolution of CeO<sub>2</sub> can be described by two distinct regimes, as shown in Figure 5; the first, rapid regime is far from

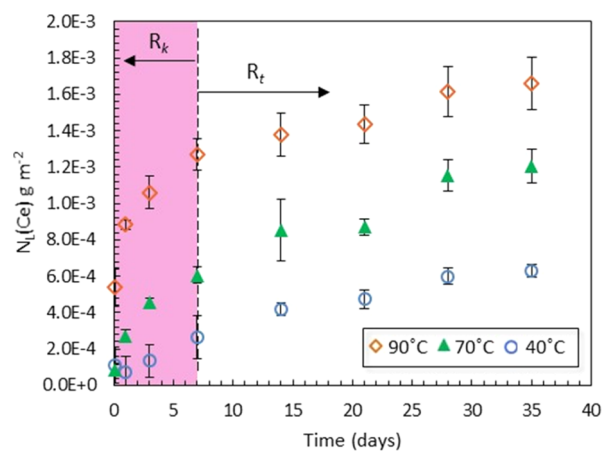


**Figure 5.** Concentration of Ce, normalized to surface area ( $\text{g m}^{-2}$ ) for non-annealed CeO<sub>2</sub> particles 25–50  $\mu\text{m}$  in size, reacted in 0.01 M HNO<sub>3</sub> at 40, 70, and 90 °C, as a function of time. Graph depicts the two main dissolution rates observed, kinetically controlled dissolution ( $R_k$ ) and thermodynamic effect-controlled dissolution ( $R_t$ ). Errors represent  $1\sigma$  from triplicate samples.

solution saturation and thus represents the kinetically controlled dissolution rate,  $R_k$ . The second regime is representative of near-solution saturation, controlled by the solubility of CeO<sub>2</sub> and concentration of Ce(OH)<sub>2</sub><sup>2+</sup> in solution. This is less rapid due to thermodynamic effects that occur close to equilibrium and is denoted  $R_t$ . To understand the role of defects in the dissolution of CeO<sub>2</sub>, it was necessary to focus only on the kinetic regime of dissolution; therefore, we herein report  $R_k$  only. Generally, the change between the kinetic and the thermodynamically controlled dissolution regimes occurred at  $\sim 7$  days, unless otherwise stated. Figure 5 shows the normalized mass loss of Ce ( $N_L$ ,  $\text{g m}^{-2}$ ) from nonannealed 25–50  $\mu\text{m}$  particles of CeO<sub>2</sub> as a function of time at 40, 70, and 90 °C. The normalized dissolution rate of Ce was  $R_k = (1.90 \pm 0.74) \times 10^{-4} \text{ g m}^{-2} \text{ d}^{-1}$  at 90 °C. The dependence of dissolution on temperature gave an activation energy of  $30.4 \pm 4 \text{ kJ mol}^{-1}$ , assuming an Arrhenius-type relationship. This is consistent with previous work on CeO<sub>2</sub> and other fluorite-type dioxides such as ThO<sub>2</sub> and PuO<sub>2</sub> ( $E_a = 20\text{--}37 \text{ kJ mol}^{-1}$ )<sup>13,25,37</sup> and is indicative of a surface-controlled dissolution mechanism.

**3.3. Effect of Defect Annealing/Surface Area on CeO<sub>2</sub> Dissolution Kinetics.** The dissolution rates of 25–50  $\mu\text{m}$  particles of CeO<sub>2</sub> annealed in air, and nonannealed CeO<sub>2</sub> of four different particle sizes, are shown in Table 3 and Figure 6.

**Table 3.** Calculated Dissolution Rates ( $R_k$ ) for CeO<sub>2</sub> and CeO<sub>2-x</sub> Reacted in 0.01 M HNO<sub>3</sub> at 90 °C between 0 and 35 Days of Dissolution, with the Corresponding Measured Surface Area and Oxygen Vacancy Content (Ce<sup>3+</sup> Fraction,  $\alpha$ )

sample treatment	surface area ( $\text{m}^2 \text{ g}^{-1}$ )	$\alpha$	$R_k$ ( $\text{g m}^{-2} \text{ d}^{-1}$ )
<i>25–50 <math>\mu\text{m}</math> samples</i>			
H <sub>2</sub> /N <sub>2</sub> atmosphere 1000 °C <sup>a</sup>	0.53 $\pm$ 0.01	0.370 $\pm$ 0.019	
H <sub>2</sub> /N <sub>2</sub> atmosphere 1000 °C <sup>b</sup>	2.49 $\pm$ 0.02	0.090 $\pm$ 0.003	(4.06 $\pm$ 0.75) $\times 10^{-4}$
Ar atmosphere 1000 °C	0.20 $\pm$ 0.01	0.221 $\pm$ 0.011	(4.62 $\pm$ 0.90) $\times 10^{-5}$
Air 1000 °C	0.11 $\pm$ 0.01	0.080 $\pm$ 0.004	(2.67 $\pm$ 0.30) $\times 10^{-5}$
Air 600 °C	0.20 $\pm$ 0.01	0.143 $\pm$ 0.007	(2.98 $\pm$ 0.50) $\times 10^{-5}$
no annealing	0.30 $\pm$ 0.01	0.021 $\pm$ 0.008	(1.90 $\pm$ 0.74) $\times 10^{-4}$
<i>Other particle sizes, no annealing</i>			
75–150 $\mu\text{m}$	0.07 $\pm$ 0.01	0.022 $\pm$ 0.007	(1.38 $\pm$ 0.28) $\times 10^{-4}$
300–600 $\mu\text{m}$	0.02 $\pm$ 0.01	0.021 $\pm$ 0.008	(1.02 $\pm$ 0.26) $\times 10^{-5}$
2–4 mm	0.01 $\pm$ 0.01	0.021 $\pm$ 0.004	(4.17 $\pm$ 1.13) $\times 10^{-5}$

<sup>a</sup>Initial surface area and Ce<sup>3+</sup> fraction, measured within minutes of removal of furnace. <sup>b</sup>Surface area and Ce<sup>3+</sup> fraction, measured 1 day after dissolution.

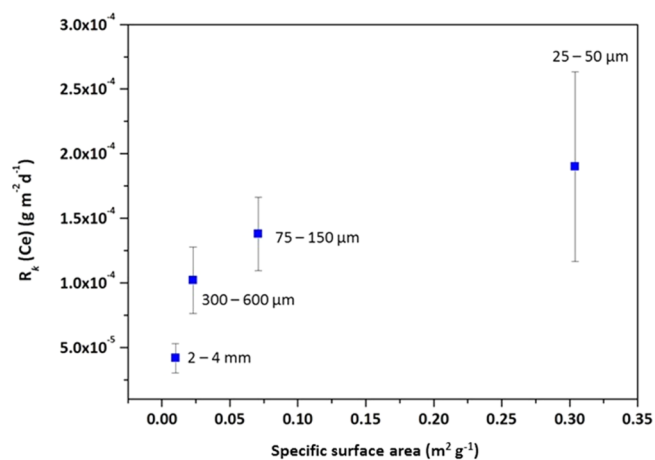


**Figure 6.** Normalized dissolution rates of Ce,  $R_k$  ( $\text{g m}^{-2} \text{ d}^{-1}$ ) as a function of specific surface area and particle size.

The surface area normalized dissolution rates were observed to increase with increasing surface area. This behavior is unexpected, since normalization to the surface area should result in similar dissolution rates. Samples of CeO<sub>2</sub> that were crushed and sieved to different size fractions clearly showed this correlation, with dissolution rates increasing from  $R_k = (4.17 \pm 1.13) \times 10^{-5} \text{ g m}^{-2} \text{ d}^{-1}$  for 2–4 mm particles to  $R_k = (1.38 \pm 0.28) \times 10^{-4} \text{ g m}^{-2} \text{ d}^{-1}$  for particles in the 75–150  $\mu\text{m}$  size fraction. The exposure of grain boundaries during particle crushing may be responsible for enhancing the reactive surface area, resulting in the observed trend, as follows: each particle is composed of a number of grains, with a grain size of 5–30  $\mu\text{m}$ . As the particle size decreases, from 2–4 mm to 75–150  $\mu\text{m}$ , the ratio of particle size to the number of grains also decreases. Because the grain size remains constant, the shrinking size of the particle exposes more grain boundaries to the dissolution medium. Grain boundaries are known to preferentially dissolve due to the presence of a greater number of energetically

reactive surface sites (e.g., defects) compared to the surfaces.<sup>11</sup> Once the smallest particle size is reached, each particle comprises only a few grains, with a high number of grain boundaries exposed to solution, which leads to the most rapid dissolution rates (Figure 6).

Similarly, thermally annealed particles of CeO<sub>2</sub> with the same particle size (25–50 μm) exhibited a factor of 7 decrease in their dissolution rate compared with nonannealed particles ( $R_k = (2.98 \pm 0.50) \times 10^{-5} \text{ g m}^{-2} \text{ d}^{-1}$  and  $(2.67 \pm 0.30) \times 10^{-5} \text{ g m}^{-2} \text{ d}^{-1}$ , for 600 and 1000 °C respectively), as shown in Figure 7. Because the reduction in surface area in these samples was

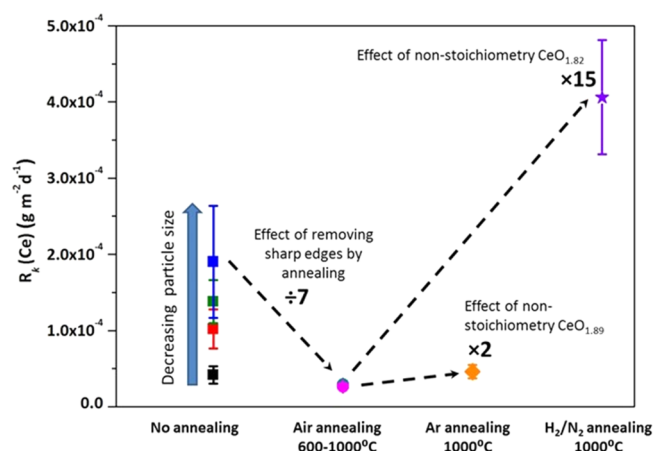


**Figure 7.** Summary of the normalized dissolution rates of Ce,  $R_k$  (g m<sup>-2</sup> d<sup>-1</sup>) as a function of particle size and annealing in air, Ar, and H<sub>2</sub>/N<sub>2</sub> atmospheres.

associated with the high temperature annealing of intrinsic defects and sharp edges generated through sample crushing, it can be concluded that these energetically reactive features influence the dissolution kinetics. This is in agreement with the

work of Claparede et al.<sup>13</sup> who found that increasing the sintering temperature of Th<sub>1-x</sub>Ce<sub>x</sub>O<sub>2</sub> powders led to a reduction in dissolution rate, attributed to the elimination of crystal defects and amorphous domains. The current work extends this hypothesis to samples prepared by crushing, generating surface defects in the form of “sharp edges”, as proposed by Corkhill et al.<sup>11</sup>

**3.4. Effect of Oxygen Vacancies on Dissolution Kinetics.** For CeO<sub>2</sub> samples annealed in different atmospheres at 1000 °C, the samples with the greatest oxygen vacancy content were found to dissolve at the most rapid rates. For example, the dissolution rate of CeO<sub>2</sub> annealed in Ar was slightly enhanced compared with CeO<sub>2</sub> annealed in air at the same temperature, by a factor of 2 (Table 3). The dissolution of CeO<sub>1.82</sub> (annealed in H<sub>2</sub>/N<sub>2</sub>) showed a significantly enhanced dissolution rate (Table 3, Figure 7). Samples of this material were analyzed by SEM at several time points during dissolution; in contrast to particles of stoichiometric CeO<sub>2</sub>, which did not change their shape or morphology upon 1 or 35 days of dissolution (Figure 8a–c), examination of the CeO<sub>1.82</sub> particles revealed a dramatic transformation. Prior to dissolution, these particles were 25–50 μm in size (Figure 6d), but within 1 day they were observed to break apart into smaller fragments ~5 μm in size, with a morphology suggestive of individual grains (Figure 8e). After 35 days of dissolution, some larger particles remained, but most of the sample had decomposed into single grain-sized fragments (Figure 8f). Post-dissolution BET analysis of these samples after 1 day of dissolution gave a surface area of  $2.49 \pm 0.01 \text{ m}^2 \text{ g}^{-1}$ , an increase by a factor of 5 compared with the initial surface area (Table 3). Normalization of the dissolution rate data to this surface area value gave a rate of  $R_k = (4.06 \pm 0.75) \times 10^{-4} \text{ g m}^{-2} \text{ d}^{-1}$ , 15 times greater than for air or Ar annealed samples of the same particle size (Figure 7). Due to the extremely rapid dissolution of this material, it was necessary to calculate the  $R_k$  between 0 and 1 day of dissolution, after which time the

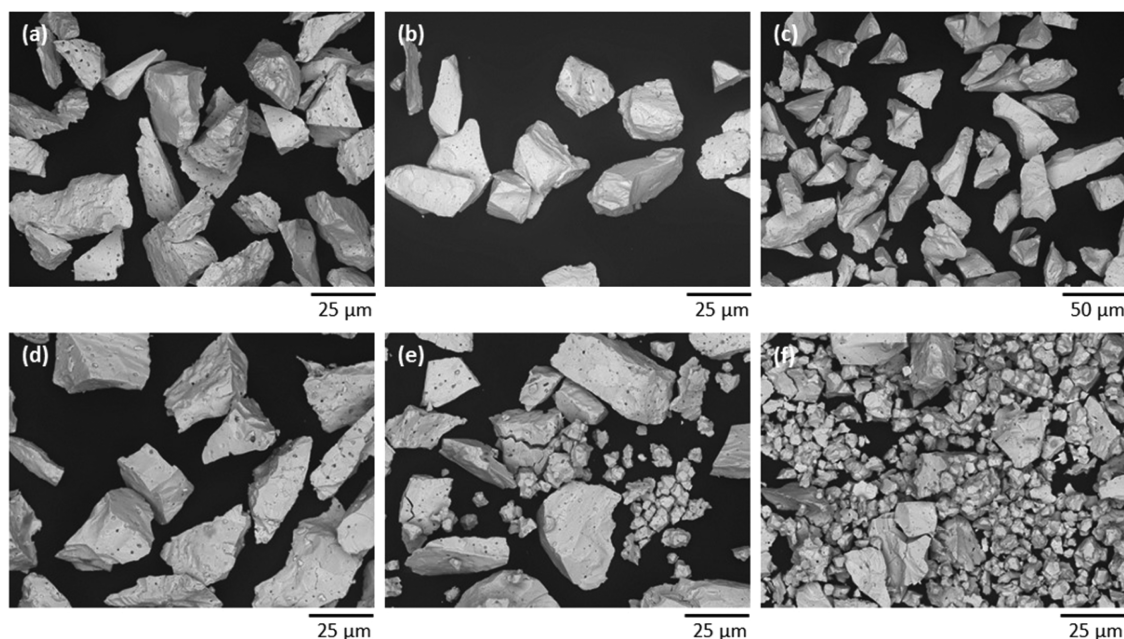


**Figure 8.** SEM images of 25–50 μm particles of non-annealed CeO<sub>2</sub> (a) prior to dissolution and after dissolution in 0.01 M HNO<sub>3</sub> at 90 °C for (b) 1 day and (c) 35 days; and H<sub>2</sub>/N<sub>2</sub> annealed CeO<sub>2-x</sub> (d) prior to dissolution; and after dissolution in 0.01 M HNO<sub>3</sub> at 90 °C for (e) 1 h and (f) 35 days.

normalized release of Ce was constant. When analyzed by XPS after 1 day of dissolution, these samples gave a surface stoichiometry of  $\text{CeO}_{1.96}$ , which indicates that a rapid oxidation of  $\text{CeO}_{2-x}$  occurred, concurrent with a significant reduction in the oxygen vacancy content.

## 4. DISCUSSION

**4.1. Microstructure and Surface Defect–Dissolution Rate Relationship in  $\text{CeO}_2$  and  $\text{CeO}_{2-x}$ .** A first-order expression that describes the concentration of Ce ( $C$ ) as a function of time ( $t$ ) has been considered

$$C = A(1 - e^{-bt}) \quad (4)$$

where  $A$  is the solubility limit of  $\text{CeO}_2$ , and  $b$  is the rate constant. Expanding eq 4 to account for the factors that are expected to contribute to the dissolution kinetics (surface area, oxygen vacancy content, and the different relative solubilities of  $\text{Ce}^{3+}$  and  $\text{Ce}^{4+}$ ) a first order dissolution rate expression can be derived for the  $\text{CeO}_2$  samples investigated in this study

$$C = \frac{S}{S_0}[\alpha A_3(1 - e^{-b_3 t}) + (1 - \alpha)A_4(1 - e^{-b_4 t})] \quad (5)$$

where  $S$  is the measured surface area (after dissolution in the case of  $\text{CeO}_{2-x}$ ),  $S_0$  is a reference surface area of  $1 \text{ m}^2 \text{ g}^{-1}$ ,  $\alpha$  is the fraction of  $\text{Ce}^{3+}$  (representing the oxygen vacancy content) at the particle surface as determined by XPS,  $A_3$  and  $A_4$  correspond to the solubility limits of  $\text{Ce}^{3+}$  and  $\text{Ce}^{4+}$  respectively, and  $b_3$  and  $b_4$  are the rate constants for  $\text{Ce}^{3+}$  and  $\text{Ce}^{4+}$ .

A genetic algorithm, which can be applied to solve constrained optimization problems,<sup>38</sup> was used to fit the individual parameters in eq 5, providing optimum solubility and rate constant values for  $\text{Ce}^{3+}$  and  $\text{Ce}^{4+}$  based on the dissolution data obtained in this study; the data and model fits are shown in Figure 9. The modeled  $\text{Ce}^{3+}$  and  $\text{Ce}^{4+}$  solubilities,  $A_3$  and  $A_4$ , gave best-fit values of  $(5.10 \pm 0.54) \times 10^{-4} \text{ mol dm}^{-3}$  and  $(1.59 \pm 0.08) \times 10^{-6} \text{ mol dm}^{-3}$ , respectively (errors represent the  $1\sigma$  confidence interval). These are in reasonable agreement with geochemically modeled solubility values, for example,  $\text{Ce}^{4+}$  solubility was calculated using PHREEQC (LLNL database) to be  $4.01 \times 10^{-6} \text{ mol dm}^{-3}$ . When considering only  $\text{CeO}_2$  annealed at various temperatures in air, and  $\text{CeO}_2$  particles of different sizes (shown in Figures 9a and b, respectively), the rate constant for  $\text{Ce}^{3+}$  was found to be  $b_3 = (0.245 \pm 0.06) \text{ d}^{-1}$ . For  $\text{Ce}^{4+}$  the scatter in the experimental data, combined with the low absolute solubility limit, resulted in poorly defined estimates for  $b_4$ ; a value of the order  $1.00 \times 10^{-7} \text{ d}^{-1}$  is tentatively suggested. Because the model to data fit was in agreement for  $\text{CeO}_2$  (Figure 9a and b), and the solubilities of the different Ce oxidation states were similar to geochemically modeled solubility values, it can be surmised that the parameters in eq 5 adequately describe the dissolution rate of stoichiometric  $\text{CeO}_2$ .

Figure 9c shows the dissolution data and model fit for  $\text{CeO}_{2-x}$  samples annealed in Ar and  $\text{H}_2/\text{N}_2$  atmospheres. The model fit to the parameters in eq 5 agrees somewhat with samples annealed in Ar; however, the model fit to the parameters is not in agreement with data from samples annealed in  $\text{H}_2/\text{N}_2$ , despite normalization to the post-dissolution surface area and consideration for the elevated content of the more highly soluble  $\text{Ce}^{3+}$  species in this sample (eq 5). Surface area data in Table 3 show that during dissolution, the surface area of  $\text{CeO}_{2-x}$

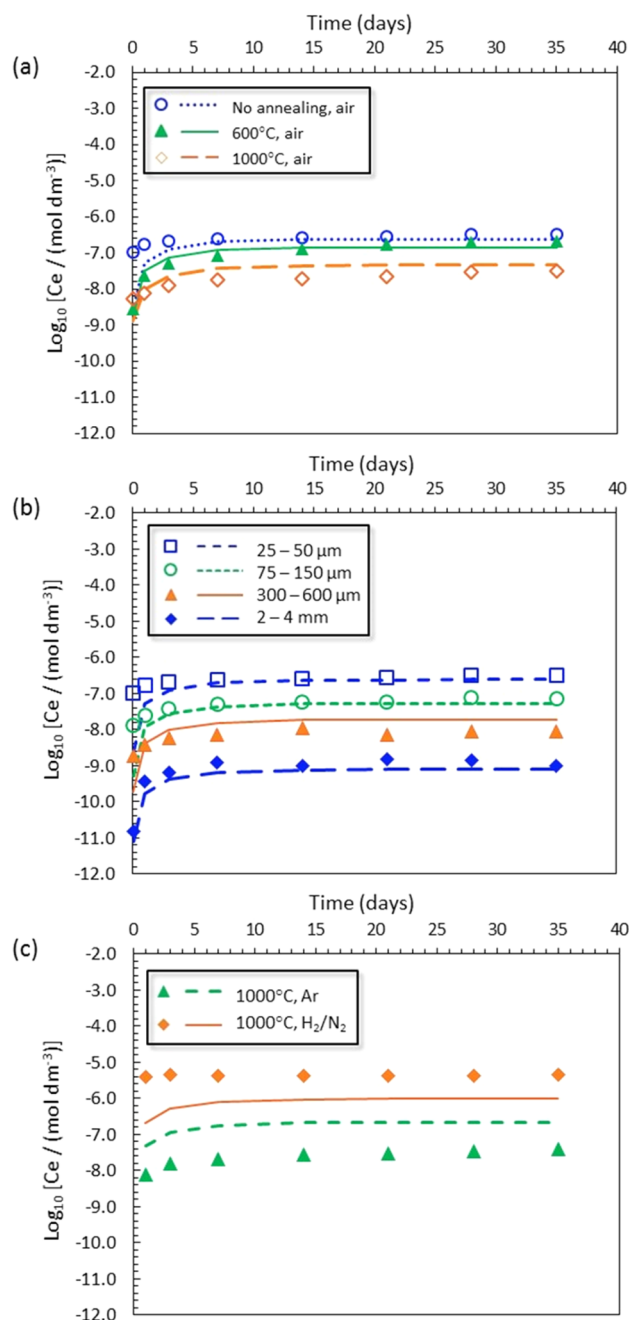


**Figure 9.** Ce concentrations ( $\text{mol dm}^{-3}$ ) derived from dissolution at  $90^\circ\text{C}$  in  $0.01 \text{ M HNO}_3$  (points) compared with modeled fit to eq 5 (lines) for (a)  $25\text{--}50 \mu\text{m}$   $\text{CeO}_2$  subject to different annealing temperatures in air; (b)  $\text{CeO}_2$  crushed to different size fractions, with no subsequent annealing; and (c)  $25\text{--}50 \mu\text{m}$   $\text{CeO}_2$  subject to annealing in different atmospheres at  $1000^\circ\text{C}$ . The parameters in eq 5 do not fit the data for  $\text{H}_2/\text{N}_2$  annealed samples shown in (c), suggesting another factor may contribute to the dissolution rate.

annealed in a  $\text{H}_2/\text{N}_2$  atmosphere increased by a factor of 5 after 1 day of dissolution. The first order dissolution model described above predicts that a surface area increase of a factor of 50 would be required to create a good fit to the parameters in eq 5, assuming all other values are correct. Specific surface area, as measured by BET, is routinely accepted to be the same as reactive surface area. However, recent studies have discussed that this may not necessarily be the case due to different activation energies of different high energy surface sites, e.g.,

grain boundaries and oxygen vacancies.<sup>39</sup> It is possible that the BET surface area measurements taken here, 1 day after dissolution, underestimated the reactive surface area of these samples during the initial stages of dissolution due to the presence of a high proportion of exposed grain boundaries, which are known to be significantly more reactive than the bulk.

**4.2. Physical Effects of Oxidation on the Kinetics of Dissolution.** As described above, not only the enhanced chemical solubility of  $\text{Ce}^{3+}$  influenced the dissolution kinetics of  $\text{CeO}_{2-x}$  but also the physical effects leading to a change in the sample surface area played a significant role. The mechanism through which this is postulated to occur for  $\text{CeO}_{2-x}$  investigated in the current study is described below.

Upon contact with air or an oxidic solution, the  $\text{Ce}^{3+}$  ions in  $\text{CeO}_{2-x}$  present as a result of charge compensation for oxygen vacancies, were rapidly oxidized to  $\text{Ce}^{4+}$ . Due to the difference in ionic radius between  $\text{Ce}^{3+}$  and  $\text{Ce}^{4+}$  (with  $\text{Ce}^{4+}$  the smaller cation), this oxidation process was associated with a contraction of the fluorite unit cell volume, on the order of  $\Delta V = -3.25 \pm 0.06 \text{ \AA}^3$  according to Rietveld analysis of XRD data (a  $6.0 \pm 0.1\%$  volume decrease relative to the starting volume). Ceramic materials that have undergone volume change-related phase transition exhibit significant internal lattice strain; according to Rietveld analysis, the lattice strain was initially high in  $\text{CeO}_{2-x}$  reducing by a factor of 2.6 during oxidation to  $\text{CeO}_2$ . Additionally, the presence of oxygen vacancies results in enhanced oxygen mobility, especially at grain boundaries where it is expected that a higher proportion of  $\text{Ce}^{3+}$  exists;<sup>35</sup> this facilitates preferential dissolution of grain boundaries.<sup>11</sup> In this study, during the dissolution of  $\text{CeO}_{1.82}$  to  $\text{CeO}_{1.96}$ , the combined influence of lattice strain and enhanced oxygen mobility, created by the removal of oxygen vacancies, resulted in the disintegration of particles, preferentially along grain boundaries, producing individual grain-sized fragments after 1 day of dissolution (Figure 8e–f). Importantly, this resulted in an increase in reactive surface area, which exposed fresh surfaces for dissolution and enhanced the overall dissolution rate. After 1 day, the dissolution rate was observed to be more or less constant, likely because there is reduced oxygen atom mobility within the nearly stoichiometric  $\text{CeO}_{1.96}$ . Hence, the combined roles of oxygen vacancies and grain boundaries should be considered significant in defining the dissolution kinetics of nonstoichiometric  $\text{CeO}_2$  and other fluorite-type materials.

The dual role of oxygen vacancies and grain boundaries in dissolution has been observed in other fluorite-type materials, albeit those comprising a solid solution of different chemical species. For example, Horlait et al.<sup>17</sup> reported the “crumbling” of  $\text{Ce}_{1-x}\text{Ln}_x\text{O}_{2-x/2}$  materials along grain boundaries during dissolution. This was associated with an increase in reactive surface area by up to a factor of 5. It was postulated that the incorporation of  $\text{Ln}^{3+}$  played a significant role in the dissolution mechanism through changes to the lattice volume.<sup>17,40</sup> Similarly, Finkeldei et al.<sup>41</sup> found that defect fluorite and pyrochlore structures in the  $\text{ZrO}_2\text{--Nd}_2\text{O}_3$  group preferentially dissolved along grain boundaries and at triple junctions, leading to disintegration. Substitution of elements into a fluorite lattice results in a volume change due to the difference in ionic radius of the substituting element;<sup>36</sup> the current study highlights the equally important role of oxygen vacancies on lattice volume change when only a single chemical species is present ( $\text{CeO}_2$ ), confirming the importance of this defect feature in dissolution rate kinetics.

The association of defect structures with grain boundaries and their influence on the dissolution of  $\text{CeO}_2$  and  $\text{ThO}_2$  analogues for spent fuel was recently hypothesized by Corkhill et al.,<sup>11</sup> who showed that the dissolution of grain boundaries was influenced by the crystallographic orientation of the grains and the corresponding mean misorientation angle of the grain boundaries. Boundaries with higher mean misorientation angles were found to dissolve at faster rates than those with low mean misorientation angles; it was hypothesized that higher misorientation angle grain boundaries contained a greater proportion of defects, with a high reactive surface area, which led to the enhanced dissolution rates. This study and others<sup>17,18</sup> have highlighted the important role of grain boundaries and particularly their association with defect structures (e.g., oxygen vacancies) on dissolution processes in spent fuel analogues. This underlines the requirement for new methodologies capable of linking grain boundary structure with dissolution kinetics, to fully understand their role in the dissolution of spent fuel materials.<sup>42</sup>

**4.3. Implications for the Dissolution of Spent Fuels.** It was recently demonstrated for a suite of fluorite type materials, including  $\text{CeO}_2$ ,  $\text{CaF}_2$ , and  $\text{UO}_2$ , that the surface stability is correlated with the proportion of high energy surfaces, even when different chemical processes of dissolution occur, for example for  $\text{CeO}_2$  and  $\text{CaF}_2$ .<sup>8</sup>  $\text{ThO}_2$  has also been shown to confirm this hypothesis.<sup>11,19</sup> Together with the results presented herein, these findings highlight the potential for energetically reactive surface sites to play a role in  $\text{UO}_2$  dissolution.

Spent  $\text{UO}_2$  fuel forms a complicated defect structure during fission within a reactor, and it is not yet clear the extent to which different types of reactive surface sites may influence the dissolution kinetics of spent fuel; however, studies on SIMFUEL have shown that doping with trivalent rare elements (to simulate fission products) resulted in lattice contraction<sup>12</sup> and a loss of cubic symmetry. On the basis of the results presented in the current study, we can hypothesize that such a lattice modification may lead to grain boundary decohesion. Evidence supporting this hypothesis includes a study of  $\text{UO}_2$  fuel stored in aerated, moist environments, which was found to degrade along its grain boundaries and become heavily fractured.<sup>43</sup> The effects of lattice volume change on the integrity of grain boundaries in these materials, and the extent to which it may affect the dissolution kinetics, requires further exploration. Recent work has shown that Mixed Oxide Fuels (MOx), containing  $\text{Pu}^{3+}$ , with a  $\text{PuO}_{2-x}$  stoichiometry of  $\text{PuO}_{1.61}$ ,<sup>44</sup> may also be prone to accommodating oxygen vacancies,<sup>45</sup> although the distribution of such defects between grains and the grain boundaries is currently not known. In light of the current limited knowledge of the atomic-scale structure of spent fuels, further work is required on inactive analogues,  $\text{UO}_2$ , and spent fuel materials to ascertain the effects of reactive surface sites on dissolution kinetics, as distinct from oxidative dissolution or radiolysis effects, to reduce the uncertainty associated with the prediction of spent fuel dissolution within a geological disposal facility.

## 5. CONCLUSIONS

We present an investigation of the role of energetically reactive surface sites on the initial dissolution rate of  $\text{CeO}_2$  to ascertain whether these features may result in overestimation of dissolution rates in the laboratory. Reactive surface sites and “sharp edges” were simulated by crushing samples to different

size fractions and through high temperature annealing. Oxygen vacancy defects in  $\text{CeO}_{2-x}$  were generated by high temperature annealing in oxygen-free conditions. Surface area was used as a measurement of “sharp edges” and intrinsic defects, and the total  $\text{Ce}^{3+}$  fraction measured by XPS was used as a measurement of the oxygen vacancy concentration. The relative dissolution rates of these materials showed that there was a quantifiable relationship between energetically reactive surface sites and dissolution rate, which was dependent upon reactive surface site concentration and the solubilities of  $\text{Ce}^{3+}$  and  $\text{Ce}^{4+}$ ; the greater the concentration of reactive surface sites, the higher the dissolution rate. The elimination of oxygen vacancies in  $\text{CeO}_{2-x}$  was found to significantly influence the dissolution rate; this was associated with changes in the lattice volume and lattice strain, manifested as grain boundary decohesion and increased surface area. Thus, it is clear that reactive surface sites, including artifacts of sample preparation, intrinsic material defects, and grain boundaries, have the potential to significantly enhance the dissolution of spent oxide fuel. We show that such effects can be quantified, thus it is possible to reduce the uncertainty associated with laboratory measurements of  $\text{UO}_2$  dissolution, albeit in a simplified analogue system. It will be essential to develop further careful studies designed to interrogate the effect of reactive surface features on the durability and dissolution of materials such as  $\text{UO}_2$  and  $\text{MO}_x$ , as distinct from solubility, surface area, and radiation effects.

## AUTHOR INFORMATION

### Corresponding Authors

\*Phone: 44 (0)1142223632. E-mail: [c.corkhill@sheffield.ac.uk](mailto:c.corkhill@sheffield.ac.uk).

\*Phone: 44 (0)1142225502. E-mail: [n.c.hyatt@sheffield.ac.uk](mailto:n.c.hyatt@sheffield.ac.uk).

### Notes

The authors declare no competing financial interest.

## ACKNOWLEDGMENTS

The research leading to these results has received funding from the European Atomic Energy Community's Seventh Framework Programme (FP7) under grant agreement No. 269903, The REDUPP (REDucing Uncertainty in Performance Prediction) project. We wish to give special thanks to the late Dr. Paul Wincott (University of Manchester) for assistance with XPS data collection. We are grateful to Dr. Virginia Oversby and Dr. Lena Z. Evins for invaluable discussion and support throughout the project. C.L.C. is grateful to The University of Sheffield for the award of a Vice Chancellor's Fellowship and EPSRC for the award of an ECR Fellowship (EP/N017374/1), N.C.H. acknowledges support from the Royal Academy of Engineering and the Nuclear Decommissioning Authority for funding, D.J.B. acknowledges financial support from the EPSRC Nuclear FiRST Doctoral Training Centre (EP/G037140/1), and F.Y.T. acknowledges support from the EPSRC PACIFIC programme (EP/L018616/1). We thank EPSRC and University of Sheffield Knowledge Transfer Account, under grant reference EP/H500170/1 for financial support. This research was performed, in part, at the MIDAS facility, at the University of Sheffield, which was established with support from the Department of Energy and Climate Change.

## REFERENCES

- (1) Cui, D.; Low, J.; Spahiu, K. Environmental Behaviours of Spent Nuclear Fuel and Canister Materials. *Energy Environ. Sci.* **2011**, *4*, 2537–2545.
- (2) Oversby, V. M. Uranium Dioxide, SIMFUEL and Spent Fuel Dissolution Rates – A Review Of Published Data. *SKB Technol. Rep.* **1999**, TR-99-22.
- (3) Shoesmith, D. W. Used Fuel and Uranium Dioxide Dissolution Studies – A Review. *Nucl. Waste Manage. Org. Rep.* **2007**, NMWO TR-2007-03.
- (4) Smellie, J.; Karlson, F. A Reappraisal of Some Cigar Lake Issues of Importance to Performance Assessment. *SKB Technol. Rep.* **1996**, TR 96-08.
- (5) Bruno, J.; Spahiu, K. The Long-Term Effect of Hydrogen on the  $\text{UO}_2$  Spent Fuel Stability under Anoxic Conditions: Findings from the Cigar Lake Natural Analogue Study. *Appl. Geochem.* **2014**, *49*, 178–183.
- (6) White, A. F.; Brantley, S. L. The Effect of Time in the Weathering of Silicate Minerals: Why do Weathering Rates Differ in the Laboratory and the Field? *Chem. Geol.* **2003**, *202*, 479–506.
- (7) Fischer, C.; Kurganskaya, I.; Schafer, T.; Luttge, A. Variability of Crystal Surface Reactivity: What do we Know? *Appl. Geochem.* **2014**, *43*, 132–157.
- (8) Maldonado, P.; Godinho, J. R. A.; Evins, L. Z.; Oppeneer, P. M. Ab Initio Prediction of Surface Stability of Fluorite Materials and Experimental Verification. *J. Phys. Chem. C* **2013**, *117*, 6639–6650.
- (9) Ollila, K.; Oversby, V. M. Dissolution of Unirradiated  $\text{UO}_2$  and  $\text{UO}_2$  Doped with  $^{233}\text{U}$  Under Reducing Conditions. *SKB Technol. Rep.* **2005**, TR-05-07.
- (10) Ollila, K. Dissolution of Unirradiated  $\text{UO}_2$  and  $\text{UO}_2$  Doped with  $^{233}\text{U}$  in 0.01M NaCl Under Anoxic and Reducing Conditions. *Posiva Oy Rep.* **2006**, 2006–08.
- (11) Corkhill, C. L.; Myllykylä, E.; Bailey, D. J.; Thorber, S. M.; Qi, J.; Maldonado, P.; Stennett, M. C.; Hamilton, A.; Hyatt, N. C. Contribution of Energetically Reactive Surface Features to the Dissolution of  $\text{CeO}_2$  and  $\text{ThO}_2$  Analogues for Spent Nuclear Fuel. *ACS Appl. Mater. Interfaces* **2014**, *6*, 12279–12289.
- (12) Razdan, M.; Shoesmith, D. W. Influence of Trivalent-Dopants on the Structural and Electrochemical Properties of Uranium Dioxide ( $\text{UO}_2$ ). *J. Electrochem. Soc.* **2014**, *161*, H105–H113.
- (13) Claparede, L.; Clavier, N.; Dacheux, N.; Mesbah, A.; Martinez, J.; Szenknect, S.; Moisy, P. Multiparametric Dissolution of Thorium-Cerium Dioxide Solutions. *Inorg. Chem.* **2011**, *50*, 11702–11714.
- (14) Claparede, L.; Clavier, N.; Dacheux, N.; Moisy, P.; Podor, R.; Ravau, J. Influence of Crystallisation State and Microstructure on the Chemical Durability of Cerium-Neodymium Mixed Oxides. *Inorg. Chem.* **2011**, *50*, 9059–9072.
- (15) Horlait, D.; Clavier, N.; Szenknect, S.; Dacheux, N.; Dubois, V. Dissolution of Cerium(IV)-Lanthanide(III) Oxides: Comparative Effect of Chemical Composition, Temperature, and Acidity. *Inorg. Chem.* **2012**, *51*, 3868–3878.
- (16) Horlait, D.; Tocino, F.; Clavier, N.; Dacheux, N.; Szenknect, S. Multiparametric Study of  $\text{Th}_{(1-x)}\text{Ln}_x\text{O}_{(2-x/2)}$  Mixed Oxides Dissolution in Nitric Acid Media. *J. Nucl. Mater.* **2012**, *429*, 237–244.
- (17) Horlait, D.; Claparede, L.; Tocino, F.; Clavier, N.; Ravau, J.; Szenknect, S.; Podor, R.; Dacheux, N. Environmental SEM Monitoring of  $\text{Ce}_{1-x}\text{Ln}_x\text{O}_{2-x/2}$  Mixed-Oxide Microstructural Evolution During Dissolution. *J. Mater. Chem. A* **2014**, *2*, 5193–5203.
- (18) Szenknect, S.; Mesbah, A.; Horlait, D.; Clavier, N.; Dourdain, S.; Ravau, J.; Dacheux, N. Kinetics of Structural and Microstructural Changes at the Solid/Solution Interface During Dissolution of Cerium(IV)-Neodymium(III) Oxides. *J. Phys. Chem. C* **2012**, *116*, 12027–12037.
- (19) Myllykylä, E.; Lavonen, T.; Stennett, M.; Corkhill, C.; Ollila, K.; Hyatt, N. Solution Composition and Particle Size Effects on the Dissolution and Solubility of a  $\text{ThO}_2$  Microstructural Analogue for  $\text{UO}_2$  Matrix of Nuclear Fuel. *Radiochim. Acta* **2015**, *103*, 565–576.
- (20) Stennett, M. C.; Corkhill, C. L.; Marshall, L. A.; Hyatt, N. C. Preparation, Characterisation and Dissolution of a  $\text{CeO}_2$  Analogue for  $\text{UO}_2$  Nuclear Fuel. *J. Nucl. Mater.* **2013**, *432*, 182–188.
- (21) ASTM. *Standard test methods for determining chemical durability of nuclear, hazardous and mixed waste glasses and multiphase ceramics:*

*The Product Consistency Test (PCT)*; ASTM C 1285-02; American Society for Testing and Materials: Philadelphia, 2008.

(22) Shirley, D. A. High Resolution X-Ray Photoemission Spectrum of Valence Bands of Gold. *Phys. Rev. B* **1972**, *5*, 4709–4714.

(23) Balzar, D. Voight-Function Model in Diffraction-Line Broadening Analysis. In *Microstructure Analysis from Diffraction*; Snyder, R. L., Bunge, H. J., Fiala, J., Eds.; Int. Union of Crystall.: 1999.

(24) Thomas, A.; Dacheux, N.; Le Coustumer, P.; Brandel, V.; Genet, M. Kinetic and Thermodynamic Study of the Thorium Phosphate-Diphosphate Dissolution. *J. Nucl. Mater.* **2000**, *281*, 91–105.

(25) Claparede, L.; Tocino, F.; Szenknect, S.; Mesbah, A.; Clavier, N.; Moisy, P.; Dacheux, N. Dissolution of  $\text{Th}_{1-x}\text{U}_x\text{O}_2$ : Effects of Chemical Composition and Microstructure. *J. Nucl. Mater.* **2015**, *457*, 304–316.

(26) Dacheux, N.; Le Dû, J.; Brandel, V.; Genet, M.; Decambox, P.; Moulin, C. Solubility Tests on Various Uranium (IV) Phosphates. *New J. Chem.* **1996**, *20*, 507–514.

(27) Stetsovych, V.; Pagliuca, F.; Dvorak, F.; Duchon, T.; Vorokhta, M.; Aulicka, M.; Lachnitt, J.; Schernich, S.; Matolinova, I.; Veltruska, K.; Skala, T.; Mazur, D.; Myslivecek, J.; Libuda, J.; Matlon, V. Epitaxial Cubic  $\text{Ce}_2\text{O}_3$  Films via Ce-CeO<sub>2</sub> Interfacial Reaction. *J. Phys. Chem. Lett.* **2013**, *4*, 866–871.

(28) Bevan, D. J. M. Ordered Intermediate Phases in the System  $\text{CeO}_2 - \text{Ce}_2\text{O}_3$ . *J. Inorg. Nucl. Chem.* **1955**, *1*, 49–59.

(29) Romeo, M.; Bak, K.; El Fallah, J.; Le Normand, F.; Hilaire, L. XPS Study of the Reduction of Cerium Dioxide. *Surf. Interface Anal.* **1993**, *20*, 508–512.

(30) Burroughs, P.; Hamnet, A.; Orchard, A. F.; Thornton, G. Satellite Structure In The X-Ray Photoelectron Spectra of some Binary and Mixed Oxides of Lanthanum and Cerium. *J. Chem. Soc., Dalton Trans.* **1976**, *17*, 1686–1698.

(31) Pfau, A.; Schierbaum, K. D. The Electronic Structure of Stoichiometric and Reduced  $\text{CeO}_2$  Surfaces: An XPS, UPS and HREELS Study. *Surf. Sci.* **1994**, *321*, 71–80.

(32) Mullins, D. R.; Overbury, S. H.; Huntley, D. R. Electron Spectroscopy of Single Crystal and Polycrystalline Cerium Oxide Surfaces. *Surf. Sci.* **1998**, *409*, 307–319.

(33) Mamontov, E.; Egami, T. Structural Defects in a Nano-Scale Powder of  $\text{CeO}_2$  Studied by Pulsed Neutron Diffraction. *J. Phys. Chem. Solids* **2000**, *61*, 1345–1356.

(34) Kümmerle, E. A.; Heger, G. The Structures of  $\text{C-Ce}_2\text{O}_{3+\delta}$ ,  $\text{Ce}_7\text{O}_{12}$ , and  $\text{Ce}_{11}\text{O}_{20}$ . *J. Solid State Chem.* **1999**, *147*, 485–500.

(35) Hojo, H.; Mizoguchi, T.; Ohta, H.; Findlay, S. D.; Shibata, N.; Yamamoto, T.; Ikuhara, Y. Atomic Structure of a  $\text{CeO}_2$  Grain Boundary: The Role of Oxygen Vacancies. *Nano Lett.* **2010**, *10*, 4668–4672.

(36) Reid, D. P.; Stennett, M. C.; Hyatt, N. C. The Fluorite Moderated Structures of the  $\text{Gd}_2(\text{Zr}_{2-x}\text{Ce}_x)\text{O}_7$  Solid Solution: An Analogue for Pu Disposition. *J. Solid State Chem.* **2012**, *191*, 2–9.

(37) Heisbourg, G.; Hubert, S.; Dacheux, N.; Purans, J. Kinetic and Thermodynamic Studies of the Dissolution of Thoria-Urania Solid Solutions. *J. Nucl. Mater.* **2004**, *335*, 5–13.

(38) Ojovan, M.; Travis, K. P.; Hand, R. J. Thermodynamic Parameters of Bonds in Glassy Materials from Viscosity-Temperature Relationships. *J. Phys.: Condens. Matter* **2007**, *19*, 415107–415122.

(39) Luttge, A.; Arvidson, R. S.; Fischer, C. A Stochastic Treatment of Crystal Dissolution Kinetics. *Elements* **2013**, *9*, 183–188.

(40) Horlait, D.; Claparede, L.; Clavier, N.; Szenknect, S.; Dacheux, N.; Ravaux, J.; Podor, R. Stability and Structural Evolution of  $\text{Ce(IV)}_{1-x}\text{Ln(III)}_x\text{O}_{2/2}$  Solid Solutions: A Coupled  $\mu$ -Raman/XRD Approach. *Inorg. Chem.* **2011**, *50*, 7150–7161.

(41) Finkeldei, S.; Brandt, F.; Rozov, A. A.; Bukaemskiy, S.; Neumeier, S.; Bosbach, D. Dissolution of  $\text{ZrO}_2$  Based Pyrochlores in the Acid pH Range: A Macroscopic and Electron Microscopy Study. *Appl. Geochem.* **2014**, *49*, 31–41.

(42) Fischer, C.; Finkeldei, S.; Brandt, F.; Bosbach, D.; Luttge, A. Direct Measurement of Surface Dissolution Rates in Potential Nuclear Waste Forms: The Example of Pyrochlore. *ACS Appl. Mater. Interfaces* **2015**, *7*, 17857–17865.

(43) Wronkewicz, D. J.; Buck, E. C.; Bates, J. K. Grain Boundary Corrosion and Alteration Phase Formation During the Oxidative Dissolution of  $\text{UO}_2$  Pellets. *Mater. Res. Soc. Symp. Proc.* **1997**, *468*, 519–526.

(44) Degueldre, C.; Pin, S.; Poonosamy, J.; Kulick, D. A. Redox state of plutonium in irradiated mixed oxide fuels. *J. Phys. Chem. Solids* **2014**, *75*, 358–365.

(45) Conradson, S. D.; Begg, B. D.; Clark, D. L.; den Auwer, C.; Ding, M.; Dorhout, P. K.; Espinosa-Faller, F. J.; Gordon, P. L.; Haire, R. G.; Hess, N. J.; Hess, R. F.; Keogh, D. W.; Morales, L. A.; Neu, M. P.; Paviet-Hartmann, P.; Runde, W.; Tait, C. D.; Veirs, D. K.; Vilella, P. M. Local and Nanoscale Structure and Speciation in the  $\text{PuO}_{2+x}\text{y}(\text{OH})_{2\text{y}}\cdot z\text{H}_2\text{O}$  System. *J. Am. Chem. Soc.* **2004**, *126*, 13443–13458.

## Ceramic Immobilization Options for Technetium

Martin C. Stennett<sup>1</sup>, Tae-Hyuk Lee<sup>1,2</sup>, Daniel J. Bailey<sup>1</sup>, Erik V. Johnstone<sup>1</sup>, Jong Heo<sup>2</sup>, and Neil C. Hyatt<sup>1</sup>

<sup>1</sup>NucleUS Immobilisation Science Laboratory, Department of Materials Science and Engineering, The University of Sheffield, Mappin Street, Sheffield, S1 3JD, UK.

<sup>2</sup>Department of Materials Science and Engineering and Division of Advanced Nuclear Engineering, Pohang University of Science and Technology (POSTECH), Pohang, Gyeongbuk, 37673, Republic of Korea.

### ABSTRACT

Long half-life biologically active fission products, such as technetium-99, present particular problems for the disposal of spent nuclear fuel (SNF). Technetium is present in relatively high concentrations in fuel (approx. 1kg tonne<sup>-1</sup> SNF) and has very high mobility in oxidizing environments. Technetium is therefore generally removed from SNF either by solvent extraction and reduction, during the PUREX process, or by sorption via ion exchange processes. Historically technetium has been disposed of via dilution and dispersion in the sea but stringent regulations now mean that the preferred long term option is immobilization in a highly stable and durable matrix. In this contribution we have looked at the synthesis of fluorite derivative crystalline host phases based on the zirconolite structure. Samples have been characterised by X-ray diffraction (XRD), scanning electron microscopy (SEM), energy dispersive spectroscopy (EDX), thermo-gravimetric analysis (TG), and mass spectroscopy (MS). We have used Mo as an inactive surrogate for Tc.

### INTRODUCTION

Of the many challenges facing the nuclear industry one of the most important is the issue of waste management; waste arising from nuclear fuel cycle operations must be rendered passively safe prior to disposal. Safe sequestration is very challenging for <sup>99</sup>Tc because it has a half-life of approximately 210000 years and it is present in spent fuel rods as the technetium (VII) oxide (Tc<sub>2</sub>O<sub>7</sub>) which is extremely water-soluble, forming the mobile anionic pertechnetate species (TcO<sub>4</sub><sup>-</sup>) in solution. Additionally <sup>99</sup>Tc is produced during nuclear fission of <sup>235</sup>U, with a yield of 6.06 % [1], which means that approximately 1 kg of <sup>99</sup>Tc is produced for every tonne of enriched <sup>235</sup>U that is used in a nuclear reactor [2].

Ceramic and vitreous materials offer promising host matrices for radionuclides however for safe immobilization the difficulties associated with processing <sup>99</sup>Tc must be addressed. Many higher oxidation state technetium species, such as Tc<sub>2</sub>O<sub>7</sub>, are highly volatile and unstable so care must be taken to retain <sup>99</sup>Tc in its Tc<sup>4+</sup> oxidation state. TcO<sub>2</sub> is considerably less volatile than Tc<sub>2</sub>O<sub>7</sub>; TcO<sub>2</sub> has a sublimation temperature of approximately 900°C, in contrast to the melting and boiling points of Tc<sub>2</sub>O<sub>7</sub>, which are 119.5°C and 311°C, respectively [3]. It is possible to immobilize Tc<sup>4+</sup> by incorporating it into the structure of a durable ceramic phase which has suitably sized crystallographic sites.

In this work CaZrTi<sub>2</sub>O<sub>7</sub>, which crystallizes with the zirconolite structure, was explored as a suitable host for Tc. The zirconolite structure has an ideal formula ABC<sub>2</sub>O<sub>7</sub> and adopts monoclinic symmetry, with space group C2/c [4, 5]. The A-site has eight fold symmetry and in

natural zirconolites contains tri- and tetra-valent lanthanides and actinides. The B-site is occupied by larger transition metals such as Zr, which adopt seven-fold coordination, and the C-site is occupied by smaller tri- and tetra-valent transition metals such as Ti and Fe [6]. Zirconolites are among a number of fluorite derivative phases that exhibit excellent chemical durability and are characterized by low rates of leaching making them an ideal radionuclide host [7]. Mo was chosen as a structural analogue for Tc as  $\text{Mo}^{4+}$  and  $\text{Tc}^{4+}$  have very similar ionic radii (0.65 Å and 0.645 Å respectively, in six fold coordination [8]) and substitution was targeted on the Ti site in  $\text{CaZrTi}_2\text{O}_7$  due to the similarity in ionic radii between  $\text{Mo}^{4+}/\text{Tc}^{4+}$  and  $\text{Ti}^{4+}$  (0.605 Å). Although Mo does not exactly replicate the chemical behaviour of Tc, it is an adequate analogue for Tc for this synthesis work.

## EXPERIMENTAL

Compositions in the series  $\text{CaZr}(\text{Ti}_{2-x}\text{Mo}_x)\text{O}_7$  were synthesized by solid state reaction of  $\text{CaCO}_3$ ,  $\text{ZrO}_2$ ,  $\text{TiO}_2$ , and  $\text{MoO}_2$  (where  $0.0 \leq x \leq 0.4$ ). The reagents (99.9% pure) were weighed out in the appropriate stoichiometric ratio to give 20 gram batches. The reagents were homogenized using a Fritsch Pulverisette 7 Mono-mill (10 minutes, 500 rpm) with a sialon milling bowl containing sialon milling media (8 x 10 mm diameter spheres). Isopropanol was added as a carrier fluid to aid the milling process. The resulting slurry was separated from the media, dried at 90 °C overnight, and passed through a 212 µm sieve to break up any agglomerates. 2 gram fractions were removed from the batch and compacted into monoliths using a 13mm hardened tool steel die at 200 MPa for 1 minute. The powder compacts were then heat treated in vacuum ( $< 10^{-5}$  bar) at between 1000 and 1400 °C for 4 hours (3 °C  $\text{min}^{-1}$  ramp rate). Pellets were sectioned and prepared for X-ray diffraction (XRD) and scanning electron microscopy (SEM). For XRD the pellet section was ground to a fine powder and analyzed in reflection mode using a Bruker D2 Phaser diffractometer with a Cu K $\alpha$  radiation source ( $\lambda = 1.5418$  Å). For SEM the pellet section was mounted in epoxy resin and ground and polished to a 0.25 µm finish. Microstructural and chemical analysis was conducted on a Hitachi TM3030 SEM with a Bruker Quantax 70 EDX system. Thermo-gravimetric (TG) analysis was performed on homogenized precursors using a Netzsch STA F3 Jupiter simultaneous thermal analyzer linked to a QMS 403D Aeolis mass spectrometer. 100 mg of sample was loaded into an alumina crucible and heated to 1400 °C under flowing argon at 20 °C  $\text{min}^{-1}$ . The TG and MS signals were measured simultaneously to allow off-gas chemistry to be correlated with any thermal events recorded.

## RESULTS AND DISCUSSION

Initial studies were conducted on un-doped  $\text{CaZrTi}_2\text{O}_7$  to optimize the synthesis conditions prior to the addition of molybdenum. The phase assemblage of the samples heat treated at temperatures between 1000 and 1400 °C are shown in Figure 1 below. As can be seen in the pattern from the unreacted material reflections due to the presence of all starting precursors were observed. The most intense peaks from each reagent are labelled according to the following nomenclature: R – rutile ( $\text{TiO}_2$ ), B – baddeleyite ( $\text{ZrO}_2$ ), and CC – calcium carbonate ( $\text{CaCO}_3$ ). After heat treatment at 1000 °C the calcium carbonate and rutile have been consumed to form a perovskite structured calcium titanate ( $\text{CaTiO}_3$  - CT) intermediate phase. The thermal stability of  $\text{CaCO}_3$  is well established and it is known to decompose above 600 °C

[9]. Perovskite formation has also been previously reported at temperatures between 725 °C and 1100 °C in titanate based ceramics formed by reactive sintering of oxide precursors [10]. Above 1000°C reflections indexed on the monoclinic zirconolite structure were observed. The relative intensity of these reflections increased with a concomitant decrease in the reflections indexed to calcium titanate and un-reacted precursors. Above 1200 °C only reflections indexed to zirconolite were observed.

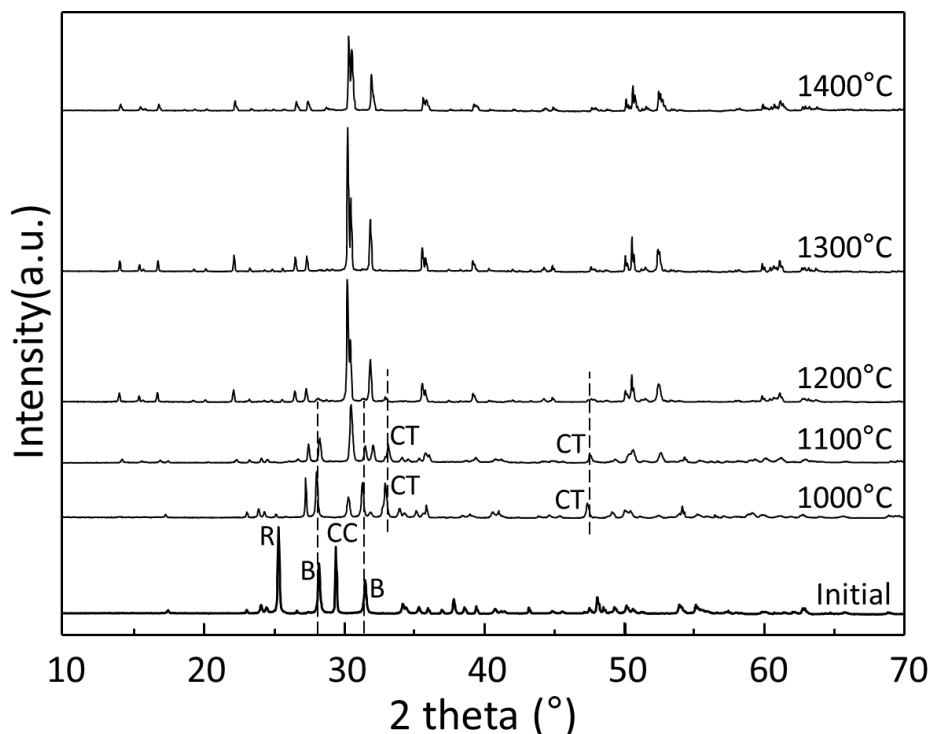


**Figure 1.** XRD patterns for  $\text{CaZrTi}_2\text{O}_7$  samples synthesized under vacuum. Major reflections for following phases labelled: R – rutile, B – baddeleyite, CC- calcium carbonate, and CT – calcium titanate. All reflections in the 1300°C and 1400°C patterns can be indexed to the zirconolite phase.

Similar sets of heat treatments and analysis were performed for samples in the  $\text{CaZrTi}_{2-x}\text{Mo}_x\text{O}_7$  series (where  $x = 0.0, 0.1, 0.2, 0.3,$  and  $0.4$ ). Figure 2 shows the XRD patterns collected for  $\text{CaZrTi}_{1.6}\text{Mo}_{0.4}\text{O}_7$  which are representative of the changes in phase assemblage observed as a function of temperature, across the whole  $\text{CaZrTi}_{2-x}\text{Mo}_x\text{O}_7$  series (where  $x = 0.0, 0.1, 0.2, 0.3,$  and  $0.4$ ). As previously observed for  $\text{CaZrTi}_2\text{O}_7$ , all the  $\text{CaCO}_3$  had decomposed by 1000 °C but now only minor amounts of calcium titanate were formed. Reflections from a new phase were observed in the diffraction patterns. The position of these reflections was consistent with  $\text{CaMoO}_4$  and with an increasing level of Mo doping the content of this phase increased. This observation was consistent with a decrease in the content of calcium titanate indicating that any free Ca in the system was now being consumed by the formation of  $\text{CaMoO}_4$ . The oxidation state of Mo in  $\text{CaMoO}_4$  is hexavalent which suggests that Mo oxidizes even when heated under anoxic conditions (vacuum). One explanation for this is that another cation such as Ti may have

been reduced to provide the required oxygen according to the following redox couple,  $2\text{Ti}^{4+} + \text{Mo}^{4+} \rightarrow 2\text{Ti}^{3+} + \text{Mo}^{6+}$ .

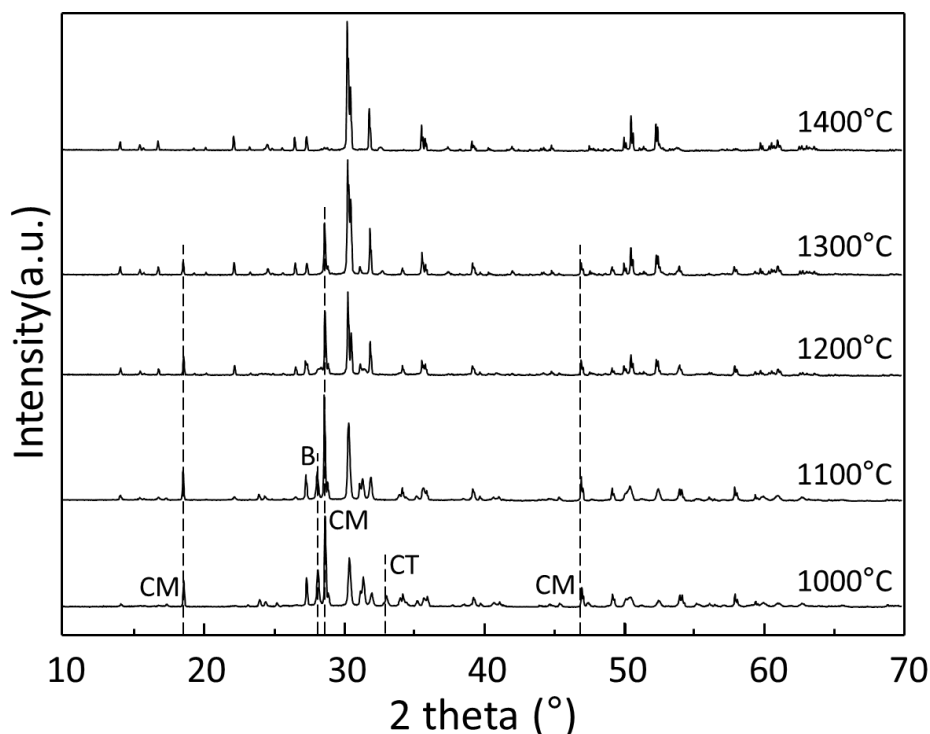


**Figure 2.** XRD patterns for  $\text{CaZrTi}_{1.6}\text{Mo}_{0.4}\text{O}_7$  samples synthesized under vacuum. Major reflections for following phases labelled: B – baddeleyite, CT – calcium titanate, and CM –  $\text{CaMoO}_4$ . All reflections in the  $1400^\circ\text{C}$  patterns can be indexed to the zirconolite phase.

With increasing reaction temperature the relative intensity of the  $\text{CaMoO}_4$  reflections decreases until at  $1400^\circ\text{C}$  only reflections indexed to monoclinic zirconolite were observed. This indicates that at higher temperatures the  $\text{CaMoO}_4$  is either reacting with existing zirconolite and free baddeleyite, or it is decomposing and the Mo is volatilizing. Combined thermogravimetry and mass spectroscopy were performed on the homogenized precursor batches to try to understand more about the formation process. Figure 3 shows the weight loss as a function of temperature  $\text{CaZrTi}_{1.8}\text{Mo}_{0.2}\text{O}_7$ . Also shown is the mass spectrometer signal associated with 44 atomic mass units which we have assigned to be due to loss of  $\text{CO}_2$ . There are two clear weight loss events in the temperature range between RT and  $1400^\circ\text{C}$ . The first event is related to the decomposition of the  $\text{CaCO}_3$  precursor liberating  $\text{CO}_2$  consistent with the mass spectrometer signal. The measured weight loss of 11 % is consistent with the expected loss of  $\text{CO}_2$  (11.2 wt%) based on the amount of  $\text{CaCO}_3$  in the batch (25.5 wt%). The second very small weight loss at between  $1000^\circ\text{C}$  and  $1200^\circ\text{C}$  could not be correlated to any expected elemental or molecular signature from the mass spectrometer so the origin of this remains unknown. The absence of any significant weight losses above  $800^\circ\text{C}$  indicated negligible volatilization of the 5.5 wt% Mo in the batch during the decomposition of the  $\text{CaMoO}_4$  intermediate phase. This suggests incorporation of the Mo within the single zirconolite phase observed in the XRD pattern at  $1400^\circ\text{C}$ . Further work is required to investigate whether the Mo is reduced to  $\text{Mo}^{4+}$  prior to

incorporation or whether it is incorporated as  $\text{Mo}^{6+}$  in the zirconolite structure. The data in Figure 3 is representative of that observed from all samples in the  $\text{CaZr}(\text{Ti}_{2-x}\text{Mo}_x)\text{O}_7$  series.

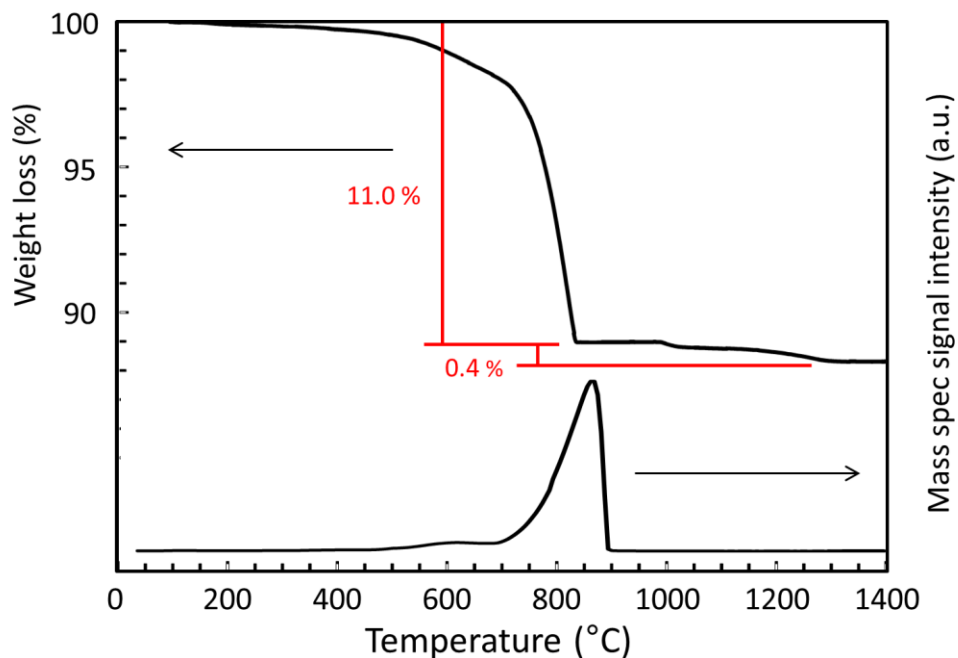


**Figure 3.** Weight loss as a function of temperature for  $\text{CaZrTi}_{1.8}\text{Mo}_{0.2}\text{O}_7$  with corresponding mass spectrometer signal intensity (arbitrary units) associated with 44 atomic mass units (assigned to  $\text{CO}_2$ ).

Further investigation of the phase assemblage and chemistry of the products formed were conducted by scanning electron microscopy (SEM) and energy dispersive spectroscopy (EDX). Figure 4 shows backscattered electron images from a  $\text{CaZrTi}_{1.8}\text{Mo}_{0.2}\text{O}_7$  sample heat treated at  $1400\text{ }^\circ\text{C}$ .

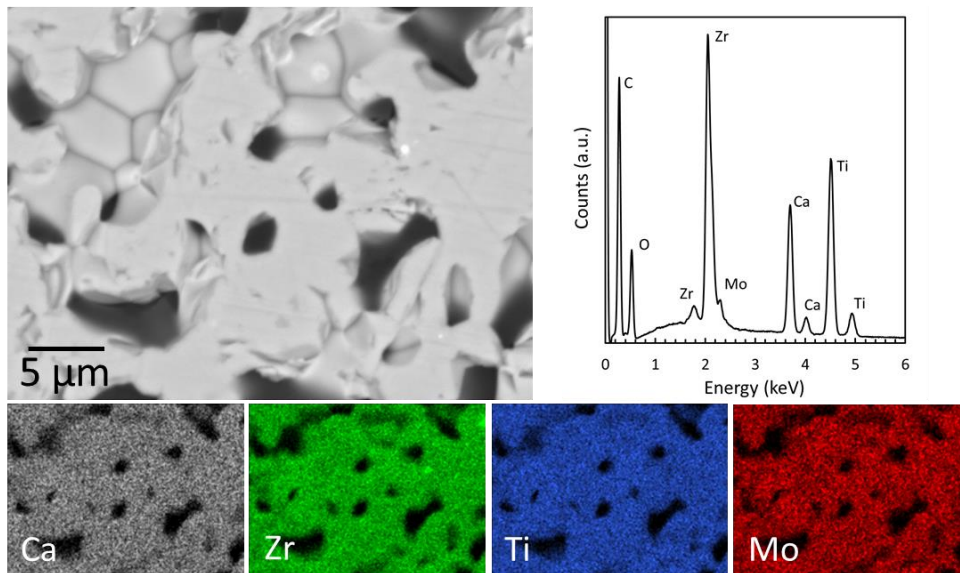


**Figure 4.** Backscattered SEM image showing the microstructure of a  $\text{CaZrTi}_{1.8}\text{Mo}_{0.2}\text{O}_7$  sample heat treated at 1400 °C. Elemental dot maps are shown along with EDX spectra on the right which was acquired from the entire field of view.

A single phase with equiaxed grains approximately 2 - 10  $\mu\text{m}$  in diameter can be observed in the backscattered images. The EDX spectrum obtained is consistent with the expected elemental content for  $\text{CaZrTi}_{1.8}\text{Mo}_{0.2}\text{O}_7$ . It can clearly be seen from both the EDX spectrum and the elemental dot maps that Mo is incorporated within the zirconolite phase.

## CONCLUSIONS

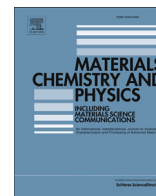
Incorporation of Mo as a structural analogue for Tc has been successfully demonstrated in single phase zirconolite ceramics synthesized under vacuum in the system  $\text{CaZrTi}_{2-x}\text{Mo}_x\text{O}_7$  (where  $0.0 < x \leq 0.4$ ). The mechanism of formation for these phases has been investigated using a combination of structural and spectroscopic techniques. It has been shown that under vacuum processing  $\text{CaMoO}_4$  is stabilized as an intermediate phase prior to full formation of a single phase with the zirconolite structure. Thermal analysis in combination with elemental analysis has indicated that even at 1400 °C there is negligible loss of Mo which indicates a promising formation route for potential Tc host phases.

## ACKNOWLEDGMENTS

This work was funded by the Engineering and Physical Sciences Research Council through grant EP/M026566/1 and the Nuclear FiRST Centre for Doctoral Training (EP/G037140/1). NCH acknowledges support from the Royal Academy of Engineering and the Nuclear Decommissioning Authority. This research was performed at the MIDAS Facility, at the University of Sheffield, which was established with support from the Department of Energy and Climate Change.

## REFERENCES

1. J. E. Till, in *Technetium in the Environment*, edited by G. Desmet and C. Myttenaere (Springer, New York, 1986), p. 1.
2. F. Chen, P. C. Burns, and R. C. Ewing, *J. Nucl. Mater.* **278**, 225 (2000).
3. M. Y. Khalil, and W. B. White, *J. Am. Ceram. Soc.* **66**, C197 (1983).
4. H. J. Rossell, *Nature* **283**, 282 (1980).
5. B. M. Gatehouse, I. E. Grey, R. J. Hill, and H. J. Rossell, *Acta Cryst.* **B37**, 306 (1981).
6. T. J. White, *Am. Mineral.* **69**, 1156 (1984).
7. G. R. Lumpkin, *Elements* **2**, 365 (2006).
8. R. D. Shannon, *Acta Cryst.* **A32**, 751 (1976).
9. I. Halikia, L. Zoumpoulakis, E. Christodoulou, and D. Prattis, *Euro. J. Min. Proc. Environ. Protection*.
10. J. C. Marra, A. D. Cozzi, R. A. Pierce, J. M. Pareizs, A. R. Jurgensen, and D. M. Missimer, in *Environmental Issues and Waste Management Technologies in the Ceramic and Nuclear Industries VII*, edited by G. L. Smith, S. K. Sundaram, and D. R. Spearing (The American Ceramic Society, Westerville, 2002), p. 381.



## Discussion

## Comment on “Preliminary assessment of modified borosilicate glasses for chromium and ruthenium immobilization”, by Farid and Rahman



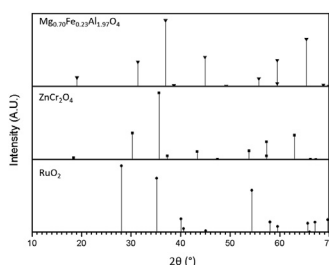
Neil C. Hyatt\*, Claire L. Corkhill, Daniel J. Bailey, Adam J. Fisher, Russell J. Hand

Immobilisation Science Laboratory, Department of Materials Science and Engineering, The University of Sheffield, S1 3JD, UK

## HIGHLIGHTS

- Inaccuracies in the report of Farid and Rahman, on UK HLW glasses, are clarified.
- A single complex spinel phase incorporates Zn and Cr, consistent with earlier studies.
- SIMS data of Farid and Rahman are apparently inconsistent with solution chemistry data.

## GRAPHICAL ABSTRACT



## ARTICLE INFO

## Article history:

Received 2 December 2016

Received in revised form

23 December 2016

Accepted 29 December 2016

Available online 18 January 2017

## Keywords:

Radioactive waste

Glass matrix

Structure immobilisation

## ABSTRACT

Farid and Rahman recently reported an investigation of the microstructure and alteration of borosilicate glasses designed for the immobilisation of UK radioactive wastes [Preliminary assessment of modified borosilicate glasses for chromium and ruthenium immobilization, Materials Chemistry and Physics, 186 (2017) 462–469]. The authors draw conclusions concerning the partitioning of elements within two devitrified spinel phases, at variance with previous studies of these materials. The authors also present solution chemistry and surface analysis data for alteration of these glasses, and postulate micro-cracks apparent in the gel layer of the altered glass to govern the extent of alteration. From analysis of data presented by Farid and Rahman, and comparison with previous studies, we show that their data are consistent with the presence of a single spinel phase of complex chemical composition, (Mg,Zn,Ni)(Cr,Fe,Al)<sub>2</sub>O<sub>4</sub>. We show the chemistry and surface analysis data presented by Farid and Rahman to be contradictory, in terms of the relative alteration behaviour of these glasses, as verified by previous studies, and deduce that an alternative explanation is required to rationalise their observations. We also comment on other aspects of the report which require clarification.

© 2016 Published by Elsevier B.V.

## 1. Introduction

In a recent publication, Farid and Rahman reported an investigation of alkali borosilicate glasses applied for the immobilisation of UK radioactive wastes [1]. Aspects of this study are inconsistent

with previous investigation of these materials [2–5] and require clarification, as we highlight in this comment on their study.

In the UK, and internationally, alkali borosilicate glasses are the material of choice for vitrification of the fission products and minor actinides arising from nuclear fuel reprocessing, classified as High Level Waste (HLW) [2–7]. Modification of the UK HLW glass composition, by addition of CaO and ZnO, has been studied with the aim of improving processing characteristics and long term durability, as discussed elsewhere [2–6].

DOI of original article: <http://dx.doi.org/10.1016/j.matchemphys.2016.11.020>.

\* Corresponding author.

E-mail address: [n.c.hyatt@sheffield.ac.uk](mailto:n.c.hyatt@sheffield.ac.uk) (N.C. Hyatt).

## 2. Analysis of glass microstructure

To fully understand the dependence of HLW glass properties on ZnO content, it is necessary to appreciate the role of Zn in the glass structure, i.e. whether a network modifier, network intermediate, or network former. In their contribution, Farid and Rahman erroneously state Zn to be a network modifier in such glasses [1], which they infer to influence the incorporation of Cr within the glass and accessory spinel phase(s). In fact, Zn K-edge X-ray absorption spectroscopy has demonstrated Zn to primarily participate in network formation in such glasses, as  $\text{ZnO}_4$  polyhedra (Zn–O distance of  $1.95 \pm 0.01$  Å), linking, on average, to  $2 \pm 1$   $\text{SiO}_4$  units via bridging oxygen atoms [2]. This conclusion was later verified by Raman spectroscopy investigation and molecular dynamics simulations of the structure of closely related UK HLW glass compositions [3,4].

Farid and Rahman focus on the presence of crystalline  $\text{RuO}_2$  and  $\text{Cr}_2\text{O}_3$  bearing phases within a CaO and ZnO modified glass, prepared in our laboratory, for the immobilisation of HLW derived principally from Magnox fuel reprocessing [2,4,5]. Farid and Rahman incorrectly attribute the source of  $\text{Cr}_2\text{O}_3$  in this glass to “the result of Magnox decladding and dissolution processes” [1]. However, the composition of Magnox fuel cladding is devoid of Cr, being an alloy of Mg with 0.8% Al and 0.002–0.05% Be, by weight [8]. In fact, the source of Cr is principally the corrosion of stainless steel process equipment and storage vessels [7], by the acidic HLW raffinate. In the case of “blended” glass compositions derived from HLW arising from reprocessing of Magnox and Advanced Gas-cooled Reactor (AGR) fuels, a contribution from leaching of AGR cladding during fuel dissolution is also likely (AGR cladding composition approximately: Fe 52.72%, Cr 20.40%, Ni 25.10%, Nb 0.60%, other 1.18%, by weight [9]).

Farid and Rahman report the presence of two distinct spinel phases in their Magnox glass material, formulated  $\text{ZnCr}_2\text{O}_4$  and  $\text{Fe}_{0.23}\text{Mg}_{0.70}\text{Al}_{1.97}\text{O}_4$ . However, we suggest that this conclusion is not adequately supported by the X-ray diffraction or SEM/EDX data presented by the authors.

Regarding the X-ray diffraction data (Fig. 1 in Ref. [1]), the Bragg reflections may be indexed uniquely as a mixture of  $\text{RuO}_2$  and a single spinel phase  $\text{AB}_2\text{O}_4$  (space group  $\text{Fd}\bar{3}\text{m}$ ), as shown by inspection of Table 1 and Fig. 1 presented here (note, reference diffraction patterns in Fig. 1 were extracted from the ICSD database [10]). The presence of a second cubic spinel phase would require double the number of observed spinel reflections; however, such additional reflections are not present at appreciable intensity, as assessed against the signal to noise ratio of the published data (compare Fig. 1 here with Fig. 1 in Ref. [1]). Farid and Rahman did not report the optical arrangement and detector configuration for their X-ray diffractometer, but a typical maximum step size is  $0.02^\circ$  for a laboratory instrument. This should be sufficient to resolve the distinct Bragg reflections of  $\text{ZnCr}_2\text{O}_4$  and  $\text{Fe}_{0.23}\text{Mg}_{0.70}\text{Al}_{1.97}\text{O}_4$ , if

**Table 1**  
Analysis of X-ray diffraction data presented in Fig. 1(b) of [1], showing the presence of only one significant spinel phase.

Bragg reflection $2\theta$ ( $^\circ$ )	Phase	Assignment
28.1	$\text{RuO}_2$	(110)
30.5	$\text{AB}_2\text{O}_4$	(220)
35.8	$\text{AB}_2\text{O}_4$	(311)
40.1	$\text{RuO}_2$	(200)
43.4	$\text{AB}_2\text{O}_4$	(400)
54.3	$\text{RuO}_2$	(211)
57.5	$\text{AB}_2\text{O}_4$	(511)
58.0	$\text{RuO}_2$	(220)
59.9	$\text{RuO}_2$	(002)

both phases were present in appreciable concentration, as shown by the reference diffraction patterns in Fig. 1.

Regarding the SEM/EDX data, the *area* EDX spectrum labelled (iv) of Fig. 3 in Ref. [1], shows the presence of Mg, Al, Cr, Fe, Ni and Zn in high concentration, associated with observable crystallites, compared to EDX spectrum labelled (iii), associated with the Magnox glass matrix. Mg, Cr, Fe, Ni and Zn are known spinel constituents and, together with the available X-ray diffraction data, it is reasonable to infer that the observed crystallites are indeed a complex spinel. However, because the EDX data are acquired from a wide *area*, and not from *points* within the crystallites, it cannot be concluded that there are two spinel phases present of distinct composition. Indeed, our studies of very closely related glass compositions identified only a single spinel phase of composition  $(\text{Zn}_{0.60}\text{Ni}_{0.20}\text{Mg}_{0.20})(\text{Cr}_{1.37}\text{Fe}_{0.63})\text{O}_4$  [4], which is broadly consistent with both the EDX data (Fig. 3 (iv)) and X-ray diffraction data (Fig. 1) presented by Farid and Rahman [1]. Note that although the glasses reported in our study did not contain  $\text{RuO}_2$ , this is not expected to significantly affect the chemical composition of the spinel given the very low solubility of  $\text{RuO}_2$  in the glass phase [11].

A key conclusion of the study by Farid and Rahman was that “Published results showed that spinel, containing chromium, iron, and nickel, is the main crystalline phase that immobilizes chromium. These results are not confirmed in this study, where the presence of zinc oxide (as modifier) has affected the nature of chromium immobilization.” [1]. We infer from this statement that the authors assert the incorporation of Cr into a spinel phase of composition  $\text{ZnCr}_2\text{O}_4$ . As noted above, within the borosilicate glass phase, Zn acts as a network former, not a modifier. Comparison of the reference diffraction patterns of  $\text{ZnCr}_2\text{O}_4$  and  $\text{Fe}_{0.23}\text{Mg}_{0.70}\text{Al}_{1.97}\text{O}_4$ , Fig. 1, showed that the  $\text{ZnCr}_2\text{O}_4$  to be a better fit to the spinel phase in the X-ray diffraction data of Farid and Rahman (based on positions of the Bragg reflections). However, this cannot be relied on as a conclusive identification of a phase of this specific composition, as appears to be the assumption of Farid and Rahman, since the cubic spinel structure is highly flexible toward isomorphic substitution. Indeed, as discussed above, the SEM/EDX data presented by Farid and Rahman are consistent with incorporation of Zn and Cr within a chemically complex spinel, similar to  $(\text{Zn}_{0.60}\text{Ni}_{0.20}\text{Mg}_{0.20})(\text{Cr}_{1.37}\text{Fe}_{0.63})\text{O}_4$  reported previously [4].

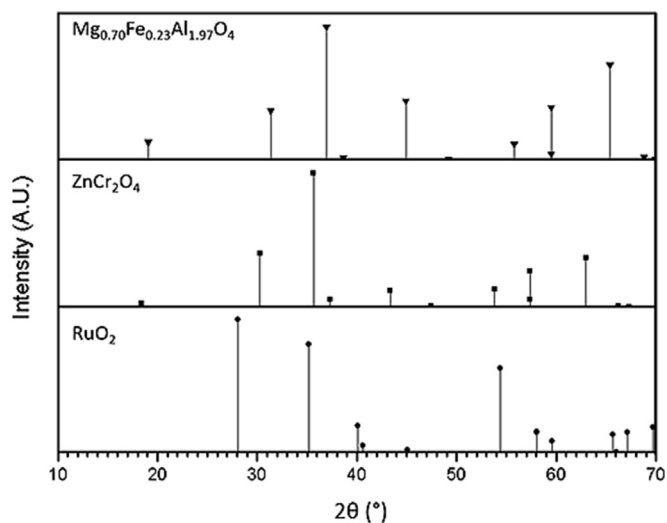


**Fig. 1.** Reference X-ray diffraction patterns for  $\text{Mg}_{0.70}\text{Fe}_{0.23}\text{Al}_{1.97}\text{O}_4$ ,  $\text{ZnCr}_2\text{O}_4$ , and  $\text{RuO}_2$ , from the ICSD database (records: 89056, 290018, 172178 respectively [10]); data are for Cu  $K\alpha$  radiation,  $\lambda = 1.5418$  Å.

### 3. Surface analysis of pristine and altered glasses

Farid and Rahman also present results of SEM observations of pristine and altered glass surfaces. Fig. 2 in Ref. [1] shows the surface of a pristine glass specimen with the composition Na<sub>2</sub>O 11.1%, Li<sub>2</sub>O 5.3%, B<sub>2</sub>O<sub>3</sub> 21.9%, SiO<sub>2</sub> 61.7% (by weight), which is commonly referred to as MW glass – this is the glass frit composition used to vitrify calcined HLW at the Sellafield site [4–7]. The features labelled (i) and (ii) in Fig. 2 of [1] are interpreted as “inclusions” due to the presence of “bubble and/or immiscible components”. Farid and Rahman note that the EDX spectra for these features “are similar and detect only structural elements (Si, Na, O)” of the glass matrix [1]. Fig. 2 is evidently a secondary electron image, given the topography apparent in features (i) and (ii), which are clearly situated on top of the polished glass surface, inconsistent with the interpretation as “inclusions” due to the presence of “bubble and/or immiscible components”. The fact that the EDX spectra of these features are essentially indistinguishable from the glass matrix suggests that the features are either: a) glass particulates of the same composition as the matrix, or b) a material of low atomic number, permitting transmission of the electron beam and the characteristic X-rays emitted from the glass sub-surface. The rounded edges of the features in question are inconsistent with glass particulates produced by brittle fracture in specimen preparation or handling, which are typically characterised by sharp edges. Taken together, these observations are consistent with features (i) and (ii) being associated with extraneous organic matter on the surface of the glass sample, rather than “bubble and/or immiscible components”. We note that the EDX spectrum associated with feature (i), Fig. 2(b) in Ref. [1], exhibits a weak C K $\alpha$  emission line, which could be consistent with the presence of organic material, although we cannot rule out a contribution from the carbon coating applied by the authors.

In the examination of altered glass samples, Farid and Rahman report “Samples morphologies are altered by the presence of pitting associated with micro-cracks of different sizes e.g. 3–5  $\mu\text{m}$  and white fibers (Fig. 5 a&b). BE-SEM of simulated Magnox-modified glass shows micro-cracks network that surrounds and connects between the pit-tings (Fig. 5c)”; where the figure numbers refer to [1]. Aqueous corrosion of glasses involves a complex series of reactions, including hydration, ion exchange, network hydrolysis, and network condensation, resulting in an interfacial alteration layer, the “gel layer”, which is depleted in soluble elements. The micro-cracks observed by Farid and Rahman are, in fact, typical of desiccation of the glass gel layer, leading to a decrease in the molar volume and development of tensile stress with respect to the underlying pristine material. Ultimately, cracks open in the gel layer to relieve this tensile stress, as highlighted by Icenhower and Steefel [12].

Finally, we highlight an apparent inconsistency in the SIMS and solution chemistry data associated with dissolution of the reference (MW) and compositionally modified simulant Magnox glass, presented by Farid and Rahman [1]. The reported normalised mass loss of boron from the reference (MW) glass ( $0.13 \text{ g m}^{-2} \text{ d}^{-1}$ ) is three times greater than for the compositionally modified Magnox glass ( $0.05 \text{ g m}^{-2} \text{ d}^{-1}$ ), Table 2 in Ref. [1]. The elemental SIMS profiles are consistent with these data, with apparent depletion of B, Li, Na and Si to a depth of >400 nm for the reference (MW) glass and 270nm for the compositionally modified simulant Magnox glass (compare Fig. 4a/7a, and Fig. 4b/7b, respectively, in Ref. [1]). Evidently, alteration of the reference (MW) glass occurred to a greater depth than the compositionally modified simulant Magnox glass. This is as expected, due to the incorporation of less soluble metal oxide constituents present in the HLW stream, and the lower proportion of soluble glass constituents (Na<sub>2</sub>O, Li<sub>2</sub>O, and B<sub>2</sub>O<sub>3</sub>), in the simulant Magnox composition (Table 1 in Ref. [1], see also

[4,5]). Our recent vapour phase hydration study of such glasses validate these findings, with the alteration rate of MW glass ( $24.8 \pm 2.5 \text{ g m}^{-2} \text{ d}^{-1}$ ) much greater than for the compositionally modified Magnox glass ( $0.9 \pm 0.3 \text{ g m}^{-2} \text{ d}^{-1}$ ) [5]. Note that although the experimental conditions of the two studies are very different, the relative glass durability is expected to be differentiated. In this context, the SIMS determined H<sup>+</sup> depth profiles of the altered surfaces of these glasses, reported by Farid and Rahman, Fig. 8 in Ref. [1], are difficult to comprehend. Since the solution chemistry data and elemental SIMS profiles of the reference (MW) composition show this to be more extensively altered than the compositionally modified Magnox glass, it could be expected that the H<sup>+</sup> concentration should be greater in the altered surface of the former, compared to the latter. However, Fig. 8 in Ref. [1] shows the opposite to be true. Farid and Rahman state that with respect to the compositionally modified Magnox glass, “This could be attributed to the presence of micro-cracks network on the surface, these cracks acts as pathway for water molecules”. This does not seem a plausible explanation, given the uncertainty over the origin of the cracks in the glass gel layer discussed above, which are consistent with post-alteration desiccation of the gel layer. Moreover, such cracks were also observed on the surface of the altered reference (MW) glass, as shown in Fig. 6(a) of [1]. A possible explanation for the discrepancy in reported H<sup>+</sup> SIMS profiles might be different storage conditions, and hence desiccation, of the glass gel layers, potentially assisted by different permeability. Alternatively, Fig. 6(a) of [1] shows areas of the altered surface of the reference (MW) glass where the gel layer has spalled, revealing the underlying substrate. The inconsistency in the SIMS H<sup>+</sup> profiles of Fig. 8 of [1] might be rationalised if the data associated with the altered reference (MW) glass were to correspond with the underlying substrate on an area of the surface from which the gel layer had spalled. Further investigation of this apparent discrepancy is warranted.

### 4. Conclusions

The microstructure of the compositionally modified Magnox glass reported by Farid and Rahman [1], is consistent with that previously reported for closely related materials, with Cr incorporated within a single (Mg,Zn,Ni)(Cr,Fe,Al)<sub>2</sub>O<sub>4</sub> spinel phase [4]. The relative alteration of the reference MW and compositionally modified Magnox glass reported by Farid and Rahman [1], as determined by analysis of solution chemistry, is consistent with both aqueous and vapour phase alteration studies of closely related materials [4,5]. However, the corresponding H<sup>+</sup> SIMS profiles reported by Farid and Rahman appear contradictory with their solution chemistry data and that previously published [4,5]. The reconciliation of this contradiction advocated by Farid and Rahman, involving water penetration through micro-cracks evident in the gel layer, seems specious, given the resemblance of the micro-cracks, present on *both* glasses, to those arising from post-alteration desiccation of the hydrated gel layer [12].

Overall, this study highlights the need for careful interpretation of glass microstructure and corrosion behaviour, to provide the robust data and mechanistic understanding required to support a safety case for radioactive waste disposal, which will engender scientific and public confidence. To address this key knowledge gap, recent studies have reported new data and mechanistic understanding of the dissolution behaviour of UK HLW glasses [13,14].

### Acknowledgements

We acknowledge financial support for our research reported here from EPSRC under grants EP/L014041/1, EP/L015390/1, EP/G037140/1, and EP/N017374/1. Fisher is grateful to RWM Ltd., for

studentship support. This research was performed, in part, at the MIDAS facility, at the University of Sheffield, which was established with support from the Department of Energy and Climate Change. The authors are grateful to the two anonymous reviewers for their careful evaluation of this contribution. Although some of the authors provided materials for the study of Farid and Rahman [1], this should not be taken as an endorsement of the methods or conclusions of their investigation.

## References

- [1] O.M. Farid, R.O.A. Rahman, Preliminary assessment of modified borosilicate glasses for chromium and ruthenium immobilization, *Mater. Chem. Phys.* 186 (2017) 462–469.
- [2] N.J. Cassingham, M.C. Stennett, P.A. Bingham, N.C. Hyatt, G. Aquilanti, The structural role of Zn in nuclear waste glasses, *Int. J. Appl. Glass Sci.* 2 (2011) 343–353.
- [3] T.R. Stechert, M.J.D. Rushton, R.W. Grimes, Predicted mechanism for enhanced durability of zinc containing silicate glasses, *J. Am. Ceram. Soc.* 96 (2013) 1450–1455.
- [4] H. Zhang, C.L. Corkhill, P.G. Heath, R.J. Hand, M.C. Stennett, N.C. Hyatt, Effect of Zn- and Ca-oxides on the structure and chemical durability of simulant alkali borosilicate glasses for immobilisation of UK high level wastes, *J. Nucl. Mater.* 462 (2015) 321–328.
- [5] N.J. Cassingham, C.L. Corkhill, M.C. Stennett, R.J. Hand, N.C. Hyatt, Alteration layer formation of Ca- and Zn-oxide bearing alkali borosilicate glasses for immobilisation of UK high level waste: a vapour hydration study, *J. Nucl. Mater.* 479 (2016) 639–646.
- [6] R. Short, Phase separation and crystallisation in UK HLW vitrified products, *Procedia Mater. Sci.* 7 (2014) 93–100.
- [7] M.T. Harrison, The effect of composition on short- and long-term durability of UK HLW glass, *Procedia Mater. Sci.* 7 (2014) 186–192.
- [8] G. Marsh, H. Eccles, Fuel fabrication, in: P.D. Wilson (Ed.), *The Nuclear Fuel Cycle: from Ore to Waste*, Oxford University Press, 1996, pp. pp40–66.
- [9] R.C. Ecob, R.C. Lobb, V.L. Kohler, The formation of G-phase in 20/25 Nb stainless steel AGR fuel cladding alloy and its effect on creep properties, *J. Mater. Sci.* 22 (1987) 2867–2880.
- [10] Inorganic Crystal Structure Database, FIZ Karlsruhe, available at: <http://icsd.fiz-karlsruhe.de>.
- [11] W. Lutze, F.C. Perez-Cardenas, K.S. Matlack, I.L. Pegg, P. Schill, “Testing and modelling the behaviour of platinoids during vitrification of high level radioactive waste. Part 1”, *Glass Technol. Eur. J. Glass Sci. Technol. A* 48 (2007) 263–275.
- [12] J.P. Icenhower, C.I. Steefel, Dissolution rate of borosilicate glass SON68: a method of quantification based upon interferometry and implications for experimental and natural weathering rates of glass, *Geochim. Cosmochim. Acta* 157 (2015) 147–163.
- [13] N. Cassingham, C.L. Corkhill, D. Backhouse, R.J. Hand, J.V. Ryan, J.D. Vienna, N.C. Hyatt, The initial dissolution rates of simulated UK Magnox-ThORP blend nuclear waste glass as a function of pH, temperature and waste loading, *Mineral. Mag.* 79 (2015) 1529–1542.
- [14] C.L. Corkhill, N. Cassingham, P.G. Heath, N.C. Hyatt, Dissolution of UK high-level waste glass under simulated hyperalkaline conditions of a collocated geological disposal facility, *Int. J. Appl. Glass Sci.* 4 (2013) 341–356.

# Contribution of Energetically Reactive Surface Features to the Dissolution of CeO<sub>2</sub> and ThO<sub>2</sub> Analogues for Spent Nuclear Fuel Microstructures

Claire L. Corkhill,<sup>\*,†</sup> Emmi Myllykylä,<sup>‡</sup> Daniel J. Bailey,<sup>†</sup> Stephanie M. Thornber,<sup>†</sup> Jiahui Qi,<sup>§</sup> Pablo Maldonado,<sup>||</sup> Martin C. Stennett,<sup>†</sup> Andrea Hamilton,<sup>⊥</sup> and Neil C. Hyatt<sup>\*,†</sup>

<sup>†</sup>Immobilisation Science Laboratory, Department of Materials Science and Engineering, The University of Sheffield, Sheffield S1 3JD, United Kingdom

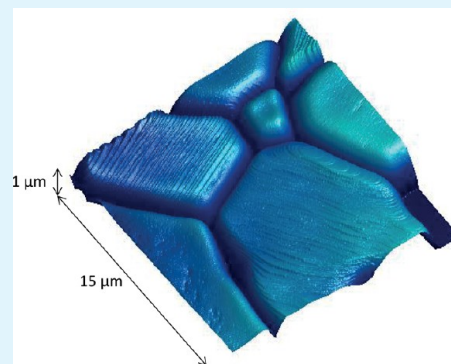
<sup>‡</sup>VTT Technical Research Centre of Finland, Espoo FI-02044, Finland

<sup>§</sup>Royal School of Mines, Imperial College London, London SW7 2AZ, United Kingdom

<sup>||</sup>Department of Physics and Astronomy, Uppsala Universitet, 751 05 Uppsala, Sweden

<sup>⊥</sup>Department of Civil and Environmental Engineering, The University of Strathclyde, Glasgow G1 1XQ, United Kingdom

**ABSTRACT:** In the safety case for the geological disposal of nuclear waste, the release of radioactivity from the repository is controlled by the dissolution of the spent fuel in groundwater. There remain several uncertainties associated with understanding spent fuel dissolution, including the contribution of energetically reactive surface sites to the dissolution rate. In this study, we investigate how surface features influence the dissolution rate of synthetic CeO<sub>2</sub> and ThO<sub>2</sub>, spent nuclear fuel analogues that approximate as closely as possible the microstructure characteristics of fuel-grade UO<sub>2</sub> but are not sensitive to changes in oxidation state of the cation. The morphology of grain boundaries (natural features) and surface facets (specimen preparation-induced features) was investigated during dissolution. The effects of surface polishing on dissolution rate were also investigated. We show that preferential dissolution occurs at grain boundaries, resulting in grain boundary decohesion and enhanced dissolution rates. A strong crystallographic control was exerted, with high misorientation angle grain boundaries retreating more rapidly than those with low misorientation angles, which may be due to the accommodation of defects in the grain boundary structure. The data from these simplified analogue systems support the hypothesis that grain boundaries play a role in the so-called “instant release fraction” of spent fuel, and should be carefully considered, in conjunction with other chemical effects, in safety performance assessments for the geological disposal of spent fuel. Surface facets formed during the sample annealing process also exhibited a strong crystallographic control and were found to dissolve rapidly on initial contact with dissolution medium. Defects and strain induced during sample polishing caused an overestimation of the dissolution rate, by up to 3 orders of magnitude.



**KEYWORDS:** nuclear fuel, dissolution, grain boundaries, faceting, surface, atomic force microscopy

## 1. INTRODUCTION

Spent nuclear fuel is a heterogeneous material composed primarily of UO<sub>2</sub>, with a minor component of actinides (e.g., Np and Pu) and fission products (e.g., Sr, Cs, and I). The preferred route for disposal of this material is within a geological disposal facility, several hundreds of meters below the ground. In such an environment, the release of radionuclides to the geo- and biospheres is controlled by the dissolution of the spent fuel in groundwater; thus it is important to understand the mechanisms and kinetics of dissolution. The dissolution behavior of spent fuel is dominated by the behavior of the UO<sub>2</sub> matrix, and, as such, a simplified system comprising UO<sub>2</sub> only is often used in experiments to determine SNF dissolution. On the basis of a wide range of dissolution investigations of SNF and UO<sub>2</sub> (see reviews<sup>1,2</sup>), it has been estimated that the fractional dissolution rate of spent

nuclear fuel is in the range of 10<sup>-6</sup> to 10<sup>-8</sup> per year, indicating that complete dissolution is likely to occur within ~10 million years.<sup>3</sup> However, natural uraninite (UO<sub>2</sub>) ores are known to be stable in the earth under reducing conditions for periods of billions of years,<sup>4,5</sup> suggesting that laboratory experiments may overestimate the dissolution rate of UO<sub>2</sub> by more than 2 orders of magnitude.

It has been demonstrated that experimentally derived dissolution rates of other minerals, such as quartz and feldspar, are also often found to be higher than the corresponding weathering rate of the rocks they comprise.<sup>6-9</sup> One of the causes of this observed behavior is specimen preparation within

Received: March 28, 2014

Accepted: July 7, 2014

Published: July 7, 2014

the laboratory; the act of crushing generates sharp edges and other surface defects, and the atoms on the surface associated with these features have high surface energy and contain fewer chemical bonds than the atoms on defect-free surfaces, which, in turn, contain fewer chemical bonds than atoms within the bulk. Defect surfaces are removed during dissolution, leaving a lower energy surface that dissolves at a slower rate.<sup>10,11</sup> Knauss and Wolery<sup>6</sup> observed that the dissolution rate of crushed albite decreased during the first 20 days by over an order of magnitude in all experimental conditions. Similarly, during sequential leaching from 52 to 114 days, crushed  $\text{UO}_2$  samples showed progressively decreasing dissolution rates.<sup>12,13</sup> Natural defects present at the surface have also been shown to affect dissolution rates; for example, Claparede et al.<sup>14</sup> found that crystal defects and initial crystallite size of mixed cerium–neodymium oxides influenced the dissolution rate.

To evidence the influence of high energy surface features on the dissolution rate of  $\text{UO}_2$ ,  $\text{CeO}_2$  and  $\text{ThO}_2$  analogues are investigated. These materials were chosen because they are isostructural to  $\text{UO}_2$  but are not sensitive to changes in oxidation state of the cation. Previously, we have synthesized  $\text{CeO}_2$  and  $\text{ThO}_2$  to closely resemble the microstructure of SNF,<sup>15,16</sup> therefore, we also make an assessment of how these physical and structural features are likely to influence the dissolution of SNF. Using an integrated approach, applying atomic force microscopy, vertical scanning interferometry, electron backscatter diffraction, and aqueous geochemical analysis, we determine how natural and specimen-induced high-energy surface sites (grain boundaries and surface defects, respectively) contribute to measured laboratory dissolution rates. Through this methodology, we aim to reduce the uncertainties associated with  $\text{UO}_2$  dissolution, and thus improve our understanding of the relationship between laboratory studies and the dissolution rates to be expected under geological disposal conditions.

## 2. EXPERIMENTAL SECTION

**2.1.  $\text{CeO}_2$  and  $\text{ThO}_2$  Preparation.** Cerium dioxide monoliths were prepared according to Stennett et al.<sup>15</sup> Monoliths were ground and polished to a  $0.05\ \mu\text{m}$  finish using SiC paper and diamond paste. To develop a grain boundary structure at the surface of some of the monoliths, thermal annealing was conducted. Monoliths were heated to  $1500\ ^\circ\text{C}$  at a ramp rate of  $5\ ^\circ\text{C}\ \text{min}^{-1}$  and held for 1 min to develop a grain boundary texture. The final microstructure (equiaxed grains ranging in size from 10 to  $30\ \mu\text{m}$  and randomly orientated) was in good agreement with those published for  $\text{UO}_2$  and SIMFUEL.<sup>17,18</sup> An area was masked with an inert glue to act as a nonreactive reference surface of constant height during the dissolution experiments.

$\text{ThO}_2$  powder (British Drug Houses Ltd., lot number G83757/541012) was used to prepare sintered  $\text{ThO}_2$  monoliths. Briefly, 1 g of powder was uniaxially pressed in a 10 mm diameter hardened stainless steel die with a load of 100 MPa. Monoliths were sintered for 4 h at  $1750\ ^\circ\text{C}$  in a standard air atmosphere muffle furnace, at a ramp rate of  $5\ ^\circ\text{C}\ \text{min}^{-1}$ , which gave a final density of  $>94\%$  of the theoretical density of  $\text{ThO}_2$  ( $10.00\ \text{g}\ \text{m}^{-3}$ ), determined using the Archimedes method. Monoliths were ground and polished to a  $0.25\ \mu\text{m}$  finish using SiC paper and diamond paste. It was found that a final polishing step using a  $0.06\ \mu\text{m}$  silica colloid solution was required to obtain surfaces flat enough for analysis by electron back scatter diffraction (EBSD)<sup>19</sup> and by atomic force microscopy (AFM) (for  $\text{ThO}_2$ , only data, not images, are given in the text due to complexities associated with surface polishing). Grain boundaries were defined by heating to  $1500\ ^\circ\text{C}$  at a ramp rate of  $5\ ^\circ\text{C}\ \text{min}^{-1}$ . The resulting grains ranged in size from  $5\text{--}30\ \mu\text{m}$ , and grains were found to be randomly orientated, consistent with  $\text{UO}_2$  and SIMFUEL microstructure.

**2.2. Dissolution Experiments.**  $\text{CeO}_2$  and  $\text{ThO}_2$  are insoluble materials; hence, they are difficult to dissolve without the application of aggressive conditions. As such, dissolution was performed at high temperature ( $90$  and  $150\ ^\circ\text{C}$ ) and in acidic media. All solutions were prepared using ultrahigh quality (UHQ) water ( $18\ \text{M}\Omega$ ). The following dissolution experiments were conducted: (1) annealed  $\text{CeO}_2$  and  $\text{ThO}_2$  dissolution at  $90\ ^\circ\text{C}$  in  $0.01\ \text{M}\ \text{HNO}_3$ ; (2) annealed  $\text{CeO}_2$  dissolution at  $150\ ^\circ\text{C}$  in  $0.01\ \text{M}\ \text{HNO}_3$ ; (3) annealed  $\text{CeO}_2$  dissolution at room temperature in  $0.01$ ,  $0.1$ ,  $1.5$ ,  $3$ , and  $15\ \text{M}\ \text{HNO}_3$ ; (4) annealed  $\text{CeO}_2$  dissolution at room temperature in a series of etching solutions ( $72\ \text{h}$  in UHQ water,  $15\ \text{h}$  in  $0.001\ \text{M}\ \text{HCl}$ ,  $4\ \text{h}$  in  $0.01\ \text{M}\ \text{HCl}$ ); and (5) polished (i.e., not annealed to define grain texture)  $\text{CeO}_2$  dissolution at  $90$  and  $150\ ^\circ\text{C}$  in  $0.01\ \text{M}\ \text{HNO}_3$ .

Dissolution experiments performed at  $90\ ^\circ\text{C}$  were conducted within  $50\ \text{mL}$  PTFE vessels, cleaned according to the ASTM PCT standard.<sup>20</sup> A single monolith of  $\text{CeO}_2$  or  $\text{ThO}_2$  was placed into a PTFE basket within the vessel, to allow contact of the whole monolith with the dissolution medium, and  $40\ \text{mL}$  of  $0.01\ \text{M}\ \text{HNO}_3$  was added. Triplicate samples and duplicate blanks (containing no monolith) were placed in a Carbolite oven at  $90\ (\pm 0.5)\ ^\circ\text{C}$  and sampled at  $0$ ,  $1$ ,  $3$ ,  $7$ ,  $14$ ,  $21$ ,  $28$ , and  $35$  days. An aliquot ( $1.2\ \text{mL}$ ) of each sample was removed for aqueous elemental analysis. One monolith from each triplicate experiment was removed for surface characterization at each sampling point, and returned to the dissolution medium after analysis. Dissolution experiments performed at  $150\ ^\circ\text{C}$  were conducted in customized reactors, consisting of  $3\ \text{mL}$  PTFE inserts with a PTFE lid (cleaned as above), within a sealed steel pressure vessel. These were placed within a heating block, where the temperature was maintained at  $150\ (\pm 1)\ ^\circ\text{C}$ . Monoliths were placed on PTFE inserts to ensure contact of the whole monolith with the dissolution medium, and  $2\ \text{mL}$  of  $0.01\ \text{M}\ \text{HNO}_3$  was added. Experiments were destructively sampled at  $1$ ,  $3$ ,  $7$ ,  $21$ , and  $35$  days, at which times the monoliths were subject to surface analysis and aqueous solutions were collected for elemental analysis. Dissolution experiments conducted at room temperature were performed within an atomic force microscopy (AFM) fluid cell containing a fragment of a  $\text{CeO}_2$  monolith cut using a diamond slow saw, immersed within  $3\ \text{mL}$  of reaction medium.

**2.3. Surface and Aqueous Analysis.** Monolith surfaces and cross sections were imaged using a JEOL JSM6400 scanning electron microscope (SEM) operating with an accelerating voltage of  $15\ \text{kV}$  and a working distance of  $18\ \text{mm}$ . Analysis of crystallographic orientation was performed using electron backscatter diffraction (EBSD) (Oxford Instruments, Abingdon, Oxfordshire, UK) in conjunction with an FEI Sirion field emission SEM. EBSD maps of  $100\ \mu\text{m}^2$  were obtained at an accelerating voltage of  $20\ \text{kV}$  and with a  $0.25\ \mu\text{m}$  step size, and analyzed using HKL Channel 5 software (Oxford Instruments). Surface topography was measured using vertical scanning interferometry (VSI) (Sensofar PLu2300 profilometer) using a confocal lens with  $50\times$  and  $150\times$  magnification, a numerical aperture of  $0.95$ , and lateral and vertical resolutions of  $111$  and  $1\ \text{nm}$ , respectively. Changes in surface morphology during dissolution were also measured using atomic force microscopy (AFM); ex situ measurements were performed using a Veeco Dimension 3100 microscope, operating in tapping mode and using high aspect ratio AFM tips, and in situ measurements were conducted using a Digital Instruments Multimode/Nanoscope IIIa in contact mode. Aqueous elemental analysis of Ce was undertaken by inductively coupled plasma-mass spectroscopy (ICP-MS) using an Agilent 4500 spectrometer, and analysis of Th was performed using high-resolution ICP-MS (Element 2, ThermoScientific). Prior to analyses, all samples were acidified with  $20\ \mu\text{L}$  of concentrated  $\text{HNO}_3$  to keep all elements dissolved in solution. Solution data are expressed as the normalized elemental leaching  $N_L(\text{Ce}, \text{Th})\ (\text{g}\ \text{m}^{-2})$  according to

$$N_L(\text{Ce}, \text{Th}) = \frac{m_{\text{Ce,Th}}}{S/V} \quad (1)$$

where  $m_{\text{Ce, Th}}$  is the total amount of Ce or Th released into solution and  $S/V$  is the surface area to volume ratio. The normalized element leaching rate  $R_L(\text{Ce}, \text{Th})\ (\text{g}\ \text{m}^{-2}\ \text{d}^{-1})$  is determined by

$$R_L(\text{Ce, Th}) = \frac{m_{\text{Ce,Th}}}{\frac{S}{V} \times \Delta t} \quad (2)$$

where  $\Delta t$  is the leaching time in days.

### 3. RESULTS

**3.1. CeO<sub>2</sub> and ThO<sub>2</sub> Dissolution Rate.** The aqueous dissolution rate data derived from all experiments are given in Table 1. The dissolution rate for CeO<sub>2</sub> dissolved at 150 °C was

**Table 1. Dissolution Rates for CeO<sub>2</sub> and ThO<sub>2</sub> Samples Dissolved in 0.01 M HNO<sub>3</sub> as a Function of Specimen Preparation and Temperature<sup>a</sup>**

specimen preparation	temp (°C)	rate (g m <sup>-2</sup> d <sup>-1</sup> )
annealed CeO <sub>2</sub>	90	$(7.26 \pm 0.2) \times 10^{-5}$
	150	$(6.34 \pm 0.1) \times 10^{-3}$
annealed ThO <sub>2</sub>	90	$(5.23 \pm 0.1) \times 10^{-7}$
polished CeO <sub>2</sub>	90	$(7.40 \pm 0.2) \times 10^{-2}$
	150	$(7.01 \pm 0.2) \times 10^{-2}$

<sup>a</sup>Errors given are the standard deviation of triplicate experiments.

$(6.34 \pm 0.1) \times 10^{-3} \text{ g m}^{-2} \text{ d}^{-1}$ ; data are shown in Figure 1a. The initial dissolution rates, between 0 and 7 days, appeared to be more rapid than those between 7 and 35 days (Figure 1a), which may be due to solution saturation effects. Under the same dissolution conditions, but at 90 °C, the dissolution rate was significantly lower, at  $(7.26 \pm 0.2) \times 10^{-5} \text{ g m}^{-2} \text{ d}^{-1}$ , but the same trend was found, with an initial, rapid dissolution followed by a slower dissolution from 7 to 35 days (Figure 1b, Table 1). Dissolution of ThO<sub>2</sub> exhibited behavior different from that of CeO<sub>2</sub>, as shown in Figure 1c. At 90 °C, the dissolution was initially rapid (between 0 and 7 days, Figure 1c) at a rate of  $(6.71 \pm 0.5) \times 10^{-5} \text{ g m}^{-2} \text{ d}^{-1}$ , but subsequently the dissolution rate significantly decreased, giving an overall rate between 0 and 28 days of  $(5.23 \pm 0.1) \times 10^{-7} \text{ g m}^{-2} \text{ d}^{-1}$  (Table 1). Rapid dissolution could result from the release of material from high energy surface sites at the ThO<sub>2</sub> surface, leading to saturation of the solution with respect to Th, to a point at which amorphous ThO<sub>x</sub>(OH)<sub>y</sub>·H<sub>2</sub>O or even polynuclear Th<sub>x</sub>(OH)<sub>y</sub> species form. These amorphous phases are known to be capable of recrystallizing; for example, Rai et al.<sup>21</sup> showed that ThO<sub>2(am)</sub> converted to crystalline ThO<sub>2(cr)</sub> upon heating at 90 °C in acidic solution. Therefore, recrystallized ThO<sub>2</sub> may be able to form a protective layer on the surface of ThO<sub>2</sub>, providing a barrier to further dissolution and giving rise to the dissolution behavior observed in Figure 1c.

**3.2. Grain Boundaries.** Grain boundaries are a well-known feature of SNF; they typically contain volatile fission products (e.g., Cs and I) and alloy particles of Mo, Tc, Ru, Rh, and Pd.<sup>22</sup> The presence of these highly radioactive elements necessitates a careful understanding of how grain boundaries behave during dissolution, and an evaluation of their contribution to the dissolution rate of spent fuel. Figure 2 shows the typical microstructure obtained for CeO<sub>2</sub>; annealing conditions were optimized to give grain boundary depths of <1 μm.

The contribution of grain boundary dissolution to the overall dissolution rate of CeO<sub>2</sub> and ThO<sub>2</sub> was investigated in 0.01 M HNO<sub>3</sub> at 90 °C, and also at 150 °C for CeO<sub>2</sub>. Figure 3 shows VSI images of CeO<sub>2</sub> before dissolution (Figure 3a) and after 3 and 7 days of dissolution at 150 °C (Figure 3b and c, respectively). It was found that after 3 days, dissolution was focused at grain boundaries and the pores between grains

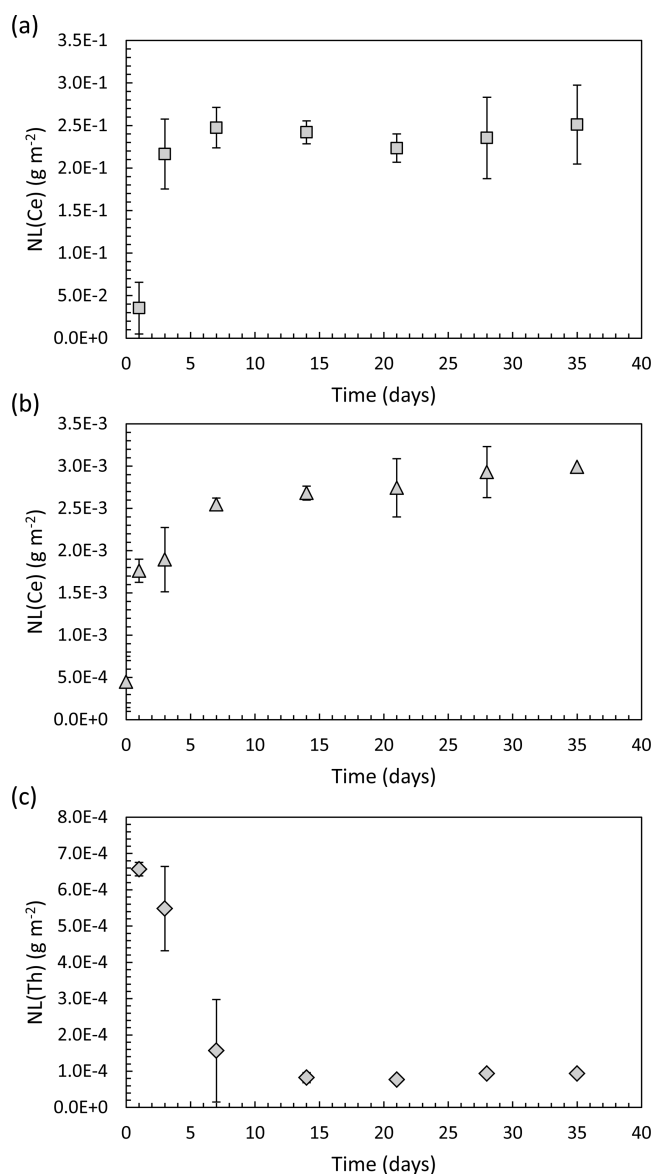


**Figure 1.** Normalized mass loss data for CeO<sub>2</sub> and ThO<sub>2</sub> dissolved in 0.01 M HNO<sub>3</sub>: (a) annealed CeO<sub>2</sub> at 150 °C; (b) annealed CeO<sub>2</sub> at 90 °C; and (c) annealed ThO<sub>2</sub> at 90 °C. Errors given are the standard deviation of triplicate experiments. Corresponding dissolution rates are shown in Table 1.

(Figure 3b). After 7 days, grain boundaries were preferentially dissolved, up to a depth of at least 0.70 μm, and the surface of the grains became rough and pitted (Figure 3c). Some of the grains dissolved at different rates, as evidenced by the height contrast in different grains (Figure 3b,c). In their analysis of CaF<sub>2</sub> dissolution (isostructural to CeO<sub>2</sub>, ThO<sub>2</sub>, and UO<sub>2</sub>), Godinho et al.<sup>23</sup> showed that the measured retreat rates of CaF<sub>2</sub> grains depended upon the crystallographic orientation of the exposed planes. They concluded that the {111} plane is the most stable and dissolved most slowly, while the {112} plane was the least stable, dissolving up to 33 times faster than {111}. First-principles calculations have shown that the surface stability of CeO<sub>2</sub> from the most to the least stable plane is in the order of {111} > {110} > {100},<sup>24,25</sup> although it should be noted that the {100} plane in such calculations is modeled and not real, due to the difficulties associated with modeling the dipolar {100} plane. The results presented here are in

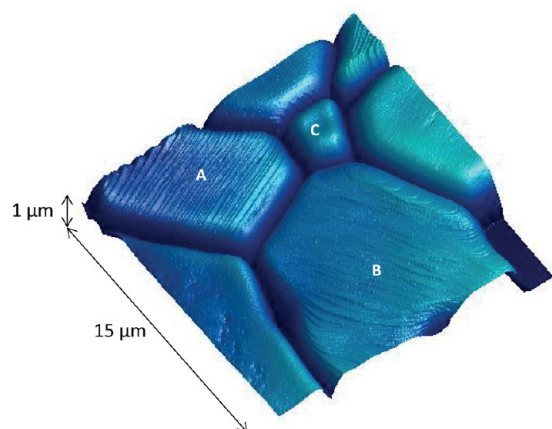


**Figure 2.** AFM image of  $\text{CeO}_2$  surface, showing grains, grain boundaries, pores, and facets. The labels A, B, and C correspond to detailed analysis of grain facets, where A shows facets generated through the intersection of  $\{665\}/\{\bar{1}11\}$  planes, B shows facets generated through the intersection of  $\{111\}/\{\bar{1}11\}$  planes, and C shows no facets.

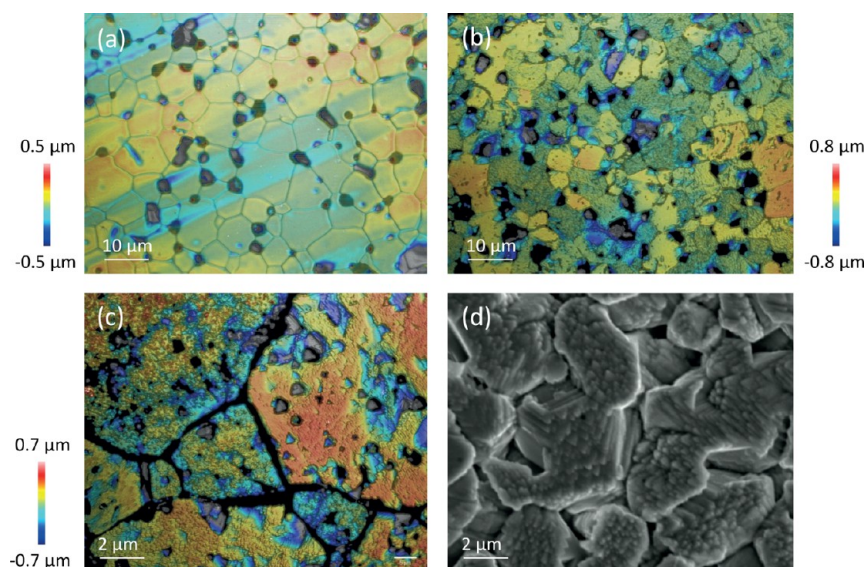
agreement with these findings; EBSD analysis of the grains in Figure 3c showed that the most stable grain had a (111) surface.

Figure 3d shows an SEM image of  $\text{CeO}_2$  after 21 days of dissolution. The grains became entirely detached from the surface and were considerably smaller than their original size prior to dissolution ( $\sim 5 \mu\text{m}$ , as compared to an initial size of  $10\text{--}30 \mu\text{m}$ ). The images in Figure 3 indicate that dissolution occurs preferentially along the grain boundaries, such that intergranular bonding becomes weakened with ongoing dissolution, eventually resulting in grain boundary decohesion. It is notable that the detached grains in Figure 3d exhibit triangular facets, indicative of  $\{111\}$  plane terminations, suggesting that surfaces that dissolve more slowly are the most stable, and persist during dissolution. Evidence for grain boundary decohesion in  $\text{CeO}_2$  under these dissolution conditions was confirmed by SEM analysis of monoliths in

cross section, with the surface of the grain just above the field of view. Figure 4a shows the cross section of a pristine, annealed sample of  $\text{CeO}_2$ . Grain boundaries were not observed in the top  $\sim 60 \mu\text{m}$  of the cross section. Monoliths of  $\text{CeO}_2$  that experienced dissolution for several durations are shown in Figure 4b–d. After 7 days, grains and grain boundaries were clearly visible (Figure 4b), and after 14 days entire grains appeared to become separated from one another (Figure 4c). After 21 days of dissolution, the grains appeared to decrease considerably in size to  $\sim 5 \mu\text{m}$ , in agreement with the surface topography shown in Figure 3d; close inspection revealed that the grains were, in fact, fractured between pores, giving rise to apparently smaller grains. These data confirm that grain boundary dissolution in  $\text{CeO}_2$  is extensive, and that grain boundaries may act as conduits for solution ingress, leading to dissolution and fracturing between pores. This process is expected to contribute substantially to the overall dissolution rate.

Analysis of the  $\text{CeO}_2$  sample used to provide solution data at  $90^\circ\text{C}$ , shown in Figure 1b, was performed using AFM and EBSD. Figure 5 shows the boundaries between several grains of different crystallographic orientation, including grain boundary “A” between surfaces of (025) and (001), and grain boundary “B” between surfaces of (001) and (356). EBSD analysis of these boundaries gave mean misorientation angles of  $36.01^\circ$  and  $59.84^\circ$ , respectively (Table 2). The dissolution of these boundaries was monitored over a period of 7 days (after which the surface became too rough to accurately measure) with reference to an inert surface mask of constant height. The mean surface retreat rates were measured as  $0.001$ ,  $0.032$ , and  $5.954 \text{ nm d}^{-1}$  for the (025), (001), and (365) surfaces, respectively, indicating surface stability in the order: (025) < (001) < (365).

The retreat rates of  $\text{CeO}_2$  grain boundaries were greater than the surface retreat rates between 0 and 1 days, and the retreat rate was different in different grain boundaries. Between 0 and 1 days of dissolution, the measured retreat of grain boundary A was  $0.13 \mu\text{m}$  on the (025) aspect and  $0.04 \mu\text{m}$  on the (001) aspect (Figure 5). Grain boundary B retreated more rapidly, increasing in depth by  $0.21 \mu\text{m}$  on the (001) aspect, and  $0.07$



**Figure 3.** Vertical scanning interferometer and SEM images of  $\text{CeO}_2$  surfaces (a) prior to dissolution and following dissolution for (b) 3 days, (c) 7 days, and (d) 21 days in  $0.01 \text{ M HNO}_3$  at  $150^\circ\text{C}$ .

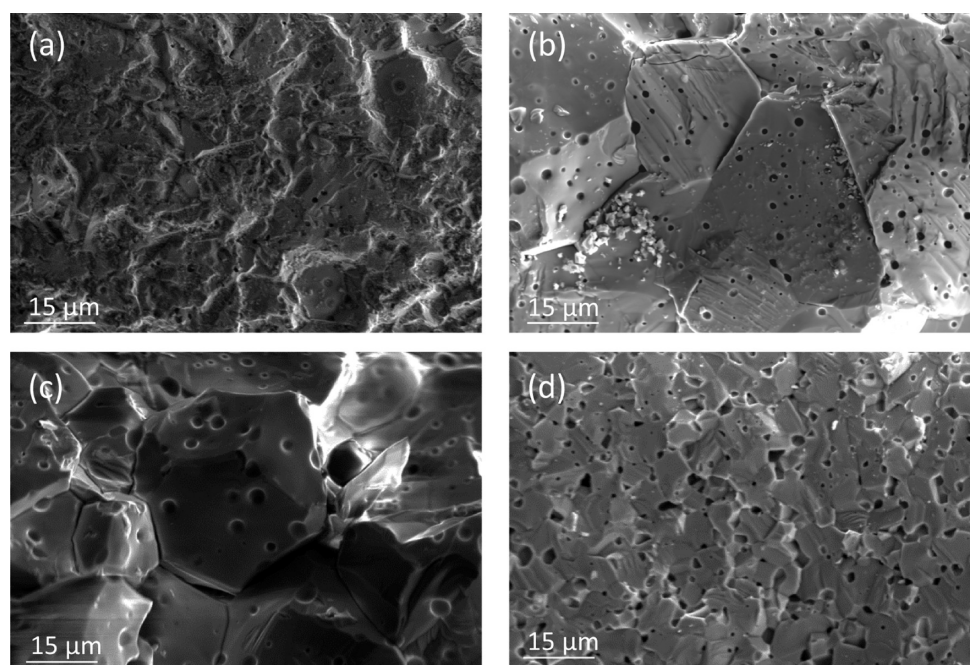


**Figure 4.** SEM images of cross sections through  $\text{CeO}_2$ , with the surface of the sample just above the top of each image: (a) nondissolved, annealed  $\text{CeO}_2$ ; and  $\text{CeO}_2$  dissolved in 0.01 M  $\text{HNO}_3$  at 150 °C for (b) 7 days, (c) 14 days, and (d) 21 days.

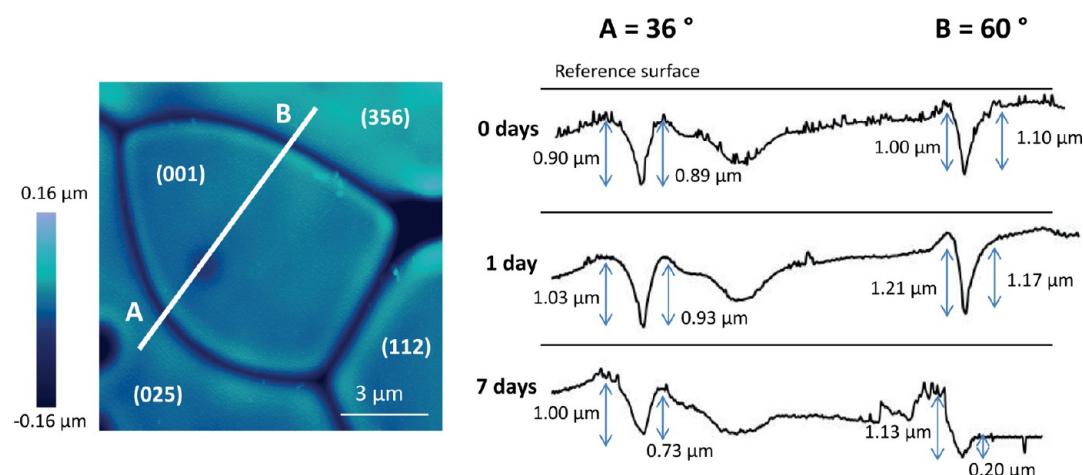


**Figure 5.** Atomic force microscopy image and cross sections of  $\text{CeO}_2$  grains, with grain boundaries of low (A) and high (B) misorientation angles. Grain surfaces are measured against an inert reference surface of constant height. Cross sections show change in depth of the grain boundaries and grain surfaces with time, during dissolution at 90 °C in 0.01 M  $\text{HNO}_3$ .

**Table 2.** Grain Boundary Depths of  $\text{CeO}_2$  (Corresponding to Figure 5) and  $\text{ThO}_2$  Grains with Different Grain Orientations and Grain Boundary Misorientation Angles, as a Function of Time during Dissolution in 0.01 M  $\text{HNO}_3$  at 90 °C

analogue composition	grain orientations	grain boundary misorientation angle (deg) ( $\pm 0.01$ )	grain boundary depth ( $\mu\text{m}$ )			grain boundary retreat rate ( $\mu\text{m d}^{-1}$ ) ( $\pm 0.001$ )
			0 days ( $\pm 0.01$ )	1 day ( $\pm 0.01$ )	7 days ( $\pm 0.01$ )	
$\text{CeO}_2$	(025)/(001)	36.01	0.90	1.03	1.00	0.014
	(001)/(356)	59.84	1.01	1.21	1.13	0.017
$\text{ThO}_2$	(103)/(506)	23.91	0.04	0.05	0.09	0.007
	(103)/(014)	39.33	0.06	0.14	0.15	0.012
	(416)/(506)	56.05	0.07	0.12	0.17	0.357

$\mu\text{m}$  on the (356) aspect (Figure 5). Grain boundaries became deeper during dissolution, suggesting the removal of material from within. Furthermore, the dissolution was greatest for the high misorientation angle boundary, as compared to the low misorientation angle grain boundary, giving grain boundary

retreat rates of 0.017 and 0.014  $\mu\text{m d}^{-1}$ , respectively (Table 2). After 7 days of dissolution, grain boundaries appeared to become shallower as a result of enhanced grain surface retreat at this time, especially for grain boundary B where the (356) surface dissolved very rapidly (Figure 5). In summary, when

CeO<sub>2</sub> samples were contacted with the dissolution medium, a rapid loss of material from grain boundaries occurred, which is in agreement with the enhanced release of Ce into solution during this time (Figure 1a). Subsequently, surface retreat rates increased, and the surface, or matrix, dissolution became the dominant dissolution mechanism. Comparison to the aqueous Ce concentrations in Figure 1a shows that the dissolution was less rapid after 7 days, confirming that grain boundary dissolution contributes significantly to the initial dissolution rate, while surface controlled dissolution leads to slower dissolution rates.

Similar experiments were conducted to monitor the dissolution of ThO<sub>2</sub> grain boundaries as a function of crystallographic orientation and grain boundary misorientation using AFM and EBSD (Table 2). The dissolution behavior of ThO<sub>2</sub> grain boundaries at 90 °C in 0.01 M HNO<sub>3</sub> was comparable to that of CeO<sub>2</sub>, whereby grain boundaries preferentially dissolved and boundaries with high misorientation angles retreated more rapidly than those with low misorientation angles. For example, a grain boundary between two grains with (103) and (506) surfaces had a misorientation angle of 23.91° and a retreat rate of 0.007 μm d<sup>-1</sup>, while another grain boundary formed between grains with (416) and (506) surfaces with a mean misorientation angle of 56.05° gave a retreat rate of 0.357 μm d<sup>-1</sup>, more than twice that of the lower misorientation angle grain boundary (Table 2). It should be noted that after 7 days of dissolution it was no longer possible to measure grain boundaries in ThO<sub>2</sub> due to the presence of a surface layer, giving further evidence to the hypothesis discussed above, that a dissolution rate drop after 7 days (Figure 1c) is due to the formation of a protective layer that results from the transformation of amorphous ThO<sub>x</sub>(OH)<sub>y</sub>·H<sub>2</sub>O to ThO<sub>2</sub>(cr) precipitates.

**3.3. Surface Facets.** Surface facets comprising flat terraces separated by inclined steps were found on annealed grains of CeO<sub>2</sub> (Figure 2). These features were not observed on ThO<sub>2</sub> because of its increased surface roughness, produced by difficulties encountered in polishing the sample. EBSD analysis of these grains was not possible due to multiple orientations arising from the faceted surfaces; however, alternative geometric measurements were used to determine the orientation of the facet features. By measuring the angle,  $\theta$ , between the facet and the surface, the best combination of planes can be found according to Maldonado et al.<sup>25</sup>

$$\theta = \arccos\left(\frac{\vec{u} \cdot \vec{v}}{|\vec{u}| |\vec{v}|}\right) \quad (3)$$

where  $\vec{u}$  and  $\vec{v}$  are the normal vectors that define the planes. Godinho et al.<sup>23</sup> showed that a dissolution surface is only made of the most stable planes, as the less stable ones are more prone to dissolution. Therefore, if we assume only the most stable planes are present at the surface, this method allows the unambiguous definition of the intersection of two distinct planes. Figure 6 illustrates this concept, showing the lateral view of a hypothetical surface comprised of two planes. These planes are the {111} and {100} planes, which intersect forming a facet with an angle  $\theta = 70.52^\circ/109.48^\circ$ .

Several different planar orientations of surface facets were observed. Grain "A" in Figure 2 exhibited regularly stepped facets across the surface of the grain, while grain "B" developed facets that increased in height from the center of the grain to the edge. According to den Brok and Morel,<sup>26</sup> these ridge and

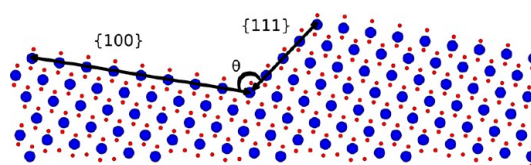


**Figure 6.** Lateral view of a hypothetical CeO<sub>2</sub> surface (large blue dots are O, small red dots are Ce), composed of the {100} and {111} surfaces, intersecting at an angle,  $\theta$ , of 70.52°/109.48° (rendered by VESTA).

valley features result from elastic strain released during annealing, lowering the surface energy. Some grains, for example, grain "C" (Figure 2), showed no facets. The facets on grain "A" enclosed an angle of  $106.83 \pm 2.1^\circ$ , indicative of a {665}/ $\{\bar{1}11\}$  plane intersection, which is known to have an angle of 107.04°. The height of these facets ranged from 4.66 to 16.71 nm, and the flat terraces between facets were consistently separated by distances of 5.74 nm. The facets on grain "B" (Figure 2) had planar orientations that met at an angle of  $110.33 \pm 1.6^\circ$ , indicative of a {111}/ $\{\bar{1}11\}$  facet orientation, which has a known angle of 109.47°. These facets ranged in height from 1.50 to 6.61 nm and had flat terraces of 24.06 nm (or multiples thereof). These {111}/ $\{\bar{1}11\}$  facets were themselves faceted, giving rise to a "zigzag" edge, as shown in Figure 7a. These "mini-facets" were found to be perpendicular to the  $\{\bar{1}11\}$  plane, suggestive of the plane {511}. The facet structures were also observed to extend into the grain boundaries (Figure 7b). Figure 7b–e shows detailed AFM images of another grain, which exhibited a ridge and valley-like morphology, with stacked concentric facets, building ridges at the grain edges (giving rise to the "tooth-shaped" grains shown in AFM profiles in Figure 5) and flat valleys in the center of the grain. The difference in height between the ridges and valleys for this grain was up to 150.36 nm. The facet heights ranged from 2.50 to 58.04 nm, were unevenly spaced at distances <20.02 nm, and enclosed an angle  $125.43 \pm 0.7^\circ$ . This is indicative of a {111}/{100} planar orientation, which has a known angle of 125.26°. It can be noted that all of the facets found at the surface of CeO<sub>2</sub> involve the most stable plane, {111}.

To understand the dissolution of the CeO<sub>2</sub> surface facets, samples were subjected to high acidity (pH <2) dissolution experiments. The surface shown in Figure 7b–e was subject to dissolution at room temperature in increasing concentrations of nitric acid, representing increasingly aggressive dissolution conditions. The resulting facet height measurements, corresponding to the facets between point 1 and point 8, shown in Figure 7e, are given in Table 3. It is clear that the addition of just 0.01 M HNO<sub>3</sub> resulted in a significant increase in height for most facets, as compared to the height prior to dissolution. Facet height increases ranged between 1.30 and 3.91 nm. Two facets were observed to become shallower (facets 2 and 5, Table 3). With increasing acidity between 0.1 and 3 M HNO<sub>3</sub>, facet height change was variable, with some facets showing little change (Table 3), while others decreased in height and others increased (suggesting addition of material to facets). This variability suggests that these surface sites are highly dynamic, changing in response to the reaction medium, but with little observable trend. However, it is clear that upon initial immersion in the reaction medium, instantaneous dissolution of the facets occurred.

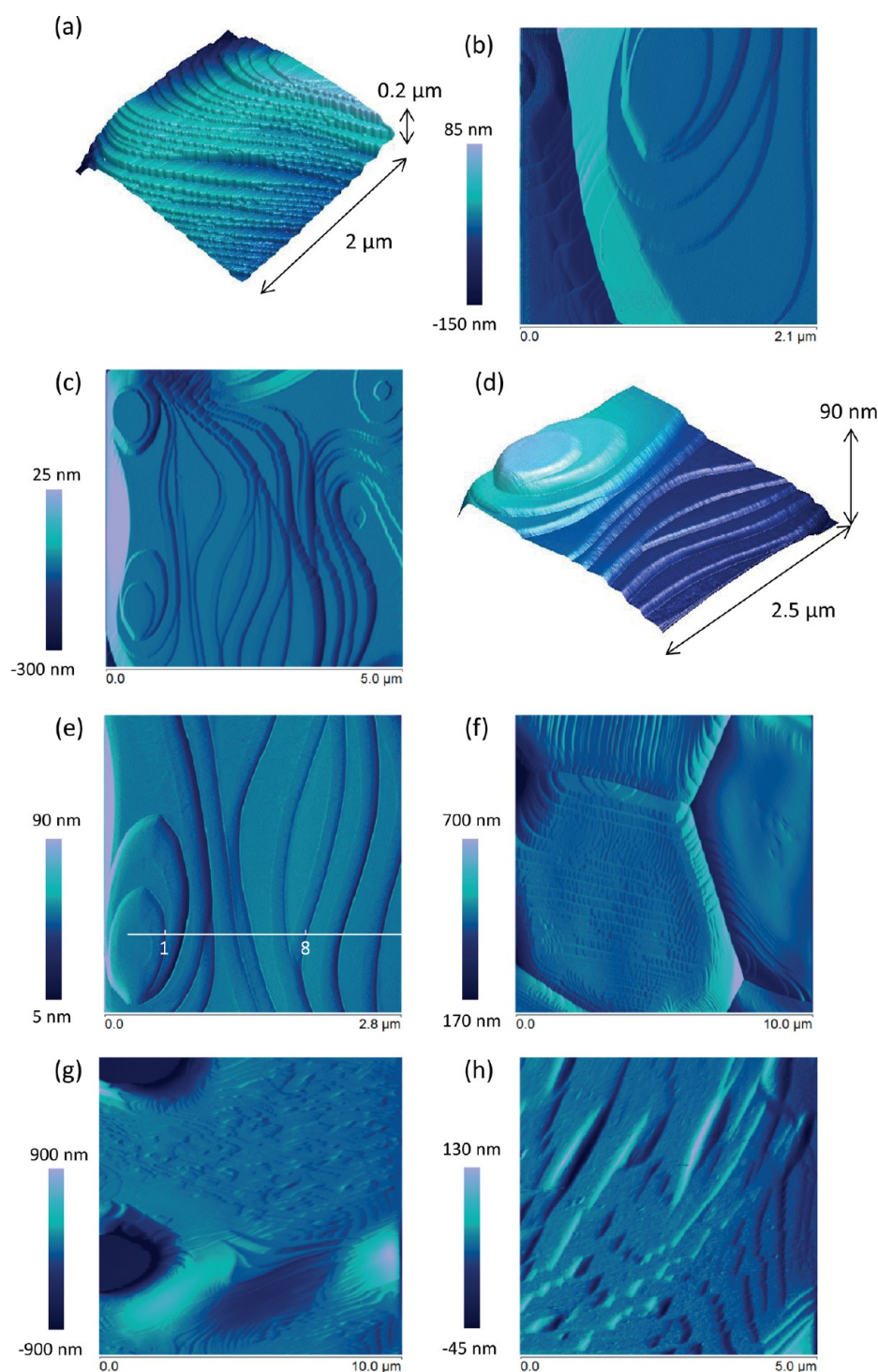


**Figure 7.** Atomic force microscopy images depicting surface features of CeO<sub>2</sub> spent nuclear fuel analogue surfaces: (a) showing  $\{\bar{2}11\}$  microfacets perpendicular to the plane  $\{\bar{1}11\}$ ; (b) facet structures extending into grain boundaries; (c) ridge and valley structure formed by intersecting  $\{111\}/\{100\}$  planes; (d and e) intersecting  $\{111\}/\{100\}$  planes showing cross section for step height measurements in Table 3; (f)  $\{\bar{2}11\}/\{\bar{1}11\}$  surface facets following dissolution in 15 M nitric acid at room temperature; and (g and h) etch pattern formed on previously smooth grains following etching in a series of media (UHQ water for 72 h, 0.001 M for 15 h, and 0.01 M HCl for 4 h) at room temperature. Images (a), (g), and (h) were taken in air, and all remaining images were taken in solution.

To investigate the effect of dissolution on the  $\{S11\}$  microfacets perpendicular to the  $\{\bar{1}11\}$  plane (grain “B”, Figure 2 and Figure 7a), a grain with these features was subject to dissolution in a 15 M HNO<sub>3</sub> solution at room temperature. The resulting surface is shown in Figure 7f. The effect of dissolution was increased microfacetting in the  $\{S11\}$  plane.

Even under these aggressive conditions, it was not possible to see any change in the smooth grains; therefore, the samples were etched in a series of media for a prolonged period (72 h in UHQ water, 15 h in 0.001 M HCl, and 4 h in 0.01 M HCl) at room temperature. The resulting AFM images show that the smooth grain became highly etched, forming “zigzag” features

Table 3. Facet Heights Measured from Figure 7e as a Function of HNO<sub>3</sub> Molarity

nitric acid concn (M)	facet height (nm) ( $\pm 0.01$ )							
	facet 1	facet 2	facet 3	facet 4	facet 5	facet 6	facet 7	facet 8
none	5.83	1.81	2.55	0.94	2.85	2.75	1.12	0.25
0.01	8.53	1.20	4.70	1.43	1.69	6.94	2.95	3.92
0.1	8.50	1.56	2.07	3.80	0.04	5.68	2.68	3.14
1.5	7.92	1.01	3.00	2.00	0.06	7.23	1.87	2.64
3	9.68	1.14	2.91	2.76	0.03	6.97	1.05	1.37

and triangular points (Figure 7g,h). Each etched layer was separated by steps, which were 30.01 nm in height (or multiples thereof). Triangular facets have been observed previously in etched CaF<sub>2</sub>,<sup>27</sup> forming lightening-shaped arrangements of intersecting (101) and (110) facets.

**3.4. Surface Treatment.** High energy surface sites may also be induced through specimen preparation, leading to over-estimated laboratory dissolution rates. Surfaces of CeO<sub>2</sub> were polished to a 0.05  $\mu\text{m}$  finish and subject to dissolution at 150  $^{\circ}\text{C}$  in 0.01 M HNO<sub>3</sub>. Dissolution data were compared to those for annealed surfaces. Figure 8 shows VSI images of the surface

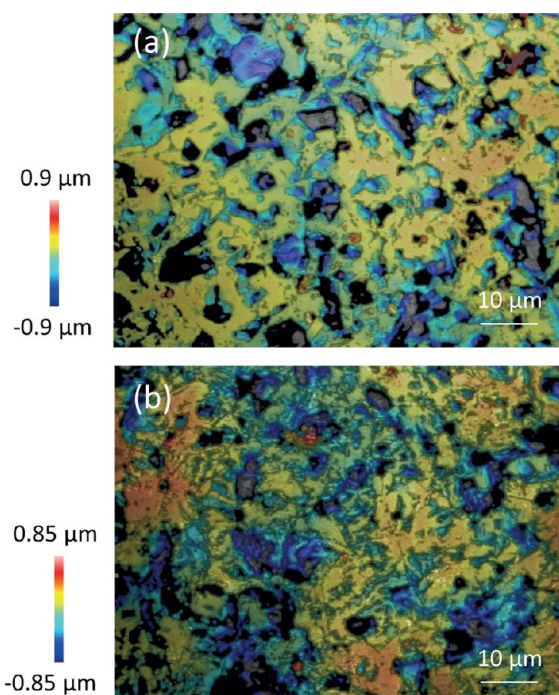


Figure 8. Polished CeO<sub>2</sub> surfaces after dissolution in 0.01 M HNO<sub>3</sub> at 150  $^{\circ}\text{C}$  for (a) 3 days and (b) 14 days.

of a polished monolith after 3 and 14 days of dissolution (Figure 8a,b, respectively). During initial dissolution, the surfaces were rough and pitted, and after 14 days exhibited areas of high and low topography, indicating further dissolution had occurred. It was found that the dissolution rate was an order of magnitude greater for the polished surface than for an annealed CeO<sub>2</sub> surface under the same conditions (Table 2). At 90  $^{\circ}\text{C}$ , the effect was similar; however, the dissolution rate of the polished surface was found to be 3 orders of magnitude greater than that of an annealed surface, with rates of  $(7.40 \pm 0.2) \times 10^{-2}$  and  $(7.26 \pm 0.2) \times 10^{-5}$  g m<sup>-2</sup> d<sup>-1</sup> for polished and annealed surfaces, respectively (Table 1).

## 4. DISCUSSION

In the results presented above, we have observed that surface features act as energetically reactive surface sites that transform during dissolution. These features can be classified into two categories: (i) natural surface features, that is, grain boundaries; and (ii) specimen preparation-induced features, that is, surface facets and polishing defects. The dissolution of these features in CeO<sub>2</sub> and ThO<sub>2</sub> is discussed below, with comparison to the dissolution behavior of UO<sub>2</sub>. It should be noted that while the chemical and redox characteristics of the analogue materials investigated here are simple when compared to those of spent fuel, it is possible to draw comparisons between CeO<sub>2</sub>, ThO<sub>2</sub>, and spent fuel that focus only on the physical and structural properties that give rise to the dissolution behavior observed. As such, in the discussion that follows, only microstructural surface features that affect dissolution are described, with a cautious interpretation for the overall behavior of spent fuel during dissolution.

**4.1. Grain Boundary Dissolution.** The results presented in this investigation give evidence that UO<sub>2</sub> and spent nuclear fuel analogue grain boundaries undergo extensive transformation during dissolution; material is rapidly removed from grain boundaries in both CeO<sub>2</sub> and ThO<sub>2</sub>, corresponding to rapid initial dissolution rates. It is hypothesized that grain boundaries are effective sinks for atomic defect high energy sites;<sup>28</sup> the greater the number of defects, the greater the proportion of high energy surface sites for dissolution. In CeO<sub>2</sub>, it has been shown that increasing the density of oxygen vacancy defects results in an increase in the dissolution rate. For example, Horlait et al.<sup>29,30</sup> showed that for every 10% of Ln<sup>3+</sup> cations added to CeO<sub>2</sub>, for which charge compensation through the formation of Ce<sup>3+</sup> occurred, the dissolution rate increased by 1 order of magnitude.<sup>28</sup> Hojo et al.<sup>31</sup> demonstrated an enrichment of Ce<sup>3+</sup> in grain boundaries as compared to the grain surfaces, indicative of a higher density of oxygen vacancy defects within the grain boundaries as compared to the surface. In UO<sub>2</sub>, evidence for defects within grain boundaries is found in the form of nonstoichiometric UO<sub>2+x</sub>. For example, Une and Kashibe<sup>32</sup> identified the presence of UO<sub>2.25</sub> within grain boundaries following dissolution of UO<sub>2</sub>, while O'Neil et al.<sup>17</sup> made the observation that grain boundaries in UO<sub>2</sub> were highly conductive, which was attributed to a high concentration of oxygen interstitial ions arising from hypo-stoichiometric UO<sub>2+x</sub>. This suggests that defects, and especially those that are concentrated within grain boundaries, may play a key role in the dissolution of UO<sub>2</sub> and its analogues. In spent fuel, grain boundaries are expected to contain more defects than laboratory-prepared UO<sub>2</sub> or UO<sub>2</sub> analogues, primarily due to the accumulation of fission gas bubbles and metallic precipitates;<sup>33</sup> therefore, the effects of such high energy surface sites might be expected to be greater.

We have observed that crystallographic orientation of the grains plays an important role in the dissolution of the grain boundaries of spent nuclear fuel analogues; grain boundaries with a high misorientation angle were found to dissolve more rapidly than those with a low misorientation angle in the current study. We hypothesize that high misorientation grain boundaries have a higher concentration of defects (or defect clusters) than grain boundaries with low misorientation angles. Indeed, simulations of  $\text{UO}_2$  grain boundaries have shown that different types of defect structure were present in grain boundaries, depending on the misorientation angle;<sup>34</sup> in grain boundaries with lower misorientation angles, edge dislocations were the most common defect, while in higher misorientation angle boundaries, oxygen point defects dominated the grain boundary structure.

Assessment of the safety of geological disposal of spent nuclear fuel requires detailed information on the rates and mechanism of release of radionuclides. This is hypothesized to occur in two main stages: (i) the so-called “instant release fraction” (IRF), which represents a rapid release of long-lived and geochemically mobile radionuclides (e.g.,  $^{129}\text{I}$ ,  $^{36}\text{Cl}$ ,  $^{135}\text{Cs}$ ,  $^{99}\text{Tc}$ ); and (ii) the slow, long-term release of radionuclides from the  $\text{UO}_2$  matrix.<sup>35,36</sup> The IRF is considered to come from two regions of the spent fuel: the gap between the cladding and the fuel, and the grain boundaries. However, the IRF rates are still largely unknown, and the contribution of grain boundary dissolution is not fully understood; in fact, there is some controversy in the literature as to whether grain boundaries make any significant contribution to the IRF.<sup>36,37</sup> The results presented in the current work, which demonstrate an “instant release fraction” of Ce and Th from the spent fuel analogues, which is directly linked to grain boundary dissolution, support the hypothesis that grain boundaries contribute to the IRF in spent fuel, and suggest that crystallographic direction of the grains and the density of defects within the grain boundary may play a role. However, it should be noted that the IRF of spent fuel is largely governed by the complicated chemical composition of the grain boundaries; therefore, the extent to which structural defects and grain boundary misorientation between adjacent grains contribute to the IRF is unknown in comparison to the chemical effects. Our results are also in agreement with the hypothesis that a second, slower stage of spent fuel dissolution occurs; in both  $\text{CeO}_2$  and  $\text{ThO}_2$ , dissolution rates were lower after the initial release. In  $\text{ThO}_2$  it was apparent that this second stage of dissolution was impeded by the formation of a protective layer. A similar effect was found in laboratory  $\text{UO}_2$  dissolution experiments, where secondary U-bearing alteration products formed a protective layer, preventing further dissolution.<sup>38</sup> On the basis of the data and arguments presented here, it is evident that grain boundary dissolution in spent fuel and spent fuel analogues requires further detailed chemical and physical analysis and that geological disposal safety performance assessment should carefully consider the contribution of grain boundaries to the dissolution rate.

**4.2. Dissolution of Specimen Preparation-Induced Features.** We show that dissolution occurs at facet edges, especially during initial contact with dissolution medium. With increasingly aggressive dissolution media, the dissolution of these features does not show a particular trend, but instead appears to experience a dynamic process, whereby facet heights constantly change in response to the dissolution medium. We have also shown that each facet contains some aspect of the

{111} plane, which is the most stable plane in fluorite-type structures, suggesting that crystallographic orientation also plays an important role in facet formation.

It is thought that facets form by a dislocation growth mechanism during annealing, where spiral-like structures form around threading dislocations likely induced through surface preparation (e.g., polishing). Each dislocation produces a step as it emerges at the surface.<sup>39,40</sup> O’Neil et al.<sup>17</sup> and He and Shoosmith<sup>40</sup> described surface morphologies similar to those identified in the current study in  $\text{UO}_2$ . Current-sensing AFM analysis showed that  $\text{UO}_2$  grains with facets were highly conducting, while smooth grains were not. Raman and EDX investigation of these features revealed a high degree of nonstoichiometry in the  $\text{UO}_2$  of faceted grains, attributed to the incorporation of interstitial oxygen atoms to locations in the {110} direction, accompanied by shifts in vacant sites in the {111} direction. It was concluded that these nonstoichiometric, defect-containing features would be more vulnerable to dissolution than defect-free surfaces. Further investigations are currently underway to understand the relative stability of different facet orientations, their degree of nonstoichiometry, and defect structures. It is clear that these high energy surface sites play a role in dissolution, but the evidence presented here suggests that the influence on dissolution rate is not as significant as that of grain boundaries. It is important to note that these features are present as a result of specimen preparation and annealing, and thus are likely to contribute to the potential overestimation of dissolution rates in the laboratory. These features are not expected to be present in spent nuclear fuel.

We found that polished surfaces of spent nuclear fuel analogues gave dissolution rates of up to 3 orders of magnitude greater than for annealed surfaces. Polishing has been shown to introduce strain and defects into oxide material surfaces, giving rise to high surface energy. For example, diamond paste polishing has been shown to result in the formation of dislocation loops, other lattice defects, and also high surface strain.<sup>41,42</sup> Thermally annealing the surface of  $\text{CeO}_2$  allowed the strain and defects to be relaxed due to recovery processes during heating, lowering the surface energy, and thus lowering the dissolution rate. It is possible that defects induced during polishing may act as nucleation sites for the observed facet structures formed during annealing. These results show that the introduction of defects to the surface through polishing can lead to a significant increase in the observed dissolution rate, demonstrating the importance of careful specimen preparation for dissolution rate determination.

## 5. CONCLUSIONS

Dissolution experiments were conducted on non-redox sensitive, isostructural  $\text{UO}_2$  and SNF analogues,  $\text{CeO}_2$  and  $\text{ThO}_2$ , to investigate the contribution of energetically reactive surface sites to dissolution, and to determine whether their presence may lead to an overestimation of dissolution rates. Grain boundaries, which are part of the natural texture of SNF, were shown to significantly enhance the dissolution rate, dissolving preferentially in the initial stages of dissolution, supporting hypotheses that grain boundaries contribute to the instant release fraction of spent fuel. A strong crystallographic control was exerted, with high misorientation grain boundaries dissolving more rapidly than those with low misorientation angles in both  $\text{CeO}_2$  and  $\text{ThO}_2$ . It was hypothesized that different crystallographic directions can accommodate different

densities of defects, explaining the observations found. Further investigation is required to ascertain the extent to which structural defects and grain boundary misorientation between adjacent grains contribute to the instant release fraction of SNF, in comparison to the chemical effects.

In addition to the natural high energy surface sites found in grain boundaries, energetically reactive sites were also found to be formed through sample preparation. Facet structures formed during annealing, likely nucleated on defects sites on polished surfaces, also exhibited a strong crystallographic control (all combined some aspect of the {111} plane), and upon introduction to dissolution media, they experienced instantaneous dissolution. Finally, the effect of surface polishing on the dissolution rate was found to increase dissolution rates by up to 3 orders of magnitude. This results from induction of strain and defects in the surface during the polishing process. We have shown that defects induced through sample preparation contribute to the dissolution rate. The dissolution from facets is low, and therefore not likely to significantly overestimate long-term dissolution rates; however, sample polishing without any further treatment is likely to cause overestimation of dissolution rates.

## AUTHOR INFORMATION

### Corresponding Authors

\*Tel.: +44 (0)1142226036. E-mail: c.corkhill@sheffield.ac.uk.

\*Tel.: +44 (0)1142224570. E-mail: n.c.hyatt@sheffield.ac.uk.

### Notes

The authors declare no competing financial interest.

## ACKNOWLEDGMENTS

The research leading to these results has received funding from the European Atomic Energy Community's Seventh Framework Programme (FP7) under grant agreement no. 269903, The REDUPP (REDucing Uncertainty in Performance Prediction) project. Special thanks goes to J. Godinho for assistance with vertical scanning interferometry. We are grateful to Dr. Virginia Oversby and Dr. Lena Z. Evins for invaluable discussion and support throughout the project. C.L.C. is grateful to The University of Sheffield for the award of a Vice Chancellor's Fellowship, N.C.H. acknowledges support from the Royal Academy of Engineering and the Nuclear Decommissioning Authority for funding, and D.J.B. and S.M.T. acknowledge financial support from the EPSRC Nuclear FIRST Doctoral Training Centre (EP/G037140/1). We are grateful to the anonymous reviewers of this contribution, for their insightful comments and suggestions, which have greatly improved the manuscript.

## REFERENCES

- (1) Oversby, V. M. Uranium Dioxide, SIMFUEL and Spent Fuel Dissolution Rates – A Review Of Published Data. *SKB Tech. Rep.*, 1999, TR-99-22.
- (2) Shoesmith, D. W. Used Fuel and Uranium Dioxide Dissolution Studies – A Review. *Nucl. Waste Manage. Org. Rep.* **2007**, NMWO TR-2007-03.
- (3) Fuel and Canister Process Report for the Safety Assessment SR-Site. *SKB Tech. Rep.*, 2010, TR-10-46.
- (4) Smellie, J.; Karlson, F. A Reappraisal of some Cigar Lake Issues of Importance to Performance Assessment. *SKB Tech. Rep.*, 1996, TR 96-08.
- (5) Gauthier-Lafaye, F.; Holliger, P.; Blanc, P. L. Natural Fission Reactors in the Franceville Basin, Gabon: A Review of the Conditions

and Results of a "Critical Event" in a Geologic System. *Geochim. Cosmochim. Acta* **1996**, *60*, 4831–4852.

- (6) Knauss, P.; Wolery, T. J. Dependence of Albite Dissolution Kinetics on pH and Time at 25 °C and 70 °C. *Geochim. Cosmochim. Acta* **1986**, *50*, 2481–2497.

- (7) White, A. F.; Bullen, T. D.; Schulz, M. S.; Blum, A. E.; Huntington, T. G.; Peters, N. E. Differential Rates of Feldspar Weathering in Granitic Regoliths. *Geochim. Cosmochim. Acta* **2001**, *65*, 847–867.

- (8) White, A. F.; Brantley, S. L. The Effect of Time on the Weathering of Silicate Minerals: Why do Weathering Rates Differ in the Laboratory and Field? *Chem. Geol.* **2003**, *202*, 479–506.

- (9) Zhu, C.; Veblen, D. R.; Blum, A. E.; Chipera, S. J. Naturally Weathered Feldspar Surfaces in the Navajo Sandstone Aquifer, Black Mesa, Arizona: Electron Microscopic Characterisation. *Geochim. Cosmochim. Acta* **2006**, *70*, 4600–4616.

- (10) Brantley, S. L.; Crane, S. R.; Creear, D.; Hellmann, R.; Stallard, R. Dissolution at Dislocation Edge Pits in Quartz. *Geochim. Cosmochim. Acta* **1986**, *50*, 2349–2361.

- (11) Blum, A. E.; Lasaga, A. C. Monte Carlo Simulations of Surface Reaction Rate Laws. In *Chemical Weathering Rates of Silicate Minerals*; Stumm, W., Ed.; Mineralogical Society of America: 1987; Vol. 31, pp 291–351.

- (12) Ollila, K.; Oversby, V. M. Dissolution of Unirradiated UO<sub>2</sub> and UO<sub>2</sub> Doped with <sup>233</sup>U Under Reducing Conditions. *SKB Tech. Rep.*, 2005, TR-05-07.

- (13) Ollila, K. Dissolution of Unirradiated UO<sub>2</sub> and UO<sub>2</sub> Doped with <sup>233</sup>U in 0.01M NaCl Under Anoxic and Reducing Conditions. *Posiva Oy Rep.* **2006**, 2006–08.

- (14) Claparede, L.; Clavier, N.; Dacheux, N.; Moisy, N.; Podor, R.; Ravaux, J. Influence of Crystallisation State and Microstructure on the Chemical Durability of Cerium-Neodymium Mixed Oxides. *Inorg. Chem.* **2011**, *50*, 9059–9072.

- (15) Stennett, M. C.; Corkhill, C. L.; Marshall, L. A.; Hyatt, N. C. Preparation, Characterisation and Dissolution of a CeO<sub>2</sub> Analogue for UO<sub>2</sub> Nuclear Fuel. *J. Nucl. Mater.* **2013**, *432*, 182–188.

- (16) Evins, L. Z.; Juhola, P.; Vahanen, M. REDUPP Final Report. *Posiva Oy Rep.* **2014**, 2014–12.

- (17) O'Neil, K. D.; He, H.; Keech, P.; Shoesmith, D. W.; Semenikhin, O. A. Anisotropy of Local Conductivity of Hyper-Stoichiometric Uranium Dioxide Revealed by Current-Sensing Atomic Force Microscopy (CS-AFM). *Electrochem. Commun.* **2008**, *10*, 1805–1808.

- (18) Lucuta, P. G.; Verall, V. R.; Maztke, H.; Palmer, B. J. Microstructural Features of SIMFUEL – Simulated High-Burnup UO<sub>2</sub>-Based Nuclear Fuel. *J. Nucl. Mater.* **1991**, *178*, 48–60.

- (19) Papin, P.; Chen, C.-F.; Forsyth, R.; Luther, E.; Necker, C. Surface Preparation for Characterising Microstructure on Transuranic Oxides by Electron Backscatter Spectroscopy and Ion Beam Imaging. *Microsc. Microanal.* **2012**, *18*, 708.

- (20) ASTM. *Standard Test Methods for Determining Chemical Durability of Nuclear, Hazardous and Mixed Waste Glasses and Multiphase Ceramics: The Product Consistency Test (PCT)*; ASTM C 1285-02; American Society for Testing and Materials: Philadelphia, PA, 2008.

- (21) Rai, D.; Moore, D. A.; Oakes, C. S.; Yui, M. Thermodynamic Model for the Solubility of Thorium Dioxide in the Na-Cl-OH-H<sub>2</sub>O System at 23 °C and 90 °C. *Radiochim. Acta* **2000**, *88*, 297–306.

- (22) Cui, D.; Low, J.; Spahiu, K. Environmental Behaviours of Spent Nuclear Fuel and Canister Materials. *Energy Environ. Sci.* **2011**, *4*, 2537–2545.

- (23) Godinho, J.; Piazzolo, S.; Evins, L. Z. Effect of Surface Orientation on Dissolution Rates and Topography of CaF<sub>2</sub>. *Geochim. Cosmochim. Acta* **2012**, *86*, 392–403.

- (24) Yang, Z.; Woo, T. K.; Baudin, M.; Hermannsson, K. Atomic and Electronic Structure of Unreduced and Reduced CeO<sub>2</sub> Surfaces: A First-Principles Study. *J. Chem. Phys.* **2004**, *120*, 7741–7749.

- (25) Maldonado, P.; Godinho, J.; Evins, L. Z.; Oppeneer, P. M. Ab initio Prediction of Surface Stability of Fluorite Materials and Experimental Verification. *J. Phys. Chem. C* **2013**, *117*, 6639–6650.

(26) den Brok, S. W. J.; Morel, J. The Effect of Elastic Strain on the Microstructure of Free Surfaces of Stressed Minerals in Contact with an Aqueous Solution. *Geophys. Res. Lett.* **2001**, *28*, 603–606.

(27) Englehardt, J. B.; Dabringhaus, H.; Wandelt, K. Atomic Force Microscopy Study of the  $\text{CaF}_2$  (111) Surface: From Cleavage via Island to Evaporation topographies. *Surf. Sci.* **2000**, *448*, 187–200.

(28) Horlait, D.; Claparede, L.; Tocino, F.; Clavier, N.; Ravau, J.; Szenknect, S.; Podor, R.; Dacheux, N. Environmental SEM Monitoring of  $\text{Ce}_{1-x}\text{Ln}_x\text{O}_{2-x/2}$  Mixed-Oxide Microstructural Evolution During Dissolution. *J. Mater. Chem. A* **2014**, DOI: 101039/c3ta14623e.

(29) Horlait, D.; Clavier, N.; Szenknect, S.; Dacheux, N.; Dubois, V. Dissolution of Cerium(IV)- Lanthanide(III) Oxides: Comparative Effect of Chemical Composition, Temperature, and Acidity. *Inorg. Chem.* **2012**, *51*, 3868–3878.

(30) Horlait, D.; Tocino, F.; Clavier, N.; Dacheux, N.; Szenknect, S. Multiparametric Study of  $\text{Th}_{(1-x)}\text{Ln}_{(x)}\text{O}_{(2-x/2)}$  Mixed Oxides Dissolution in Nitric Acid Media. *J. Nucl. Mater.* **2012**, *429*, 237–244.

(31) Hojo, H.; Mizoguchi, T.; Ohta, H.; Findlay, S. D.; Shibata, N.; Yamamoto, T.; Ikuhara, Y. Atomic Structure of a  $\text{CeO}_2$  Grain Boundary: The Role of Oxygen Vacancies. *Nano Lett.* **2010**, *10*, 4668–4672.

(32) Une, K.; Kashibe, S. Corrosion Behaviour of Irradiated Oxide Fuel Pellets in High Temperature Water. *J. Nucl. Mater.* **1996**, *232*, 240–247.

(33) Marchetti, I.; Carbol, P.; Himbert, J.; Belloni, F.; Fanghanel, T. Room-Temperature Diffusion Coefficients for Oxygen and Water in  $\text{UO}_2$  Matrices: A SIMS Study. *Surf. Interface Anal.* **2013**, *45*, 360–363.

(34) Van Brutzel, L.; Vincent-Aublant, E. Grain Boundary Influence on Displacement Cascades in  $\text{UO}_2$ : A Molecular Dynamics Study. *J. Nucl. Mater.* **2008**, *377*, 522–527.

(35) Johnson, L. H.; Tait, J. C. Release of Segregated Radionuclides from Spent Fuel. *SKB Tech. Rep.*, 1997, TR-97-18.

(36) Johnson, L.; Gunther-Leopold, I.; Kobler Waldis, J.; Linder, H. P.; Low, J.; Cui, D.; Ekeroth, E.; Spahiu, K.; Evins, L. Z. Rapid Aqueous Release of Fission Products from High Burn-Up LWR Fuel: Experimental Results and Correlations with Fission Gas Release. *J. Nucl. Mater.* **2012**, *420*, 54–62.

(37) Serrano-Purroy, D.; Clarens, F.; Gonzalez-Robles, E.; Glatz, J. P.; Wegen, D. H.; de Pablo, J.; Casas, I.; Gimenez, J.; Martinez-Esparza, A. Instant Release Fraction and Matrix Release of High Burn-Up  $\text{UO}_2$  Spent Nuclear Fuel: Effect of High Burn-Up Structure and Leaching Solution Composition. *J. Nucl. Mater.* **2012**, *427*, 249–258.

(38) Wronkiewicz, D. J.; Buck, E. C.; Bates, J. K. Grain Boundary Corrosion and Alteration Phase Formation During the Oxidative Dissolution of  $\text{UO}_2$  Pellets. *Mater. Res. Soc. Symp. Proc.* **1997**, *465*, 519.

(39) Schick, M.; Dabringhaus, H.; Wandelt, K. Macrosteps on  $\text{CaF}_2$  (111). *J. Phys.: Condens. Matter* **2004**, *16*, L33–L37.

(40) He, H.; Shoesmith, D. W. Raman Spectroscopic Studies of Defect Structures and Phase Transition in Hyper-Stoichiometric  $\text{UO}_{2+x}$ . *Phys. Chem. Chem. Phys.* **2010**, *12*, 8108–8117.

(41) Johansson, S.; Schweitz, J.; Lagerlof, K. P. D. Surface Defects in Polished Silicon Studied by Cross-Sectional Transmission Electron Microscopy. *J. Am. Ceram. Soc.* **1989**, *72*, 1136–1139.

(42) Saito, T.; Hirayama, T.; Yamamoto, T.; Ikuhara, Y. Lattice Strain and Dislocations in Polished Surfaces on Sapphire. *J. Am. Ceram. Soc.* **2005**, *88*, 2277–2285.